JOURNAL
AerospaceLab

ONERA
THE FRENCH AEROSPACE LAB

return on innovation

Issue 9
June 2015

DOI : 10.12762/2015.AL09

Life Prediction Methodologies for Materials and Structures

Publisher
Stéphane Andrieux

Editor in Chief
Alain Appriou

Production
ONERA Scientific
Information Department

On line
www.aerospacelab-journal.com
Webmaster ONERA

Contact
E-mail: aerospacelab@onera.fr

Produced by
Onera - BP 80100
Chemin de la Hunière
et des Joncherettes
91123 PALAISEAU CEDEX
France
www.onera.fr

ISSN: 2107-6596

Serge Kruch
(ONERA)
Special Adviser Coordination of Activities Mechanical Couplings and Materials
Metallic Materials and Structures Department

Esteban Busso
(ONERA)
Scientific Director of the Materials and Structures Branch

DOI : 10.12762/2014.AL09-00

Introduction to Life Prediction Methodologies for Materials and Structures

In his book “Citadelle» Antoine de Saint Exupéry wrote “Intelligence examines the material while the mind only sees the ship”. Such a quote sets the context of this issue of ONERA’s Aerospace Lab Journal entitled “Life Prediction Methodologies for Materials and Structures” very well. In order to predict the mechanical integrity and lifetime of complex components and structures, it is essential to understand the physical mechanisms that control local deformation and damage phenomena at the relevant scales in the material. This issue of the Aerospace Lab Journal addresses this problem by providing a forum for some of the leading members of the mechanics of materials community to report on recent theoretical and computational modeling approaches to describe the mechanics of materials at scales ranging from the atomistic, through the microstructure, and up to the continuum. A broad range of materials and physical phenomena are addressed, including metallic and composite materials, dislocation behavior, crystallographic slip, fatigue and damage, and other macroscopic and structural behavior.

This issue contains the eleven invited contributions that have successfully gone through the standard review process of the journal. They reflect the strong interactions between universities, research institutes and industry in the topic of this issue, and underline the importance and challenging nature of the scientific issues addressed.

The various topics covered range from the defect and microstructural scales (dislocations in Articles 1 and 2, and individual grains in Articles 3 and 9) to the structure scale (Article 6), including intermediate scales described by various continuum mechanics approaches (Articles 4, 5, 7, 8 and 11). Furthermore, Article 10 deals with the thermodynamic aspects governing the evolution of superalloy microstructures. Two articles discuss approaches developed to predict the deformation, damage and fatigue behavior of composite materials. This includes topics that have not been widely reported in the literature, such as the behavior of composite materials subjected to dynamic and crash loads, addressed in Article 4, or the treatment of fatigue damage discussed in Article 6.

Contributions to this issue scan the entire life prediction workflow of a structure, which can be broken down into the following steps:

- Observations and characterization of the material microstructure.
- Measurements and prediction of the local strain and stress fields, which control local deformation and damage phenomena.
- Determination of the component and/or structure behavior through the stress redistributions within the structure.
- Identification, through adequate fatigue damage laws, of the number of cycles for crack initiation.
- Determination of either stable or unstable crack growth behavior, including catastrophic failure.

While these steps are consistent with current practices, there are still challenges to be addressed in the coming years. Indeed, it would be unrealistic to propose a structural analysis today where the material behavior is described at, for instance, the defect level by discrete dislocation dynamics, or by explicitly accounting for all of the heterogeneities in a composite material even though theoretical tools are available for some idealized cases. Despite such challenges, the scientific community continues to work towards developing closer integration of the various modeling and life prediction approaches.

Finally, we would like to thank all of the authors for their contributions to what we hope will be an important reference in the field, as well as the reviewers who spent a considerable amount of time commenting on the scientific merits of the manuscripts. It is hoped that this collection of overview articles will provide readers with the current state-of-the-art in some of the key modeling approaches required to predict the mechanical integrity of components and structures on the basis of physical principles ■

References

[1] C. DÉPRÉS, C. ROBERTSON, M. FIVEL - *3D Discrete Dislocation Dynamics Investigations of Fatigue Crack Initiation and Propagation.* Aerospace Lab Issue 09, june 2015

[2] B. DEVINCRE, R. GATTI - *Physically Justified Models for Crystal Plasticity Developed with Dislocation Dynamics Simulations.* Aerospace Lab Issue 09, june 2015

[3] E. BUSSO - *On the Deformation Heterogeneities Described by Crystal Plasticity.* Aerospace Lab Issue 09, june 2015

[4] E. DELETOMBE, J. BERTHE, D. DELSART, J. FABIS, B. LANGRAND, G. PORTEMONT - *Experimental and Numerical Simulation Strategies for the Prediction of the Macroscopic Behaviour and Rupture of Structural Materials under Fast Dynamic Loadings.* Aerospace Lab Issue 09, june 2015

[5] R. DESMORAT, A. DU TERTRE, P. GABORIT - *Multiaxial Haigh Diagrams from Incremental Two Scale Damage Analysis.* Aerospace Lab Issue 09, june 2015

[6] M. KAMINSKI, F. LAURIN, J.-F. MAIRE, C. RAKOTOARISOA, E. HÉMON - *Fatigue Damage Modeling of Composite Structures: the ONERA Viewpoint.* Aerospace Lab Issue 09, june 2015

[7] J. CORMIER, F. MAUGET, J.-B. LE GRAVEREND, C. MORICONI - *Issues Related to the Constitutive Modeling of Ni-Based Single Crystal Superalloys under Aeroengines Certification Conditions.* Aerospace Lab Issue 09, june 2015

[8] S. KRUCH, P. KANOUTE, V. BONNAND - *ONERA's Multiaxial and Anisothermal Lifetime Assessment for Engine Components.* Aerospace Lab Issue 09, june 2015

[9] E. ANDRIEU, B. MAX, B. VIGUIER - *Oxidation Assisted Intergranular Cracking in Alloy 718: Effect of Strain Rate and Temperature.* Aerospace Lab Issue 09, june 2015

[10] M. PERRUT - *Thermodynamic Modeling by the CALPHAD Method and its Applications to Innovative Materials.* Aerospace Lab Issue 09 june 2015

[11] S. POMMIER - *Development of an Incremental Model for Fatigue Crack Growth predictions.* Aerospace Lab Issue 09, june 2015

C. Déprés
(SYMME)
C. Robertson
(SRMA, CEA)
M. Fivel
(SIMaP, CNRS)

E-mail: Marc.Fivel@simap.grenoble-inp.fr

DOI : 10.12762/2015.AL09-01

3D Discrete Dislocation Dynamics Investigations of Fatigue Crack Initiation and Propagation

Both nucleation and propagation of fatigue cracks in fcc metals are investigated, using 3D discrete dislocation dynamics (DDD) simulations. Firstly, DDD simulations explain the mechanisms leading to the formation of persistent slip bands in surface grains loaded in fatigue. Extrusions are evidenced where the bands intercept the free surface. The extrusion growth rate is estimated for different material parameters and loading conditions. Energy and stress calculations performed inside the simulated grain lead to a possible scenario for the crack initiation at the interface between the band and the matrix, as reported in the literature. Secondly, a crack is inserted at the persistent slip band interface and the crack tip slip displacement evolutions are evaluated. It is shown that the crack growth rate is strongly related to the grain size and to the distance to the grain boundary; the smaller the grain, the faster the crack growth. Finally, the crack propagation to the next grain is investigated by conducting DDD fatigue simulations in a surface grain next to a cracked grain. It is shown that the development of the persistent slip band is modified by the presence of the crack. The crack orientation affects the orientation of the persistent slip band, as well as the extrusion rate, and consequently the crack propagation in the next grain.

Introduction

In single phased fcc materials, such as Copper or 316L stainless steels, stage-I fatigue cracks initiate in surface grains and the crack location is strongly correlated to the extrusion relief associated with the development of persistent slip bands [1, 10, 14, 15]. After the initiation stage, micro-cracks grow and cut the primary grain up to a first micro-structural barrier (a grain boundary, for example). At this point, subsequent propagation can be delayed for a certain time, depending on the loading amplitude and the orientation of the next grain [4]. Under high cycle fatigue (HCF) conditions, plasticity developing ahead of the first micro-structural barrier is a crucial and yet poorly understood phenomenon, possibly controlling the fatigue lifetime [2, 11, 13, 23].

Our goal in this work is to revisit the literature data on fatigue crack initiation and propagation in the low strain regime [19], using 3D discrete dislocation dynamics simulations. This numerical tool has the unique capacity to relate the organization of the dislocation lines to the mechanical properties of the material using very few model parameters.

Simulation setup

All of the DDD simulations presented here use the edge-screw model TRIDIS developed by Verdier et al. [21]. The simulation box consists of a polygonal grain, typically a truncated dodecahedron or a faceted cylinder (figure 1). All surfaces are impermeable to dislocation motion, except for one free surface from which dislocations can escape, leaving a step. The image forces are not accounted for, since their effect was shown to be negligible [6]. The evaluation of the dislocation displacement at the surface is computed using a dedicated algorithm proposed in [12]. The loading conditions correspond to a uniaxial tension applied along the direction [-123]. The fatigue load is applied in a quasi-static manner. The stress is incremented when the dislocations have all reached a stable position. The stress rate is reversed when the cumulated plastic strain reaches the desired strain amplitude (typically 10^{-3}). The initial configuration for the dislocations consists of a single Frank-Read source located in the center of the simulation box. It was demonstrated that such a simple configuration was sufficient to develop the expected fatigue microstructure.

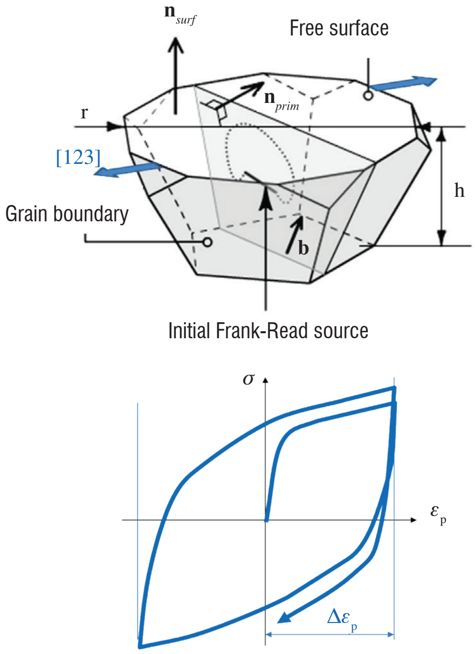

Figure 1 - DDD configuration and applied loading for the fatigue simulations of surface grains

Experimental observations of persistent slip bands developed in 316L stainless steels loaded in fatigue yielded the typical orientations of the simulation box. Typically, the normal to the free surface is fixed at $\mathbf{n}_{surf}$ = (221) and the primary slip system for the Frank-Read source is $a/2$[110](1-1-1).

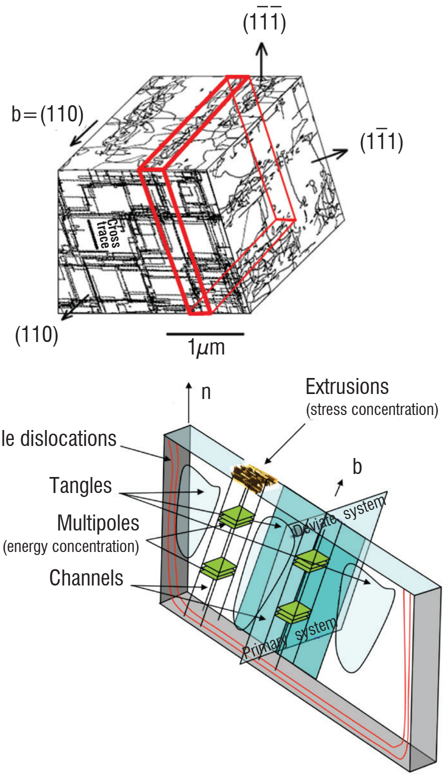

Figure 2 - Typical 3D dislocation microstructure and description of a single slip band [7]

Persistent slip band formation

When the load is applied, the dislocation source quickly activates and emits dislocation loops in the simulated volume. Then, numerous cross slip events take place that spread the dislocation lines on the two associated slip systems: the primary slip system $a/2$ [110] (1-1-1) and the deviate slip system $a/2$ [110] (1-11). This tends to homogenize the dislocation density and consequently the plasticity in the entire grain, which is beneficial to the fatigue life of the material. After a few cycles however, cross slip events and line reconnections modify the dislocation microstructure, which now becomes localized in bands [7].

A close look at a typical slip band shows that the band is made of channels, multipoles, tangles and mobile dislocations, as depicted in figure 2b. The multipoles consist of dipolar prismatic loops that can glide in the channels. The tangled dislocations are located near the channels, where dislocations hardly move.

Extrusion growth mechanisms

The plastic steps imprinted on the surface by the escaping dislocations are calculated in the vicinity of the persistent slip bands. It is shown that an extrusion progressively develops at the intersection of the channels and the free surface [8]. Note that the surface relief consists mainly of extrusions (figure 3a), with very few intrusions in good agreement with experimental observation [10]. Interestingly, the predominance of extrusion compared to intrusions is obtained here using purely conservative dislocation motion and dislocation reactions, since in the DD model, dislocation climb and point defect diffusion are not taken into account.

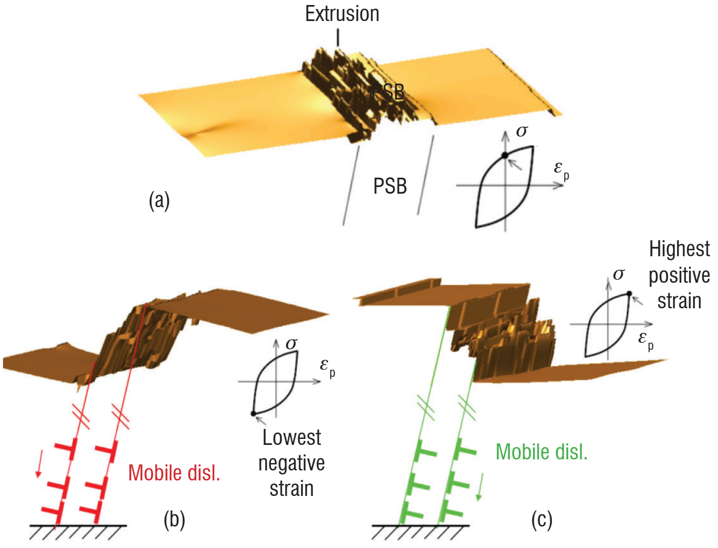

Figure 3 - Extrusion at the surface plotted for different instant of a given cycle

In figures 3b and 3c, the same surface zone is plotted when the plastic strain is maximum, negative and positive, respectively. The surface profile shows that most of the deformation is accommodated by two slip planes located at the interface between the band and the matrix. This demonstrates that these two planes contain highly mobile dislocations that can easily propagate in any of the two directions, depending on the sign of the applied stress. These mobile dislocations play a key role in the extrusion mechanism, since they generate stress gradients that can sweep the multipoles located in the channels. The multipoles then reach the surface and create the extrusions, as shown in figure 3. The fact that on average the number of intrusions is lower than the number of extrusions means that most of the multipoles are made of interstitial prismatic loops. More work needs to be done to explain why vacancy prismatic loops are not swept toward the surface, but one should bear in mind that the DDD model is fully conservative, so that the dislocation microstructure contained in the grain is geometrically equivalent to the set of vacancy loops needed to exactly compensate the extrusions forming at the surface.

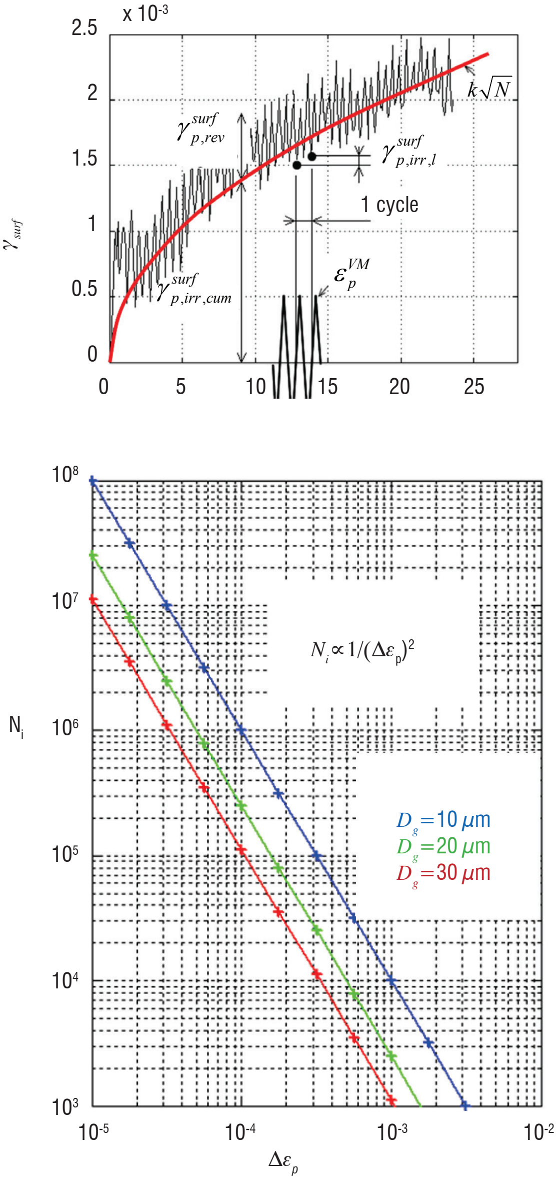

Figure 4 - Evolution of the irreversibility defined as the surface shear γ_{surf} and number of cycles needed to obtain a critical value of γ_{surf}

In order to quantify the irreversibility cumulated with the cycles, we have defined the surface shear γ_{surf} as the total length per unit area of the plastic steps left on the free surface and projected along the surface normal vector $\mathbf{n}_{surf}$. A typical curve of γ_{surf} versus the number of cycles is given in figure 4. Although some part of γ_{surf} is recovered during a given cycle, the curves can be nicely fitted using a square root relationship, with the number of cycles demonstrating a monotonic increase of the irreversibility. This means that the extrusion amplitude is continuously increasing, based on plasticity mechanisms.

A parametric study was conducted in order to measure the effect of the strain amplitude $\Delta\varepsilon_p$, the mean strain ε, the grain height h_g and the grain diameter D_g. It is found that the surface shear can be fitted by equation (1) below.

$$\gamma_{surf}\left(N\right) = K\frac{h_g}{D_g}\Delta\varepsilon_p\left(1+2\frac{\left|\bar{\varepsilon}\right|}{\Delta\varepsilon_p}\right)\sqrt{N} \qquad (1)$$

According to various authors, a critical value could be defined for the surface shear (or the extrusion height) that could initiate a crack [5, 17]. Figure 4 shows the number of cycles, N_i, required to reach a critical value of the cumulated shear γ_{surf} as a function of the strain amplitude and for different grain diameters. The power law scales with $\Delta\varepsilon^{-2}$.

Crack initiation scenario

In order to check where and when the first crack would most probably initiate, we have calculated the evolutions of the stresses and energies developed inside the slip bands. Figure 5a shows the typical distributions of the stored elastic energies at cycles number 5 and 19. Figure 5b shows the evolution of the maximum energy, evaluated as the standard deviation of the distribution. One can see that the maximum energy increases with the number of cycles. Assuming that such behavior could be extrapolated to a larger number of cycles, this means that after a given number of cycles a sufficient amount of elastic energy will be stored in the volume, which could lead to the formation of a crack. However, the crack will nucleate only if in the same region the stress tensor is able to promote atomic de-cohesions of the (111) planes. This effect can be evaluated using the same statistical analysis on the stress components (namely the shear and normal components), as plotted in figures 5c and 5d. The DD simulations show that the shear component (figure 5c) increases with the number of cycles, which is explained by the densification of the multipoles in the channels. However, the normal stress component, plotted in figure 5d, quickly saturates after a few cycles. Consequently, there will never be sufficient stress to be able to open a crack within the slip bands. Such a component is however present at the surface, where the extrusion shape concentrates the applied loading. Since the extrusion height is always increasing, the stress concentration also continuously increases up to the critical stress needed for atomic de-cohesions.

Finally, a complete crack initiation scenario could be drawn from the DD simulations (figure 6). The first crack will be nucleated for a given value of the irreversibility indicator, γ_{surf}, i.e., a given extrusion height, when a set of multipoles swept by the mobile dislocations will reach the surface, causing the strain energy to be sufficient at this location to open the crack. In practice, the de-cohesion stress needed to open the crack is reduced by the contaminations of the fresh surface steps developed with the cycles.

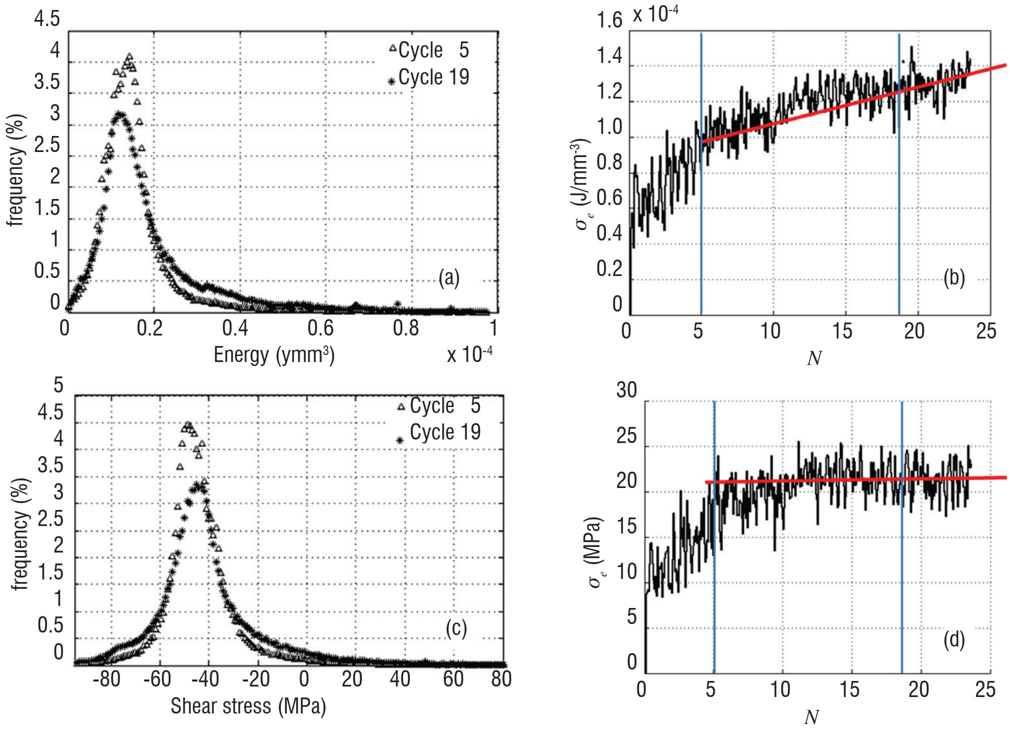

Figure 5 - Statistic analysis of the strain energy (a) and the stress components (c) and corresponding evolutions of the maximum strain energy (b) and the normal stress (d)

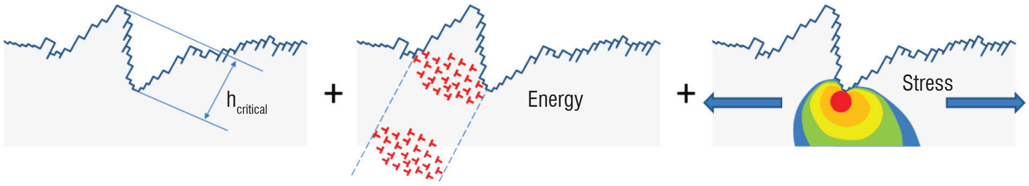

Figure 6 - Schematic description of the crack initiation scenario. The threshold condition is reached when the elastic energy (associated to the multipoles) and the stress concentration (related to the extrusion shape) coincide

Crack propagation in the first grain

According to the crack initiation scenario presented in the previous section, the first crack should nucleate at the interface between the slip band and the matrix. In this section we will artificially insert a crack at this location by modifying the DD code in three manners [9].

(i) The two free surfaces corresponding to the crack lips are introduced in the simulated volume. The opening angle of the crack is fixed at 10^{-2} radians. Similarly to the top free surface, the dislocations are allowed to cross the crack surfaces and to imprint plastic steps simulating the blunting process. Note that in this study, the image forces induced by the free surfaces are not accounted for, since their effect on the crack propagation was demonstrated to be limited in [7].

(ii) The crack stress field is introduced as Irwin's singular analytical expression for a 2D infinite crack [19] p.289. For each dislocation segment, the crack stress field is superimposed to the local effective stress.

(iii) Additional dislocation sources (one per slip system) are randomly inserted ahead of the crack tip, in order to account for crack tip plasticity.

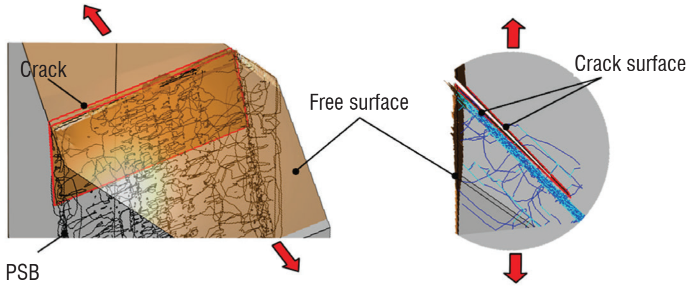

Figure 7 - Insertion of a crack in the 3D DD simulations

Figure 8 shows the dislocation microstructure and the evolution of the dislocation densities on the twelve slip systems in the case of a grain of diameter 10 microns. It is observed that the dislocation microstructure is not drastically modified by the insertion of crack.

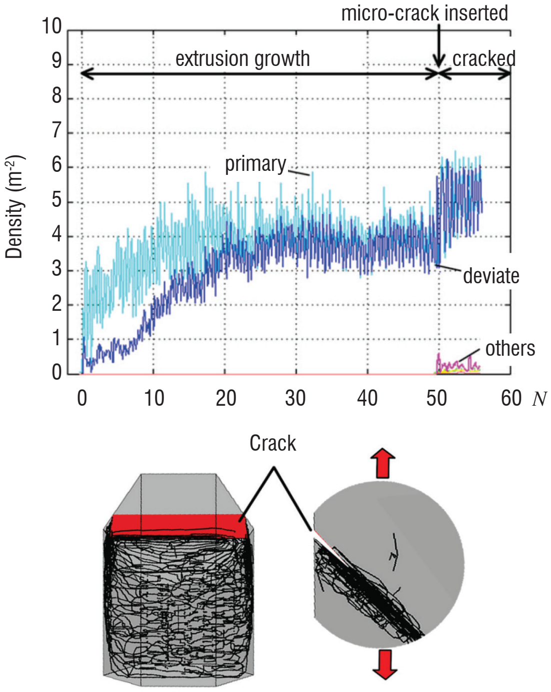

Figure 8 - Evolution of the dislocation densities and corresponding final dislocation microstructure developed in the cracked grain.
The crack is inserted at cycle number 50

This is confirmed by the dislocation density accumulation rate, which remains similar after the crack insertion. It is also found that the crack shape remains sharp with highly reversible slip at the tip. Complementary simulations were performed in the case of a grain for which the crack was inserted from the beginning of the simulation, i.e., without a prior persistent slip band dislocation structure [9]. In this case, the dislocation microstructure is not planar anymore at the crack tip and the dislocation densities are more dispersed on the twelve possible slip systems, leading to crack tip blunting. This demonstrates that the slip band microstructure facilitates crack propagation through the first grain.

The crack propagation mechanism is also affected by the grain boundary. When the crack becomes close to the grain boundary, it is no longer possible to accommodate the plasticity ahead of the tip using only the primary and deviate slip systems. Consequently, the dislocation microstructure spreads on all of the slip systems, resulting in strong blunting effects, as shown in figure 9.

The effect of the distance to the grain boundary depends on the grain size, D_g. The slip dispersion is less pronounced in smaller grains. The consequence for small grains is that plasticity is more localized, so the crack propagation is faster. Such a feature is confirmed experimentally [20]. This effect is now quantified by computing the Crack Tip Slip Displacement ($CTSD$) for different distances to the grain boundary and for different grain sizes, the grain shape ratio being conserved. The $CTSD$ is calculated by averaging displacement profiles taken along 100 lines crossing the crack tip. Results are given in figure 10. The ratio $CTSD/D_g$ is found to be almost independent from the grain size for crack lengths smaller than 50% of the grain size. In other words, the $CTSD$ is proportional to the grain size, so the number of cycles needed for the crack to move over half the grain is more or less the same, regardless of the grain size. For a greater crack length, i.e., for a crack closer to the grain boundary, the $CTSD$ is strongly reduced for larger grains, indicating that crack propagation is slower in coarser grains, as reported in [19] and [3].

The curves in figure 10a can be nicely fitted using equation (2) below [9],

$$\frac{CTSD}{D_g} \cong \Delta\varepsilon_p\left(1-\exp\left(-\frac{\lambda}{\Delta\varepsilon_p}\frac{b}{D_g}\left(1-\frac{a}{D_g}\right)\right)\right) \qquad (2)$$

where a is the crack length and $\lambda=25$ is a fitting parameter.

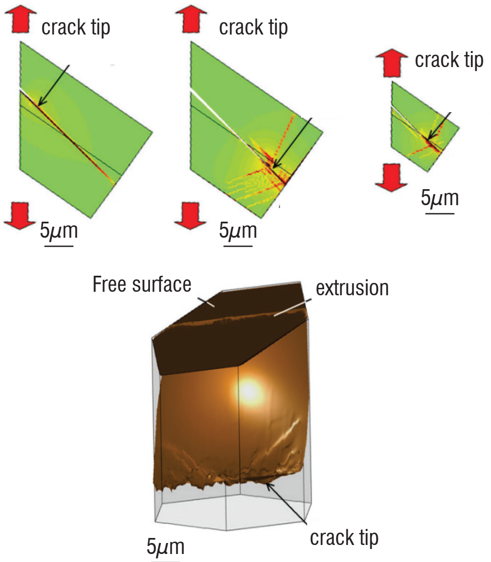

Figure 9 - Effect of the distance to the grain boundary. Dispersed plastic slip and crack tip blunting is observed for the shortest distances

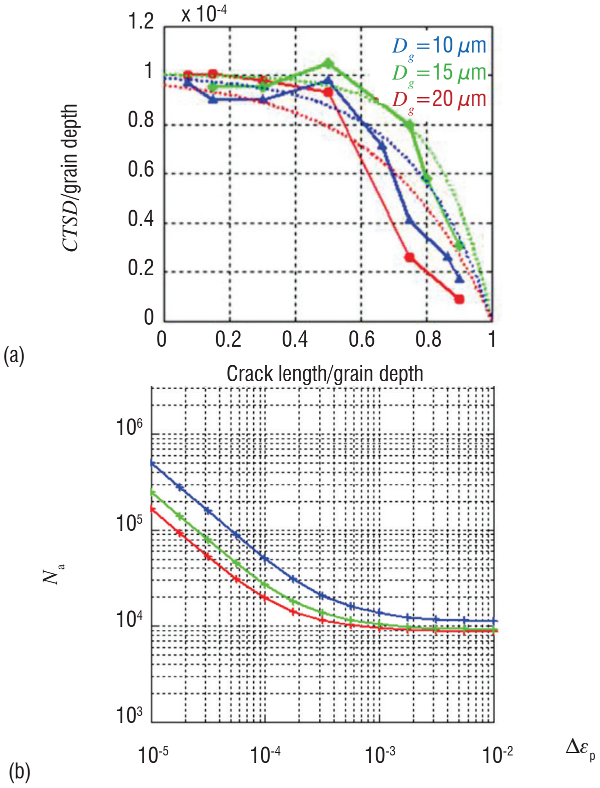

Figure 10 - Crack Tip Slip Displacement versus the distance between the crack and the grain boundary for different grain sizes and numbers of cycles to obtain a 5 μm length crack using equation (1)

Assuming that the crack propagates over a distance $CTSD$ every N_i cycles, we can integrate Equation (2) in order to estimate the number of cycles required for a crack to propagate over a given length. Figure 10b shows the curves corresponding to a crack propagation of $a=5\,\mu m$ for different grain sizes. For low plastic strain amplitudes, the number of cycles is found to be proportional to $\Delta\varepsilon_p^{-1}$, whereas for higher strain amplitudes the number is almost constant. Note also that this number is very low compared to the number of cycles needed for crack initiation, which is proportional to $\Delta\varepsilon_p^{-2}$ as shown by Equation (1) and plotted in figure 4. This shows that crack initiation takes much longer than crack propagation.

Crack propagation towards the next grain

Focusing on the crack propagation in surface grains, the objective of this section is to investigate the crack interaction with the first microstructural barrier. The study of the crack propagation in the first grain showed that most of the plasticity at the crack tip was accommodated by the Burgers vector of the primary/deviate slip systems forming the persistent slip band. Such a Burgers vector is almost perpendicular to the free surface (figure 1) and, consequently, coplanar with the grain boundary. Thus, the scenario for the crack transmission mechanism from one grain to the next grain is more likely to be an 'indirect transmission', as depicted in figure 11. This means that the cracks will not be able to shear and cross the grain boundary, but will rather generate a new slip band in the next grain, which will later initiate a crack in the same way as in the first grain.

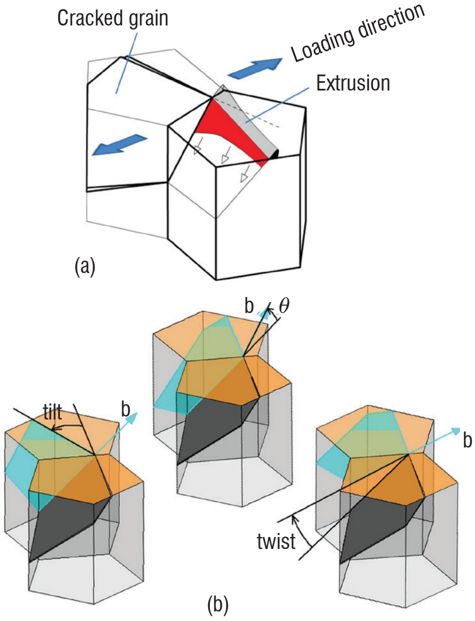

Figure 11 - Simulation setup.
(a) Indirect transmission mechanism
(b) Definition of the three relative angles defining the relative position of the crack with respect to the slip band

The simulation setup consists of a cracked grain, for which the crack is once again represented by the singular stress field of a 2D infinite crack. The next grain corresponds to the DD simulation box. The initial dislocation microstructure includes 24 Frank-Read sources, randomly distributed in the simulated grain on all of the possible slip systems. The fatigue load is imposed with a plastic strain amplitude of $\Delta\varepsilon_p=10^{-4}$ relevant to High Cycle Fatigue (HCF) conditions. The crack orientation is defined by the tilt, twist and theta angles between the crack and the slip band planes.

A typical result is shown in figure 12. The curve marked as (a) shows the surface shear accumulated in the grain before the crack is inserted. The corresponding dislocation microstructure obtained after a few cycles is given in the same figure. The formation of a slip band can be clearly seen. The crack is inserted at cycle number 34 and the surface shear is modified into curve (b), which shows a larger accumulation rate of the surface shear. The corresponding dislocation microstructure obtained after a few more cycles shows that the slip band has been destroyed and a new one has formed on a different set of slip systems.

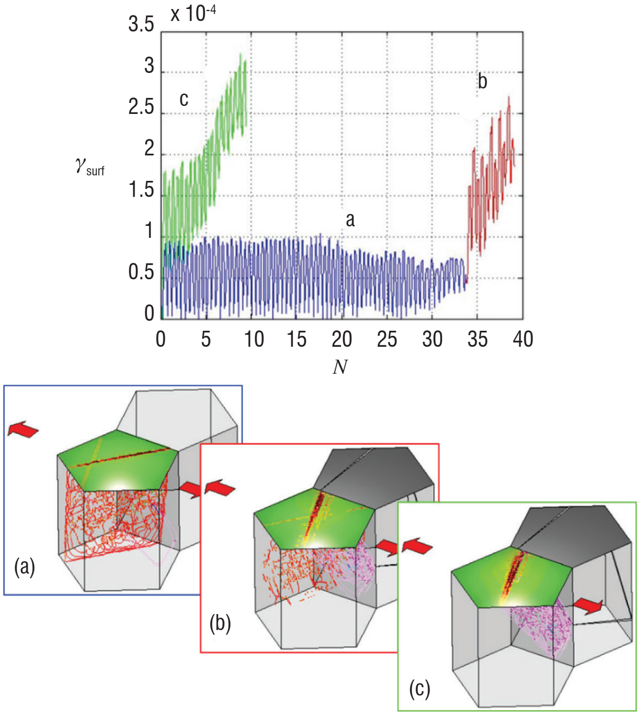

Figure 12 - Effect of the crack on the irreversibility
(a) The crack has not yet been introduced
(b) The crack is introduced, after 34 fatigue cycles
(c) The crack has been introduced as from the beginning

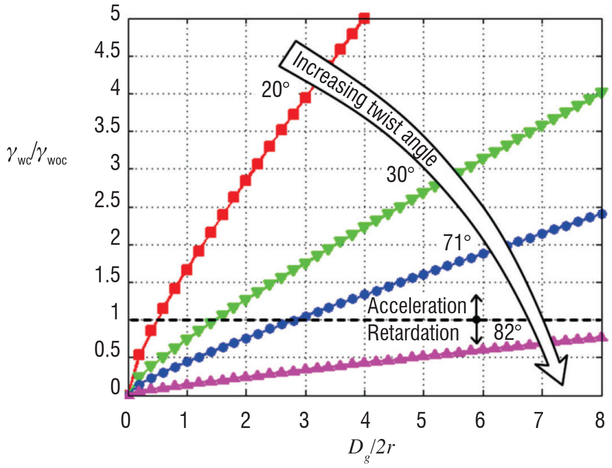

Fig. 13 - Ratio of the surface shear in the presence of the crack / surface shear without any crack for a tilt angle of 24° and for different twist angles

If the crack is introduced from the beginning of the fatigue simulation, it gives the surface shear and dislocation microstructure indicated as (c) in figure 12. Both are similar to sequence (b) obtained when the crack was inserted after a few cycles. This means that the crack imposes both its own dislocation microstructure and its own extrusion rate. In other words, the dislocation microstructure formed in the grain could not have been predicted from Schmid's law predictions, as used in continuum models.

A parametric study was conducted by varying the twist and tilt angles [16]. It is found that in some cases the crack insertion can speed up the accumulation rate and for other situations it can slow down the extrusion growth. This is illustrated in figure 13, where the surface shear accumulated in the grain has been divided by the reference surface shear accumulated in a grain without any crack. If the ratio is greater than 1, the crack increases the extrusion growing rate, whereas a value below 1 is the signature of a delaying effect of the crack on the extrusion growth rate. The curves are plotted as a function of the distance to the crack tip, r.

Concluding remarks

3D DD simulations helped in understanding persistent slip band formation and the associated surface extrusion growth mechanisms. A detailed scenario for the crack initiation is proposed, where the mechanism for the crack propagation along the slip band is explained and quantified as a function of the grain size. Finally, the crack transmission to the next grain is investigated for diverse crack orientations, showing that the crack plays a major role in the development of plasticity in the neighboring grains.

Despite the promising results obtained in this study, the DD simulations conducted here have several limitations. The first one is related to the calculation time required for a simulation, which limits the maximum number of simulated cycles. Moreover, neither the surface contamination, nor diffusion mechanisms are taken into account in the model. Finally, the DDD simulations were all performed in a single crystal. The perspectives of this work consist in overcoming these limitations by improving the model, both in terms of the physics and computational efficiency ■

Acknowledgements

The funding of this research through CPR-SMIRN as well as ANR AFGRAP is gratefully acknowledged.

References

[1] Z.S. BASINSKI, S.J. BASINSKI - Prog. Mater. Sci., Vol. 36, 1992.
[2] TR BIELER, P. EISENLOHR, F. ROTERS, D. KUMAR, D.E. MASON, M.A. CRIMP, D. RAABE - Int J of Plast, Vol. 25, 2009.
[3] C. BLANKENSHIP, E. STARKE - Fat. Frac. Eng. Mat. Str., Vol. 14, 1991.
[4] H.J. CHRIST, O. DUBER, C.P. FRITZEN, H. KNOBBE, P. KÖSTER, U. KRUPP, B. KÜNKLE - Comput Mater Sci Vol. 46, 2009.
[5] L. CRETEGNY AND A. SAXENA - Acta Mater. Vol. 49, No. 18, 2001.
[6] C. DÉPRÉS - Ph.D. Thesis, Grenoble INP, 2004. (download from http://www.numodis.fr/tridis)
[7] C. DÉPRÉS, C.F. ROBERTSON, M.C. FIVEL - Phil. Mag., Vol. 84, No. 22, 2004.
[8] C. DÉPRÉS, C.F. ROBERTSON, M.C. FIVEL - Phil. Mag., Vol. 86, No. 1, 2006.
[9] C. DÉPRÉS, V.G. PRASAD REDDY, C.F. ROBERTSON, M.C. FIVEL - Phil. Mag., Vol. 94, No.36, 2014.
[10] U. ESSMANN, U. GÖSELE, H. MUGHRABI - Phil. Mag. A, Vol. 44, No. 2, 1981.
[11] E. FERRIÉ M. SAUZAY - J. Nucl Mater, Vol. 386-388, 2009.
[12] M. FIVEL AND C. DÉPRÉS - Phil. Mag., Vol. 94, No. 28, 2014.
[13] Y. HONG, Y. QIAO, N. LIU, X. ZHENG - Fat. Fract Eng Mater Struct, Vol 21, 1998.
[14] J. MAN, K. OBRTLIK, C. BLOCHWITZ, J. POLAK - Acta Mater. Vol. 50, 2002.
[15] J. MAN, K. OBRTLIK, J. POLAK - Phil. Mag. A, Vol. 89, No. 16, 2009.
[16] V.G. PRASAD REDDY, C.F. ROBERTSON, C. DÉPRÉS, M.C. FIVEL - Acta Mater., Vol. 61, 2013.
[17] M. RISBET, X. FEAUGAS, C. GUILLEMER-NEEL, M. CLAVEL - Scripta Mat. Vol. 49, 2003.
[18] C.S. SHIN, C.F. ROBERTSON, M.C. FIVEL - Phil. Mag., Vol. 87, No. 24, 2007.
[19] S. SURESH - *Fatigue of Materials.* Cambridge University Press, Cambridge, 1998.
[20] A. VAN DER VEN, G. CEDER - Acta Mater, Vol. 52, 2004.
[21] M. VERDIER, M. FIVEL, I. GROMA - *Modelling Simul.* Mater. Sci. Eng., Vol. 6, No.6, 1998.
[22] Y. QIAO, S.S. CHAKRAVARTHULA - Int J Fatigue 2005, Vol. 27, 1251.
[23] Y. QIAO - Mate. Sci Eng 2003, Vol. A361:350.

Christophe Déprés graduated from the Ecole Normale Supérieure de Cachan, France and obtained a Ph.D. in Mechanics from the Grenoble Institute of Technology in 2004. He is now an assistant professor at the Laboratoire SYMME, Université Savoie Mont Blanc. His research field focuses on plasticity problems, such as fatigue or dislocation based model development, taking advantage of the potential of Discrete Dislocation Dynamics simulations.

Christian Robertson graduated from the Ecole Polytechnique de Montréal (Canada) in 1995 with a Masters Degree in Physical Engineering and then, in 1998, achieved a Doctoral Degree from the Université de Paris 6 (France), in Materials Science. In 2000, he started his career at CEA, the French Atomic Energy Commission (Nuclear Materials Department), as a research engineer. He became an expert in micro-plasticity mechanisms in metallic materials under extreme conditions (high temperature, high radiation dose, fatigue, etc.). His research activity combines microscopic observations and numerical simulations.

Marc Fivel graduated from the Ecole Normale Supérieure de Cachan, France and obtained a Ph.D. in Mechanics from the Grenoble Institute of Technology in 1997. After a post-doctoral position at Lawrence Livermore National Laboratory (USA), he was hired at CNRS in 1998. He is now a CNRS Research Professor at SIMaP-GPM2, University Grenoble Alpes. His areas of interest include multiscale simulations of crystal plasticity with a special focus on discrete dislocation dynamics simulations.

B. Devincre[1]**, R. Gatti**[1]
(ONERA-CNRS)

E-mail: benoit.devincre@onera.fr

DOI: 10.12762/2015.AL09-02

Physically Justified Models for Crystal Plasticity Developed with Dislocation Dynamics Simulations

This article highlights how dislocation dynamics (DD) simulations provide a unique opportunity for establishing scale transitions in crystal plasticity. Recent progress in this numerical method is briefly reviewed. Based on the standard problem of plasticity in fcc crystals, we show that DD simulation insight provides guidelines for modeling material mechanical properties controlled by the collective behavior of dislocation microstructures. Hence, DD simulation allows more physical input to be incorporated into continuum models for strain hardening, thereby improving their predictive ability.

Introduction

Due to its importance in many technological problems, including some aerospace industry issues, the development of a plasticity theory based on dislocation mechanics, rather than on an empirical basis, is a long-standing goal in materials science. However, due to its intrinsically multi-scale nature, the problem of reducing dislocation mechanics to a system of partial differential equations compliant with standard continuum computational methods turns out to be a non-trivial problem. In the last decade, important progress has been made with the development of multi-scale modeling strategies bridging models of crystal plasticity from the atomistic to the continuum domains. Within such multi-scale strategies, 3D simulations of dislocation dynamics (DD) that give a physically justified description of the motions and the interactions of large ensembles of dislocations at the mesoscale are strategic [17]. Indeed, DD simulation allows the statistical analysis and integration of the many and complex dislocation properties controlling the plastic deformation of metals and alloys. This is why this simulation technique is essential to improve the constitutive laws used at large scale in continuum mechanics simulations. In addition, DD simulation allows fair and direct comparison with experiments.

The purpose of this paper is to briefly present some of the progress that we have made in the DD simulation method and in the development of physically justified constitutive equations for continuum simulations. We first provide an overview of an important model, the discrete-continuous model, coupling DD simulations and finite-element simulations. Then, we present recent results associated to the key topics of isotropic and kinematic strain hardening modeling. Finally, we present the conclusion and perspective.

From dislocation dynamics simulation to the discrete-continuous model

The "microMegas" project

Three-dimensional DD simulations compute plastic strain by integrating the equations of motion for dislocation lines under stress in an elastic continuum. The mutual interactions of dislocations, the formation and destruction of junctions, their line tension and their interactions with other defects are essentially drawn from the elastic theory. Whereas some differences remain among DD simulation codes, there are basic features that all of these have in common. All of the simulation codes discretize dislocations into a finite set of degrees of freedom attached to line segments. The forces on these discrete lines are estimated from the elastic theory of dislocations and the positions of the dislocation segments are updated according to material-dependent equations of motion. Applying periodic boundary conditions to the simulated volume allows a representative volume element of a macroscopic sample to be monitored at the scale of a few tens of microns. A difficult aspect of DD simulation consists in the definition of constitutive or " local " rules that account for dislocation core properties like dislocation cross-slip and nucleation. For this reason, attention must always be paid to these parts of the simulation codes, since they control the peculiarities of the materials. Such validations can be made either from comparison with atomistic simulation results or from dedicated experiments.

The LEM[1] is at the origin and is the main contributor of a free and open source DD simulation code called microMegas[2] *(mM)*. *mM* is today one of the most popular lattice-based DD simulation codes and is used by many research groups to investigate different aspects of

---

[1] Laboratoire d'Etude des Microstructures, UMR104, CNRS-ONERA

[2] http://zig.onera.fr/mm_home_page/index.html

crystal plasticity. A full description of this computer code has been presented in numerous studies [7][21] and was recently described in some detail in [8]. Readers interested in DD simulation applications to micro-plasticity problems involving size-effects, such as in sub-micronic objects and nano-structured materials, are referred to this paper.

The discrete-continuous model

DD simulation codes present some limitations when they have to deal with complex boundary conditions. Indeed, standard simulations compute dislocation-dislocation interactions using classical expressions of the dislocation stress field in infinite media, not taking into account the interactions of dislocations with free surfaces and interfaces. To overcome these limitations, we develop in collaboration with the ONERA Department DMSM the Discrete-Contiuum Model (DCM). The DCM is based on a coupling between a DD code and a finite element (FE) code via the Eigenstrain "formalism". In this formalism, a dislocation is introduced in the FE simulation as Volterra loops, regularized in a plate-like inclusion of thickness h [19][10][25]. In particular, at each time step, the area swept (dS) in the DD simulation by each dislocation segment is transmitted to FE and the associated plastic Eigenstrain $(d\varepsilon^p)$ is computed using the following expression:

$$d\varepsilon^p = w(r,h).dS\frac{(b\otimes n + dS\otimes n)}{2} \quad (1)$$

where $w(r,h)$ is an isotropic distribution function of radius r with regularization thickness h, b and n are respectively the dislocation Burgers vector and a unit vector normal to the dS.

The sum of all of the elementary $d\varepsilon^p$ gives the total plastic eigenstrain in the FE part. Once the eigenstrain distribution is calculated, the FE code solves the boundary value problem, computing the mechanical equilibrium (stress, strain and displacement field) in the simulated volume. Then, the DD code exploits the FE stress field to compute the dislocation motion.

Unlike with other coupling techniques (e.g., the superposition principle), as stated above, the DCM is able to compute the full mechanical equilibrium in the simulated domain. This is a key property of the method; it thus allows plastic deformation to be naturally simulated in anisotropic media, to simply access periodic boundary conditions and to couple the DCM with other constitutive laws (crystal plasticity).

In order to better illustrate the capability of the DCM, two examples are presented.

The first one in figure 1 highlights the possibility of running micromechanic calculations within the framework of anisotropic elasticity. The plastic relaxation onset of SiGe heteroepitaxial nanoislands, due to the lattice mismatch with the Si substrate, has been studied using anisotropic elastic constants. Panel (a) of figure 1 shows the dislocation equilibrium position inside the nano-island, while panel (b) shows the plastic Eigenstrain induced by the dislocation dynamics. Once the equilibrium is computed, it is possible to have access to the stress field (panel c) and to the displacement field (panel d) associated with the plastic deformation inside the nano-object.

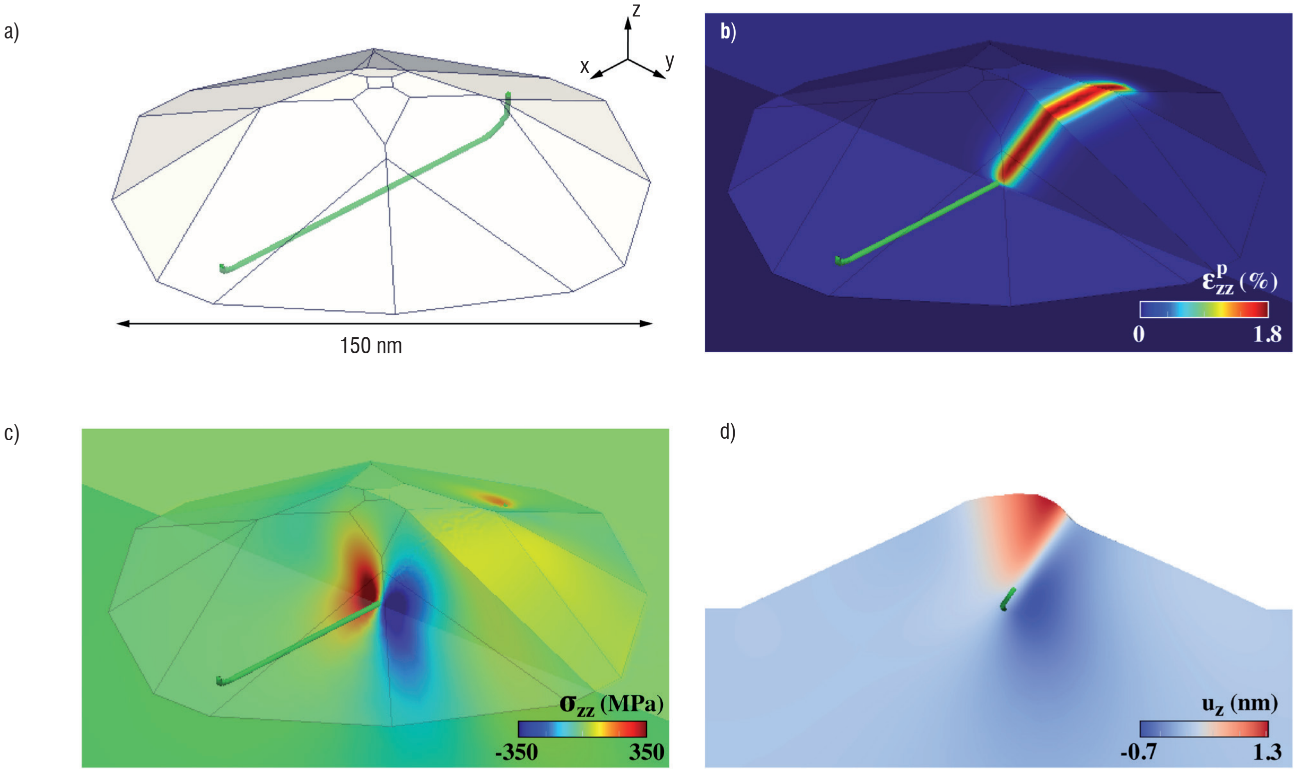

Figure 1 - DCM simulation of a misfit Dislocation line deposited inside a SiGe island
(a) The dislocation line location and displacements are calculated with the DD code
(b) The plastic shear associated to dislocation dynamics is locally homogenized and exported to the FE problem
(c) Dislocation stress field inside the nanoisland at the mechanical equilibrium
(d) The DCM boundary value problem is solved accounting for crystal rotations and volume shape variations (displacement fields induced by dislocations).

The second example describes the capability of coupling the DCM with other methods, to predict plastic deformation in crystalline materials. In order to model the deformation of a Cu polycrystal in figure 2, a mesh with 16 grains has been created. The central grain exploits the DCM constitutive law, while the surrounding 15 grains are treated with a more phenomenological crystal plasticity model [23][12]. The images of panel (a) and (b) show the Von Mises stress in the polycrystal after 2% of deformation in the z direction, to highlight the difference between the two different model predictions (DCM vs. crystal plasticity). In panel (a), the dislocation microstructure in the central grain is superposed to the stress field and panel (b) illustrates how, unlike the continuous crystal plasticity model, the DCM is able to capture the stress concentration due to the accumulation of dislocations at the grain boundaries. Hence, it is possible to quantitatively capture the physical process controlling size effects.

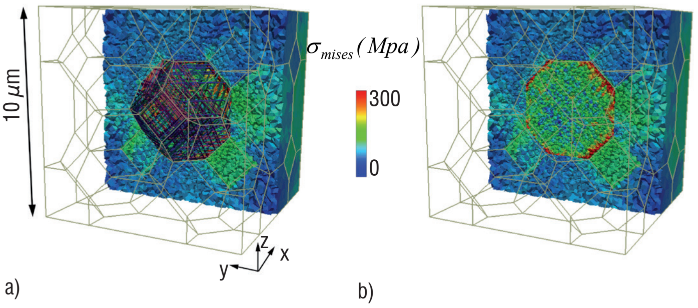

Figure 2 - Example of how the DCM can be coupled with other constitutive law in the FE framework: deformation of a Cu polycrystal. The central grain exploits the DCM constitutive law, while the other 15 Grains in the periodic mesh deform following a phenomenological crystal plasticity law.
In panel (a), the dislocation microstructure has been superposed in the central grain to the stress field.
Panel (b) highlights how the DCM captures the stress heterogeneities in comparison with the solutions obtain in the other grains.

Modeling plastic strain hardening

The identification of reliable material constitutive equations for continuum mechanics is an essential ingredient for the development of new materials and structures. Such equations are essential to model the relation between strain and stress inside a material, which is a simple linear relation in the case of elastic analyses (Hooke's law) and a much more complex relation when plastic deformation is involved. Here, we show that the validity of plasticity laws can be considerably improved by making use of information arising from DD simulations. For this purpose, the plasticity of fcc metals is used as a standard problem. It must be noted that the methodology proposed can be extended to other materials, as illustrated by a recent paper dedicated to $\alpha - Fe$ [22].

Among the many possible choices of constitutive equations for plasticity [2], in this study we consider a well-known dislocation density based model [24] derived from the storage–recovery framework first developed by Kocks and Mecking (see [14] for a review). Nevertheless, the results that we obtained for this model can also be incorporated to alternative continuous models for crystal plasticity. A small strain framework is assumed here, for simplicity reasons.

During plastic deformation, dislocations multiply and their mutual long and short-range interactions hinder their motions. As a consequence, a shear stress increase $d\gamma$ has to be imposed to produce a shear strain increase $d\gamma$. By definition, the ratio $\theta = d\tau / d\gamma$ is the strain hardening rate. In a physically justified approach to crystal plasticity, the density of dislocations in each slip systems $'i'$ is a key internal state variable. For this reason, the calculation of the strain hardening can usefully be decomposed in three parts. First, a flow stress relation, has to be identify in order to calculate the critical stress τ_c^i for the activation of slip systems. Secondly, the rate at which the critical stress evolves with strain or, equivalently, the rate at which dislocation density evolves under strain in the slip systems $(d\rho^i/d\gamma^i)$ (see § " Dislocation storage rate and isotropic strain hardening ") must be defined. Lastly, the plasticity problem is in a closed form by including a flow rule. The latter expression relates, in each slip system, the resolved applied stresses to the critical stress τ^i and the strain rate $\dot{\gamma}^i$. In fcc materials and for conventional strain rates, a power law expressions is usually considered:

$$\dot{\gamma}^i = \dot{\gamma}_0^i \langle \frac{\tau^i - X^i}{\tau_c^i} \rangle^m \tag{2}$$

where $<>$ are the Macaulay brackets, $\dot{\gamma}_o^i$ is a reference strain rate and m is a material parameter accounting for the strain rate sensitivity. In fcc metals, m is related to the energetics of jog formation and it does not influence the modeling of plastic strain since at low temperatures its value is large. In eq. (2), X^i is a long-range back-stress term accounting for the accumulation of polarized dislocation, i.e. the accumulation of geometrically necessary dislocations in regions of the deformed material [1]. For instance, the grain-boundaries (GB) in a polycrystal act as strong barriers to dislocations glide. Then, dislocations are accumulated on both sides of the grain boundaries during plastic deformation. This feature limits the slip system activity and therefore decreases forward deformation of the grains (see § " Modeling kinematic strain hardening ").

The flow stress relation

Following the work of Franciosi et al. [9], the critical stress for the onset of plastic slip in a system $'i'$ interacting with slip systems $'j'$ with density ρ^j can be expressed in a tensor form:

$$\tau_c^i = \mu b \sqrt{\sum_j a_{ij} \rho^j} \tag{3}$$

where μ is the elastic shear modulus and b is the dislocation Burgers vector. In equation (3), coefficients a_{ij} are the components of a matrix that describes the strength of the interactions between slip systems. In fcc crystals, the number of distinct interaction coefficients between the 12 <0 1 1>{1 1 1} slip systems is reduced to six. Four coefficients are needed to describe slip system interactions involving particular dislocation reactions, that is, the glissile junction, the Hirth and Lomer locks and the collinear annihilation. This last reaction occurs between slip systems that share a common Burgers vector. It does not produce junctions but rather athermal annihilation over an extended range of dislocation line characters [20].

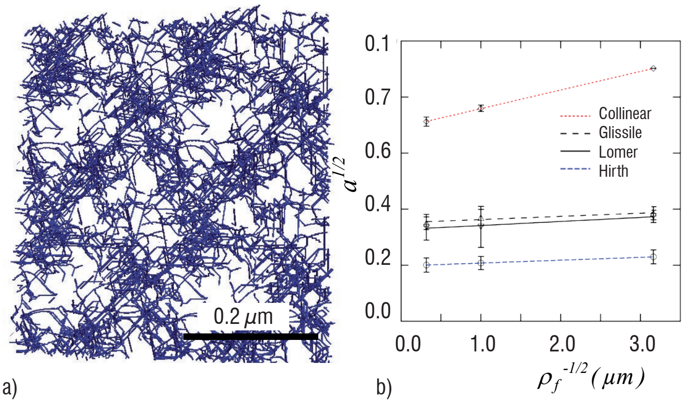

Figure 3 - (a) Example of periodic dislocation microstructure in a (001) foil of thickness 0.2 μm extracted from a simulated volume of Cu deformed under multi-slips conditions. (b) Measurements of slip system interaction strength $(a^{1/2})$ for different forest dislocation densities $(\rho_f^{-1/2})$ including only one type of dislocation reaction, i.e., the collinear annihilation and the glissile, Lomer and Hirth junctions.

Calculation of the a_{ij} values as a function of the dislocation density is a task that we performed with DD simulations [18][6]. As shown in figure 3-b, for a reference forest density of $\rho = 10^{12}\ m^{-2}$, the strength of slip system interaction involving the Lomer junction is found identical to a standard value calculated with the forest model, $\sqrt{a} \approx \alpha \approx 0.35$. This result reflects the predominance of the Lomer reaction in the strengthening of fcc single crystals. For the Hirth, glissile and collinear types of interactions, the calculated strengths are approximately 0.6α, α and 2.3α , respectively. It is interesting to note that due to the large value of the collinear annihilation coefficient, we explained why, in contradiction with the Schmid law prediction, the simultaneous activity of two slip systems shearing the same Burgers vector can hardly be observed experimentally [15].

The two remaining a_{ij} coefficients are those associated with the interaction of a slip system with itself and the interaction between coplanar slip systems. DD simulations dedicated to these particular configurations show that the coefficients of the latter are much larger than is often assumed, close to that associated with the Lomer interaction [5].

Dislocation storage rate and isotropic strain hardening

As illustrated in figure 4, the process of dislocation density storage is, under many deformation conditions, directly related to the dislocation avalanche feature. For this purpose, the concept of dislocation mean free path, which is the distance traveled by a mobile dislocation segment of unit length before it is stored by interaction with the microstructure, is essential. It is intuitive that dislocations mean free path decreases with increasing stored density and depends on the strength of the dislocation obstacles opposing the dislocation motion. A formal modeling of this quantity was performed with DD simulations [3][16]. The full expression of the storage rate derived from DD simulations is too complex to be reported here. Instead, we restrict ourselves to the rather simple form obtained in the absence of dynamics recovery processes and for loading conditions imposing symmetric activity of the slip system. For each mobile slip system and taking into account only forest interactions, we demonstrated that:

$$\frac{d\rho^i}{d\gamma^i} = \frac{\tau_c^i}{\mu b^2 K_{hkl}} \text{ with } K_{hkl} = \left[\frac{\bar{a}^{1/2} n (1+\kappa)^{3/2}}{p_0 k_0 (n-1-\kappa)}\right] \tag{4}$$

In eq. 4, τ_c^i is the critical stress for the onset of slip systems activity and K_{hkl} is an orientation-dependent mean free path coefficient. In the K_{hkl} definition, n is the number of active slip systems and $\bar{a}^{1/2}$ is the average value of the interaction coefficients a_{ij}. The three coefficients $p_0 = 0.117, k_0 = 1.08$ and $\kappa = 0.29$ are dimensionless constants. They are related respectively to the probability for forming a stable junction upon crossing a forest dislocation, to the average length of the stored dislocation line segments and to the density of junctions in the microstructure. As illustrated in figure 4, value of these coefficients could be determined from DD simulations [4].

Equations (3) and (4) constitute two essential building blocks for modeling isotropic strain hardening in fcc crystals and in other materials when strain hardening is dominated by dislocation-dislocation interactions. Demonstration was made that their integration on a meshed sample using a crystal plasticity FE code allows for predicting quantitatively the first two hardening stages of FCC single crystals without fitting procedure [16].

Modeling kinematic strain hardening

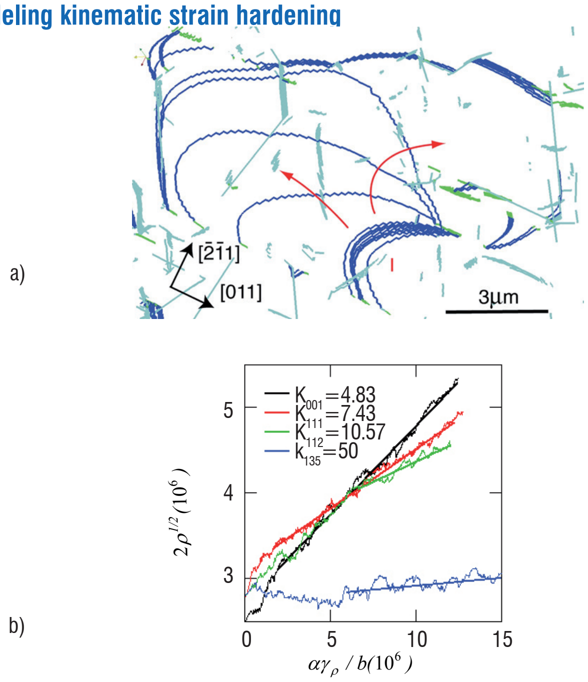

Figure 4 - (a) Dislocation avalanche (or strain burst) observed with DD simulation in a tensile test of a [001] Cu crystal. This dynamic feature controls the relation between plastic strain production and dislocation density storage (b) Determination of the dislocation mean free path coefficients by DD simulations for different single crystal tensile test orientation.

Other obstacles than dislocations can contribute to strain hardening. For instance, in a polycrystal with grain size d_g, GB distances necessarily limit the mean free path of dislocations. For this reason in a polycrystal, an additional storage term accounting for the accumulation of polarized dislocations (GND) must be added to eq. (4). For simple dimensional reasons, this term take the form:

$$\frac{d\rho_{GND}^i}{d\gamma^i} = \frac{k_{GND}}{b\, r_{GB}} \tag{5}$$

with r_{GB} the shortest distance to GBs and $k_{GND} \approx 0.5$ a storage rate parameter accounting for a specific organization of the GND density

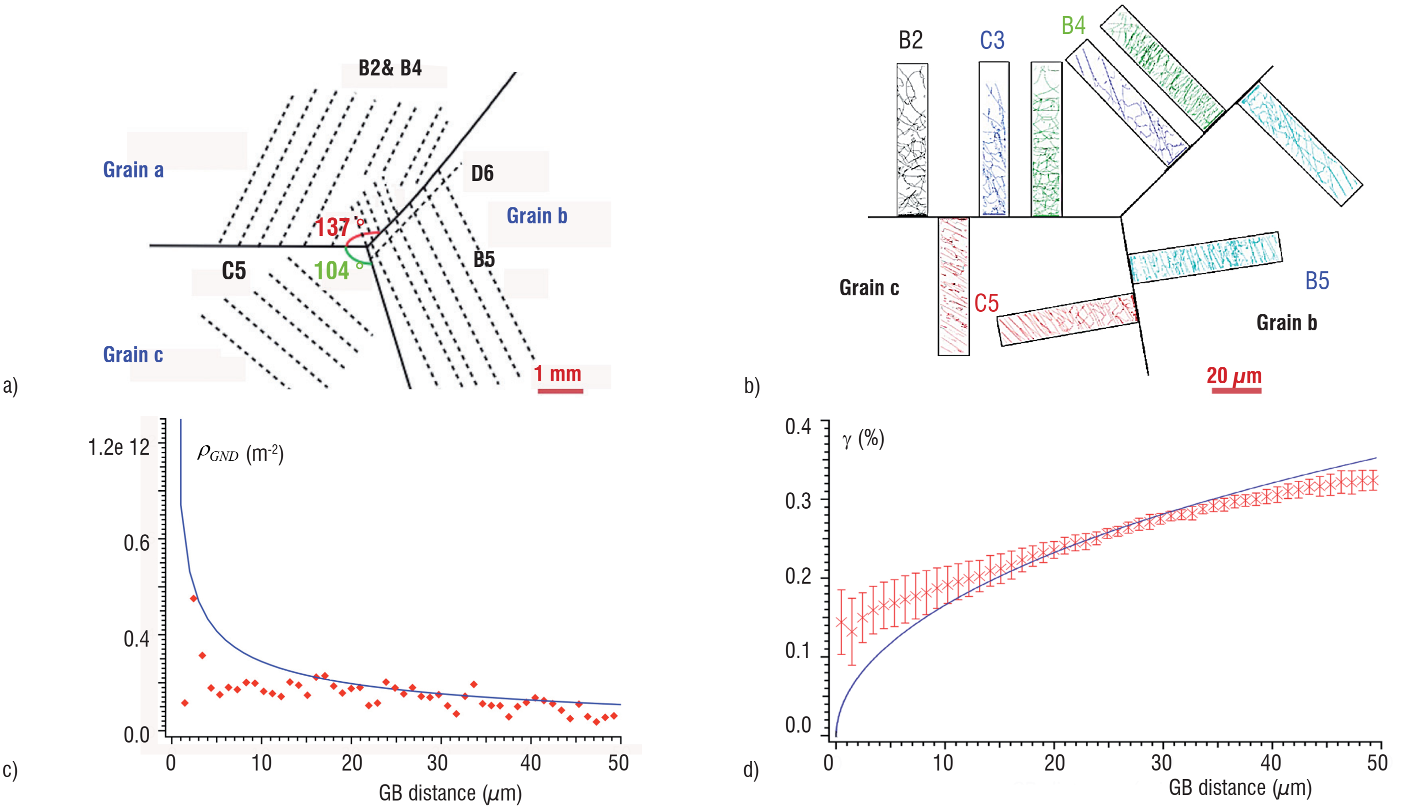

Figure 5 - (a) Schematic of the slip systems activity observed at yield in a Cu tri-crystal compression test (Schmid&Boas slip system notation is used). (b) Illustration of the slip system-GB configurations investigated with DD simulations and reproduced from a Cu tri-crystal deformation test. Dimensions of the simulated volume are $75\times13\times10\,\mu m$. (c) and (d) are respectively, the average profiles of GND density and plastic shear calculated with the DD simulations illustrated in (b). Continuous blue lines are solutions of the classical equation of a one-dimensional pile-up profile and the equations (5) holding from the average dislocation density in the simulated volume.

close to a GB. Integration of eq. 5 reproduces the formation of heterogeneous densities of GND known as a dislocation pile-up distribution. Such configurations are essential since they are the basis for the notion of back stress and the foundation of many size effects like the Hall-Petch mechanism [11]. Again, calculation of the parameters monitoring the formation of 3D pile-up configurations against GBs has been made with DD simulations. As illustrated in figure 5, we systematically studied the dislocation microstructures formed against a GB with different slip system geometries (i.e. different misorientation between slip planes and GB planes). Such simulated configurations were identified from a real Cu tri-crystal deformation test (figure 5-a) and the analysis of active slip system traces at yield.

Unsurprisingly, simulated 3D dislocation microstructures are different from the ideal pile-up configurations discussed in textbooks. The back-stress fields we found are complex construction of the long-range stress fields associated to dislocations sharing the same glide plane, but also from many dislocations positioned on neighboring, parallel or tilted glide planes. Nevertheless, averaging the plastic strain and the GND density, as function of the GB normal distance, shows that simulated 3D dislocation configurations can still be interpreted with a generalized concept of pile-up stress. Hence, a new expression for the back-stress associated to 3D GND microstructures accumulated against a GB was proposed as function of r_{GB} :

$$X^i(r_{GB}) = \beta\cos(\theta^i)\mu b\sqrt{\rho_{GND}(r_{GB})}\sqrt{r_{GB}} \qquad (6)$$

In eq. 6, θ^i is the angle between the GB and the slip system, and β is a geometrical parameter accounting for the organization of dislocations in 3D configurations. The latter value was numerically estimated to 37 from many DD simulation results.

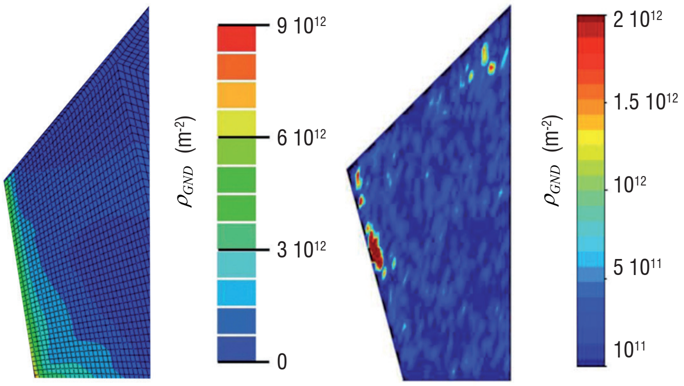

Figure 6 - Comparison between simulated and measured GND density distribution at 0.2% compression strain in a grain part of a tri-crystal (see figure 5-a for the total geometry).

The predictive ability of eq. (5) and (6) in addition with the equations previously defined for isotropic strain hardening was tested with a crystal plasticity code in the case of a Cu tri-crystal compression test. As shown in figure 6, the GND density distribution at 0.2% strain was calculated in a meshed tri-crystal and compared with measurements made with the μLaue-XRD technique in the real sample [13]. In the early stage of plastic deformation observed experimentally, excellent agreement is found for the slip systems activity between simulation and experience. In addition, good agreement (within the limits of the experimental errors) is found for the GND density amplitude and distribution (i.e. rotation fields) in the grains.

Conclusion and perspectives

In this paper we have first presented the progress we made in the development and numerical implementation of DD simulations. More specifically, we emphasized the breakthrough made in the last two years in a coupling of DD and FE simulations to solve complex boundary problems. The numerical strategy developed, called the discrete-continuous model (DCM), is now mature and offer many advantages. Then, we have shown that the internal state variables and the mathematical forms used in crystal plasticity calculations can be physically justified and identified with DD simulations. An important effort was first devoted to the modeling of isotropic strain hardening in pure fcc metals. Recently, we started to investigate more complex phenomena at the origin of kinematic strain hardening.

Modeling complex loading with large strain in a multi-phased polycrystalline materials is still a long-term goal, but important progresses have been made that extend the domain of validity of the existing crystal plasticity models. Simulations of the Bauschinger effect and cyclic deformation conditions are the next steps. The constitutive equations used for these problems involve back-stress formulations opening the door to many different interpretations at the dislocation scale. A study with the DCM simulation of the collective and dynamic properties involved here should gives useful information for design methods against fatigue of structural materials [13].

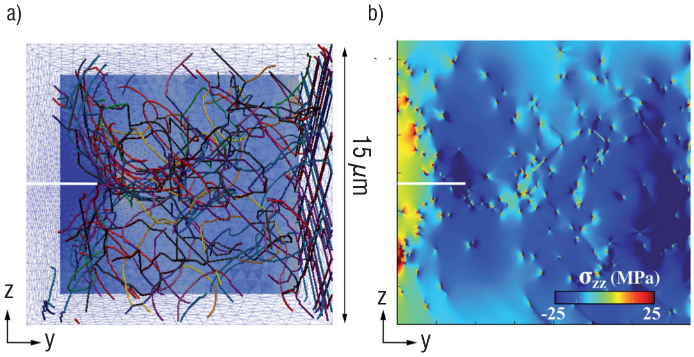

Figure 7 - (a) Example of a dislocation microstructure formed at a crack tip in a Cu sample loaded in Model. The crack location is the thin white segment and the dislocation lines are plotted with colors according to their slip systems. (b) The elastic shielding effect caused by the dislocation microstructure is illustrated in a plane normal to the crack tip. The plotted quantity σ_{ZZ} is the sum of the dislocation stress fields in the sample and is clearly opposed to the crack opening (Courtesy of L. Korzeczek, PhD work).

Another important problem in which the capability of the DCM simulation will be exploited is the study of plastic relaxation at crack-tip in ductile materials. Here, two main phenomena take place: a dislocation microstructure is locally developed to decrease stress concentration ahead of the crack (shielding effect) and the crack tip changes its shape due to the emission/absorption of dislocations (blunting effect). The DCM is suitable to simulate these two phenomena, on the one hand the proper boundary conditions can be imposed to compute the mechanical equilibrium in a material including a crack and on the other hand the evolution of the dislocation microstructure can be precisely investigated. Figure 7 shows one of the first results obtained using the DCM. Here a Cu single crystal is deformed in the z direction to open a crack in mode I. The crack plane is normal to the (100) direction with a crack tip parallel to the [010] direction. Panel (a) shows how the dislocation pre-existing in the sample reacts to the stress field ahead of the crack tip and rapidly build a plastic zone. The elastic shielding of the dislocation microstructure that works to reduce crack opening is shown in panel (b). Ongoing work is dedicated to this problem for cyclic deformation conditions and in a polycrystalline material to better understand grain size effects ■

References

[1] A. Arsenlis & D. M. Parks - *Crystallographic Aspects of Geometrically-Necessary and Statistically-Stored Dislocation Density*. Acta Materialia 47, p. 1597 (1999).
[2] J. L. Chaboche - *A Review of Some Plasticity and Viscoplasticity Constitutive Theories*. International Journal of Plasticity 24, p. 1642 (2008).
[3] B. Devincre, T. Hoc & L. Kubin - *Dislocation Mean Free Paths and Strain Hardening of Crystals*. Science 320, p. 1745 (2008).
[4] B. Devincre & L. Kubin - *Scale Transitions in Crystal Plasticity by Dislocation Dynamics Simulations.* Comptes Rendus Physique 11, p. 274 (2010).
[5] B. Devincre, L.Kubin & T. Hoc - *Collinear Superjogs and the Low-Stress Response of FCC Crystals.* Scripta Materialia 57, p. 905 (2007).
[6] B. Devincre, L.Kubin & T. Hoc - *Physical Analyses of Crystal Plasticity by DD Simulations*. Scripta Materialia 54, p. 741(2006).
[7] B. Devincre, L.Kubin, C. Lemarchand & R. Madec - *Mesoscopic Simulations of Plastic Deformation*. Materials Science and Engineering A 309-310, p. 211 (2001).
[8] B. Devincre, R. Madec, G. Monnet, S. Queyreau, , R. Gatti & L. Kubin - *Modeling Crystal Plasticity with Dislocation Dynamics Simulations: The 'microMegas' Code, in Mechanics of Nano-Objects.* Presses de l'Ecole des Mines de Paris (2011).
[9] P. Franciosi, M. Berveiller & A. Zaoui - *Latent Hardening in Copper and Aluminium Single Crystals*. Acta metall. 28, p. 273 (1980).
[10] S. Groh, B. Devincre, L.Kubin, A. Roos, F. Feyel & J.-L. Chaboche - *Dislocations and Elastic Anisotropy in Heteroepitaxial Metallic Thin Films*. Phil. Mag. Letters 83, p. 303 (2003).
[11] I. Groma, F. F. Csikor & M. Zaiser - *Spatial Correlations and Higher-Order Gradient Terms in a Continuum Description of Dislocation Dynamics.* Acta Materialia 51, p. 1271 (2003).
[12] C. Gérard, B. Bacroix, M. Bornert, G. Cailletaud, J. Crépin & S. Leclercq - *Hardening Description for FCC Materials under Complex Loading Paths*. Computational Materials Science 45, p. 751 (2009).
[13] G. E. Ice & R. I. Barabash - *White Beam Microdiffraction and Dislocations Gradients*. Dislocations in Solids, F. R. N. Nabarro and J. Hirth, editors. Elsevier, Vol. 13, p. 499 (2007).
[14] U. F. Kocks, & H. Mecking - *Physics and Phenomenology of Strain Hardening: the FCC Case*. Progress in Materials Science 48, p. 171 (2003).
[15] L. Kubin, B. Devincre & T. Hoc - *Toward a Physical Model for Strain Hardening in FCC Crystals*. Materials Science and Engineering: A 483-484, p. 19 (2008).
[16] L. Kubin, B. Devincre & T. Hoc - *Modeling Dislocation Storage Rates and Mean Free Paths in Face-Centered Cubic Crystals*. Acta Materialia 56, p. 6040 (2008).
[17] L. Kubin - *Dislocations, Mesoscale Simulations and Plastic Flow*. Vol 5 in Oxford Series On Materials Modelling, A. Sutton and R. Rudd, editors, Oxford University Press (2013).

[18] L. Kubin, R. Madec & B. Devincre - *Dislocation Intersections and Reactions in FCC and BCC Crystals*. Multiscale Phenomena in Materials-Experiments and Modeling, vol 779 of Mat. Res. Soc. Symp. Proc., p. W1.6 (2003).
[19] C. Lemarchand, B. Devincre & L. Kubin - *Homogenization Method for a Discrete-Continuum Simulation of Dislocation Dynamics*. J. Mech. Phys. Solids 49, p. 1969 (2001).
[20] R. Madec, B. Devincre, L. Kubin, T. Hoc & D. Rodney - *The Role of Collinear Interaction in Dislocation-Induced Hardening*. Science 301, p. 1879 (2003).
[21] G. Monnet, B. Devincre & L. Kubin - *Dislocation Study of Prismatic Slip Systems and Their Interactions in Hexagonal Close Packed Metals: Application to Zirconium*. Acta mater. 52, p. 4317 (2004).
[22] G. Monnet, L. Vincent & B. Devincre - *Dislocation-Dynamics Based Crystal Plasticity Law for the Low- and High-Temperature Deformation Regimes of BCC Crystal.* Acta Materialia 61, p. 6178 (2013).
[23] L. Méric, P. Poubanne & G. Cailletaud - *Single Crystal Modeling for Structural Calculations: Part 1 Model Presentation*. Trans. ASME 113, p. 162 (1991).
[24] C. Teodosiu, J. L. Raphanel & L. Tabourot - *Finite Element Simulation of the Large Elastoplastic Deformation of Multicrystals*. Large Plastic Deformations, C. Teodosiu, J. Raphanel, and F. Sidoroff, editors, Rotterdam, p. 153 (1993).
[25] A. Vattré, B. Devincre, F. Feyel, R. Gatti, S. Groh, O. Jamond & A. Roos - *Modelling Crystal Plasticity by 3D Dislocation Dynamics and the Finite Element Method: The Discrete-Continuous Model revisited*. Journal of the Mechanics and Physics of Solids 63, p. 491 (2014).

AUTHORS

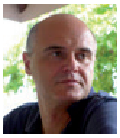

Benoit Devincre is Director of Research at CNRS. Graduated as an Engineer from University Paris IX Orsay (1989), with a PhD degree (1993) and a Research Habilitation Thesis in Material Science from University Paris IX (2005). He is working in the fields of dislocation dynamics and crystal plasticity simulations in fundamental research domains including metallurgy, semi-conductors and geophysics. His main interests are in linking the dynamical properties of crystal defects and the mechanical properties of materials. He is one of the pioneers of three-dimensionals Dislocation Dynamics simulations and has published more than 90 scientific articles.

Riccardo Gatti is a CNRS researcher (CR2) since October 2012. Graduated in Materials Science at the University of Milano–Bicocca (2006), he has got his PhD degree in 2010. His current affiliation is the Department of Microstructure Studies (LEM) at ONERA in Chatillon (France). He is working in the field of plasticity of small-scale materials. He is actively contributing to the development of the coupling between the discrete dislocation dynamics simulation code microMegas and finite element methods, with the goal of study plastic deformation in objects with complex boundary and loading conditions.

E.P. Busso
(ONERA)

E-mail: esteban.busso@onera.fr

DOI: 10.12762/2015.AL09-03

On the Deformation Heterogeneities Described By Crystal Plasticity

The deformation fields within grains in polycrystalline materials are generally highly heterogeneous and can be the precursors to the nucleation of micro-cracks or cavities. Such behavior is conditioned by microstructural features, such as grain structure, texture, morphology, size, etc. The understanding of such complex phenomena is crucial to enable structural integrity assessments of engineering components, since it constitutes the physical bases on which to describe the local mechanisms of deformation and failure to be incorporated into structural integrity codes. This work provides a brief overview of the different continuum mechanics approaches used to describe the deformation behavior of either single crystals or individual grains in polycrystalline metallic materials. The crucial role played by physics based local and non-local crystal plasticity approaches in the prediction of heterogeneous deformation is discussed. Representative examples are given regarding the use of dislocation mechanics-based crystal plasticity frameworks to describe localized plastic deformation behavior of FCC polycrystalline metallic materials.

Introduction

The macroscopic phenomena that control the physical and mechanical properties of materials are known to originate from the underlying microstructure. As the material characteristic length scales become smaller, its resistance to deformation becomes increasingly determined by local discontinuities, such as grain boundaries and dislocation cell walls. The interplay between grain boundary effects and slip mechanisms within a single crystal grain may result in either strength or weakness, depending on their relative sizes. Although experimental observations of plastic deformation heterogeneities are not new, the significance of these observations has not been addressed until very recently. Some experimental and numerical studies addressing the local interactions between deformation and grain boundaries have revealed how highly heterogeneous deformation states can develop locally, despite the grains being subjected to a uniformly applied macroscopic stress (e.g., [21,27,55,61,62]).

Grain interaction studies are typically concerned with the way in which uniform deformation patterns breakdown into highly localized regions of plastic deformation. Strain localization effects can differ significantly, depending on the initial texture of the material. For instance, the extent of in-grain subdivision leading to strain localization can vary significantly depending on texture ([1,44,54]). Furthermore, the initiation and subsequent development of localized deformation patterns is strongly influenced by the microstructure, particularly so in the case of somehow idealized polycrystalline systems. For example, if samples containing a small number of grains are derived from a directionally solidified material, the localization process is expected to be particularly sensitive to the relative grain sizes, arrangement and in-plane lattice misorientation between adjacent grains and within grains. The microstructural inhomogeneities resulting from these factors can easily lead to potentially ‘soft’ regions, which are more susceptible to extensive plastic deformation and promote strain localization. As shown in Poullier et al. [53], strain localization can be primarily driven by non-uniform lattice rotations leading to a ‘geometric softening’ of the crystal. The extent of the lattice rotation depends on the relative orientation between adjacent grains and on whether or not lattice misorientations are present within the grains. This is further supported by an experimental study on aluminum bicrystals [62], which showed that both low- and high-angle grain boundaries led to strain heterogeneities in the form of macroscopic shear bands. However, in this work, the extent of lattice rotation was found not to depend on the degree of misorientation between the crystals. Instead, it was found to depend on the initial pairing of orientations between adjacent crystals. In the limiting case, it is the length scales associated with the deformation patterns (e.g., the size of dislocation cells, the ladder spacing in persistent slip bands, or coarse shear band spacing) that control the material strength and ductility.

The issues discussed above, in addition to the ever increasingly powerful and sophisticated computer hardware and software available, are driving the development of novel material modeling approaches to study deformation behavior at the grain level. This work provides a brief overview of some of these approaches, based on the continuum mechanics modeling of plasticity at the grain / single crystal level. Special emphasis is placed on highlighting the crucial role that local and non-local crystal plasticity plays in developing an understanding of microstructure-related size effects on the local stress and strain fields responsible for damage initiation in polycrystalline metallic materials. Representative examples are also given about the use of such types of single crystal theories to predict size effects and localization behavior in polycrystalline FCC materials.

Single crystal plasticity

Constitutive models developed to predict the anisotropic behavior of single crystal materials generally follow either a Hill-type or a crystallographic approach. As a common feature, they treat the material as a continuum, in order to describe properly plastic or visco-plastic effects. Hill-type approaches (e.g., [56]) are based on a generalization of the Mises yield criterion proposed by Hill [40] to account for the non-smooth yield or flow potential surface required to describe the anisotropic flow stress behavior of single crystals. By modeling polycrystal structures with an appropriate crystallographic formulation based on microstructural internal state variables (e.g., dislocation densities), greater insight into the grain interaction and deformation behavior of polycrystals can be achieved. In constitutive formulations based on crystallographic slip, the macroscopic stress state is resolved onto each slip system following Schmid's law. Internal state variables are generally introduced in both formulations to represent the evolution of the microstructural state during the deformation process. Although recent developments of these two approaches have now reached an advanced stage, the major improvements made have been by crystallographic models, due to their ability to incorporate complex slip micromechanisms within their flow and evolutionary equations.

The inelastic response of metallic single crystal materials or grains is fully anisotropic and depends strongly on the shearing rate relations for the potentially active slip systems: 12 for FCC, 24 for BCC and 24 for HCP lattices. Kinetics and hardening-recovery mechanisms can also vary greatly. Typically, in dislocation density-based models, the evolution of the dislocation structure is described by processes of dislocation multiplication and annihilation, as well as by the trapping of dislocations [52,64]. Further discretization into pure edge and screw types enables their individual roles to be more clearly distinguished [8,20]. For example, edge and screw dislocations are associated with different dynamic recovery processes (i.e., climb for edges and cross-slip for screws), combining to influence the evolving dislocation structure of a deforming material. Comprehensive discussions of these issues can be found in, for instance, [17,18,35,48].

In what follows, local and non-local crystal plasticity approaches are discussed and representative applicative examples given.

Local single crystal approaches

A generic internal variable based crystallographic framework is said to be a local one when the evolution of its internal variables can be fully determined by the local conditions at the material point. The description of the kinematics of most crystal plasticity theories follows that originally proposed by Mandel [47] and by Asaro and Rice [10], which has been widely reported in the computational mechanics literature (e.g., [2,3,14,15,16,38,39]). The multiplicative decomposition of the total deformation gradient, $\mathbf{F}$ into an inelastic component $\mathbf{F}^p$, and an elastic component $\mathbf{F}^e$ is classical; i.e., under isothermal conditions,

$$\mathbf{F} = \mathbf{F}^e\,\mathbf{F}^p \tag{1}$$

Although single crystal laws can be formulated in a co-rotational frame, i.e., the stress evolution is computed on axes that rotate with the crystallographic lattice, the most widely used approach is to assume that the material's response is hyperelastic, that is, that its behavior can be derived from a potential (i.e., free energy) function. Such a potential function may be expressed in terms of the elastic Green-Lagrange tensorial strain measure,

$$\mathbf{E}^e = \frac{1}{2}\left(\mathbf{F}^{e^T}\mathbf{F}^e - 1\right) \tag{2}$$

and the corresponding objective work conjugate (symmetric) stress, or second Piola-Kirchhoff stress, $\mathbf{T}$. Note that the Cauchy stress is related to $\mathbf{T}$ by

$$\sigma = det\left\{\mathbf{F}^e\right\}^{-1}\mathbf{F}^e\mathbf{T}\,\mathbf{F}^{e^T} \tag{3}$$

The hyperelastic response of the single crystal is governed by,

$$\mathbf{T} = \frac{\partial\Phi\left\{\mathbf{E}^e\right\}}{\partial\mathbf{E}^e} \tag{4}$$

where $\partial\Phi/\partial\mathbf{E}^e$ represents the Helmholtz potential energy of the lattice per unit reference volume. If small elastic stretches are assumed, then

$$\mathbf{T} \cong \boldsymbol{L} : \mathbf{E}^e \tag{5}$$

where $\boldsymbol{L}$ is the anisotropic linear elastic moduli. In rate-dependent formulations, the time rate of change of the inelastic deformation gradient, $\mathbf{F}^p$, is related to the slipping rates on each slip system as

$$\dot{\mathbf{F}}^p = \left(\sum_{\alpha=1}^{n_\alpha}\dot{\gamma}^\alpha\mathbf{P}^\alpha\right)\mathbf{F}^p \text{ with } \mathbf{P}^\alpha \equiv \mathbf{m}^\alpha\otimes\mathbf{n}^\alpha \tag{6}$$

Here, $\mathbf{m}^\alpha$ and $\mathbf{n}^\alpha$ are unit vectors defining the slip direction and the slip plane normal to the slip system.

In rate-independent formulations, in contrast, flow rules are based on the well-known Schmid law and a critical resolved shear stress, τ_c^α, whereby the rate of slip is related to the time rate of change of the resolved shear stress, $\tau^\alpha(=\mathbf{T}:\mathbf{P}^\alpha)$. Then,

$$\dot{\tau}^\alpha = \dot{\tau}_c^\alpha = \sum_{\beta=1}^{m_\alpha} h^{\alpha\beta}\dot{\gamma}^\beta \text{ if } \dot{\gamma}^\beta > 0 \tag{7}$$

In the above equation, $h^{\alpha\beta}$, the slip hardening matrix coefficients, incorporate latent hardening effects. Due to the severe restrictions placed on material properties, such as latent hardening, to ensure uniqueness in the slip mode (e.g., [8,17]) and the associated difficulties in its numerical implementation, the use of rate-independent formulations has been somehow restricted and much more limited than rate-dependent ones. This has been compounded by the fact that, by calibrating their strain rate sensitivity response accordingly, rate-dependent models have been successfully used in quasi-rate-independent regimes. Thus, the focus of the discussions will henceforth be on rate-dependent approaches.

The slip rate in eq. 6 can functionally be expressed as,

$$\dot{\gamma}^\alpha = \hat{\dot{\gamma}}^\alpha\left\{\tau^\alpha, S_1^\alpha, \ldots, S_{m_s}^\alpha, \theta\right\} \tag{8}$$

where, S_i^α (for $i = 1,\ldots,m_s$),denotes a set of internal state variables for the slip system α and θ is the absolute temperature. A useful and generic expression for the overall flow stress in the slip system can be conveniently found by inverting eq. 8. Let us, for instance, consider a case with three slip resistances $(m_3=3)$. Then,

$$\tau^{\alpha} = \pm\hat{f}_{v}^{\alpha}\left\{\dot{\gamma}^{\alpha}, S_{3}^{\alpha}, \theta\right\} \pm c_{dis} S_{1}^{\alpha} \pm c_{ss} S_{2}^{\alpha} \tag{9}$$

where c_{dis} and c_{ss} are scaling parameters, S_i^{α} and S_2^{α} represent additive slip resistances and S_3^{α} is a multiplicative component. Here the distinction between the additive (S_1^{α} and S_2^{α}) and the multiplicative (S_3^{α}) slip resistances is motivated by the additive nature of non-directional scalar hardening mechanisms. By expressing the flow stress as in eq. 9, the contributions from viscous effects (first term in eq. 9), and dissipative (e.g., hardening, recovery) mechanisms arising from, for instance, forest dislocation and solid solution strengthening (i.e., second and third terms), can be clearly identified. The majority of formulations rely on power law functions for eq. 8, where the resolved shear stress is normalized by a slip resistance or hardening function, which corresponds to $S_3^{\alpha} \neq 0$ and $S_1^{\alpha} = S_2^{\alpha} = 0$ in eq. 9. This introduces a coupling between the viscous term and microstructure that is inconsistent with the aforementioned additive nature of most strengthening mechanisms. Works such as those of [14,15,19] have proposed flow stress $S_1^{\alpha} \neq 0$ and $S_2^{\alpha} = S_3^{\alpha} = 0$ which allows a more physically meaningful interpretation of strengthening phenomena controlled by the dislocation structure. The particular application for FCC polycrystals to be discussed in the next section assumes that $S_1^{\alpha} \neq 0$, $S_2^{\alpha} \neq 0$ and $S_3^{\alpha} = 0$. For a more detailed discussion of these issues, see also [17].

The relation between the overall slip resistance associated with statistically stored dislocation forest-type obstacles and the individual dislocation densities is defined by,

$$S_i^{\alpha} = \lambda\,\mu\,\mathrm{b}^{\alpha}\left\{\sum_{\beta} h^{\alpha\beta}\rho_i^{\beta}\right\}^{1/2} \quad (\text{for } i=1,\ldots,n_s) \tag{10}$$

Here, λ is a statistical coefficient, which accounts for the deviation from regular spatial arrangements of the dislocations, and b^{α} represents the magnitude of the Burgers vector. The corresponding total athermal slip resistance due to forest dislocations can then be expressed as

$$S_{dis}^{\alpha} = \left\{\left(S^{\alpha}\right) + \left(S^{\alpha}\right) + \ldots. + \left(S_{ns}^{\alpha}\right)\right\}^{1/} \tag{11}$$

where $r=1$ is used when a linear sum of the slip resistances is desired, and $r=2$ is used for a mean square value.

In order to complete the set of constitutive relations, separate evolutionary equations need to be formulated for the individual dislocation densities, with dislocation multiplication and annihilation forming the bases of their evolutionary behavior [14,15].

An application of local crystal plasticity to the study of deformation heterogeneities in FCC polycrystals

In this section, the classical local single crystal framework described in the previous section will be applied to the study of intergranular cracking in an FCC Al-0.5%Mg alloy. The work to be described here is based on that by Cheong and Busso [21], who studied the effects of lattice misorientations on the development of strain heterogeneities in FCC polycrystals in a thin Al–0.5% Mg polycrystalline specimen under uniaxial tension. The geometry and test conditions of the tensile specimen were based on the experimental work of Zhang and Tong [63], using a flat specimen gauge section containing 10 mm-size grains, with one very large grain spanning almost the entire specimen width (i.e., Grain 10 in figure 1(a)).

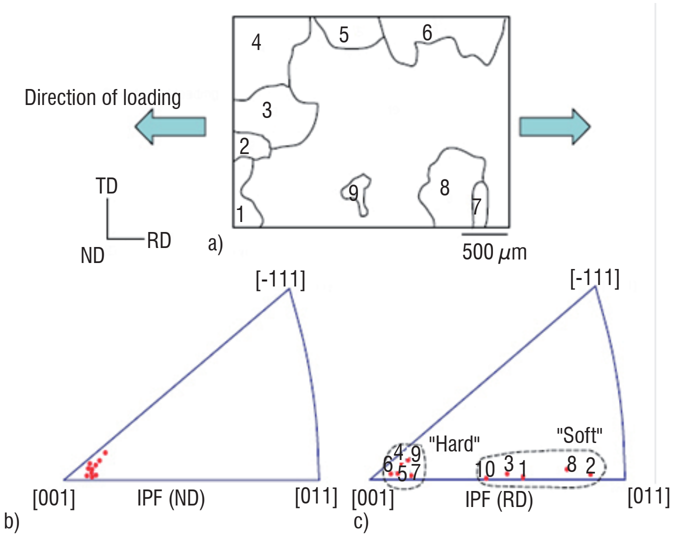

Figure 1 - (a) Initial microstructure of the Al–0.5% Mg tensile specimen (center gauge section). The inversed pole figures (IPFs) with respect to the ND direction, (b) highlights the strong ½(001) texture of the g rains with respect to the RD direction and (c) identifies the corresponding 'hard' and 'soft' orientations of the specimen's grains

Single crystal formulation

The single crystal model used for the individual grains of the FCC Al alloy was based on the original formulation proposed by [20] for Cu. The generic form of the slip rate, $\dot{\gamma}^{\alpha}$, given in eq. 8, is assumed to be dominated by the thermally activated glide of dislocations over obstacles. The slip rate is related to the resolved shear stress, τ^{α}, through the exponential function proposed by Busso [14] (see also [15,16]),

$$\dot{\gamma}^{\alpha} = \dot{\gamma}_{o} exp\left[-\frac{F_{o}}{k\theta}\left\{1-\left\langle\frac{\left|\tau^{\alpha}\right| - S^{\alpha}\mu/\mu_{o}}{\hat{\tau}}\right\rangle^{p}\right\}^{q}\right] sign(\tau^{\alpha}) \tag{12}$$

which accounts for the absolute temperature (θ, K) and the stress dependence of the activation energy. In eq. 12, F_0 represents the Helmholtz free energy of activation at $0\,K$, k is the Boltzmann constant, $\dot{\gamma}_{o}^{\alpha}$ is a reference slip rate and is the maximum glide resistance at which dislocations can be mobilized without thermal activation. Furthermore, μ and μ_0 are the shear moduli at θ and $0\,K$, respectively. The exponents p and q describe the shape of the energy barrier vs. the stress profile associated with interactions between dislocations and obstacles.

The athermal slip resistance, S^{α}, is expressed as

$$\mathrm{S}^{\alpha} = \lambda\mu b^{\alpha}\sqrt{\left(\sum_{\beta=1}^{N} h^{\alpha\beta}\rho_{T}^{\beta}\right)} \tag{13}$$

where the overall dislocation density for a given slip system β, ρ_s^{β} is obtained from a discretization of the dislocation structure into pure edge and pure screw types, of densities ρ_e^{β} and ρ_s^{β}, respectively. Thus,

$$\rho_T^{\beta} = \rho_e^{\beta} + \rho_s^{\beta} \tag{14}$$

The evolutionary equations of the individual dislocation densities account for the competing dislocation storage-dynamic recovery processes and are expressed as [19,21],

$$\dot{\rho}_e^\alpha = \frac{C_e}{b^\alpha}\left[K_e\sqrt{\sum_{\beta=1}^{N}\rho_T^\beta} - 2d_e\rho_e^\alpha\right]\left|\dot{\gamma}^\alpha\right| \tag{15}$$

and

$$\dot{\rho}_s^\alpha = \frac{C_s}{b^\alpha}\left[K_s\sqrt{\sum_{\beta=1}^{N}\rho_T^\beta} - \rho_s^\alpha\left(\pi d_s^2 K_s\sqrt{\sum_{\beta=1}^{N}\rho_T^\beta} + 2d_s\right)\right]\left|\dot{\gamma}^\alpha\right| \tag{16}$$

Here, the parameters C_e and C_s describe the relative contributions to the overall slip from edge and screw dislocations, while K_e and K_S are mobility constants associated with their respective mean free paths. Recovery processes are associated with the parameters d_e and d_s, which represent critical annihilation distances between dislocations of opposite Burgers vectors for both edge and screw types.

The calibration of the model's parameters was inspired by those reported for pure aluminum by [21]. In order to account for the increase in yield strength from solid-solution strengthening, the initial value of the slip resistance, S^α, was adjusted to provide a suitable yield strength value associated with the Al–0.5% Mg alloy. For details about the implicit numerical implementation of the above constitutive theory into the finite element method, refer to ref. [16].

Predicted deformation patterns and plastic strain distribution

Two cases with slightly different microstructural textures were considered. In Case 1, the lattice orientation of each grain was assumed to be uniform. In contrast, Case 2 assumed that within each grain, there exists a random distribution of misorientations ranging from 0° to 6°, which is typical of those found in polycrystalline aggregates. The measured and predicted deformed shape of the tensile specimens after 12% true strain is shown in figure 2. In figure 2(a), the middle section shows the distinct formation of a macroscopic shear band spanning the entire specimen width for Case 1. This is less apparent in figure 2(b) for Case 2, where deformation appears more homogeneous. Figure 2(c) presents the experimentally measured contour plots of the accumulated plastic axial strain, which reveal that the predicted local strain measurements are in agreement with those in the actual deformed specimen. In both cases, the central region of the shear bands is tilted approximately 25° from the transverse direction. However, the predicted magnitude and distribution of the accumulated plastic axial for Case 2 are closer to those in the actual specimen than Case 1. Figure 3 shows the corresponding plastic strain distributions across the specimens for Case 2 after 5 and 1% true strain. Here, the plotted strain quantity is simply defined as $\left(\varepsilon_{11}^{p} = F_{11}^{p} - 1\right)$, where the subscript '11' represents the axial component of the plastic deformation gradient, which coincides with the rolling direction (RD). Qualitatively, both Cases 1 and 2 predict the distinct formation of an inclined macroscopic shear band, which extends across the width of the specimen, in agreement with the local strain measurements in the actual deformed specimen. In both cases, the central region of the shear bands are tilted approximately 25° anti-clockwise from the transverse direction, similar to the measurements on the actual deformed specimen. However, they differ from each other as well as from the actual specimen in terms of the magnitude and distribution of the accumulated plastic axial strain. In Case 1, a rather sharp and highly localized shear band is predicted in the middle of the gauge section, with local strains more than seven times greater than the macroscopically applied uniaxial strain. In the surrounding regions, the plastic strain distribution is uniform and significantly lower, indicating that the bulk of the plastic deformation in the specimen is now accommodated within the band. In contrast, the Case 2 assumption leads to the development of a less intense shear band in the same region, which agrees more closely with the experimental evidence.

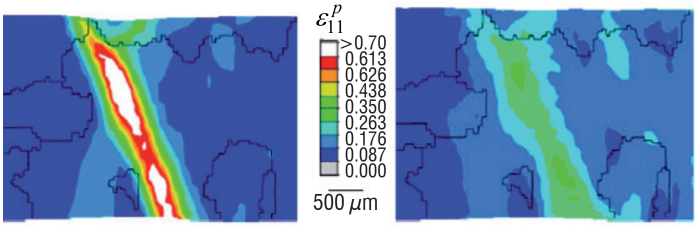

a) Case 1 (max $\varepsilon_{11}^{p} = 0.87$) b) Case 2 (max $\varepsilon_{11}^{p} = 0.36$)

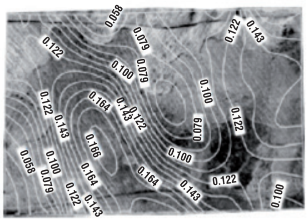

c) Case 3 (max $\varepsilon_{11}^{p} = 0.185$)

Figure 2 - Comparison between the predicted and experimentally measured distributions of accumulated plastic axial strain ε_{11}^{p} in the polycrystal for (a) Case 1 (uniform lattice orientations within each grain), (b) Case 2 (intragranular lattice misorientations) and (c) the actual tensile specimen after 12% true strain [63].

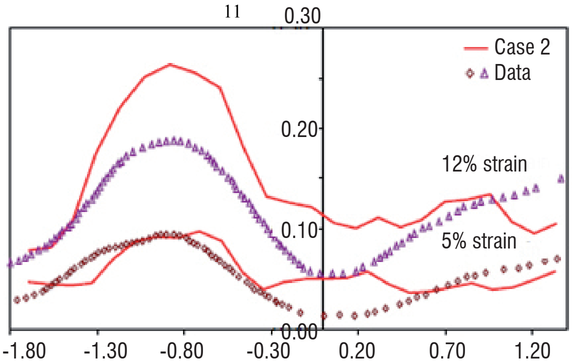

Figure 3 - Comparison between the accumulated plastic axial strain profiles along the specimen center line at 5% and 12% true strains. The open symbols are experimentally measured values [63], and the solid lines are the Case 2 predictions.

These results are consistent with a recent study on a Cu tensile specimen [19], which showed that the presence of intragranular misorientations serves to redistribute plastic strain and reduces the extent of the strain localization region, resulting in a higher average deformation within each grain.

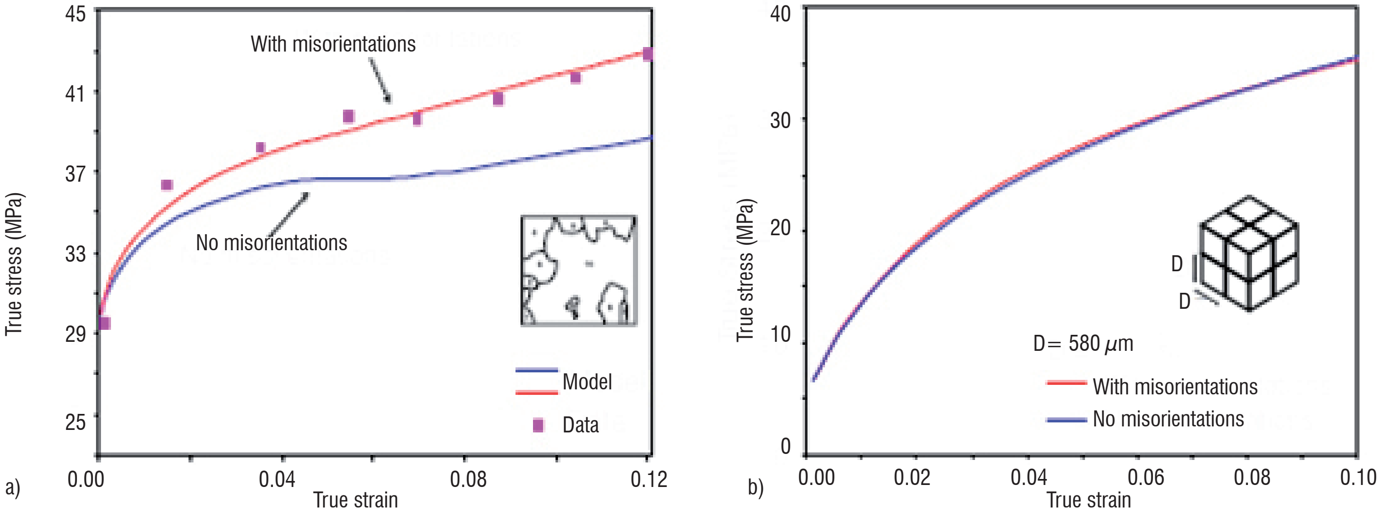

Figure 4 - The effect of intragranular misorientations on (a) thin and (b) bulk polycrystals. In (a), the experimental true stress–strain data from [63] is included to highlight the higher work hardening rate associated with the presence of intragranular lattice misorientations.

Effect of lattice misorientations on macroscopic stress-strain behavior

The difference in the macroscopic behavior of the polycrystal specimen for the case with and without intragranular lattice misorientations is shown in figure 4. The figure reveals that a higher work-hardening rate is predicted when lattice misorientations within the grains are accounted for, in agreement with the measured stress–strain response. The sensitivity of the macroscopic response to the inclusion of intragranular misorientations stems from the small number of grains in the microstructure. When high-angle boundaries are few and far between, deformation behavior is primarily dictated by the significantly larger number of low angle grain boundaries. This suggests that the mechanical behavior of such quasi two-dimensional polycrystals is more sensitive to grain substructural changes than bulk polycrystalline specimens. To confirm this, a simple study was carried out on bulk polycrystalline Al represented by an 8-grain representative volume element (RVE) with imposed periodic boundary conditions. The predicted macroscopic responses of the polycrystalline RVE up to 10% tensile strain are given in figure 4(b). It can be seen that, when compared with the thin polycrystal response of figure 4(a), the influence of intragranular misorientations in the polycrystal aggregate is negligible.

Additional results reported by [21] showed that a change of one most dominant grain in the polycrystal from a 'soft' to 'hard' initial orientation in relation to the direction of applied loading, resulted in a significant change in deformation behavior of the specimen, leading in turn to a stronger macroscopic polycrystalline response and a change in location of the localized deformation region. It could then be implied that shear bands can be expected to typically initiate in, and propagate through, grains with 'soft' orientations, thus avoiding grains with 'hard' orientations. Thus, in such thin polycrystalline specimens, a shear band need not necessarily follow a continuous straight line path but would take a path dependent upon the crystallographic orientation of the grains.

In summary, the results reported in this section have shown that a dislocation density based crystal plasticity model is capable of capturing the development of a macroscopic shear band identified experimentally. It has also been found that intragranular misorientations exert a strong influence on the deformation behavior of such polycrystals, where the total number of grains is small. However, their influence diminishes when the number of grains increases and is effectively negligible when bulk polycrystals are considered. At the local level, the prediction of the accumulated plastic axial strain distribution was found to be consistent with the experimental trend.

Non-local single crystal approaches

Most continuum approaches and formulations dealing with experimentally observed size effects in metallic materials are based on strain-gradient concepts and are known as non-local theories since the material behavior at a given material point depends not only on the local state but also on the deformation of neighboring regions. Gradient-dependent behavior becomes important once the length scale associated with the local deformation gradients becomes sufficiently large when compared with the controlling microstructural feature (e.g., average grain size in polycrys-tal materials). In such cases, the conventional crystallographic framework discussed in the previous sections will be unable to predict properly the evolution of the local material flow stress. Examples of such phenomena include particle size effects on composite behavior (e.g., [50]), precipitate size in two-phase single crystal materials [16,49], increase in measured micro-hardness with decreasing indentor size (e.g., [60]), and decreasing film thickness (e.g., [41]), amongst others.

The modeling of size effects in crystalline solids has been addressed by adding strain gradient variables into the constitutive framework, either in an explicit way in the flow rule (e.g., [6]); or in the evolutionary equations of the internal slip system variables (e.g., [4,12,16]), or by means of additional degrees of freedom associated with higher order boundary and interface conditions (e.g., [57]). The resulting strain gradient components are related to the dislocation density tensor introduced by Nye [51]. For the later, the dislocation density tensor is computed from the rotational part of the gradient of plastic deformation, so the resulting partial differential equations to be solved are generally of higher order than those used in classical mechanics. In what follows, examples of the last two types of formulations will be discussed.

Non-local models based on internal strain gradient variables

The more physically intuitive continuum approaches to describe strain gradient effects are constitutive theories (e.g., [4,9,12,16,20,29]) which rely on internal state variables to describe the evolution of the obstacle or dislocation network within the material and generally introduce the strain gradient effects directly in the evolutionary laws of the slip system internal variables without the need for higher order stresses. This requires that the overall slip resistance arising from the dislocation network, S_{dis}^{α} (see eq. 11), incorporates contributions from both statistically stored (SS) and geometrically necessary (GN) forest dislocations.

The general form for the functional dependency of the slip system internal variable evolutionary laws, extended to include the additional dependency on the GNDs and the gradient of the slip rates, $\nabla\dot{\gamma}^{\alpha}$, is

$$\begin{aligned}
\dot{\rho}_1^{\alpha} &= \hat{\dot{\rho}}_1^{\alpha}\left\{\dot{\gamma}^{\alpha},\rho_1^{\alpha},\ldots,\rho_{n_s+n_G}^{\alpha},\theta\right\}\\
&\vdots\\
\dot{\rho}_{n_s}^{\alpha} &= \hat{\dot{\rho}}_{n_s}^{\alpha}\left\{\dot{\gamma}^{\alpha},\rho_1^{\alpha},\ldots,\rho_{n_s+n_G}^{\alpha},\theta\right\}\\
\dot{\rho}_{n_s+1}^{\alpha} &= \hat{\dot{\rho}}_{n_s+1}^{\alpha}\left\{\dot{\gamma}^{\alpha},\rho_{n_s+1}^{\alpha},\ldots,\rho_{n_s+n_G}^{\alpha},\nabla\dot{\gamma}^{\alpha},\theta\right\}\\
&\vdots\\
\dot{\rho}_{n_s+n_G}^{\alpha} &= \hat{\dot{\rho}}_{n_s+n_G}^{\alpha}\left\{\dot{\gamma}^{\alpha},\rho_{n_s+1}^{\alpha},\ldots,\rho_{n_s+n_G}^{\alpha},\nabla\dot{\gamma}^{\alpha},\theta\right\}
\end{aligned} \tag{17}$$

where n_s and n_G denote the number of SSD and GND types, respectively. Consider the particular case where $n_s = 2$ and $n_G = 3$. Then, the total dislocation density on an arbitrary slip system becomes,

$$\rho_T^{\alpha} = \left(\rho_e^{\alpha} + \rho_s^{\alpha}\right) + \left(\rho_{Gs}^{\alpha} + \rho_{Get}^{\alpha} + \rho_{Gen}^{\alpha}\right) \tag{18}$$

where $\left(\rho_e^{\alpha},\rho_s^{\alpha}\right)$ are the SS densities and $\left(\rho_{Gs}^{\alpha},\rho_{Get}^{\alpha},\rho_{Gen}^{\alpha}\right)$ the GND densities, which have in addi-tion, been discretized into pure edge and screw components. Note that the inclusion of the out-of-plane edge dislocation density component accounts for dislocation segments, which may either have a non-planar orientation or an out-of-plane kink component with respect to the slip plane.

The evolution of the GNDs can be expressed in terms of a mathematically equivalent GND density vector, $\dot{\boldsymbol{\rho}}_G^{\alpha}$, defined so that its projection into the local $(\mathbf{m}^{\alpha}, \mathbf{n}^{\alpha}, \mathbf{t}^{\alpha})$ orthogonal reference system is as follows [16,19],

$$\dot{\boldsymbol{\rho}}_G^{\alpha} = \dot{\rho}_{Gs}^{\alpha}\mathbf{m}^{\alpha} + \dot{\rho}_{Get}^{\alpha}\mathbf{t}^{\alpha} + \dot{\rho}_{Gen}^{\alpha}\mathbf{n}^{\alpha} \tag{19}$$

Subsequently, the evolutionary law for each set of GNDs is determined from Nye's dislocation density tensor, $\boldsymbol{\Gamma}$ [51], in terms of the spatial gradient of the slip rate,

$$\dot{\boldsymbol{\Gamma}} = \operatorname{curl}\left(\dot{\gamma}^{\alpha}\mathbf{n}^{\alpha}\mathbf{F}^{p}\right) = b^{\alpha}\left(\dot{\rho}_{Gs}^{\alpha}\mathbf{m}^{\alpha} + \dot{\rho}_{Get}^{\alpha}\mathbf{t}^{\alpha} + \dot{\rho}_{Gen}^{\alpha}\mathbf{n}^{\alpha}\right) \tag{20}$$

Under small strains and rotations, eq. 20 simplifies to

$$\begin{aligned}
\dot{\rho}_{Gs}^{\alpha} &= \frac{1}{b^{\alpha}}\nabla\dot{\gamma}^{\alpha}\cdot\mathbf{t}^{\alpha}\\
\dot{\rho}_{Get}^{\alpha} &= \frac{1}{b^{\alpha}}\nabla\dot{\gamma}^{\alpha}\cdot\mathbf{m}^{\alpha}\\
\dot{\rho}_{Gen}^{\alpha} &= 0
\end{aligned} \tag{21}$$

The slip resistance contributions from the SSDs and GNDs can then be determined from eq. 13, using the definition of the overall dislocation density given by eq. 18. This class of theories has been shown to be capable of providing a good physical insight into the effects of microstructure on the observed macroscopic phenomena, including rate-independent plastic deformation and visco-plasticity in both single crystal and polycrystalline materials. An additional attractive feature of these theories is that they are relatively easy to implement numerically and do not require higher order stresses and additional boundary conditions or independent degrees of freedom. However, some of their limitations are that (i) they are unable to describe problems that may require non-standard boundary conditions, such as the boundary layer problem modeled in [57] and that (ii) they may exhibit a mesh sensitivity in cases where there is a predominance of geometrically necessary dislocations relative to statistically stored dislocations [20].

An application to the prediction of deformation in a channel die compression test

In this section, a study by Abrivard [1] about the deformation heterogeneities and grain fragmentation induced by the deformation of pure Al in a channel using the non-local single crystal formulation described in the previous section [19] is summarized. Such type of test is generally used to simulate cold rolling of aluminum, see figure 5. Here, the die imposes a nominally plane strain deformation gradient on the metal similar to that experienced by the aluminum passing through a rolling mill. Furthermore, the channel walls suppress the lateral material flow and induce heterogeneous lateral stresses in the deforming material. Details about the experiment can be found in [1].

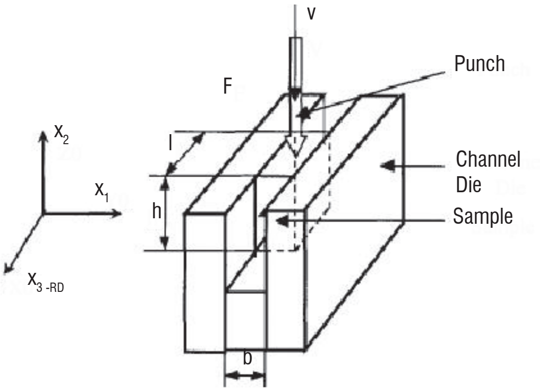

Figure 5 - Channel die compression test layout

The investigation of in-grain subdivision and inter-grain misorientations in a polycrystalline aggregate requires that the local density of geometrically necessary boundaries (GNB) be accounted for. The polycrystal material used in the channel die test model was assumed to be composed of a random distribution of grain orientations, with the initial texture as shown in figure 5(a). Here, polycrystalline aggregates containing either 20 or 40 grains with an average 100 μm size were considered in this study. Boundary conditions were applied such that a sample height reduction by compression along the x_2 axis (ND) of up to 60% was achieved. The numerical results of the deformed aggregate under plane strain compression are discussed next.

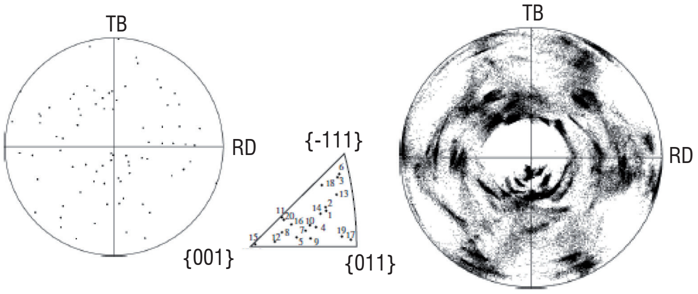

Figure 6 - (a) {111} pole and {001} inverse pole figures showing the polycrystalline aggregate initial grain orientations and (b) {111} pole figure after 60% height reduction

During deformation, grains rotate and break into subgrains with different slip system activity. As GNDs build-ups are associated with gradients of slip-rate, the number of GNDs increases signifi-cantly inside the grains. Contrary to the second gradient and Cosserat theories, no term in the free energy penalizes their development. Therefore, the determination of slip-rate gradients with the non-local theory used here could be sensitive to the mesh size. In order to attenuate this problem when solving the evolutionary laws for the GNDs densities, a quantity defined as $A = \gamma^{\alpha} n^{\alpha} F^{p}$ is calculated at the Gauss point of interest, as well as at neighboring ones found within a critical distance linked to the GNDs spread from the grain boundary [45]. Here, that distance was assumed to be given by the mean grain size. The field of the quantity A is then used to compute curl(A) at that point through a linear interpolation and the latter subsequently used to evaluate the evolution of the individual GND densities as per eq. 19 and 21.

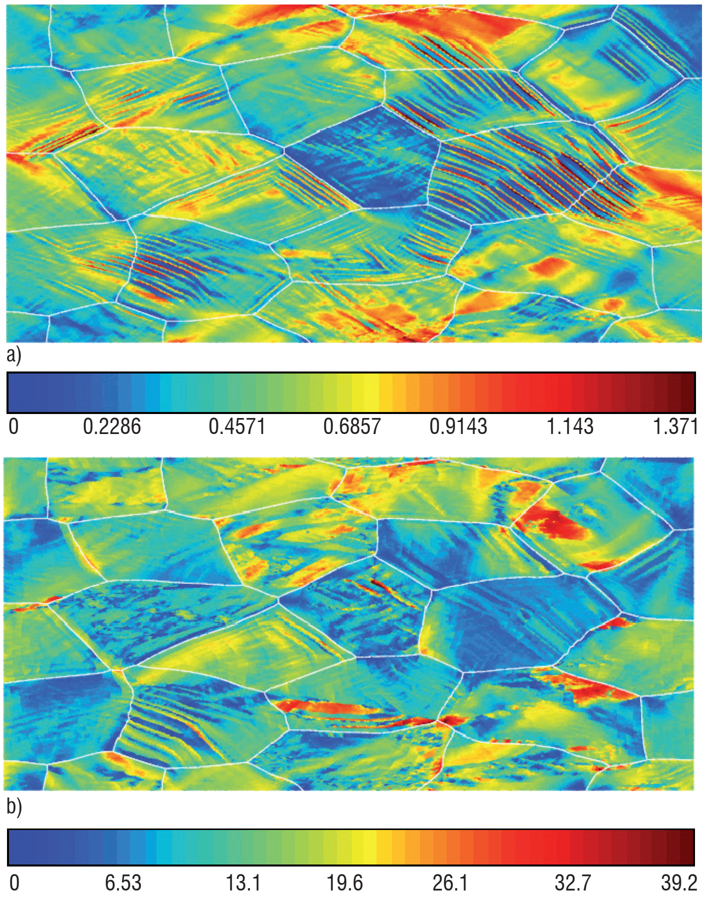

Figure 7 - (a) Accumulated inelastic strain contours
(b) Corresponding lattice rotations distribution after 30% height reduction

Figure 7 shows the predicted (a) accumulative inelastic strain contours and (b) the corresponding accumulated lattice rotations up to 30% compression. It can be seen that the predictions reveal deformation heterogeneities: grains break up into macroscopic deformation bands aligned along the 40° shear directions (towards the rolling direction, x3-axis in figure 5). This deformation process leads finally to the formation of a micro-band structure as straight dense dislocation walls run parallel to each other along preferred directions, leading to the multiplication of GNDs inside the grains. Since GNDs accommodate lattice incompatibilities in regions where the deformation is inhomogeneous, their local density can be related to the local lattice curvature described by the predicted accumulated lattice rotations in figure 7(b). It can also be seen that rotation bands are found in the same grains as those that have developed deformation bands.

Substructure description

During the deformation of high stacking fault energy of pure metals such as Al and its alloys, grains generally develop substructures, which may be classified into two different types: incidental dislocation boundaries (IDB) and geometrically necessary boundaries (GNB), see figure 9. These two types of boundary form differently: IDBs do so by the random trappings of glide dislocations, while GNBs form to accommodate the increasing subdivision of grains during confined deformation into smaller regions with rather different lattice orientations. IDBs are made up mostly of statistically stored dislocations, which do not contribute significantly to a net lattice rotation, whereas GNBs are composed of excess dislocations, which are geometrically necessary and contribute to the net lattice rotation. The size of either such regions or dislocation cells depends on the deformation level, the grain orientation and the loading path. At small strains, GNBs form elongated cell blocks surrounding regions that are almost dislocation free. At larger levels of strain, the average GNB misorientation increases and their spacing decreases.

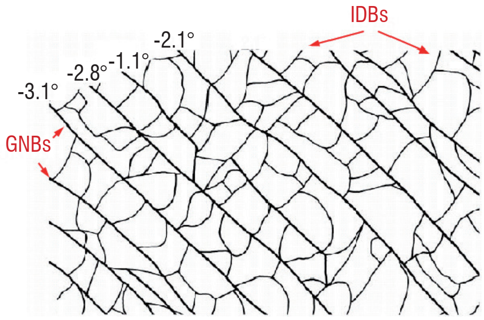

Figure 9 - Schematic representation of a grain subdivided into regions delimited by geometrically necessary boundaries (GNBs) and intense dislocation boundaries (IDBs) [46]

Under large deformations, IDs can be further sub-divided into dislocation cells whose sizes are generally reported to be less than 3 μm for pure aluminum. Thus, since the smallest finite ele-ment size used in the simulations is of the order of 4 μm, the model resolution is insufficient to describe the formation of dislocation cells explicitly. Nevertheless, it will be shown here that it is possible to predict the fragmentation of the grain in a realistic way. An example is shown in the inverse pole figure of figure 10 of the polycrystal aggregate after a

40% height reduction. The grain fragmentation is underlined through the relative misorientation between neighboring points, which have been superimposed onto the inverse pole figure of the aggregate. Here, black points or lines represent material points with neighboring sites having a relative lattice misorientation of at least 15°, blue points those with misorientations of between 5° and 15°, and gray points with those between 1° and 5°. From such type of information, as well as the local dislocation densities, it is possible to estimate the cell size statistically. It should be noted that TEM observations have shown that cell shape can vary with the grain orientation, here such dependency was not considered for simplicity.

In order to determine the cell size from the spacing between intense dislocation bands (IDBs) formed by the random trappings of glide dislocations, a relation was used by [1] which relies on statistically stored dislocation densities such that,

$$d_{IDB} = \frac{K_{IDB}}{\sqrt{\rho_{SSD}}} \tag{22}$$

where K_{IBD} is a parameter to be calibrated from experimental data. From the IDB measurements on pure Al reported by [42], $K_{IBD} = 8.5$. The resulting predicted IDB spacings calculated at each integration point of the FE model are plotted in figure 11(a) as a cloud of gray points, with their average predictions given by the red line. It can be seen that a broad range of IDBs spacing is found for the same level of equivalent strain and that the associated average predicted curve exhibits the same trend as the experimental data reported by [42].

Since geometrically necessary boundaries (GNBs) are also generated between regions to accommodate the lattice rotation differentials, only geometrically necessary dislocations are taken into account in a relation of the same type as that of eq. (22),

$$d_{GNB} = \frac{K_{GNB}}{\sqrt{\rho_{GND}}} \tag{23}$$

where $K_{IBD} = 8.5$. In figure 11(b), the predicted GNB spacing vs. the equivalent strain is in good agreement for strains greater than 25 %. Experimental data from [42] showed that GNB spacing ranges from 3 μm for strains of approximately 12% to 0.3 μm for 100% strain, just in the limits of the FE model resolution. Thus these results should be perceived as a statistical average.

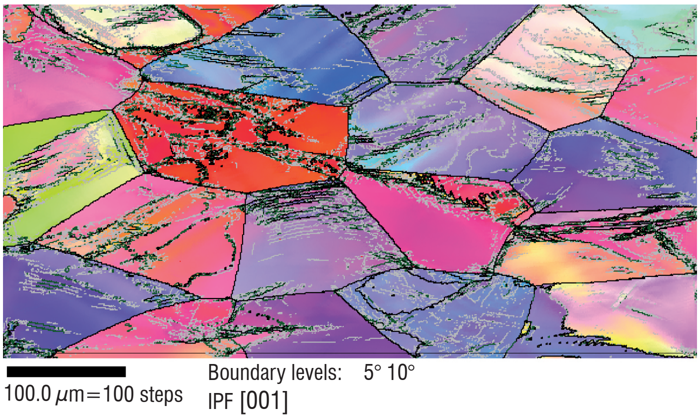

Figure 10 - [001] inverse pole figure of the polycrystalline aggregate after 40% height reduction

The above numerical predictions of the confined deformation behavior of an aluminum aggregate using a non-local dislocation density based crystal plasticity framework have shown to capture the main characteristics of the deformation heterogeneities seen experimentally, such as grain fragmentations and the development of deformation bands. Such realistic simulations are obtained despite the inherent spatial resolution limitations of the finite element model in the channel die compression test.

Non-local models based on the mechanics of generalized continua

Approaches based on the so-called mechanics of generalized continua incorporate, as a common feature, extra-hardening effects associated with the dislocation density tensor. Generalized crystal plasticity models developed in the past forty years can be classified into two main groups. In the first one, strain gradient plasticity models involve either the rotational part of the plastic distortion (i.e., the plastic rotation), its full gradient, or just the gradient of its symmetric part [32,36,37,58]. The second group involves generalized continuum theories with additional degrees of freedom accounting for either the rotation or the full deformation of a triad of crystal directors and the effect of their gradients on hardening, such as Cosserat-type models [22,33], and those based on the micromorphic theory [11,23,24,25,31].

Most of these theories have been shown to capture size effects, at least in a qualitative way. However, a clear demonstration that they can reproduce the scaling laws expected in precipitate hardening or grain

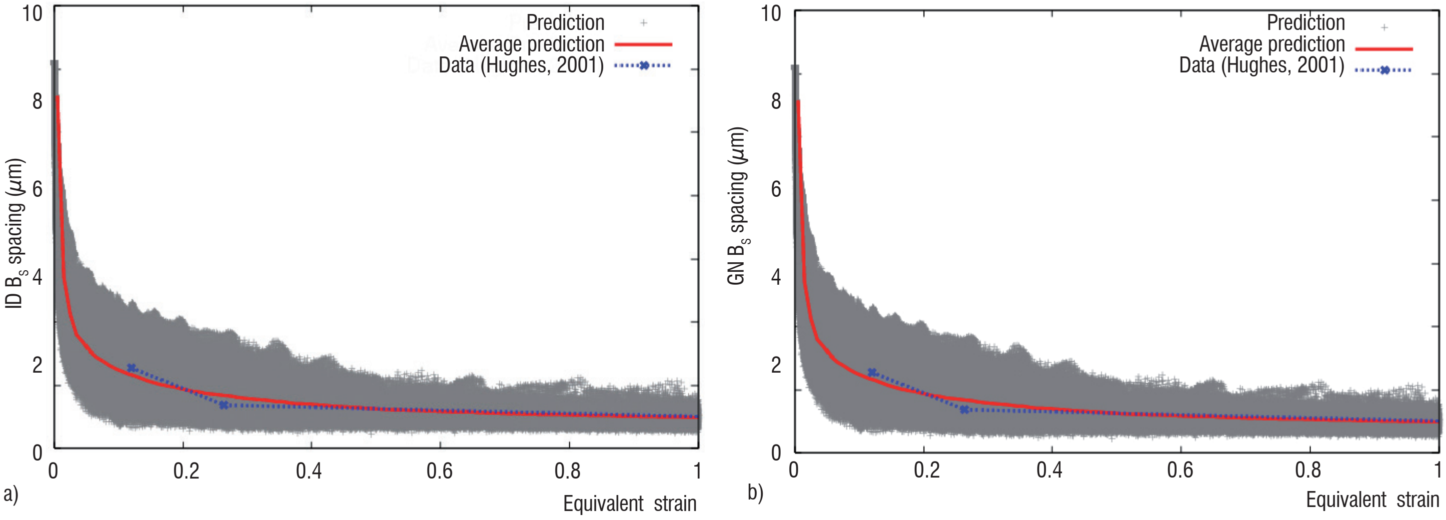

Figure 11 - Comparison between the predicted and experimental (a) IDB and (b) GNB spacing

size effect has not been fully provided yet. The additional hardening effects inherent in generalized continuum crystal plasticity models can be summarized by the main fea-tures identified in figure 12. Here, the effect of the dominant microstructural length scale, l, such as grain or precipitate size, on the material flow stress, is shown schematically in a log–log diagram. The curve can be characterized by three main features: the stress range, $\Delta\Sigma$, the characteristic length, l_c, and the slope of the intermediate region, defined by a scaling law of the form, $\Sigma \propto l^n$ at $l=l_c$. Here, $\Delta\Sigma$ corresponds to the maximum increase in strength due to size effects relative to the size-independent level. Figure 12 shows that when the characteristic size of the microstructure decreases, the material strengthens. For large values of l, the asymptotic behavior corresponds to the size-independent response of conventional crystal plasticity models reviewed in a previous section. In contrast, for small values of l, a bounded or unbounded asymptotic behavior can be obtained, depending on the type of model considered. Cosserat-type crystal plasticity models (e.g., [33]), for instance, predict an asymptotically saturated over-stress $\Delta\Sigma$ as in figure 12. In the intermediate region, when l is close to the characteristic length, l_c, the size-dependent response is characterized by the scaling law, $\Sigma \propto l^n$. The parameters $\Delta\Sigma$, l_c and n can be derived explicitly for the different classes of generalized material models described above. However, an analytic description of the size-dependent behavior of materials is possible only for some specially simplified geometrical situations. Examples are the shearing of a single crystal layer under single (or double) slip for strain gradient plasticity models considered in [13,23,24,25,43,57], and the single slip in a two-phase laminate microstructure by [34].

When crystal plasticity is considered under small strain assumptions, the gradient of the velocity field can be decomposed into the elastic and plastic distortion rates:

$$\dot{\mathbf{H}} = \dot{\mathbf{u}} \otimes \nabla = \dot{\mathbf{H}}^{\mathrm{e}} + \dot{\mathbf{H}}^{\mathrm{p}} \tag{24}$$

where

$$\dot{\mathbf{H}}^{\mathrm{p}} = \sum_{\alpha} \dot{\gamma}^{\alpha} \mathbf{P}^{\alpha} \tag{25}$$

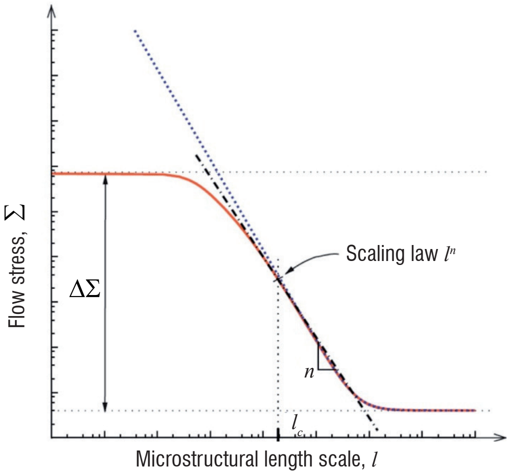

Figure 12 - Effect of the dominant microstructural length scale, l, on the material flow stress, Σ, predicted by various types of models, such as those exhibiting two asymptotic regimes (solid line) and others that exhibited an unbounded flow stress for small length scales (dotted line). Also included is the scaling law in the transition domain (dot-dashed line) [43]

with, u, the displacement field, α the number of slip systems, $\dot{\gamma}^{\alpha}$ the slip rate for the slip system α, and $\mathbf{P}^{\alpha}$ as defined in eq. 6. The elastic distortion tensor, $\mathbf{H}^e$, which represents the stretch and rotation of the lattice, links the compatible total deformation, $\mathbf{H}$, with the incompatible plastic deformation, $\mathbf{H}^p$, which describes the local lattice deformation due to the flow of dislocations. On account of eq. 24 and since applying the curl operator to the compatible field represented by $\mathbf{H}$ is equal to zero, it follows that

$$\mathrm{curl}\ \dot{\mathbf{H}} = 0 = \mathrm{curl}\,\dot{\mathbf{H}}^{\mathrm{e}} + \mathrm{curl}\,\dot{\mathbf{H}}^{\mathrm{p}} \tag{26}$$

The incompatibility of the plastic distortion is characterized by its curl part, also known as the dislocation density tensor or Nye's tensor [4,51,58], defined as

$$\mathbf{\Gamma} = -\mathrm{curl}\ \mathbf{H}^{\mathrm{p}} = \mathrm{curl}\ \ \mathbf{H}^{\mathrm{e}} \tag{27}$$

The tensors $\mathbf{H}$, $\mathbf{H}^e$, and $\mathbf{H}^p$, are generally non-symmetric, thus they can be decomposed into their symmetric and skew-symmetric parts:

$$\mathbf{H} = \mathbf{E} + \mathbf{W}, \mathbf{H}^e = \mathbf{E}^e + \mathbf{W}^e, \mathbf{H}^p = \mathbf{E}^p + \mathbf{W}^p \tag{28}$$

Combining eqs. 26 and 28 leaves

$$0 = \mathrm{curl}\ \mathbf{E}^e + \mathrm{curl}\ \mathbf{W}^e + \mathrm{curl}\ \mathbf{H}^p \tag{29}$$

Neglecting the curl part of the elastic strain, $\mathbf{E}^e$, leads to the following approximation of the dislocation density tensor derived by Nye:

$$\mathbf{\Gamma} = \mathrm{curl}\ \mathbf{H}^e = \mathrm{curl}\ \mathbf{E}^e + \mathrm{curl}\ \mathbf{W}^e \approx \mathrm{curl}\ \mathbf{W}^e \tag{30}$$

Thus, Nye's formula sets a linear relationship between the dislocation density tensor and the lattice curvature defined by $\mathbf{W}^e$. The Cosserat crystal plasticity theory accounts for the effect of lattice curvature on the crystal hardening behavior by incorporating the three additional independent degrees of freedom associated with the components of the lattice rotation, $\mathbf{W}^e$. In contrast, theories such as those proposed by [36] and [59], for example, include the full curl of the plastic distortion, $\mathbf{H}^p$, as an independent internal variable of the constitutive model. This requires, in general, nine additional degrees of freedom associated with the generally non-symmetric plastic distortion tensor, $\mathbf{H}^p$. This sub-class of models is sometimes referred to as 'curl $\mathbf{H}^p$'- type [23]. A consequence of neglecting the curl of the elastic strain tensor in Cosserat-type models is that Cosserat effects can arise, even in the elastic regime, as soon as a gradient of ''elastic'' rotation exists (i.e., $\mathrm{curl}\ \mathbf{W}^e \neq 0$). This implies that as soon as the $\mathrm{curl}\ \mathbf{E}^e \neq 0$, the $\mathrm{curl}\ \mathbf{W}^e \neq 0$. In contrast, in the curl -type theories, strain gradient effects can only arise when plastic deformation has developed. As has been shown in [23], this can lead to discontinuities in the generalized tractions at the interface between elastic and plastic regions. For the $\mathrm{curl}\,\mathbf{H}^p$-type models, it is necessary to identify numerically higher order boundary conditions at the elasto-plastic boundaries, which poses difficulties in the numerical implementation of this type of formulations, as discussed in [23].

To overcome the limitations of both the Cosserat and $\mathrm{curl}\,\mathbf{H}^p$-type theories, a new regularization method has recently been proposed by Cordero et al. [23] (see also [24,25]). Their model, which they have called *microcurl*, falls into the class of generalized continua with additional degrees of freedom. Here, the effect of the dislocation density tensor is introduced into the classical crystal plasticity framework by means of the micromorphic theory of single crystals. It relies on the introduction of an additional plastic micro-deformation variable, $\boldsymbol{\chi}^p$, a second-rank generally non-symmetric tensor. It is distinct from the plastic distortion tensor $\mathbf{H}^p$, which is still treated as an internal variable of the problem, in the same way as in $\operatorname{curl}\mathbf{H}^p$-type theories. For the general three dimension case, the nine components of $\boldsymbol{\chi}^p$ are introduced as independent degrees of freedom. For full details about the microcurl theory, the reader is referred to [18,23,24,25].

An application of the microcurl model to study the deformation behavior of a polycrystalline aggregate

The microcurl model was applied to study the global and local responses of two-dimensional polycrystalline aggregates with grain sizes ranging from 1 to 200 microns (For full details about this work, refer to [25]). A typical result from this work about the effect of grain size on the way plastic deformations in polycrystals evolve is shown in figure 13 for a 52-grain aggregate. These contour plots show the field of equivalent plastic deformation, $\tilde{\varepsilon}^p$, defined as the time-integrated value of

$$\dot{\tilde{\varepsilon}}^p = \sqrt{\frac{2}{3}\dot{\mathbf{H}}^p : \dot{\mathbf{H}}^p} \tag{31}$$

From figures 13(a) and (b), it can be seen that, at the onset of plastic deformation, plasticity starts in the same grains and at the same locations in 100-μm grains as in 1-μm grains. This is due to the fact that the same critical resolved shear stress is adopted for both grain sizes, that is, the same initial dislocation densities are assumed in both cases. In contrast, at higher mean plastic strain levels, the strongly different values of the plastic micro-deformation gradients lead to significantly different plastic strain fields. Two main features are evidenced in figure 13(c) to (f). Firstly, a tendency to strain localization in bands is observed for small grain sizes. The strain localization bands cross several grains, whereas plastic strain becomes more diffuse at larger grain sizes, which is something that had already been seen in the simulations presented in [24]. Secondly, a consequence of this localization is that some small grains are significantly less deformed than the larger ones. These features are also visible on the plastic deformation maps of figure 13 for the same aggregate but different grain sizes. This figure also shows the field of the dislocation density tensor norm:

$$\left\|\mathbf{\Gamma}_\chi\right\| := \sqrt{\mathbf{\Gamma}_\chi : \mathbf{\Gamma}_\chi} \tag{32}$$

This scalar quantity indicates the presence of GNDs and has the physical dimension of lattice curvature (mm−1). In large grains, GNDs are mainly located close to grain boundaries. At smaller grain sizes, the GND densities become significantly greater and spread over larger zones within the grains. Note also that pile-up like structures close to grain boundaries are clearly visible in the 10-μm grain aggregate. It should be noted that strain gradient plasticity models may be prone to strain localization when plasticity is confined to small regions. The reason for such behavior is that intense slip bands that exhibit a strong gradient of plastic slip perpendicular to the slip plane are not associated with GND formation. In contrast, regions of high lattice curvature or kink bands lead to an energy increase. This explains why, at small scales, intense slip bands are preferred to strongly curved regions and pile-ups.

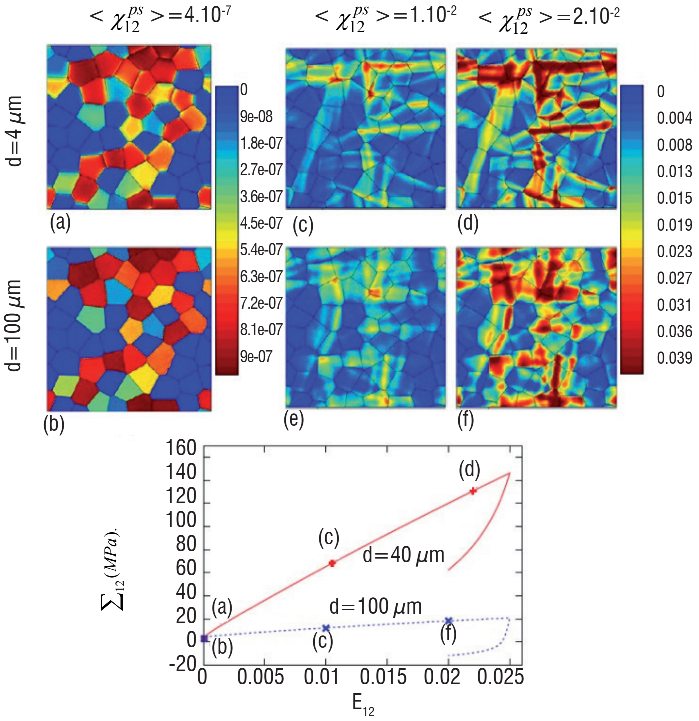

Figure 13 - (a)–(f) Contour plots of the accumulated plastic strain $\tilde{\varepsilon}^p$ for two grain sizes, d = 100 and 4 μm, and different mean values of the plastic strain: $\chi_{12}^{ps} \approx 0.0$, 0.01 and 0.02, obtained with a 2D 55-grain aggregate under simple shear, (g) macroscopic stress–strain response of the corresponding aggregate, with the letters indicating the different loading steps corresponding to the (a)–(f) contour plots [23]

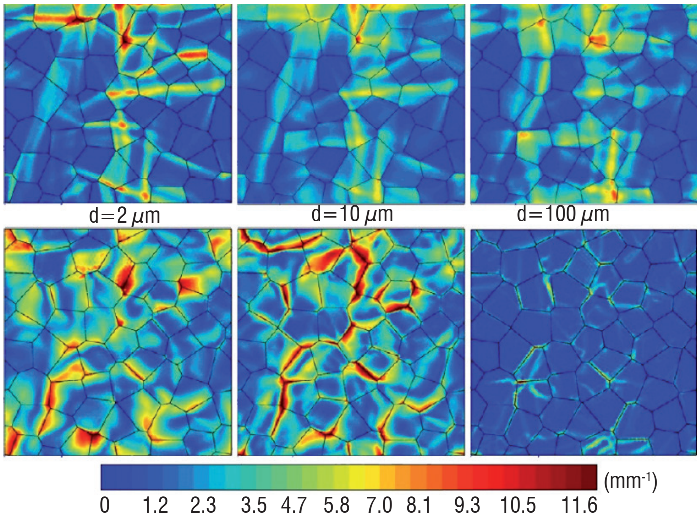

Figure 14 - Grain size effect on the accumulated plastic strain, (top figures), and on the norm of the dislocation density tensor, (bottom figures). These contour plots are obtained with the 2D 55-grain aggregate for the same mean value of $\chi_{12}^{ps} = 0.01$. The color scale for the plastic strain field of the top figures is the same as that of figure 12 on the right. The color scale at the bottom is that for the dislocation density tensor fields [23]

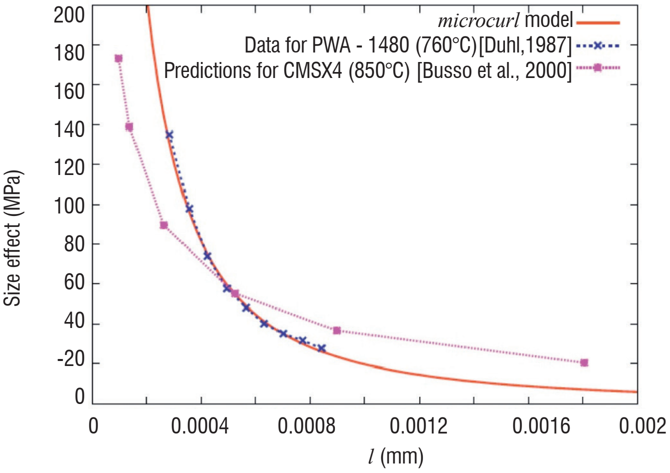

Figure 15 - Comparison between experimental data, in the form of precipitate size vs. size effect strengthening from a two-phase material (elasto-viscoplastic γ phase matrix with an embedded 68% quasi-elastic γ' precipitates) from Duhl (1987), the prediction of [16] and that obtained using the *microcurl* model [25]

In summary, the microcurl model was found to naturally predict a size-dependent kinematic hardening behavior, which is responsible for the observed strong size effects. Furthermore, the study showed that the flow stress attained at a given averaged plastic strain follows a power law scaling relation with the grain size, for grain sizes larger than a critical value. Likewise, the predicted plastic deformation fields were found to be strongly affected by grain size, with micron-size grain regions exhibiting the formation of intense slip bands crossing several grains. Finally, the dislocation density tensor, $\mathbf{\Gamma}_{\chi}$, was found to impact not only the overall polycrystal behavior, but also to control the way in which plastic deformation develops within the grains.

In Cordero et al. [23], it was shown that the microcurl approach could also be successfully used to predict experimentally observed precipitate size effects in two-phase single crystal nickel based superalloys. This is shown in figure 15, where a comparison between experimental data, in the form of precipitate size vs. size effect strengthening from a two-phase superalloy material (γ phase matrix with an embedded 68% γ' precipitates), the predictions of Busso et al. [16] and that obtained using the microcurl model [25] are shown. It can be seen that the microcurl model is able to simulate a precipitate size effect naturally. Moreover, the identified characteristic length, $lc=200\ nm$, is approximately the matrix channels width in Ni-base superalloys.

Concluding remarks

The various constitutive modeling approaches that address a broad range of phenomena at either the single crystal or the polycrystalline levels have been discussed. This overview has also highlighted the rich variety of physical, computational and technological issues within the broad area of micromechanics, which have been successfully addressed, and has identified some theoretical and computational difficulties and challenges for future developments. Recent advances in measuring and observation techniques, such as 2D and 3D image correlation, tomography, high resolution EBSD, in-situ TEM and SEM testing, combined spectroscopy and SEM, computational power and parallel processing are opening great new opportunities for the validation and implementation of predictive crystal plasticity based models. In this overview, it has been shown that size effects can be captured realistically by the curl of the plastic strain, or dislocation density tensor; however a better accounting of physical properties via cross-graining (multi-scale links) is needed. In future research, statistical effects will also need to be considered more thoroughly. The effects of grain dislocation substructures are also still too phenomenological. Crystal plasticity is also increasingly relied upon to study grain boundary - dislocation interaction (e.g., pile-ups) phenomena. Moreover, the coupling of crystal plasticity with phase field approaches to study grain complex phenomena, such as grain boundary / inter-face migration or phase transformation has now became a reality. However, even though it is still computationally too expensive, its potential is huge. Finally, the coupling of multi-physics approaches with crystal plasticity to account for time-dependent processes (e.g., dislocation climb, point-defect diffusion, irradiation damage) has recently been shown to be a logical and promising evolution and to open up exciting new opportunities to study complex coupled phenomena ■

Acknowledgements

The author would like to acknowledge the contributions of his PhD students and Post-Doctoral researchers to this work over the years, in particular F. Meissonnier, K. Cheong, G. Abrivard, N. Cordero, and his colleagues S. Forest (Ecole des Mines de Paris) and N. ODowd (University of Limerick). The support received from Siemens-UK, Hitachi-Japan, the European Commission (through the project DIGIMAT, contract number NMP3-CT-2006-017105), the UK's EPSRC and France's ANR to study single crystal behavior is greatly appreciated

References

[1] G. ABRIVARD - *A Coupled Crystal Plasticity - Phase Field Formulation to Describe Microstructural Evolution in Polycrystalline Aggregates during Recrystallisation*. Doctoral Thesis, Centre des Matériaux, Ecole des Mines de Paris, France (2009).
[2] G. ABRIVARD , E.P. BUSSO, S. FOREST, B. APPOLAIRE - *Phase Field Modelling of Grain Boundary Motion Driven by Curvature and Stored Energy Gradient*. Part I – Theory and Numerical Implementation, Philo-sophical Magazine, V. 92, Issue 28-30: 3618-3642 (2012a).
[3] G. ABRIVARD, E.P. BUSSO, S. FOREST, B. APPOLAIRE - *Phase Field Modelling of Grain Boundary Motion Driv-en by Curvature and Stored Energy Gradient.* Part II – Application to Thermal Recrystalisation", Philo-sophical Magazine, V. 92, Issue 28-30: 3643-3664 (2012b).
[4] A. ACHARYA, J.L. BASSANI - *Lattice Incompatibility and a Gradient Theory of Crystal Plasticity.* Journal of the Mechanics and Physics of Solids 48: 1565–1595 (2000).
[5] A. ACHARYA, A.J. BEAUDOIN - *Grain Size Effects in Viscoplastic Polycrystals at Moderate Strains*. Journal of the Mechanics and Physics of Solids 48: 2213–2230 (2000).
[6] E.C. AIFANTIS - *On the Microstructural oOrigin of Certain Inelastic Models*. Journal of Engineering Mate-rials and Technology 106: 326–330 (1984).
[7] E.C. AIFANTIS - *The Physics of Plastic Deformation*. International Journal of Plasticity 3: 211–248 (1987).

[8] L. ANAND, M .KOTHARI - *A Computational Procedure for Rateindependent Crystal Plasticity*. J. Mech. Phys. Solids 44: 525-558 (1996).
[9] A. ARSENLIS, D. PARKS - *Modeling the Evolution of Crystallographic Dislocation Density in Crystal Plasticity*. J. Mech. Phys. Solids 50: 1979-2009 (2001).
[10] R.J. ASARO, J.R. RICE - *Strain Localization in Ductile Single Crystals*. J. Mech. Phys. Solids 25: 309-338 (1977).
[11] D.J. BAMMANN - *A Model of Crystal Plasticity Containing a Natural Length Scale*. Materials Science and Engineering A 309–310: 406–410 (2001).
[12] J.L. BASSANI - *Incompatibility and a Simple Gradient Theory of Plasticity*. Journal of the Mechanics and Physics of Solids 49: 1983–1996 (2001).
[13] E. BITTENCOURT, A. NEEDLEMAN, M. GURTIN, E .VAN DER GIESSEN - *A Comparison of Nonlocal Continuum and Discrete Dislocation Plasticity Predictions.* Journal of the Mechanics and Physics of Solids 51 (2): 281–310 (2003).
[14] E.P. BUSSO - PhD Thesis, Department of Mechanical Engineering, Massachusetts Institute of Technology, Cambridge, MA,USA (1990).
[15] EP. BUSSO, F. MCCLINTOCK - *A Dislocation Mechanics-Based Crystallographic Model of a B2-Type Intermetallic Alloy*. Int. J. Plasticity 12: 1-28 (1996).
[16] E.P. BUSSO, F.T.MEISSONNIER, N.P. O'DOWD - *Gradient-Dependent Deformation of Two-Phase Single Crystals*. J. Mech. Phys. Solids 48: 2333-2361 (2000).
[17] E.P. BUSSO, G.CAILLETAUD - On the Selection of Active Slip Systems in Crystal Plasticity. Int. J. Plasticity, 21: 2212–2231 (2005).
[18] E.P. BUSSO - Chapter on *"From Single Crystal to Polycrystal Plasticity: An Overview of Main Ap-proaches".* "Handbook of Damage Mechanics: Nano to Macro Scale for Materials and Structures", George Z. Voyiadjis (ed.), Spinger (publ.), 369-394 (2014).
[19] K.S. CHEONG, E.P. BUSSO - *Discrete Dislocation Density Modelling of Single Phase FCC Polycrystal Aggregates*. Acta Materialia 52: 5665–5675 (2004).
[20] K.S. CHEONG, E.P. BUSSO, A. ARSENLIS - *A Study of Microstructural Length Scale Effects on the Behavior of FCC Polycrystals Using Strain Gradient Concepts.* International Journal of Plasticity 21: 1797–1814 (2004).
[21] K.S. CHEONG, E.P. BUSSO - *Effects of Lattice Misorientations on Strain Heterogeneities in FCC Polycrystals*. Journal of the Mechanics and Physics of Solids 54 (4): 671–689 (2006).
[22] J.D. CLAYTON, D.L. MCDOWELL, D.J. BAMMANN - *Modeling Dislocations and Disclinations With Finite Mi-Cropolar Elastoplasticity*. International Journal of Plasticity 22: 210–256 (2006).
[23] N.M. CORDERO, A. GAUBERT, S. FOREST, E.P. BUSSO F. GALLERNEAU, S. KRUCH - *Size Effects in General-Ised Continuum Crystal Plasticity for Two-Phase Laminates*. Journal of the Mechanics and Physics of Solids, 58 : 1963–1994 (2010).
[24] N.M. CORDERO, S. FOREST, E.P. BUSSO, S. BERBENNI, M. CHERKAOUI - *Grain Size Effects on Plastic Strain and Dislocation Density Tensor Fields in Metal Polycrystals*. Computational Materials Science, 52 : 7-13 (2012a).
[25] N.M. Cordero, Forest S, E.P. BUSSO - *Generalised Continuum Modelling of Grain Size Effects in Polycrystals*. Comptes Rendus Mécanique, 340 : 261-264 (2012b).
[26] M.A. CRISFIELD - *Non-linear Finite Element Analysis of Solids and Structures*. Vol. 1 & 2, 4th edn, John Wiley & sons, New York (1997).
[27] F. DELAIRE, J.L. RAPHANEL, C. REY - *Plastic Heterogeneities of a Copper Multicrystal Deformed in Uniaxial Tension: Experimental Study and Finite Element Simulations.* Acta Mater; 48: 1075–87 (2000).
[28] F.P.E. DUNNE, R. KIWANUKA, A.J.WILKINSON - *Crystal Plasticity Analysis of Micro-Deformation, Lattice Rotation and Geometrically Necessary Dislocation Density*. Proc. Royal Society A-Math. Phys. And Eng. Sciences, Vol 468: 2509-2531 (2012).
[29] F.P.E. DUNNE, D. RUGG, A. WALKER - *Length Scale-Dependent, Elastically Anisotropic, Physically-Based HCP Crystal Plasticity: Application to Cold-Dwell Fatigue in Ti Alloys*. Int. J. of Plasticity, Vol 23: 1061-1083 (2007).
[30] D.N. DUHL - *Directionally Solidified Superalloys.* Superalloys II - High Temperature Materials for Aerospace and Industrial Power. Wiley-Interscience, John Wiley and Sons, pp. 189–214 (1987).
[31]A.C. ERINGEN, W.D. CLAUS - *A Micromorphic Approach to Dislocation Theory and its Relation to Several Existing Theories*. Simmons, J.A., de Wit, R., Bullough, R. (Eds.), Fundamental Aspects of Dislocation Theory. National Bureau of Standards (US) Special Publication 317, II,: 1023–1062 (1970).
[32] N.A. FLECK, J.W. - HUTCHINSON - *Strain gradient plasticity*. Advances in Applied Mechanics 33: 295–361 (1997).
[33] S. FOREST, F. PRADEL, K. SAB - *Asymptotic analysis of heterogeneous Cosserat media*. International Journal of Solids and Structures 38: 4585–4608 (2001).
[34] S. FOREST, R. SEDLACEK - *Plastic Slip Distribution in Two-Phase Laminate Microstructures: Dislocation-Based VS. Generalized-Continuum Approaches*. Philosophical Magazine A 83: 245–276 (2003).
[35] N.M. GHONIEM, E.P. BUSSO, H. HUANG, N. KIOUSSIS - *Multiscale Modelling of Nanomechanics and Micromechanics: an Overview*. Philosophical Magazine, 83: 3475-3528 (2003).
[36] ME GURTIN - *A Gradient Theory of Single-Crystal Viscoplasticity that Accounts for Geometrically Necessary Dislocations*. Journal of the Mechanics and Physics of Solids 50: 5–32 (2002).
[37] M.E. GURTIN, L. ANAND - *Thermodynamics Applied to Gradient Theories Involving the Accumulated Plastic Strain: the Theories of Aifantis and Fleck & Hutchinson and Their Generalization*. Journal of the Mechanics and Physics of Solids 57: 405–421 (2009).
[38] S. KALIDINDI, C. BRONKHORST, L. ANAND - *Crystallographic Texture Theory in Bulk Deformation Processing of FCC Metals*. J. Mech. Phys. Solids 40: 537 (1992).
[39] T.M. HATEM, M.A. ZIKRY - *Dislocation Density Crystalline Plasticity Modeling of Lath Martensitic Microstructures in Steel Alloys.* Philosophical Magazine, 89(33): 3087-3109 (2009).
[40] R. HILL - *The Mathematical Theory of Plasticity*. 4th edn, Clarendon Press,Oxford, U.K. (1950).
[41] N. HUBER, C. TSAKMAKIS - *Determination of Constitutive Properties from Spherical Indentation Data Using Neural Networks*. *Part II: Plasticity with Nonlinear Isotropic and Kinematic Hardening*. J. Mech. Phys. Solids 47: 1589-1607 (1999).
[42] D. HUGHES - *Microstructure Evolution, Slip Patterns and Flow Stress*. Materials Science and Engineering A-Structural Materials Properties Microstructure and Processing, 319:46–54 (2001).
[43] A. HUNTER, M. KOSLOWSKI - *Direct Calculations of Material Parameters for Gradient Plasticity.* Journal of the Mechanics and Physics of Solids 56 (11): 3181–3190 (2008).
[44] U.F. KOCKS, C.N. TOME, H.R. WENK - *Texture and Anisotropy: Preferred Orientations in Polycrystals and their Effect on Material Properties.* Cambridge University Press, UK (2000).
[45] H. LIANG, F. P. E. DUNNE - *GND Accumulation in Bi-Crystal Deformation: Crystal Plasticity Analysis and Comparison With Experiments.* International Journal of Mechanical Sciences, 51(4):326–333 (2009).
[46] Q. LIU, D. JENSEN, N. HANSEN - *Effect of Grain Orientation on Deformation Structure in Cold-Rolled Polycrystalline Aluminium.* Acta Materialia, 46(16):5819–5838 (1998).
[47] J. MANDEL - *Plasticité classique et viscoplasticité*. CISM Course N°. 97, Springer-Verlag, Wien(1972).
[48] D.L. MCDOWELL - Materials Cience and Engineering Reports; 62(3°: 67-123 (2008).
[49] F. MEISSONNIER, E.P. BUSSO, N.P. O'DOWD - *Finite Element Implementation of a Generalised Non-Local Rate-Dependent Crystallographic Formulation for Finite Strains*. International Journal of Plasticity, V. 17, Issue 4: 601-640 (2001).

[50] C-W. Nan, D. Clarke - *The Influence of Particle Size and Particle Fracture on the Elastic-Plastic Deformation of Metal Matrix Composites.* Acta Mater. 44: 3801-3811 (1996).
[51] J.F. NYE - *Some Geometrical Relations in Dislocated Crystals*. Acta Metallurgica 1: 153–162 (1953).
[52] B. PEETERS, M. SEEFELDT, C. TEODOSIU, S.R. KALIDINDI, P. VANHOUTTE, E. AERNOUDT - *Work-Hardening/Softening Behaviour of B.C.C. Polycrystals Udring Changing Strain Paths: I. An integrated Model Based on Substructure and Texture Evolution, and its Prediction of the Stress–Strain Behaviour of an IF Steel During Two-Stage Strain Paths*. Acta Mater V 49:1607–19 (2001).
[53] E. POUILLIER, A.F. GOURGUES, D. TANGUY, E.P. BUSSO - *A Study of Intergranular Fracture in an Aluminium Alloy Due to Hydrogen Embrittlement.* International Journal of Plasticity, 34: 139-153 (2012).
[54] D. RAABE, Z. ZHAO, M. MAO - *On the Dependence of in-Grain Subdivision and Deformation Texture of Aluminum on Grain Interaction*. Acta Mater. 50: 4379–4394 (2002)..
[55] D. RAABE, M. SACHTLEBER, , H. WEILAND, G. SCHEELE, Z. ZHAO - *Grain-Scale Micromechanics of Polycrystal Surfaces During Plastic Straining*. Acta Mater. 51: 1539–1560 (2003).
[56] F. SCHUBERT, G. FLEURY, T. STEINHAUS - *Modelling of the Mechanical Behaviour of the SC Alloy CMSX-4 During Thermomechanical Loading*. Modelling Simul. Sci. Eng. 8: 947-957 (2000).
[57] J.Y. SHU - *Scale-Dependent Deformation of Porous Single Crystals*. International Journal of Plasticity 14: 1085–1107 (1998).
[58] P. Steinmann - *Views on Multiplicative Elastoplasticity and the Continuum Theory of Dislocations*. International Journal of Eng. Science 34: 1717–1735 (1996).
[59] B. SVENDSEN - *Continuum Thermodynamic Models for Crystal Plasticity Including the Effects of Geometrically-Necessary Dislocations.* Journal of the Mechanics and Physics of Solids 50: 1297–1329 (2002).
[60] J. SWADENER, A. MISRA, R. HOAGLAND, M. NASTASI - *A Mechanistic Description of Combined Hardening and Size Effects*. Scripta Met. 47: 343-348 (2002).
[61] A. TATSCHL, O. KOLEDNIK - *On the Experimental Characterization of Crystal Plasticity in Polycrystals*. Mater. Sci. Eng. A 342, 152–168 (2000).
[62] S. ZAEFFERER, J.C. KUO, Z. ZHAO, M. WINNING, D. RAABE - *On the Influence of the Grain Boundary Misorientation on the Plastic deformation of Aluminum Bicrystals*. Acta Mater: 51, 4719–4735 (2003).
[63] N. ZHANG, W. TONG - *An Experimental Study on Grain Deformation and Interactions in an Al–05% Mg Multicrystal*. Int. J. Plasticity 20: 523–542 (2004).
[64] M.A. ZIKRY, M. KAO - *Inelastic Microstructural Failure Mechanisms in Crystalline Materials With High Angle Grain Boundaries.* J Mech Phys Solids V 44(11):1765–98 (1996).

AUTHORS

Esteban P. Busso is currently the Scientific Director of ONERA's Materials and Structures Branch. He was formerly Professor of Mechanics of Materials at the Ecole des Mines de Paris and director of the Ecole's Centre des Matériaux and, from 1994 till 2005, Professor at Imperial College's Department of Mechanical Engineering in London, UK. He obtained his MSc and PhD degrees from the Massachusetts Institute of Technology (MIT) in Cambridge, USA, in 1987 and 1990, respectively. He also worked in industry in the UK, Japan, South Africa and Argentina. His research involves micromechanics studies of deformation and fracture of materials and interfaces, with an emphasis on the development of multiscale and multiphysics concepts in mechanistic models to predict deformation and fracture processes.

E. Deletombe, J. Berthe,
D. Delsart, J Fabis,
B. Langrand, G. Portemont
(ONERA)

E-mail: eric.deletombe@onera.fr

DOI : 10.12762/2015.AL09-04

Experimental and Numerical Simulation Strategies for the Prediction of the Macroscopic Behavior and Rupture of Structural Materials under Fast Dynamic Loadings

The presented research works have been done at ONERA – The French Aerospace Lab, in collaboration with many academic and industrial partners. They are aimed at improving the safety and protection of passengers and crew in aircraft transport, thanks to an increased resistance of structures and decrease of high energy impacts vulnerability. This paper gives an overview of recent progress made in the experimental and numerical fields to better predict the dynamic behavior and strength of primary structure materials. In this frame, the particular questions of the mechanical characterization and numerical modeling of behavior and damage laws, of crack initiation and propagation, and of failure (be it ductile or fragile) are addressed. The described results concern both bulk materials (e.g., metals) and structured materials (e.g., composite laminates), at the macroscale level for the former and mesoscale level for the latter.

Introduction

One of the main missions of ONERA – The French Aerospace Lab, is to perform applied research in the Aeronautic and Space fields, for military and civil applications. The ONERA researchers of the Materials and Structures Scientific Branch are interested in Material Sciences (to produce knowledge and models), in Process and Technologies (to mature the readiness level of innovations) and in Applied Mathematics (to develop the numerical tools that will integrate fundamental concepts into new aircraft concept design). The works in this paper, performed in the ONERA Aeroelasticity and Structural Dynamics Department, contribute to the achievement of these objectives.

The design and manufacturing of structures is one of the main skills of the airframe and engine industry: any aircraft or spacecraft is a propelled vehicle, the first requirements of which include lightness and mechanical strength. These basic properties are directly linked to their constitutive materials. Due to specific application requirements (civil transport, space, defense, etc.), a large variety of properties, and hence performance-driven aerospace materials, must be studied and developed. Among the most common material properties are the weight, mechanical stiffness and strength, thermal stability and durability (ageing and fatigue), but more exotic ones should also be considered, such as stealth and conductivity or, also recently, environmental ones, etc. Metallic and organic matrix composite materials are both massively, but not solely, used today in the aircraft, rotorcraft, power plant, missile and spacecraft industry. One of the research objectives discussed hereafter consists, on the one hand, in studying their properties and, on the other hand, in developing knowledge and numerical models that will help the European industry to design, size and optimize improved or innovative flying structures of the next decades. From this perspective, the increase in the use of composite materials (especially organic matrix based ones) and their hybridization with metals seems inevitable, despite all of the processing and modeling difficulties that this trend still presents. This challenge cannot be viably addressed without the structural design question being considered as a whole. Obviously, material weight and mechanical stiffness cannot be separated from structural dynamics issues (hence aeroelastic coupling, fatigue vibrations, acoustic nuisance, etc.). The material thermal and mechanical strength cannot be separated from structures life-expectancy, damage tolerance and vulnerability issues. Finally, the material manufacturing and assembling processes cannot be dissociated from aerospace structure design optimization, reliability and safety issues.

Consequently, the ONERA research activities in the material and process fields are closely connected to taking into account the operational environment of the final structures. In particular, this paper describes a research that is mainly aimed at improving structural safety for crew and passengers, by increasing the mechanical strength against highly dynamic and high-energy harmful situations (either intentional or accidental). Such situations may of course also suddenly and definitely reduce the aircraft exploitation expectancy below that expected by initial design durability considerations. The research topics concern the understanding and prediction of the dynamic behavior and rupture of materials relative to structure bearing loads, such as impacts, crashes, or even explosions. These topics are not specific to Aeronautics and Space, they are more broadly of interest for Defense (Land, Marine, etc.), and also remarkably for Civil Transport (crashworthiness). Nevertheless, aerospace specificities exist here, arising from the use of different kinds of materials and processes, or simply because of different threats that must be considered (e.g., bird strike, hail impact, ditching, etc.). Compared to other industry sectors, these threats also differ in their range of load parameters (impact speeds and energy levels). In any case, fast dynamic structural analysis using Finite Elements Methods (FEM) has been greatly developing over the past decades in the aerospace industry, with ONERA being involved in many developments and with all of the previously mentioned impact scenarios being studied, such as bird strike [26] and hail impact [34], as well as flying stones, tires or fragments, or crashworthiness [11] [13] [14], ditching [37] and hydrodynamics in the fuel tanks [9] [12] [15] [39].

In order to study such events using numerical simulation codes, increasingly more complex material models are required for metals and composites, in order to take their highly non-linear and rupture dynamic behaviors into account. The authors will not discuss the numerical methods (basically natural finite elements, but possibly extended-FE or particle based methods when a complex numerical description of rupture is required), the numerical formulations (mainly Lagrangian, but not solely when very large material transformations are considered), or the resolution algorithms (explicit in this case, to solve transient regimes due to wave propagation equations in continuum media, parallel, etc.) in this paper. They will also not discuss the numerical simulation of other mechanical problems involved, such as contact, friction, heat, etc.). Let us just say that the standard numerical tools used to perform fast dynamic structural analysis are not a priori energy conservative, stable or convergent and that their predictive capabilities are not necessarily and sufficiently linked to the material model accuracy or the mesh size. Concerning rupture, it is also important to understand that the point here is not to simply predict its appearance, but rather to simulate its propagation within a large structure until a transferred part of the impact energy is internally (deformation) or kinetically (fragmentation) dissipated or accommodated. In the end, a relevant material behavior and rupture model for explicit structural finite element simulations must be understood as a compromise between model accuracy (meaning complexity) and calculation efficiency (CPU cost and robustness). This is the reason why the development of enhanced dynamic material models available in fast dynamic structural tools is still often performed separately to their quasi-static counterparts. It also explains why these dynamic models mostly cope with the macroscopic or mesoscopic material responses, and why they were historically empirical ones. More phenomenological models are proposed today in the explicit code library, which can sometimes be thermodynamically based (French school), but none of them are yet physically or mechanistically based on the purely material sense.

These material models still require characterization tests to identify their mechanical parameters. Now, in these studied impacted structures, the strain and strain rate range is a broad continuum, with areas experimenting very high levels of both, where location phenomena occur, for instance at impact points or in singular parts (because of the geometry and/or assembly [22] [23] [27] [28] [38]). The experimenter then faces several difficulties to answer the numericist who wants to run his model. The first is that no unique standard and universal dynamic testing machine exists to cover the previously mentioned large strain and strain rate ranges: the experimenter needs to have several testing machines available in the lab and to be skilled in their use, mainly hydraulic machines and Hopkinson bars here for the subsonic range of impacts considered [20] [21]. Second, while performing dynamic testing can be considered to be quite easy, the difficulty lies in succeeding to obtain proper results from it that will definitely and objectively enable the intrinsic behavior parameters of the tested material to be characterized. Third, due to the destructive nature of these tests (up to rupture) and the possible model complexity (e.g., in the case of damageable anisotropic and unsymmetrical composite materials), the experiment plan can become very large, with highly expert exploitation work being needed: the characterization issue for such models can eventually become questionable with respect to the modern aircraft development cycle, including cost and time ("too many tests kill testing").

This paper introduces some basic concepts to properly deal with these difficulties and points out some noticeable recent developments concerning experimental and numerical strategies, which will contribute to the improvement of the material and structure dynamic resistance prediction capabilities in the aerospace domain. It focuses more specifically on the characterization and modeling of macroscopic (e.g., for bulk metals) and mesoscopic (e.g., for OMC composite laminates) dynamic material behaviors, including some aspects related to crack initiation, propagation, and rupture.

The first part of the paper presents specificities and inherent difficulties in the use of dynamic jacks and small size test specimens to characterize the dynamic behavior of materials, compared to the use of quasi-static machines and normalized specimen geometry at lower strain rates. The second part of the paper discusses the measurement, the signal processing and the exploitation of the data that will be used to identify material model parameters under dynamic loadings, for non-linear behaviors (stress/strain curves). In particular, solutions that can be used to solve various issues, such as vibratory noise and inhomogeneity of experimental responses in space (in the specimen) and in time (during the test) are described. While the two previous parts of the paper address metallic and composite materials as well, the third focuses only on organic matrix composite materials, which are very fashionable at the moment in the aeronautical sector and hence at ONERA. These composite materials, which are by nature heterogeneous and anisotropic, associating polymeric matrices and various fiber reinforcements, exhibit very complex behaviors, which are non-linear, damageable, viscous and highly dependent on temperature and that turn out to be a modeling challenge compared to metallic materials under dynamic loadings. Last, general conclusions and some research outlooks conclude the paper.

Presentation of the medium speed dynamic testing machines and associated experimental protocols

The topic of interest here concerns the characterization and identification of non-linear material models in the [1.10^{-3} s^{-1}, 1.10^{+4} s^{-1}] medium range of strain rates. Let us recall that the main objective of the proposed experiments is theoretically to perform uniaxial

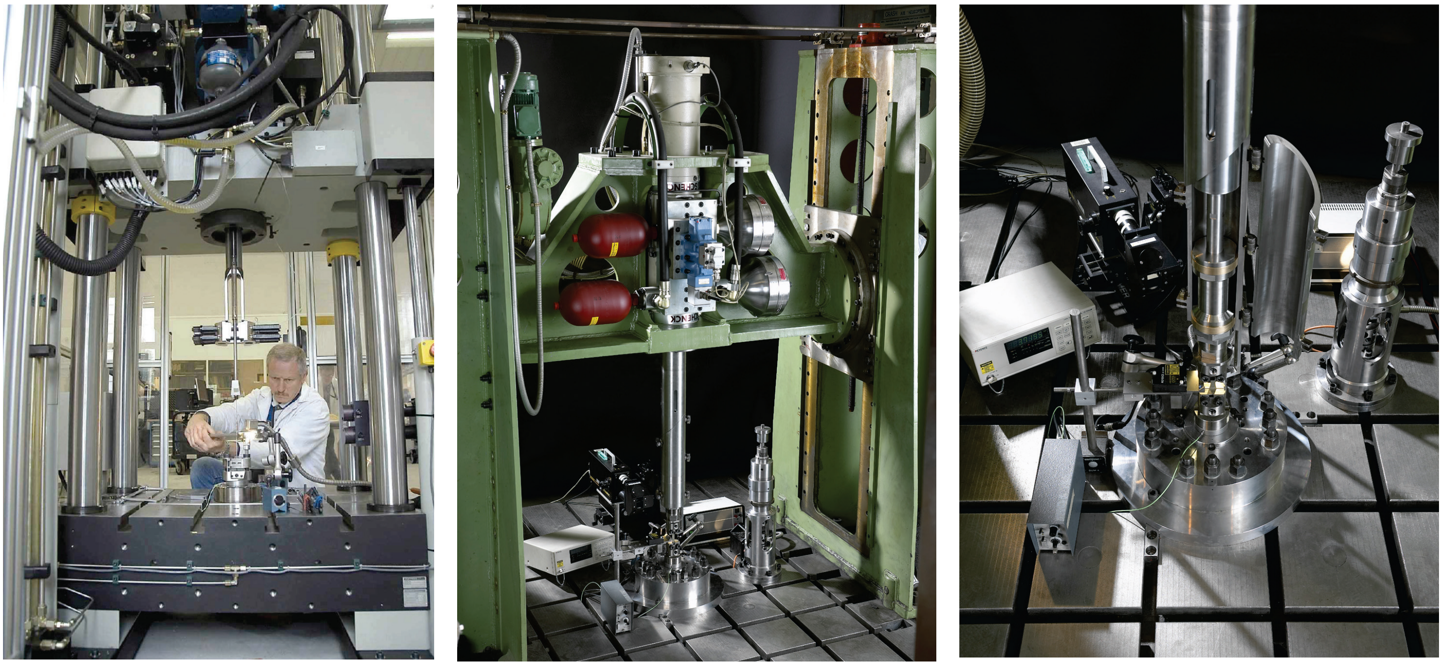

Figure 1 - INSTRON Hydraulic Jack (on the shelf, left), SCHENCK hydraulic machine (specific design, middle) and ONERA Titanium test rig developed for the SCHENCK facility (right)

load tests, monotonous from rest to rupture, tension and/or compression, at constant strain rate. One could think that such uniaxial mechanical tests at non "extreme" speeds would be perfectly mastered today, which is only true for the lowest "quasi-static" speeds in the range (a few mm/mn, up to 10^{-1} s^{-1}) with normalized test protocols being available even, and only true for long-used and known materials. This is not the case for higher test speeds (over 1 m/s and 1 s^{-1}) and for many of the modern aircraft materials. As the reader will see, apart from the mechanical limitations of the available testing machines, other causes explain the persisting difficulties to obtain test results that would allow the dynamic characterization of intrinsic material behavior and rupture model parameters: among these, the possible influence of the sample geometry on the "material" response, the difficult introduction of perfectly controlled dynamic loads into these samples, a more "miserable" instrumentation in terms of dynamic measurements compared to static ones, and a need for very rigorous data acquisition, treatment and exploitation. Some of these points will be discussed hereafter, together with some solutions currently being studied at ONERA and other research labs.

Nothing will be said about electro-mechanical testing machines, which are generally used to perform quasi-static normalized material characterization tests. The important point to be aware of is that they can be used to properly study – with some care being taken – strain rates from 10^{-4} up to 10^{-1} s^{-1}. They enable the lower range of strain rates reachable using hydraulic jacks to be overlapped. These hydraulic jacks comprise a large hydraulic framework, in which the operating jack, the test rigs (needed for load introduction and load measurement) and the material sample can be found. The size of the framework limits the testing capabilities, in terms of jack displacement range, test rig dimensions and hence of the size of material samples. The hydraulic system may directly accelerate the jack or part of the framework to which the jack is connected. Note that the weight (inertia) and stiffness of the various fixed and mobile parts have a decisive influence on the final performances of the test facility. The ONERA hydraulic jacks (INSTRON and SCHENCK respectively) have the following general capabilities: 250 and 300 mm displacement range, 10 m/s and 20 m/s maximum operating speeds, and maximum applied loads of 50 kN and 80 kN. Nevertheless, the maximum capabilities are rarely reached during tests. According to the test speed, the jack velocity V_{jack} is controlled in a closed or open loop manner. The hydraulic power being limited, such a speed instruction may be difficult to maintain when the load or speed limits of the testing machine are challenged ($P \# FV$, where P is the hydraulic power available, F is the applied load and V is the imposed velocity).

In order to perform dynamic tension tests (compression tests can be done, but they raise supplementary difficulties, e.g. samples buckling, etc.), a groove/wings concept has been proposed, each part of it being fixed respectively to the moving jack and the clamped sample, in order that the groove can be set in motion and reach the targeted velocity before it impacts the wings end to load the sample. It is then necessary to design and set up such a specific mechanical system, with its weight, stiffness, gaps and vibration modes (figure 1). An optimization work is required to prevent this new mechanical system from degrading the original dynamic characterization capabilities of the testing machine [20]. The different parts of the test rigs used at ONERA are often designed and validated using finite element analysis and made of Titanium in order to minimize their weight and maximize their stiffness, obtaining Eigenfrequencies that are high enough to be eliminated (filtered) more easily without losing information about the material sample response itself.

From the displacement speed theoretically imposed to the sample, it is possible to calculate the engineering strain rate using (1):

$$\dot{\varepsilon} = \frac{V_{sample}}{l_{free}} \qquad (1)$$

where V_{sample} is the test speed imposed to the sample and l_{free} is the deformable length of the sample (between the grips, if the grip is perfect). As a first approximation, if the imposed test speed is assumed to remain constant and the sample elongation (and deformation) is assumed to be small during the dynamic test before rupture, it is easy

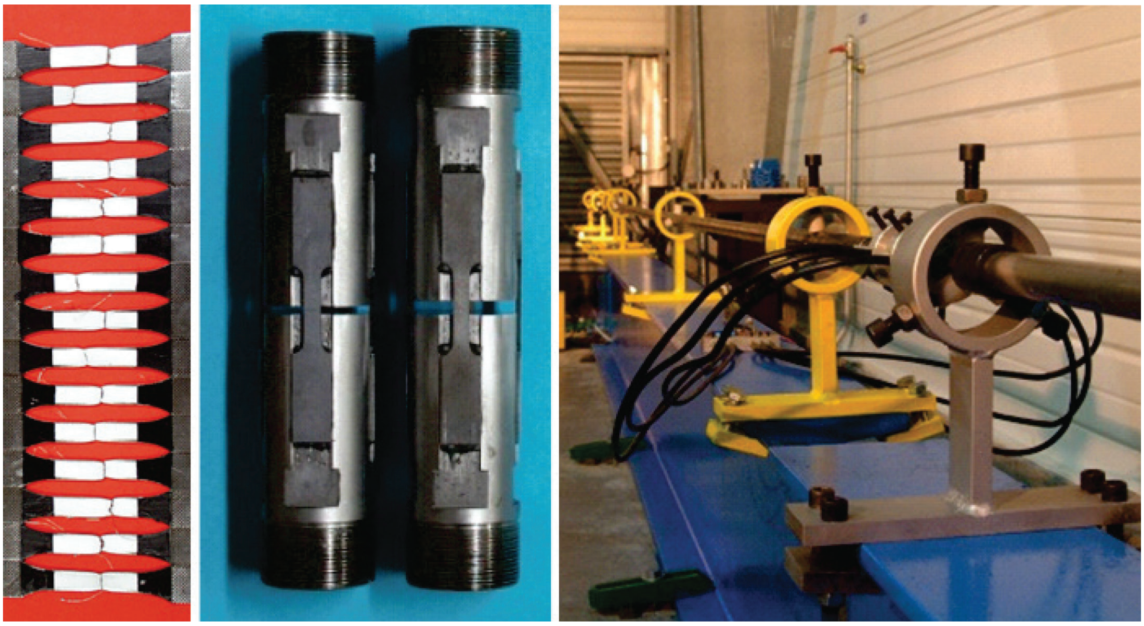

Figure 2 - Deformation of metallic specimens (middle) up until rupture using the optical extensometer technique (left) and tensile Hopkinson bars (right)

to plan experiments that enable the strain rate sensitivity of the material response to be characterized for various constant strain rates, just by playing with the sample free lengths and imposed velocities. The necessary hypothesis for this is to assume that the strain and strain rate fields are homogeneous over the free length of the specimen.

By the way, though the various parts of the hydraulic machines are made very massive and stiff, some of them, such as the beams and jack (figure 1) can become deformed, or the hydraulic control may struggle to maintain the imposed speed when very high loads are developed. The contact between the groove and the wings (that is to say, between the jack and the sample) can also be temporarily lost when the highest test speeds are challenged (inertia effects, bounces, vibrations). Thus, it can turn to be very difficult to really loop on the instantaneous velocity of the jack that would give a constant strain rate test at the material specimen level. This is why it is generally necessary (usually above 1 m/s) to measure the specimen deformation by a direct and ad-hoc experimental technique, in order to detect and deal with any deviation from the expected rate. As will be seen later, specific measurement techniques are used today quite as a standard to obtain accurate dynamic strain data for the free length of tested specimens: gauge extensometry, optical extensometry and, more recently, digital image correlation techniques.

Given an imposed test speed, it is evident that the strain rate that will develop in a material test depends on the sample free length. Many works are underway that concern the definition of the relevant specimen geometry for dynamic material testing (figures 2 and 3). These specimens are usually symmetrical, with smaller free lengths and working sections than standard material specimens, and depend on the tested materials, of course.

With a specific geometry, the ONERA hydraulic testing machines enable elastic strain rates of about 10^{+2} s^{-1} to be reached, for non-normalized 10 to 20 mm free-length specimens. In order to obtain these accurately, both the gauge and optical extensometry techniques are used; in addition, the gauge extensometry is always used to obtain the Poisson coefficient, if required. In the case of perfect (homogeneous) localization of a nonlinear material response across the specimen section over a smaller length area than the specimen overall free length, the use of more costly specific strain gauges (e.g., 0.6 mm grids, 20% strain capability and high cut-off frequency) enables higher measured strain rate levels to be obtained compared to the elastic regime (for instance, when plasticity develops in metallic specimens).

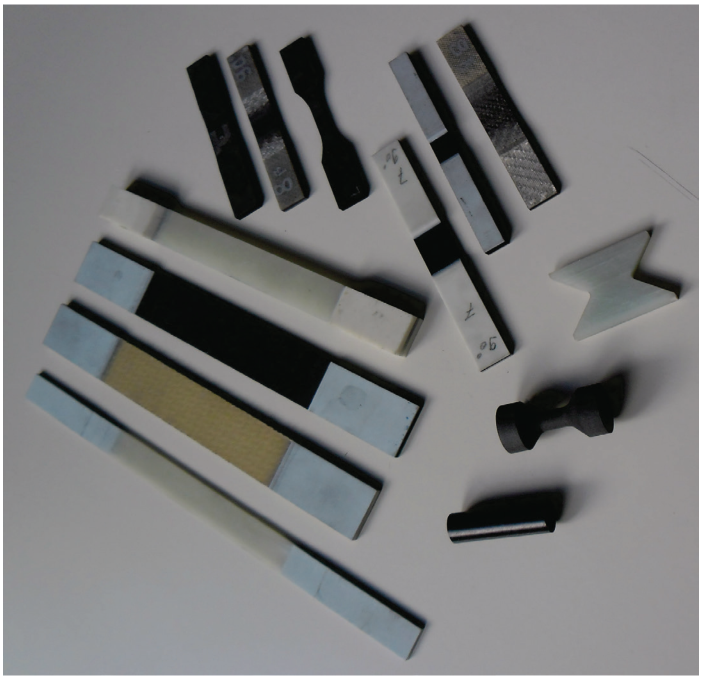

Figure 3 - Examples of specimen geometry for composite tension, compression and shear tests with hydraulic jacks

Strain rates of up to 500 s^{-1} have been obtained with such test protocols and the ONERA hydraulic testing machines. An important point to mention here concerns the care that must be taken when using such small specimen geometry: geometry effects and/or scale effects can take place that can dodge the results and prevent the intrinsic material

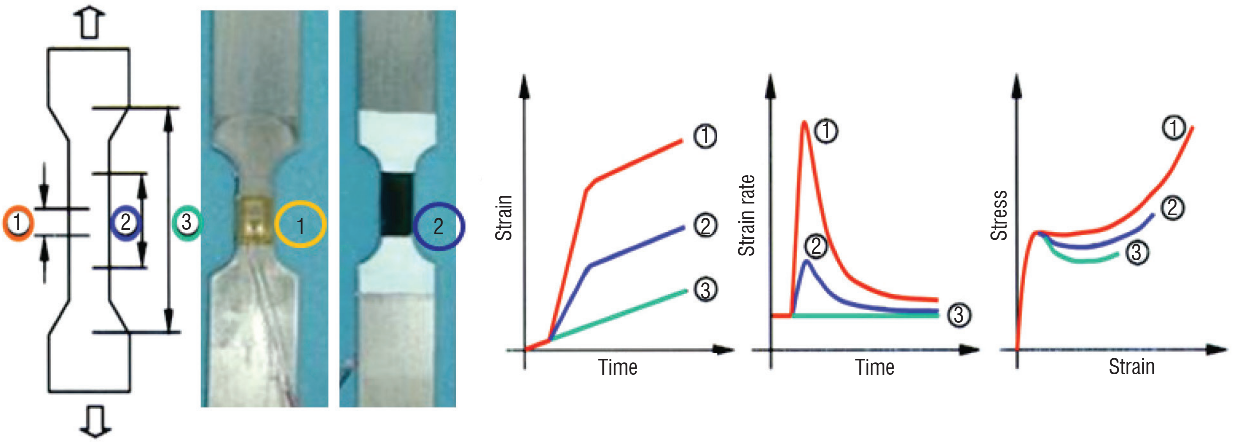

Figure 4 - Illustration of various strain acquisition methods on tensile specimens by (1) strain gauge, (2) optical extensometer, (3) hydraulic jack/grip displacement and influence on results with regard to strain/time, strain rate/time and stress/strain curves

behavior from being obtained. It is thus highly recommended to check that the dynamic specimen geometry gives, at low strain rates, the same results as those obtained with the quasi-static normalized geometry. A satisfying dynamic geometry can reasonably be obtained that way, when the elastic material data are compared. It is far more difficult when highly non-linear material behaviors are studied [4].

In order to study material behaviors for strain rates over the previously mentioned limits, Hopkinson bars systems [10] have historically been used, which can provide access to a range of strain rates from 10^{+3} s^{-1} to 10^{+4} s^{-1}. Given the plentiful papers dealing with Split Hopkinson Bars – as opposed to hydraulic jacks – in the literature, nothing will be said in this paper concerning this kind of dynamic testing machine, but rather about the fact that small specific specimen geometries are also required (thus with possible geometry and scale effects), which means that it is also highly recommended to check that the test results obtained at lower Hopkinson bars strain rates are consistent with those obtained at higher hydraulic jacks strain rates, or to adapt the test protocols to obtain these [20] [40]. Note also that, inversely to hydraulic jacks, compression tests with Hopkinson bars are easier to perform than tension tests (due to gripping difficulties): for sample geometries or materials with clear unsymmetrical tension/compression responses, additional care must be taken before extrapolating test results from both hydraulic jacks and Hopkinson bars.

Mechanical measurements and exploitation methods for the dynamic characterization of materials

The establishment of the existing relation between stress and strain in a given material during a dynamic test is desired. Several questions must systematically be considered, which consist in the measurement validity (nature, acquisition and exploitation), their objectivity (no influence of the instrumentation and protocol on the measured data) and accuracy (known measurement uncertainties). Stress is commonly calculated as the ratio between the applied load force and the working section of the material specimen. In order to obtain the dynamic load measured, piezoelectric load cells are generally used (a single one is enough when mechanical equilibrium is assumed for the specimen at each time during the test, otherwise, two should be used to measure forces at both ends of the sample and then subtract them to obtain the resultant one). Such a load cell (a uniaxial Kistler 9031A for instance at ONERA, with 80 kHz Eigenfrequency, 60 KN load measurement capacity and 6.10^{+9} N/m stiffness) should be pre-stressed under compression to be used for tensile tests. This means that the mechanical test rig dynamics become complicated, with heavy and stiff parts being added again. Note that the force measurement in this case is diverted away from the material specimen itself (clamping grips are set between the specimen and the load cells): the force and the strain signals must be shifted synchronously if the Young modulus value is sought, which can be a tricky point in dynamic testing if poor care is taken in this respect. The load cell must be regularly calibrated and possible drifts must be taken into consideration (e.g., thermal drifts). Other load measurement techniques have been proposed, for instance using staged specimen geometry with a strain gauge being placed in an elastic response area of the sample. Such a technique is of interest when the linear behavior of the tested material is known and the nonlinear behavior is studied. Then, the main load cell drawback (measurement of all the dynamics of the test rig and mean) is eliminated, with a supplementary cost however (extra specimen manufacturing and strain gauge instrumentation costs).

The most commonly proposed dynamic mechanical tests remain classical, in the sense that they are supposed to be statically determined: together with the assumption that the mechanical equilibrium of the specimen is fulfilled during tests, uniaxial stress and plane strain hypotheses are made, hence homogeneous deformation can be measured at one point along a specimen section, by strain gage for instance. In order to face some limitations concerning the strain range that can be measured with strain gauges (even the “large deformation” ones are limited to an elongation of about 20%, or the glue fails prior to the gauge), the preferred technique used today in many test labs consists in using fast optical extensometers (e.g., a 500kHz cut-off frequency Rudolph type one, with a 0.01 μm resolution for a 10 mm displacement, at ONERA). Such an apparatus enables the evolving distance between test cards (e.g. black & white patterns set on the sample) at very high speeds to be measured. An average strain can then be measured between the test cards, up until the specimen rupture (figure 4).

Finally, the objective would be to obtain stress/strain material responses by decades of strain rates, under tension and compression loadings. Figure 5 shows that it is not always possible to obtain such a detailed characterization, some strain rates being not accessible

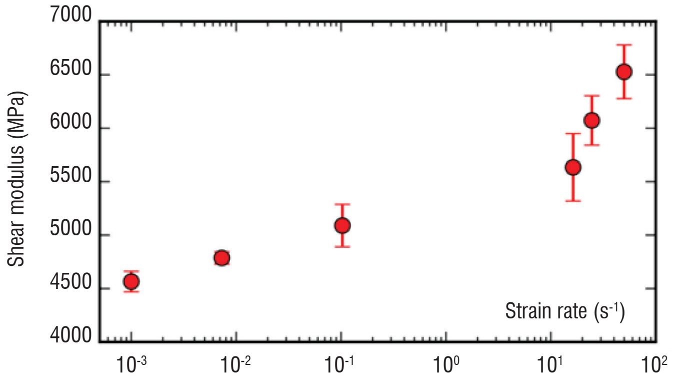

Figure 5 - Dynamic characterization test results: influence of the strain rate on the T700GC/M21 shear modulus obtained with +/-45° tensile Rosen tests

(here 1. s^{-1}) because of the various phenomena mentioned before (pumping mode, loss of contact, etc.), occurring according to the tested material (T700GC/M21 here), which cannot be predicted before the tests are done. It is nevertheless possible to see in the same figure that such a decade characterization reveals a transition effect that would have been completely ignored if only test results at the lowest and highest strain rates were sought (by means of a quasi-static normalized test or Split Hopkinson bars tests, for instance).

Figure 6 also shows that the strain rate obtained with hydraulic jacks (here performed on metallic XES steel) can vary a lot during tests at the limit capacity of the testing machine. Recent works have thus attempted to derive benefit from this undesired fact: given that the changing strain rate is calculated throughout the test, the test result is plotted in a 3D space (stress, strain and strain rate). Using a specifically designed experiment plan, a surface response can be established in this 3D space, a set of test curves being fitted by an appropriate (polynomial) mathematical function. Thus, a simple projection of this mathematical 3D surface onto constant strain rate planes gives the corrected stress/strain curves at true constant strain rates, which can then be used to characterize the strain rate dependency parameters of the material model. Once the exploitation toolbox has been implemented, the need to perform constant strain rate tests ceases [29] [32].

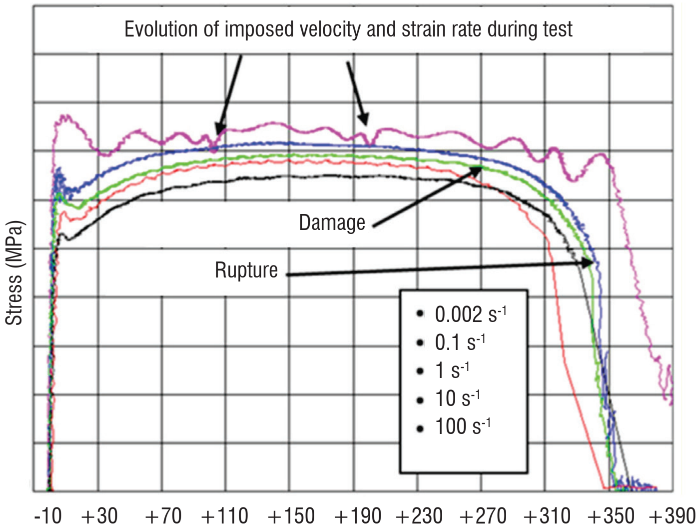

Figure 6 - Dynamic characterization test results: damageable visco-plastic behavior of steel according to strain rate

Another measurement technique makes it possible to use and exploit dynamic tests that do not fulfill the previously mentioned academic hypotheses (here uniaxial stress and plane strain), which are otherwise necessary to characterize material behaviors. It relies on the measurement of strain fields over the sample surface, instead of punctual strains at gauge locations. This technique has been made far easier with the development of the (stereo) digital image correlation technique; digital images can be recorded now at high frame rates, with high resolution, using new generation high-speed digital cameras (e.g., Photron, 12500 f/s, up to 1024x1024 pixels, at ONERA). This technique still requires highly skilled experimenters today, with long preparation (pattern deposition, calibration) and long exploitation times. However, statically determined tests are no longer required, which means that non-standard specimens of various geometries can be used, with inhomogeneous and multi-axial stress, strain, strain rate fields spreading through the sample during the tests (figure 7), up to rupture [1] [19] [36]. It also enables the true boundary conditions to be checked, as well as the way in which the load is progressively introduced into the samples.

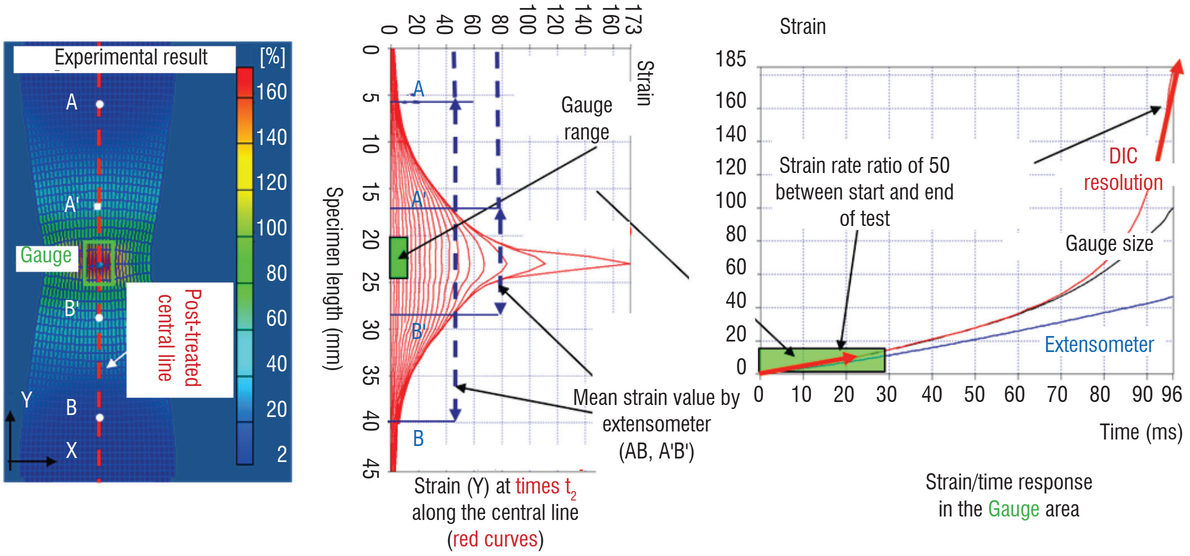

Figure 7 - Example of strain and strain rate fields obtained during an average 10.s^{-1} tensile test on a metallic specimen, using the digital image correlation technique (GOM system)

The test instrumentation with strain field measurement obtained using the digital image correlation (DIC) technique, together with non-statically determined tests, considerably increases the current capabilities of dynamic material characterization with hydraulic jacks and even Split Hopkinson Bars. Such tests deliver a huge amount of qualitative information and quantitative data and make it possible to cover a large local strain rate range with a single test, as well as to reach higher strain rates than with traditional protocols. Due to the tremendous progress in digital high speed camera technology, new exploitation methods (there is a family of them) are proposed today to identify complex non-linear dynamic behavioral, damage and rupture material models, as possible alternatives compared to traditional direct methods [25], or inverse ones by Finite Element Model Updating for instance (which will not be discussed in this paper, because they are not specific to the dynamic problem). One of these methods, currently studied at ONERA, is the Virtual Field Method, to which the authors would like to simply refer to [33].

Models for the dynamic behavior and rupture of organic matrix composites

The paper only discusses meso-macro models, which cannot yield insight into experiments at the material level, but rather only at the structural level. They would thus provide a better understanding of the global dynamic behavior of large components, when various areas of the structure undergo a large variety of strain and strain rate ranges, which may modify the ruin phenomenology and chronology when strain rates are taken into account. On the other hand, these meso-macro models cannot be fully representative of the physical mechanisms that develop at the material micro-structural level: an experimentally based calibration, or at least a verification step, should then always be done to clearly establish their confidence domain with regard to predictive capabilities.

Concerning organic matrix composites (whatever the fibers), these prove to be particularly complex (much more than metallic bulk materials) to study in their non-linear behavioral domain, because of well-known scale effects [30] and because of anisotropic and unsymmetrical mechanical properties that the specimen geometry can accentuate [6] [14]. As far as material characterization is concerned, scale effects are often claimed to appear when less than 4 composite plies of UD tape or fabric materials are used in the laminated test specimens (for thin ply composites of the aerospace kind). However, the use of a more than four-ply Representative Elementary Volume of materials for laminated test specimens often leads to difficulties with respect to the load and stiffness capabilities of the traditional hydraulic testing machines, especially when Carbon Fiber Reinforced Plastics are studied in their fiber direction. Specific preparation is sometimes necessary (dogbone specimens, use of tabs) to avoid non-linear mechanisms and the development of failures in the load introduction area (between grips) [11] [17] rendering test results useless for material characterization purposes. Due to these various reasons, the homogeneity of strains in the composite specimen section (be it profiled or not) should again be carefully assessed. Another difficulty arises, due to the development of new generations of composites by the industry, e.g., 3D interlocks, the dynamic characterization of which is a veritable headache for experimenters, with the same but greatly amplified difficulties. Last, let us say that while great care is needed in the manufacturing of the specimens (curing, machining, etc.) and the setup of the test specimens (tightening, alignment, etc.) to achieve acceptably repeatable test results in terms of stress/strain dynamic behavior of organic matrix composite materials, their dynamic rupture is very dispersive and far more so than for metallic materials, which is something that is currently not being properly dealt with in regard to the modeling question.

A large variety of dynamic behavior laws, linear or non-linear, already exists to deal with the various materials of interest for aerospace applications: visco-elastic, visco-plastic, visco-elasto-plastic-damageable, etc. However, one can see in the literature that the behavior and dependency on the load speed of a given material can lead to different models, according to the strain and strain rate ranges considered, for instance when small strains and very low speeds (creep), or large strain and high speeds (impacts) are studied. This for a very simple reason: a full spectrum model, developed at the smallest material scale, would cause the number of its parameters to increase so much that not only would the difficulties mentioned in the previous chapter (in terms of characterization) become inextricable, but also the resolution of such complex equations within an explicit simulation of a large structure would be unacceptable for any user. Nevertheless, the growing computing capabilities make it possible to progressively increase the complexity of dynamic material models, taking of course into account the research work done in the quasi-static, more experimentally friendly, domain. As mentioned in the introduction, this paper only deals with possibly physically justified behavioral material models, at best phenomenological ones, written at the macroscale or mesoscale material levels.

Concerning organic matrix composite materials, recent works have extended an existing spectral visco-elastic formulation [31] developed for creep analysis, to high load speed solicitations. In a first step, a bi-spectral model was proposed for a T700GC/M21 composite tape material, to represent the different influence of the load speed on the shear modulus observed during creep and high speed material tests [3], this difference is explained by the existence of two families of elastic viscous mechanisms in the organic matrix constituent, having two very different sets of characteristic times. These two families were easily revealed and justified thanks to the physical β-transition of the M21 resin. In the second step, the use of the well-known time-temperature equivalence in polymers enabled an extension of the bi-spectral model to a large range of room temperature to be proposed (see Figure 8). These proposals were confirmed by experiments [5] and the new visco-thermo-elastic model parameters were identified on a [-100°C, +20°C] temperature range and a [10^{-5} s^{-1}, 10^{+2} s^{-1}] strain rate range [7]. Eventually, Berthe's model, with only 3 more parameters than the original creep model, enables the dynamic elastic response, at ambient temperature, of T700GC/M21 composite material from 10^{-5} s^{-1} up to 10^{+4} s^{-1} to be described. Note that the research also benefitted from interesting technological progress over several years in field measurements and fast infrared thermography digital cameras [8] [16]. The current research in the community is mainly focused now on the study and modeling of visco-damage in composite materials, at the mesoscale (ply) level, meaning here the effects of load speed on the damage evolution law (mainly in the matrix phase, in the DDR team).

Parallel to these works on the behavior of organic matrix composite materials, the modeling of delamination in composite laminates, especially epoxy resin and carbon fiber based ones, constitutes a singular field of research in the aerospace domain.

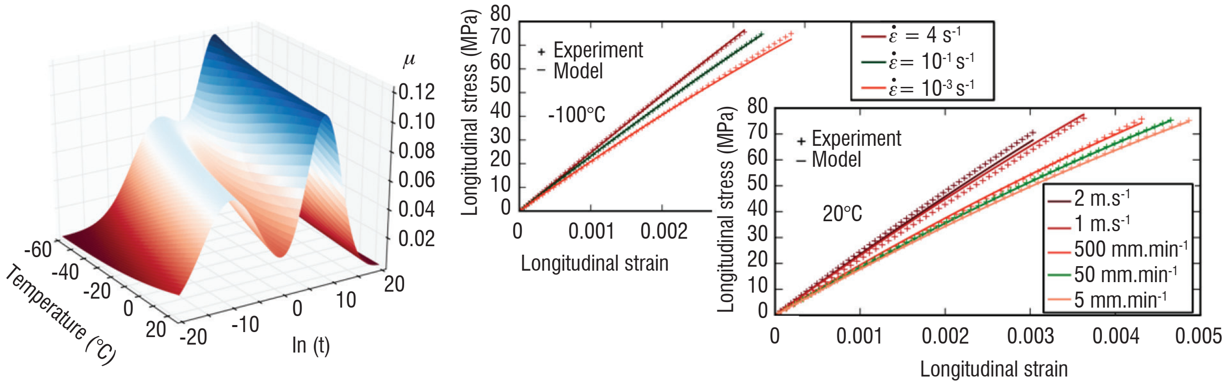

Figure 8 - Representation of Berthe's bi-spectral visco-elastic model with temperature dependency (left) and comparison of its shear response with dynamic tests at various temperatures for T700GC/M21 tape material (right)

These very tough but brittle materials – such as T700GC/M21 – are known to be fragile under impact, with delamination being a very favored degradation mode of the structure integrity in case of out-of-plane dynamic solicitation. Here again, the epoxy resin is directly involved in the degradation process, amorphous polymers being known to become brittle after curing.

The main trend to predict delamination by FEM simulations consists today in using Cohesive Zone Models [2], which rely on a local approach to model rupture in solids. Phenomenologically speaking, for epoxy resin composites, CZM enables the crazing mechanism in polymers to be described, during which molecular chains organize into fibrils to resist, by exerting a cohesive stress σ_{coh} against the interlaminar crack opening. The fibrils stretch until they reach a critical elongation δ_c and then break after having dissipated an amount of internal energy that can be related to the material toughness and its energy release rate, which are both fundamental quantities in the linear rupture mechanics theory (figure 9).

The dynamic rupture of epoxy resins under impact is combined with a local heating around the crack tip, which propagates very rapidly, and several works [24] [38] have shown that the energy release rate of vitreous polymers depends on the crack speed $\dot{a}$. As many studies have revealed, the material viscosity in the crazing zone is responsible for this important local heat at the crack tip and the thermal phenomenon can be assumed to be adiabatic when the crack propagates very fast. When the T_f temperature in the active zone becomes close to the glassy transition temperature T_g, noticeable changes appear in the crazing mechanism that modifies the dynamic toughness of the material. It has been previously observed that other transition mechanisms – which can also be associated with characteristic temperatures and relaxation times – already exist below the T_g temperature and can influence the dynamic behavior of the T700GC/M21 composite material. Thus, in order to characterize the influence of the crack speed on the energy release rate of a delamination crack, Joudon proposed to develop a 3-point bending test protocol. Hence the setup, initiation and propagation of a Mode I crack in a thick epoxy HexPly M21resin specimen would be studied. Indeed, in the case when a straight, stable and constant speed crack propagation is obtained, it is possible to characterize the material toughness, energy release rate and dependency on the crack speed (figure 10).

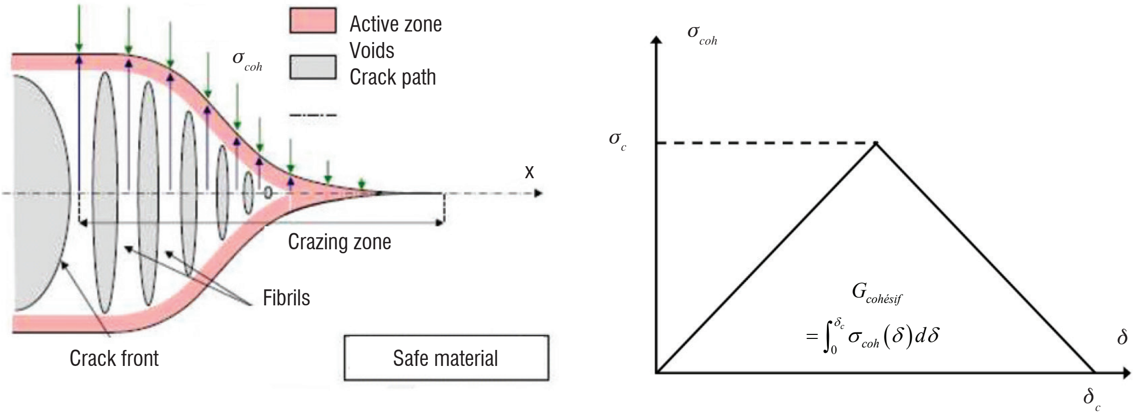

Figure 9 - Illustration of crazing phenomenon in amorphous polymers (left)
and standard bilinear cohesive zone model (right)

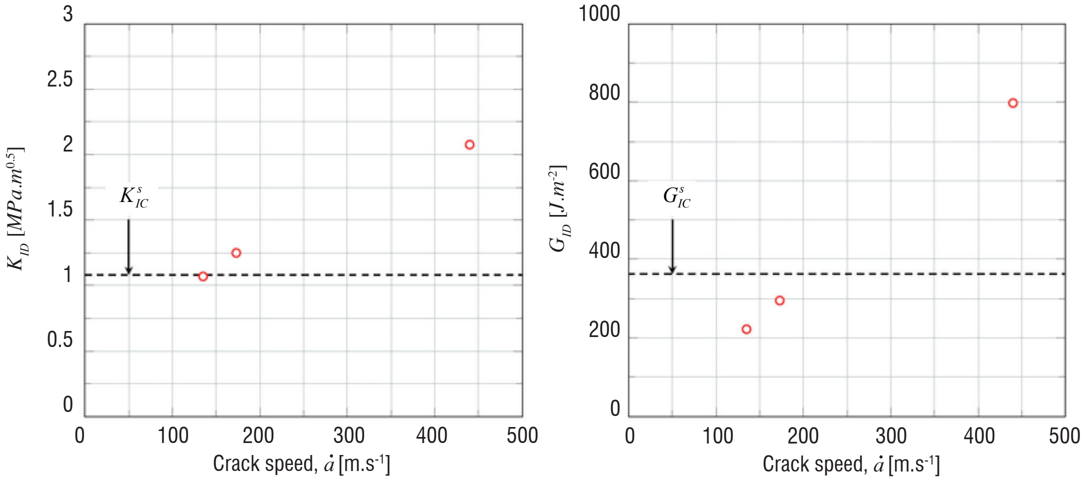

Figure 10 - Influence of crack velocity on the Mode I stress intensity factor K_{ID} and energy release rate G_{ID} for the epoxy M21 resin

It is thus possible to propose CZM formulations that depend on the crack speed, for example using a phenomenological expression (2) of the dynamic energy release rate G_{ID} close to that proposed by Zhou in [41]:

$$G_{ID}(\dot a) = G^d_{IC} + G_0.\ln\left(\frac{c_R}{c_R - \dot a}\right) \tag{2}$$

where G^d_{IC} is a (dynamic dependent) parameter for crack initiation, G_0 is a constant parameter for crack propagation and c_R is the Rayleigh waves celerity.

Concerning M21 resin, Joudon managed to identify (in his PhD work) – using dynamic tests performed at 1 m/s on notched and pre-cracked specimens - the following values for the proposed model: G^d_{IC} = 48.5 J/m^2, G_0 = 1080.25 J/m^2, with c_R = 873 m/s. The questions of the dependency of the crack set up (σ_{coh}) and of the initiation of the propagation (G^d_{IC}) on the load speed are currently being studied in the DDR lab, together with the question of the influence of temperature on cohesive zone models.

Conclusions

In the case of dynamic testing, several testing means are used to characterize material models, which cover a broad range of strain rates. This means that it is necessary to make sure that the delivered test results are consistent throughout the tested domain. This can be done by designing tests in such a way that the partial strain rate range overlaps are reached between the various testing machines (quasi-static electro-mechanical testing machine, hydraulic jacks and Hopkinson bars). When new materials are developed, it is often necessary to adapt the capabilities of existing testing machines and protocols, and the consistency of results must again be checked. Indeed, the experimental characterization of the dynamic behavior of materials is a tricky exercise, with many difficulties along the path. No normalized dynamic test protocol exists yet today that would make it a routine, while the aerospace industry need for nonlinear dynamic material models has been increasing for many years. The associated characterization costs also increase directly with the number of tests in the experiment plan and indirectly with the associated preparation and exploitation times needed by highly skilled experimenters to perform these tests. This can be a really dissuasive factor for the industry to invest in research in this field. Given this fact, many research works are presently aimed at developing methods and techniques that would make such dynamic characterization tests easier and cheaper, and would enable at least best practices, if not standardization of such dynamic material tests, to be achieved. The development of new digital image technologies (visible, thermo or tomography), together with digital image correlation techniques, probably constitutes a real opportunity to achieve such a difficult objective.

Concerning the modeling of material behaviors and rupture to predict the structure response to high energy dynamic solicitations, the main research topics remain very pragmatically focused on the development of phenomenological material models at the mesoscale or macroscale levels: an exaggeration of the model complexity not only cannot be justified with respect to the level of complexity and accuracy of the other mechanical models involved in high energy impact simulations (contacts, friction, heating, etc.), but also would be unusable in terms of implied CPU costs for complex structural analysis in the industry context. Nevertheless, more traditional problems, such as creep or fatigue analysis, developing at lower load speeds and for lower strain ranges, are dynamic in essence and the influence of the loading rate on the material behaviors for this range of dynamic solicitations has been studied for a long time, at the smallest material scale. If the corresponding models cannot be directly and simply transferred to explicit fast dynamic simulation codes as they are, they still constitute a very interesting and relevant basis, in terms of understanding and justification, for the progressive development of less empirical, more phenomenological, and hence more predictive, material behavior models for fast dynamics. This is clearly the path that the ONERA research teams have been exploring for many years now ■

Acknowledgements

The authors would like to thank the European Union, the French Government (MENRT, MoD), the DGA (French Armament Procurement Directorate),) and the Nord-Pas de Calais Region (especially within the context of the CISIT project) for funding research studies and equipment that contributed to this research work.

References

[1] S. AVRIL et al. - *Overview of Identification Methods of Mechanical Parameters Based on Full-Field Measurements*. Experimental Mechanics, Vol. 48, pp. 381-402, 2008.

[2] G. I. BARENBLATT - *The Mathematical Theory of Equilibrium Cracks in Brittle Fracture*. Advances in applied mechanics. Vol. 7(1), pp. 55-129, 1962.

[3] J. BERTHE, M. BRIEU, E. DELETOMBE - *Improved Formulation of Viscoelastic Model for Composite Laminates under Static and Dynamic Solicitations*. Journal of Composite Materials, Vol. 47(14), pp.1717-1727, 2013.

[4] J. BERTHE, M. BRIEU, E. DELETOMBE, G. PORTEMONT, P. LECOMTE-GROSBRAS, A. DEUDON - *Consistent Identification of CFRP Viscoelastic Models from Creep to Dynamic Loadings*. Strain, 49, pp. 257–266, 2013.

[5] J. BERTHE, M. BRIEU, E. DELETOMBE, G. PORTEMONT - *Temperature Effects on the Time Dependent Viscoelastic Behavior of Carbon/Epoxy Composite Materials: Application to T700GC/M21.* Materials & Design, Vol. 62, Pages 241-246, 2014.

[6] J. BERTHE, E. DELETOMBE, M. BRIEU, G. PORTEMONT, P. PAULMIER - *Dynamic Characterization of CFRP Composite Materials – Toward a Pre-Normative Testing Protocol – Application to T700GC/M21 Material*. Procedia Engineering, Vol. 80, pp. 165-182, 2014.

[7] J. BERTHE, M. BRIEU, E. DELETOMBE - *Thermo-Viscoelastic Modeling of Organic Matrix Composite Behavior - Application to T700GC/M21*. Mechanics of Materials, Vol. 81, pp. 18–24, 2015.

[8] J. BERTHE, G. PORTEMONT, A. DEUDON - *Essais de matage sur composites avec mesure des champs de déplacement et de température.* JNC 19, Lyon, 2015.

[9] A. COMBESCURE, B. MAUREL, S. POTAPOV, J. FABIS - *Full SPH Fluid-Shell Interaction for Leakage Simulation in Explicit Dynamics.* Int. J. for Numerical Methods in Engineering, Vol. 80, pp. 210-234, 2009.

[10] R. M. DAVIES - *A Critical Study of the Hopkinson Pressure Bar.* Phil. Trans. R. Soc. Lon. A, Vol. 240, pp. 375–457, 1948.

[11] E. DELETOMBE, D. DELSARD, D. KOHLGRUEBER, A. JONHSON - *Improvement of Numerical Methods for Crash Analysis in Future Composite Aircraft Design*. Aerospace Science and Technology, Vol. 4(3), pp. 189-199, 2000.

[12] E. DELETOMBE,J. FABIS, J. DUPAS, J.-M. MORTIER - *Experimental Analysis of Hydrodynamic Ram Pressure in Liquids*. Journal of Fluids and Structures, Vol. 37, pp. 1–21, 2013.

[13] D. DELSARD, D. DORMEGNIE, V. LASSUS, D. COUTELLIER - *Résistance au crash des structures d'hélicoptères composites - Vers la réduction des coûts de conception.* Revue de la Défense, Vol. 2, pp. 28-33, 2002.

[14] D. DORMEGNIE, D. COUTELLIER, D. DELSART, E. DELETOMBE - *Studies of Scale Effects for Crash on Laminated Structures*. Applied Composite Materials, Vol. 10, pp. 49–61, 2003.

[15] T. FOUREST, J.-M. LAURENS, E. DELETOMBE, J. DUPAS, M. ARRIGONI - *Analysis of Bubbles Dynamics Created by Hydrodynamic Ram in Confined Geometries Using the Rayleigh-Plesset Equation*. Int. J. of Impact Engineering, Vol. 73, pp. 66-74, 2014.

[16] R. K. FRUEHMANN, J. M. DULIEU-BARTON, S. QUINN - *Thermoelastic Stress and Damage Analysis Using Transient Loading*. Experimental mechanics, 2010, Vol. 50(7), pp. 1075-1086, 2010.

[17] P. B. GNING, D. DELSART, J.-M. MORTIER, D. COUTELLIER - *Through-Thickness Strength Measurements Using Arcan's Method*. Composites Part B, Vol. 41(4), pp. 308-316, 2010.

[18] M. GRÉDIAC - *Principle of Virtual Work and Identification*. C.R. Académie des Sciences de Paris, Vol. 309 (II), pp.1-5, 1989.

[19] M. GREDIAC, F. HILD - *Mesures de champs et identification en mécanique des solides*. Traité MIM, Hermès Ed., France, 2011.

[20] G. HAUGOU, E. MARKIEWICZ, J. FABIS, G. GARY - *Contribution to the Definition of a Partial Overlapping Plastic Strain Rates Domain for Moderate Loadings - Application to Tensile Testing on Metallic Materials*. Int. J. of Crashworthiness, Vol. 9(2), pp.187-194, 2004.

[21] G. HAUGOU, E. MARKIEWICZ, J. FABIS - *On the Use of the Non Direct Tensile Loading on a Classical Split Hopkinson Bar Apparatus Dedicated to Sheet Metal Specimen Characterization.* Int. J. of Impact engineering, Vol. 32(5), pp. 778-798, 2006.

[22] C. HENNUYER, N. LECONTE, B. LANGRAND, E. MARKIEWICZ - *Toward the Modeling of Riveted Assemblies by Super-Elements in Fast Dynamics*. Mechanics & Industry, Vol. 15, pp. 133-137, 2014.

[23] C. HENNUYER, N. LECONTE, B. LANGRAND, E. MARKIEWICZ - *Interpolation Functions of a Hybrid-Treftz Perforated Super-Element Featuring Nodes on the Hole Boundary*. Finite Elements in Analysis and Design, Vol. 91, pp. 40-47, 2014.

[24] V. JOUDON, G. PORTEMONT, F. LAURO, B. BENNANI - *Experimental Procedure to Characterize the Mode I Dynamic Fracture Toughness of Advanced Epoxy Resins*. Engineering Fracture Mechanics, Vol. 126, pp. 166–177, 2014.

[25] B. LANGRAND,P. GEOFFROY, J.-L. PETITNIOT, J. FABIS,E. MARKIEWICZ, P. DRAZÉTIC - *Identification of Constitutive Model Parameters for Crashworthiness Modeling.* Aerospace Science and Technology, Vol. 3(4), pp. 215-227, 1999.

[26] B. LANGRAND, A.-S. BAYART, Y. CHAUVEAU, E. DELETOMBE - *Assessment of Multi-Physics FE Methods for Bird Impact Modeling – Application to a Metallic Riveted Airframe.* Int. J. of Crashworthiness, Vol. 7(4), pp. 415-428, 2002.

[27] B. LANGRAND, L. PATRONELLI, E. DELETOMBE, E. MARKIEWICZ, P. DRAZÉTIC - *An Alternative Numerical Approach for Full Scale Characterisation for Riveted Joint Design.* Aerospace Science and Technology, Vol. 6(5), pp.343-354, 2002.

[28] B. LANGRAND, E. MARKIEWICZ - *Strain Rate Dependence in Spot Welds: Non-Linear Behavior and Failure in Pure and Combined Modes I/II*. Int. J. of Impact Engineering, Vol. 37(7), pp. 792-805, 2010.

[29] F. LAURO, B. BENNANI, D. MORIN, A.F. EPEE - *The SEE Method for Determination of Behavior Laws for Strain Rate Dependent Material: Application to Polymer Material.* Int. J. of Impact Engineering, Vol. 37, pp. 715-722, 2010.

[30] D. LEGUILLON - *Strength or Toughness? A Criterion for Crack Onset at a Notch*. European Journal of Mechanics-A/Solids, Vol. 21(1), pp. 61-72, 2002.

[31] J.-F. MAIRE, J.-L. CHABOCHE - *A New Formulation of Continuum Damage Mechanics for Composite Materials.* Aerospace Science and Technology, Vol. 1(4), pp. 247–257, 1997.

[32] D. MORIN, G. HAUGOU, B. BENNANI, F. LAURO - *Identification of a New Failure Criterion for Toughened Epoxy Adhesive*. Engineering Fracture Mechanics, Vol. 77, pp. 3481-3500, 2010.

[33] D. NOTTA, B. LANGRAND, E. MARKIEWICZ, F. LAURO, G. PORTEMONT - *Identification of Johnson-Cook's Viscoplastic Model Parameters Using the Virtual Fields Method: Application to Titanium Alloy Ti6Al4V*, Strain, Vol. 49(1), pp. 22-45, 2013.

[34] R. ORTIZ, E. DELETOMBE E., Y. CHUZEL-MARMOT - *Assessment of Strain Rate Effects on the Stress/Strain Response of Ice Material.* Int. J. of Impact Engineering, Vol. 76, pp. 126-138, 2015.

[35] J. PEIRS, P. VERLEYSEN, J. DEGRIECK - *Experimental Study of the Influence of Strain-Rate on Fracture of Ti6Al4V.* Procedia Engineering. Vol. 10, pp. 2336-2341, 2011.

[36] F. PIERRON, S. AVRIL, V. THE TRAN - *Extension of the Virtual Fields Method to Elasto-Plastic Material Identification with Cyclic Loads and Kinematic Hardening*. Int. J. of Solids and Structures, Vol. 47, pp. 2993-3010, 2010.

[37] G. PORTEMONT, E. DELETOMBE, P. DRAZÉTIC - *Assessment of Basic Experimental Impact Simulations for Coupled Fluid/Structure Interactions Modeling.* Int. J. of Crashworthiness, Vol. 9(4), pp. 333-339, 2004.

[38] M. POSTEC, E. DELETOMBE, D. DELSART, D. COUTELLIER - *Study of the Infuence of the Number of Inter-Ply Interfaces on the Bearing Rupture of Riveted Composite Assemblies.* Composite Structures, Vol. 84(2), pp. 99-113, 2008.

[39] S. POTAPOV, B. MAUREL, A. COMBESCURE, J. FABIS - *Modelling Accidental Fluid-Structure Interaction Problems with the SPH Method*. Computers & Structures, Vol. 87, pp.721-734, 2008.

[40] H. ZHAO, G. GARY - *The Testing and Behavior Modeling of Sheet Metals at Strain Rates from 10−4 to 10+4 s−1*. Materials Science and Engineering, Vol. 207, pp. 46–50, 1996.

[[41] F. ZHOU, J.-F. MOLINARI, T. SHIOYA - *A Rate-Dependent Cohesive Model for Simulating Dynamic Crack Propagation in Brittle Materials*. Engineering Fracture Mechanics, Vol. 72, pp. 1383-1410, 2005.

Acronyms

ASDS	(Aeroelasticity and Structural Dynamics Department)
CFRP	(Carbon Fiber Reinforced Plastic)
CZM	(Cohesive Zone Models)
DDR	(Design and Dynamic Resistance)
DIC	(Digital Image Correlation)
FEM	(Finite Element Method)
OMC	(Organic Matrix Composite)
ONERA	(Office National d'Etudes et de Recherches Aérospatiales)
REV	(Representative Elementary Volume)

Nomenclature

$a, \dot{a}$	crack length, crack velocity
c_R	celerity of Rayleigh waves
δ	crack opening (Mode I)
δ_c	critical crack opening
ε	strain
$\dot{\varepsilon}, \dfrac{d\varepsilon}{dt}$	strain rate
F	force
G	energy release rate
G_{ID}	critical energy release rate
G_{ID}^{s}	critical static energy release rate
G_{IC}^{d}, G_0	parameters of the dynamic energy release rate model
K_{ID}	dynamic stress intensity factor
K_{IC}^{s}	critical static stress intensity factor
l_{free}	free length of the material sample
P	power
σ	stress
σ_c	critical stress
σ_{coh}	cohesive stress
T_f	temperature at the crack tip
T_g	glassy transition temperature
V	speed
V_{jack}	speed imposed to the hydraulic jack
V_{sample}	speed applied to the material sample

AUTHORS

Julien Berthe. A graduate from the Ecole Normale Supérieure de Cachan in 2010, he received a Ph.D. degree from the Ecole Centrale de Lille in 2013. His research deals with the strain rate and temperature dependencies of organic matrix composite material behavior with two main aspects: the experimental characterization and the numerical modeling of such dependencies.

Eric Deletombe. A graduate from the Ecole Nationale Supérieure de l'Aéronautique et de l'Espace (1988) and graduate from the University of Valenciennes (Habilitation à Diriger des Recherches, 2013), he is now a Special Scientific Advisor in the Aeroelasticity and Structural Dynamics Department of the French Aerospace Lab (ONERA). He has also been a Research Engineer at ONERA in Structural and Solid Mechanics (Design and Dynamic Resistance of Materials and Structures) since 1990.

David Delsart. A graduate from the Ecole Centrale de Lille (1994) and a graduate from the University of Sciences and Technologies of Lille (Post-graduate diploma in Mechanics, 1994), he has been a Research Engineer at ONERA in the Design and Dynamic Resistance Research Unit since 1997, specialized in the dynamic characterization of materials and assemblies and in the development of dynamic mechanical models and Finite Element explicit modeling (Radioss, Abaqus, Europlexus). He is now the manager and technician responsible for the ONERA/DLR/AIRBUS-Helicopters common Research program on the crashworthiness/vulnerability of helicopter structures.

Jacky Fabis. Jacky Fabis, research engineer at ONERA, has led the development of the mechanical testing laboratory dedicated to dynamics since 1978.

Bertrand Langrand. A graduate from the university of Valenciennes, he received his PhD degree in Solid Mechanics and Mechanical Engineering in 1998 and his Habilitation degree in 2011. A research scientist at ONERA in Computational Structural and Solid Mechanics since 1999, his research activities are mainly related to crashworthiness, impact and blast-loaded structure problems. His research has also been focused on material behavior characterization, parameter identification, assembly modeling and Fluid/Structure interaction.

Gérald Portemont. Graduate from the university of Valenciennes, he received his PhD degree in 2004. Research scientist at ONERA since 2008 in crashworthiness and high velocity impact. Main achievements include the development of experimental methods for material (metallic, composite CMO) behavior characterization (strain-rate and temperature dependencies), sub-components (assemblies and panels) and structures. Recently, he put interest in crack propagation and delamination in fast loading conditions.

Life Prediction Methodologies for Materials and Structures

R. Desmorat
LMT (ENS Cachan / CNRS / U. Paris Saclay)
A. du Tertre, P. Gaborit
(Snecma)

E-mail: desmorat@lmt.ens-cachan.fr

DOI : 10.12762/2015.AL09-05

Multiaxial Haigh Diagrams from Incremental Two Scale Damage Analysis

In High Cycle Fatigue, plasticity and damage are localized at a microscale, a scale smaller than the Representative Volume Element (RVE) scale of continuum mechanics. An incremental two-scale damage model has been built on this basis by Lemaitre et al, and has been mainly applied to alternated loading with no plasticity at the RVE scale. A modified Eshelby-Kröner scale transition law is derived here, taking into account RVE mesoscale plasticity and also microscale plasticity and damage. The ability of the corresponding two-scale damage model to deal with multiaxiality in a wide range of load ratios (from -1 to 0.9) is then focused on.

The crack initiation conditions for axisymmetric notched specimens loaded at different mean stresses are studied on the basis of several fatigue tests on TA6V specimens at a low temperature. Both the notch first loading pre-plastification and the biaxial stress state are naturally taken into account by the incremental analysis. Two multiaxial Haigh diagrams are finally drawn for TA6V at a low temperature. Their main features, such as a horizontal asymptote, are highlighted. A piecewise linear extension for a stronger mean stress effect is finally given within the two-scale damage framework considered.

Introduction

High fatigue is often addressed in terms of stress amplitude, i.e., with laws directly relating the stress amplitude to the number of cycles to failure or to crack initiation [2, 49, 1, 39, 28]. The mean stress effect is then simply represented by the introduction into the previous law, as a parameter, of the stress ratio $R = \sigma_{min}/\sigma_{Max}$ (minimum stress divided by the maximum stress over a cycle). The difficulty is then to extend such a modeling to 3D cases and to non-cyclic loading conditions [60, 7, 13, 34, 14, 55, 56, 53, 52].

On the other hand, Continuum Damage Mechanics, naturally a 3D model, can also be used for fatigue [40, 41, 42, 8, 10, 54, 25, 31, 48, 57, 61, 24, 18, 51, 11, 29, 23, 47]. The cyclic relationships are obtained first from the time integration over one cycle of the damage and the constitutive laws, and second from the integration over the entire loading [43]. The introduction of the stress ratio is then not natural and may become a difficult task [46, 3]. One possibility is to model the microdefect or microcrack closure effect (also called quasi-unilateral condition, [36, 9, 21]) and its coupling with damage growth [32, 22]. With this in mind and with the additional fact that High Cycle Fatigue (HCF) corresponds most often to fatigue in the elastic regime, an incremental two scale damage model has been proposed with good fatigue capabilities [44, 45, 17, 38, 26]. Such a model is extended in this work, in order to recover the mean stress effect obtained in simple but nevertheless representative structures, namely in axisymmetric notched specimens made of a TA6V titanium alloy. The tests have been performed at a low temperature by Snecma, with the support of CNES, within the framework of rocket engine applications.

These specimens have been chosen to represent real loading conditions, i.e., multiaxial conditions with stress triaxialities greater than that encountered under tension and with localized yielding. In order to characterize the model response over the entire stress ratio range from $R = -1$ to $R = 0.9$, TA6V notched specimens with different stress concentration factors $K_T = 1.5, 2.5$ and 3.5 have been tested at different nominal stress – or load – ratios. Axisymmetric notched specimens are found to be very useful to test the HCF behavior of a material submitted to bi-axial stresses at a given – and especially at a high – stress ratio R. It is indeed quite difficult to "explore" the upper stress ratio domain with classical uniaxial (smooth) specimens, since most of the time, for high numbers of cycles to rupture (i.e., over 10^6), the mean stress required to obtain $R > 0.6$ is so high that the yield stress, or even the ultimate stress, are rapidly reached. On the contrary, axisymmetric notched specimens encounter small scale yielding and allow local yielding to be obtained in a biaxial state of stress (the longitudinal and hoop stresses in the notch can represent 70% and 30%

of the stress tensor trace respectively). Once plastified, they allow the material fatigue response to be tested in a simple manner at high stress ratios R. They can be considered as representative of industrial cases encountered in certain engine components submitted to high static loads and to high frequency alternate loads.

Multiaxial Haigh diagrams are constructed in this work, using a two-scale damage analysis of such tests.

Two-scale damage model

A two-scale damage model has been built [44, 45, 17, 20, 58] considering that High Cycle Fatigue, either thermally or mechanically activated, occurs for an elastic regime at the RVE scale, the mesoscale of continuum mechanics. It accounts for micro-plasticity and micro-damage at the defect scale (or microscale). The model is phenomenological, describing micro-plasticity with classical 3D Von Mises plasticity equations and describing micro-damage by the Lemaitre damage evolution law $\dot{D} = (Y/S)^s \dot{p}$ [43, 42] of damage governed by the accumulated plastic strain rate $\dot{p}$ and enhanced by the strain energy density (with Y denoting the thermodynamic force associated with the damage variable D). Parameters S and s are material and temperature dependent. A scale transition law, such as the Eshelby-Kröner localization law, links both the mesoscopic and microscopic scales.

Incremental two-scale analysis

The general principles for building an initial two-scale damage model for complex fatigue applications are as follows (figure 1). Only isothermal conditions are considered in this work (for the anisothermal case, refer to [21]).

- At the mesoscale, the scale of the RVE of continuum mechanics, the behavior is considered as elastic, the material yield stress σ_y usually not being reached in HCF.

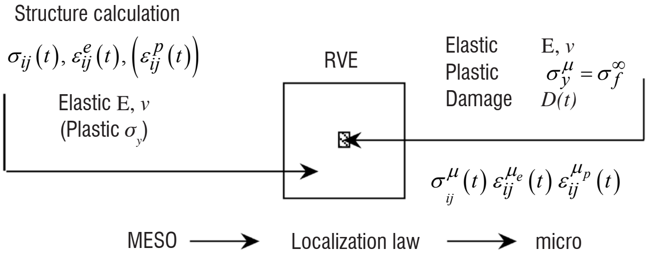

Figure 1 - Micro-element embedded in an elastic Representative Volume Element

- The microscale is the defect scale, with defects conceptually gathered as a weak inclusion embedded in previous RVE. The behavior considered for the microscale is (thermo-)elasto-plasticity coupled with damage, the weakness of the inclusion being represented by a yield stress at the microscale $\sigma_y^\mu < \sigma_y$ considered equal to the asymptotic fatigue limit of the material σ_f^∞.

At the mesoscale, the stresses are denoted by σ and the total, elastic and plastic strains are denoted by ε, ε^e, ε^p. These are known from an elasto-plastic Finite Element computation. The values at the microscale have an upper-script μ, except for the damage variable $D = D^\mu$ at the microscale, which has no upper-script.

Scale transition law

In earlier developments within the two-scale damage framework of Lemaitre et al, plasticity and damage were assumed to occur at the microscale only, thus setting $\varepsilon^{p\mu} \neq 0$, $D = D^\mu \geq 0$ but also setting a zero value for the plastic strains at the mesoscale ($\varepsilon^p = 0$). In the notched specimen fatigue case considered, the yield stress will be reached at some stress concentration points and plasticity will occur, localized, but nevertheless present at the mesoscale (i.e., present in Finite Element computations of the notched specimens).

The two-scale damage model must be extended, in order to take into account non-zero plastic strains ε^p, either constant or evolving ($\varepsilon^p(t)$) at each time step of an incremental fatigue analysis. A (quite) simple way to proceed is to extend the Eshelby-Kröner scale transition law of a spherical inclusion embedded in an infinite elastic isotropic matrix to our case. In the initial problem [27, 35], the inclusion has the same elastic properties $\mathbb{E}$ as the matrix and is subject to free strains ε_F; the matrix is subjected to a far field strain ε (or stress σ).

The strain in the inclusion is then the sum of the far field strain and of an additional strain due to the inclusion free strains and the matrix elasticity (case (a) in figure 2),

$$\varepsilon^\mu = \varepsilon + \mathbb{S} : \varepsilon_F \tag{1}$$

Which is equivalent to

$$\sigma^\mu = \sigma + \mathbb{E} : (\mathbb{S} - \mathbb{I}) : \varepsilon_F \tag{2}$$

where $\mathbb{I}$ is a fourth order identity tensor and where $\mathbb{S}$ is an isotropic Eshelby tensor such that

$$\mathbb{S} : \mathbf{1} = \alpha \mathbf{1} \qquad \alpha = \frac{1+\nu}{3(1-\nu)} \tag{3}$$

for a second order identity tensor $\mathbf{1}$ and

$$\mathbb{S} : \mathbf{T}' = \beta \mathbf{T}' \qquad \beta = \frac{2}{15}\frac{4-5\nu}{1-\nu} \tag{4}$$

for any deviatoric tensor $\mathbf{T}'$. By setting ε_F equal to the micro-plastic strain $\varepsilon^{\mu p}$, the localization law for an undamaged inclusion used so far [14, 45] is obtained

$$\varepsilon^\mu = \varepsilon + \beta \varepsilon^{\mu p} \quad \text{or} \quad \sigma^\mu = \sigma - 2G(1-\beta)\varepsilon^{\mu p} \tag{5}$$

where G is the shear modulus.

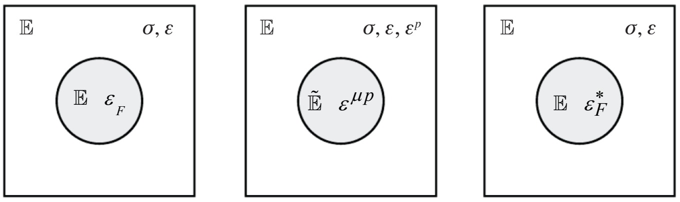

initial eshelby problem (a)

Considered problem with a damage inclusion (b)

Equivalent eshelby problem (c)

Figure 2 - a) Initial Eshelby problem of an inclusion with free strain ε_F, b) Considered problem with matrix plasticity and damaged inclusion, c) Problem making both cases a) and b) equivalent, due to an adequate choice of the free strain $\varepsilon_F^\star$.

The problem considered in this work is slightly different, given that the elastic properties of the inclusion $\tilde{\mathbb{E}} = \mathbb{E}(1-D)$ are affected by the damage D and given that the matrix withstands (mesoscopic) plastic strains ε^p (case (b) of figure 2). It is possible to derive the corresponding localization law from previous Eshelby analysis. Due to the elastic mismatch between both scales, the inclusion must be conceptually changed into an equivalent inclusion with the same total strains and stresses, but with undamaged elasticity (case (c) in figure 2, [30]). In order to do this, an equivalent free strain $\varepsilon_F^\star$ is derived, in which the damage effect is embedded, so that for $\varepsilon_F^\star$ classical expressions (1)-(2) the following is enforced

$$\begin{cases} \sigma^\mu = \tilde{\mathbb{E}} : (\varepsilon^\mu - \varepsilon^{\mu p}) \\ \sigma = \mathbb{E} : (\varepsilon - \varepsilon^p) \\ \varepsilon^\mu = \varepsilon + \mathbb{S} : \varepsilon_F^\star \\ \sigma^\mu = \sigma + \mathbb{E} : (\mathbb{S} - \mathbb{I}) : \varepsilon_F^\star \end{cases} \tag{6}$$

This therefore defines $\varepsilon_F^\star$,

$$\varepsilon_F^\star = \left[\mathbb{E} - (\mathbb{E} - \tilde{\mathbb{E}}) : \mathbb{S} \right]^{-1} : \left[(\mathbb{E} - \tilde{\mathbb{E}}) : \varepsilon + \tilde{\mathbb{E}} : \varepsilon^{\mu p} - \mathbb{E} : \varepsilon^p \right] \tag{7}$$

The equivalent strain $\varepsilon_F^\star$ replaces ε_F in equation (1) so that, after some mathematical arrangements and bearing in mind the fact that a plastic strain tensor is a deviatoric tensor, the modified Eshelby-Kröner scale transition law coupled with damage is obtained:

$$\varepsilon^\mu = \frac{1}{1-\beta D} \left[\varepsilon + \frac{(\alpha - \beta) D}{3(1-\alpha D)} \mathrm{tr}\varepsilon \mathbf{1} + \beta \Big((1-D) \varepsilon^{\mu p} - \varepsilon^p \Big) \right] \tag{8}$$

where α and β are the previous Eshelby parameters. For an undamaged inclusion ($D = 0$) in an elasto-plastic matrix, the previous law is simplified, as expected, to $\varepsilon^\mu = \varepsilon + \beta\left(\varepsilon^{\mu p} - \varepsilon^p\right)$.

Plasticity and damage at the microscale

The history of the stresses $\sigma(t)$, strains $\varepsilon(t)$ and plastic strains $\varepsilon^p(t)$ at the RVE mesoscale is assumed to be known from an elasto-plastic (incremental) finite element calculation. The scale transition is made using equation (8), which must be solved altogether with microscale constitutive equations (still incremental).

A law of elasto-plasticity coupled with damage is considered at the microscale. The elasticity law is then written as (recall that the μ-upper-script stands for "variable at the microscale"):

$$\varepsilon^{\mu e} = \frac{1+\nu}{E} \tilde{\sigma}^\mu - \frac{\nu}{E} \mathrm{tr} \tilde{\sigma}^\mu \mathbf{1} \qquad \tilde{\sigma}^\mu = \frac{\sigma^\mu}{1-D} \tag{9}$$

In the yield criterion, the hardening $\mathbf{X}^\mu$ is kinematic, linear, and the yield stress is the asymptotic fatigue limit of the material, denoted by σ_f^∞,

$$f^\mu = (\tilde{\sigma}^\mu - \mathbf{X}^\mu)_{eq} - \sigma_f^\infty \tag{10}$$

where $(.)_{eq}$ is the Von Mises norm and where $\tilde{\sigma}^\mu = \sigma^\mu / (1-D)$ is the effective stress and $f^\mu < 0 \rightarrow$ elasticity. This ensures that micro-plasticity, and therefore damage and failure, occurs for stresses ranging between the fatigue limit σ_f^∞ and the RVE yield stress σ_y.

The set of constitutive equations at the microscale is thus:

$$\begin{cases} \varepsilon^\mu = \varepsilon^{\mu e} + \varepsilon^{\mu p} \\ \varepsilon^{\mu e} = \dfrac{1+\nu}{E} \tilde{\sigma}^\mu - \dfrac{\nu}{E} \mathrm{tr} \tilde{\sigma}^\mu \mathbf{1} \\ \dot{\varepsilon}^{\mu p} = \dfrac{3}{2} \dfrac{\tilde{\sigma}^{\mu D} - \mathbf{X}^\mu}{(\tilde{\sigma}^\mu - \mathbf{X}^\mu)_{eq}} \dot{p}^\mu = \dot{p}^\mu \mathbf{n} \\ \dot{\mathbf{X}}^\mu = \dfrac{2}{3} C_y (1-D) \dot{\varepsilon}^{\mu p} \\ \dot{D} = \left(\dfrac{Y^\mu}{S} \right)^s \dot{p}^\mu \\ D = D_c \rightarrow \text{crack initiation} \end{cases} \tag{11}$$

with the plastic modulus C_y, the damage strength S, the damage exponent s and the critical damage D_c as material parameters. The damage growth is smaller in compression than in tension, due to the consideration of the micro-defect closure parameter h within the strain energy release rate Y^μ,

$$\begin{aligned} Y^\mu = \; & \frac{1+\nu}{2E} \left[\frac{\langle \sigma^\mu \rangle^+ : \langle \sigma^\mu \rangle^+}{(1-D)^2} + h \frac{\langle \sigma^\mu \rangle^- : \langle \sigma^\mu \rangle^-}{(1-hD)^2} \right] \\ & - \frac{\nu}{2E} \left[\frac{\langle \mathrm{tr} \sigma^\mu \rangle_+^2}{(1-D)^2} + h \frac{\langle \mathrm{tr} \sigma^\mu \rangle_-^2}{(1-hD)^2} \right] \end{aligned} \tag{12}$$

since $0 < h < 1$ and usually for metals $h \approx 0.2$ [43], and where $\langle . \rangle_+$, $\langle . \rangle_-$ stand for the positive and negative parts of a scalar and $\langle . \rangle^+$, $\langle . \rangle^-$ for the positive and negative parts of a tensor (in terms of principal values). Note that equation (12) is simplified to

$Y_{tens}^\mu = (\sigma^\mu)^2 / 2E\left(1-D\right)^2$ for tension at the microscale and in

$Y_{comp}^\mu = h(\sigma^\mu)^2 / 2E\left(1-hD\right)^2$ for compression at the microscale,

so that the damage rate in compression $\dot{D}_{comp} = (Y_{comp}^\mu / S)^s \dot{p}^\mu$ is much lower, for a small h, than the damage rate in tension $\dot{D}_{tens} = (Y_{tens}^\mu / S)^s \dot{p}^\mu$.

In previous constitutive equations, $p^\mu = \int (\frac{2}{3} \dot{\varepsilon}^{\mu p} : \dot{\varepsilon}^{\mu p})^{1/2} \mathrm{d}t$ is the accumulated plastic strain at the micro-scale and no damage threshold is considered (for loading dependent thresholds, refer to [45, 46]). The plastic multiplier $\dot{\lambda} = \dot{p}^\mu (1-D)$ is determined from the consistency condition $f^\mu = 0$ and $\dot{f}^\mu = 0$.

The internal variables $\varepsilon^{p\mu}$, p^μ and $D^\mu = D$ are often considered to be equal to zero at $t = 0$. A pre-hardening or pre-damage correspond to non-vanishing initial values ε^{p0}, p_0, D_0 for the time integration of the differential equations (11): pre-hardening is naturally accounted for in a rate form modeling [5]. Note also that the localization law takes into account the plastic strain evolution $\varepsilon^p(t)$ at the RVE scale. This means that the pre-plastification stage of the structures before undergoing elastic fatigue is taken into account by means of the ε^p-term of the scale transition law (8). Further study of notched specimens loaded at high mean stresses uses this feature (§ "Fatigue of axisymmetric notched specimens").

Numerical implementation

With regard to the numerical implementation, a post-processing approach is proposed. The strain and plastic strain histories at the mesoscale are assumed to be known from a reference Finite Element elastic or elasto-plastic computation. The micro-plasticity and damage are obtained by the time integration, step by step, of the incremental constitutive equations. At each time step t_{n+1} and for a known strain increment at the mesoscale $\Delta\varepsilon = \varepsilon_{n+1} - \varepsilon_n$, the numerical scheme must calculate, by time integration of the constitutive equations at the microscale together with the consideration of the localization law, the strain ε^μ_{n+1}, stress σ^μ_{n+1}, plastic strain $\varepsilon^{\mu p}_{n+1}$, accumulated plastic strain p^μ_{n+1} and damage D_{n+1} at microscale. The Euler backward scheme is used to discretize their rate form, as for classical single scale plasticity and damage models. The 3 stages for the numerical resolutions of the two-scale model equations are classically [44, 46, 20]: 1) an elastic prediction at the microscale, taking into account the localization law, 2) a test over the criterion function f^μ, and 3) if f^μ is found to be positive, a plastic-damage correction (still at the microscale).

Elastic Prediction

The elastic prediction assumes an elastic behavior at the microscale with constant plastic strain $\varepsilon^{\mu p}_{n+1} = \varepsilon^{\mu p}_n$, constant kinematic hardening $\mathbf{X}^\mu_{n+1} = \mathbf{X}^\mu_n$ and constant damage $D_{n+1} = D_n$. The elastic prediction gives a first estimate for the total strain, the elastic strain and the effective stress at the microscale at time t_{n+1},

$$\begin{aligned}
\varepsilon^\mu &= \frac{1}{1-\beta D_n}\Big\{ \ \varepsilon_{n+1} + \frac{(\alpha-\beta)D_n}{3(1-\alpha D_n)}\mathrm{tr}\varepsilon_{n+1}\mathbf{1} \\
&\qquad + \beta\left[(1-D_n)\varepsilon^{\mu p}_n - \varepsilon^p_{n+1}\right] \ \Big\} \\
\varepsilon^{\mu e} &= \varepsilon^\mu - \varepsilon^{\mu p}_n \\
\tilde{\sigma}^\mu &= \mathbb{E} : \varepsilon^{\mu e} \\
\sigma^\mu &= (1-D_n)\tilde{\sigma}^\mu
\end{aligned} \tag{13}$$

Plastic-damage correction

The previous elastic prediction gives the estimate $\tilde{\sigma}$ of the effective stress $\tilde{\sigma}_{n+1}$ at time t_{n+1}, with unchanged kinematic hardening $\mathbf{X} = \mathbf{X}_n$, and allows the yield criterion to be calculated. If the condition $f^\mu_{n+1} \leq 0$ is fulfilled, the calculation is over and $\varepsilon^{\mu p}_{n+1} = \varepsilon^{\mu p}_n$, $\mathbf{X}_{n+1} = \mathbf{X}_n$, $D_{n+1} = D_n$ is set. If not, this elastic solution is corrected by ensuring the consistency condition $f^\mu_{n+1} = 0$. The Euler Backward scheme is used for all variables except damage: $D = D_n$ is considered over a time step $\Delta t = t_{n+1} - t_n$ in the strain localization law and in plasticity equations coupled with damage. This is of course not a limitation at all in fatigue, since over an entire cycle – made up of many time steps – the damage increment usually does not exceed $D_c / N_R < 10^{-3}$ where $D_c \leq 1$ is the critical damage and N_R is the number of cycles to crack initiation.

Assuming then that the damage does not increase much over a time step, the set of nonlinear equations (11) must be solved, including the localization law,

$$\begin{aligned}
&\Delta\varepsilon^{\mu e} + \frac{1-\beta}{1-\beta D_n}\Delta\varepsilon^{\mu e} - \frac{1}{1-\beta D_n}\Delta\varepsilon \\
&\quad + \frac{\beta}{1-\beta D_n}\Delta\varepsilon^p \ - \frac{(\alpha-\beta)D_n}{(1-\beta D_n)(1-\alpha D_n)}\mathrm{tr}\Delta\varepsilon\mathbf{1} = 0
\end{aligned} \tag{14}$$

and the yield condition $f^\mu = 0$ at time t_{n+1}

$$f^\mu_{n+1} = (\tilde{\sigma}^\mu_{n+1} - \mathbf{X}^\mu_{n+1})_{eq} - \sigma^\infty_f = 0 \tag{15}$$

Equations (14)-(15) are combined with the normality rule for plastic strain and with the evolution law for kinematic hardening, discretized as $\Delta\varepsilon^{\mu p} = \frac{3}{2}\frac{\tilde{\sigma}^{\mu D}_{n+1} - \mathbf{X}^\mu_{n+1}}{(\tilde{\sigma}^\mu_{n+1} - \mathbf{X}^\mu_{n+1})_{eq}}\Delta p^\mu = \frac{3}{2}\frac{\mathbf{s}^{\mu D}_{n+1}}{(\tilde{\mathbf{s}}^\mu_{n+1})_{eq}}\Delta p^\mu$ and $\Delta\mathbf{X}^\mu = \frac{2}{3}C_y\left(1-D_n\right)\Delta\varepsilon^{\mu p}$. These equations can of course be solved using the Newton iterative method, but must be rewritten in the following form,

$$\begin{cases}
\dfrac{\mathbf{s}^\mu_{n+1}}{E} + \Gamma\dfrac{\mathbf{s}^{\mu D}_{n+1}}{(\mathbf{s}^\mu_{n+1})_{eq}}\Delta p^\mu + \mathbf{Q}_s = 0 \\
\qquad\qquad (\mathbf{s}^\mu_{n+1})_{eq} - \sigma^\infty_f = 0
\end{cases} \tag{16}$$

a function of the unknown accumulated plastic strain increment Δp^μ and of the unknown variable $\mathbf{s}^\mu_{n+1} = \tilde{\sigma}^\mu_{n+1} - \mathbf{X}^\mu_{n+1}$ allows a closed-form solution to be obtained explicitly. The following is set in Equations (16) (details can be found in [20]):

$$\begin{aligned}
\mathbf{Q}_s &= -\frac{\tilde{\sigma}^\mu_n - \mathbf{X}^\mu_n}{E} - \frac{1}{E(1-\beta D_n)}\times \\
&\qquad \left[\mathbb{E} : \Delta\varepsilon + K\frac{(\alpha-\beta)D_n}{1-\alpha D_n}\mathrm{tr}\Delta\varepsilon\mathbf{1} - 2G\beta\Delta\varepsilon^p\right] \\
\Gamma &= \frac{1}{E}\left(3G\frac{1-\beta}{1-\beta D_n} + C_y(1-D_n)\right)
\end{aligned} \tag{17}$$

where $G = E/2(1+\nu)$ and $K = E/3(1-2\nu)$ are the shear and bulk moduli.

The exact solution of the set of equations (16) for the plastic-damage correction is:

$$\begin{aligned}
s^\mu_{H\,n+1} &= -EQ_{sH} \\
\Delta p^\mu &= \frac{1}{\Gamma}\left(Q_{seq} - \frac{\sigma^\infty_f}{E}\right) \\
(\mathbf{s}^\mu_{n+1})' &= -\frac{E\mathbf{Q}'_s}{1 + \dfrac{\Gamma E}{\sigma^\infty_f}\Delta p^\mu} \\
\mathbf{s}^\mu_{n+1} &= (\mathbf{s}^\mu_{n+1})' + s^\mu_{H\,n+1}\mathbf{1}
\end{aligned} \tag{18}$$

where $Q_{seq} = \sqrt{\frac{3}{2}\mathbf{Q}'_s : \mathbf{Q}'_s}$ is the Von Mises norm of $\mathbf{Q}_s$, $Q_{sH} = \frac{1}{3}\mathrm{tr}\mathbf{Q}_s$ is its hydrostatic part and $\mathbf{Q}'_s = \mathbf{Q}_s - Q_{sH}\mathbf{1}$ is its deviatoric part.

The proposed scheme is implicit but does require iterations.

Variable updating

Once the previous plastic-damage correction has been made, all of the variables at the microscale are updated as follows:

- normal to the yield surface: $\mathbf{m}^{\mu} = \frac{3}{2}\frac{\mathbf{s}^{\mu D}_{n+1}}{\sigma^{\infty}_{f}}$
- plastic strain: $\varepsilon^{\mu p}_{n+1} = \varepsilon^{\mu p}_{n} + \mathbf{m}^{\mu}\Delta p^{\mu}$
- kinematic hardening: $\mathbf{X}^{\mu}_{n+1} = \frac{2}{3}C_y(1-D_n)\Delta\varepsilon^{\mu p}_{n+1} + \mathbf{X}^{\mu}_{n}$
- effective stress: $\tilde{\sigma}^{\mu}_{n+1} = \mathbf{s}^{\mu}_{n+1} + \mathbf{X}^{\mu}_{n+1}$
- damage:

$$D_{n+1} = D_n + \left(\frac{Y^{\mu}_{n+1}}{S}\right)^{s}\Delta p^{\mu} \qquad \text{with}$$

$$Y^{\mu}_{n+1} = \frac{1+\nu}{2E}\left[\langle\tilde{\sigma}^{\mu}_{n+1}\rangle^{+} : \langle\tilde{\sigma}^{\mu}_{n+1}\rangle^{+} + h\left(\frac{1-D_n}{1-hD_n}\right)^{2}\langle\tilde{\sigma}^{\mu}_{n+1}\rangle^{-} : \langle\tilde{\sigma}^{\mu}_{n+1}\rangle^{-}\right]$$
$$-\frac{\nu}{2E}\left[\langle \mathrm{tr}\tilde{\sigma}^{\mu}_{n+1}\rangle^{2}_{+} + h\left(\frac{1-D_n}{1-hD_n}\right)^{2}\langle \mathrm{tr}\tilde{\sigma}^{\mu}_{n+1}\rangle^{2}_{-}\right]$$

- stress tensor : $\sigma^{\mu}_{n+1} = (1-D_{n+1})\tilde{\sigma}^{\mu}_{n+1}$

and the calculation can then be started at time t_{n+2}

DAMAGE EAS post-processor for multiaxial fatigue

The DAMAGE_EAS post-processor solves the two-scale damage model constitutive equations and allows the micro-plasticity and damage history to be determined for complex loading. For a given material parameter file and for a given loading sequence (made up of the repetition by blocks of complex cycles defined at the RVE mesoscale), the post-processor calculates the damage history $D(t)$ and the time to crack initiation, i.e., the time for D to reach the critical damage D_c. The inputs (mesostrains, total and plastic) come from a Finite Element reference computation and are thus at one or several user chosen structure Gauss points. Given that the maximum number of increments used to describe a cycle is large (actually 5000), the program allows quasi random fatigue calculations. The post-processor DAMAGE_EAS has a graphical interface with material parameter identification and result plotting capabilities [19].

The inputs are thus a material file and a loading file. The outputs of any calculation are:

- the number of cycles to crack initiation for the case considered;
- a standard result file made up of 50 lines with the values (the histories) versus the number of cycles of the accumulated plastic strain and of the damage at the microscale;
- optional (large) files for complete results at the mesoscale and microscale (stresses, strains and plastic strain components versus time).

Fast identification procedure

The purpose of this work is to study the ability of the model to handle notched structure fatigue, when the material parameters are first identified on tensile uniaxial (or "smooth") testing specimens. For the parameter identification, the following is proposed.

Stage 1. The mesoscale parameters (Young modulus E, Poisson ratio ν, yield stress σ_y, plastic modulus C_y) are identified at each temperature on the monotonic tensile curve.

Stage 2. The asymptotic fatigue limit σ^{∞}_{f} is guessed from an experimental Wöhler curve as the horizontal "asymptote" at a very high number of cycles to rupture (at least $N_R > 10^7$),

$$\frac{\Delta\sigma}{2} \to \frac{(\Delta\sigma)^{\infty}}{2} = \sigma^{\infty}_{f} \Rightarrow N_R \to \infty$$

For a non-symmetric fatigue loading (and in this model because of the Von Mises yield criterion at the microscale), the asymptote in terms of the stress amplitude $\frac{(\Delta\sigma)^{\infty}}{2} = \sigma^{\infty}_{f}$ is independent from the load ratio $R = \sigma_{min}/\sigma_{Max}$. In terms of maximum stress, the corresponding asymptote is $\sigma^{\infty}_{Max} = 2\sigma^{\infty}_{f}/(1-R)$ – it is still due to $\frac{(\Delta\sigma)^{\infty}}{2} = \frac{\sigma_{Max}}{2}(1-R) = \sigma^{\infty}_{f}$ – and is dependent on R.

If the σ_{Max} *vs.* N_R diagram is used, the guessed horizontal asymptote σ^{∞}_{Max} at a given load ratio R thus allows the – material parameter – fatigue limit σ^{∞}_{f} to be identified as:

$$\sigma^{\infty}_{f} = \frac{1}{2}(1-R)\sigma^{\infty}_{Max} \tag{19}$$

Stage 3. The parameters h and D_c are considered to be equal to the default constant values for metals, $h = 0.2$, $D_c = 0.3$ [43].

Stage 4. The damage parameters S and s are pre-identified from a non-linear curve fitting in Wšhler diagram (figure 3) using an approximate closed-form expression for N_R (under the assumption $h = 1$ of a no micro-defect closure effect). This allows a first estimate of the damage parameters S and s to be easily determined. For a cyclically varying stress of $\Delta\sigma = \sigma_{Max} - \sigma_{min}$ between σ_{min} and σ_{Max}, the following closed form expression for the number of cycles to rupture is used [15, 16], here with no damage threshold,

$$N_R \approx \frac{(2ES)^{s}\mathcal{G}D_c}{\sigma^{\infty\,2s}_{f}\left[\Delta\sigma - 2\sigma^{\infty}_{f}\right]\left[R^{s}_{\nu min} + R^{s}_{\nu Max}\right]}$$
$$\mathcal{G} = 3G(1-\beta) + C_y(1-D) \approx 3G(1-\beta),$$
$$R_{\nu min} = \frac{2}{3}(1+\nu) + \frac{1}{3}(1-2\nu)\left[\frac{\sigma_{min}}{\sigma^{\infty}_{f}}\right]^{2} \tag{20}$$
$$R_{\nu Max} = \frac{2}{3}(1+\nu) + \frac{1}{3}(1-2\nu)\left[\frac{\sigma_{Max}}{\sigma^{\infty}_{f}}\right]^{2}$$

where G is the shear modulus.

Stage 5. At this final identification stage, the values for all parameters are kept identical, except for the damage strength S; $h = 0.2$ is set and the parameter S is re-adjusted by comparison with the reference Wöhler curve. The full set of constitutive equations is solved – numerically this time – instead of using the approximate formula (20).

An illustration of Stages 4 and 5 of the identification procedure is given for a TA6V alloy at a low temperature in figure 3, in which the experimental fatigue curve and the analytic (from equation 20) and computed (DAMAGE_EAS) model responses are sketched and compared.

The final set of material parameters is only composed of the elasticity parameters E, $\nu \approx 0.3$, the plastic modulus C_y, the asymptotic fatigue limit σ_f^{∞}, the damage strength S (in MPa), the damage exponent s, the micro-defect closure effect parameter $h = 0.2$ and the critical damage $D_c = 0.3$. Let us point out that the identification of parameters S, s and σ_f^{∞} is carried out by using a first population of uniaxial (smooth) specimens at $R = 0.1$ (test results reported as marks in figure 3). Next, the model is evaluated on a second independent population of notched specimens made of the same material, tested at the same temperature, but at higher stress ratios.

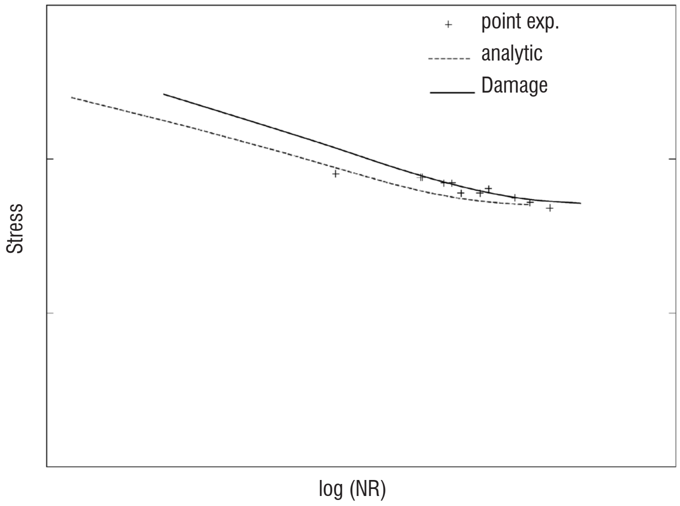

Figure 3 - Illustration of Stages 4 and 5 of the identification procedure on the Wöhler curve for TA6V at a low temperature (marks: experimental, analytical: Eq. (20), DAMAGE: numerical solution by DAMAGE_EAS of set of equations (8) and (11)).

Fatigue of axisymmetric notched specimens

Axisymmetric Finite Element computations of 3 notched specimens have been performed with a refined mesh in the notch (figure 4). The three elastic stress concentration factors are $K_r = 1.5$, 2.5 and 3.5. The specimen height is 60 mm.

Elasto-plastic constitutive equations with linear kinematic hardening are used to model TA6V behavior. The considered stress ratios are positive, the notch plastification only occurs at the first load application. The microscale behavior is represented by the elasto-plasticity coupled with damage constitutive equations (11). The scale transition law is Eq. (8).

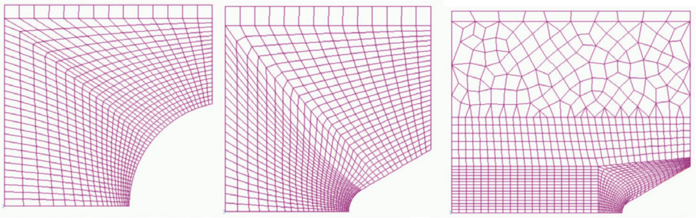

Figure 4 - Details of the meshes in the notch for $K_r = 1.5$ (left), $K_r = 2.5$ (middle) and $K_r = 3.5$ (right).

Structure computations with pre-plastification

The applied loading is presented in figure 5. It consists in a uniaxial (longitudinal) load varying between a maximum load F_{Max} and a minimum load F_{min}. Various maximum loads are considered, corresponding to different numbers of cycles to crack initiation. Various positive load ratios $R_F = F_{min} / F_{Max}$ are also considered, which are equal to the (applied) far field stress ratio and to the local longitudinal stress ratio $\sigma_{min} / \sigma_{Max}$ obtained in elastic computations. As mentioned already, plastification takes place in the stress concentration zone during the first load application (a stage therefore called pre-plastification) making the local stress ratio R obtained in plasticity different from the applied load ratio R_F (The value of obtained is lower than R_F).

An example of a map of accumulated plastic strains in the notch is given in figure 6 for $F_{min} = 46\ kN$, $F_{Max} = 52\ kN$, $R_F = 0.88$. Simply note that this pre-plastification is naturally taken into account within the two-scale damage model, through the use of the localization law (8) (through the existence of a mesoscopic plastic strain ε^p).

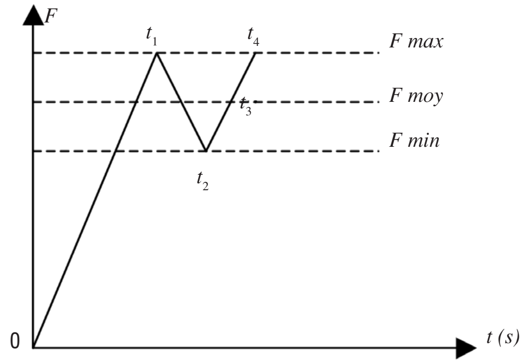

Figure 5 - Applied loading

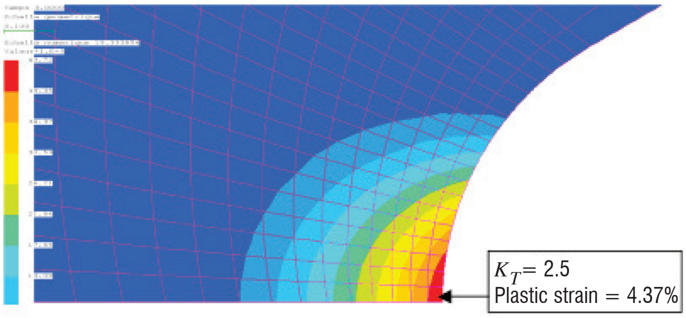

Figure 6 - Maps of plastic strain after pre-plastification for one of the $K_T = 2.5$ specimens (applied load ratio $R_F = F_{min} / F_{Max} = 0.88$, computed stress ratio $R = \sigma_{min} / \sigma_{Max} = 0.72$).

Number of cycles to rupture from two-scale damage analysis

For the calculations of the numbers of cycles to crack initiation (or for the prediction of the "no crack initiation" events), the total ε and plastic ε^p strain tensors have been interpolated at the node located at the surface of the notch. These data constitute the input of the DAMAGE EAS post-processor and are entered in the form of an ASCII file. The tensors are extracted from the plasticity computations at time steps t_1, t_2, t_3 and t_4 defined in figure 5. Only the second part of the loading – the part between F_{Max} and F_{min} – is repeated. A maximum number of repetitions of this sequence or block must be set when using DAMAGE_EAS (10^7 in these calculations). The 21 damage post-processings corresponding to 21 tested notched specimens were made in a single (batch) operation taking approximately 45 min on a PC.

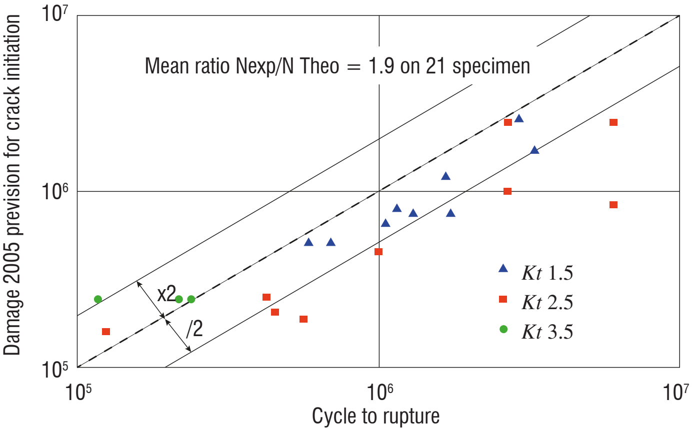

Figure 7 - Comparison between the experimental and predicted lifetimes for axisymmetric notched specimens

Failure is interpreted here as the mesocrack initiation condition, which corresponds to when the damage D reaches the critical value D_c (a material parameter here equal to 0.3).

The results obtained show an average ratio Experimental number of cycles to failure N_R^{exp} / Calculated number of cycles $N_R^{calc} = N\left(D = D_c\right)$ of 1.9 (figure 7). As far as the unbroken specimens at cycles are concerned, the model correctly predicts the non-initiation of a crack in 10 out of 12 cases (83%). The fact that most of the predictions underestimate the experimental fatigue lifetimes seems logical. We must indeed recall that the model only predicts the crack initiation at the RVE mesoscale and does not take into account the cycles necessary to make these small cracks propagate to the final structural failure.

As far as the results obtained here for the TA6V alloy at a low temperature are concerned, the mean factor ≈ 2 obtained is quite a good result: this corresponds to the expected performance of a model for its industrial use, when the results are obtained from an independent identification on uniaxial (smooth) fatigue specimens. What is also of utmost importance is the ability of the model to correctly predict the time to crack initiation of a specimen subjected to a high mean stress effect, with more or less plastification (up to 5% here) and for a multiaxial stress state.

Computed Haigh diagram for TA6V alloy at a low temperature

The classical Haigh diagram corresponds to the curve given, at a given number of cycles to failure, by the stress amplitude $\sigma_a = \frac{1}{2}(\sigma_{Max} - \sigma_{min})$ versus the mean stress $\overline{\sigma} = \frac{1}{2}(\sigma_{min} + \sigma_{Max})$.

First, in order to better characterize the model response over the entire stress ratio range, $R \in [-1, 0.9]$, several theoretical times to crack initiation have been calculated using uniaxial strain and plastic strain tensors (i.e., corresponding to uniaxial stress states of smooth specimens) generated for different maximum stresses at a given R. The corresponding points are reported on the different iso-R lines (R = 0.1, 0.5, 0.6, 0.8 and 0.9, figure 9). Each

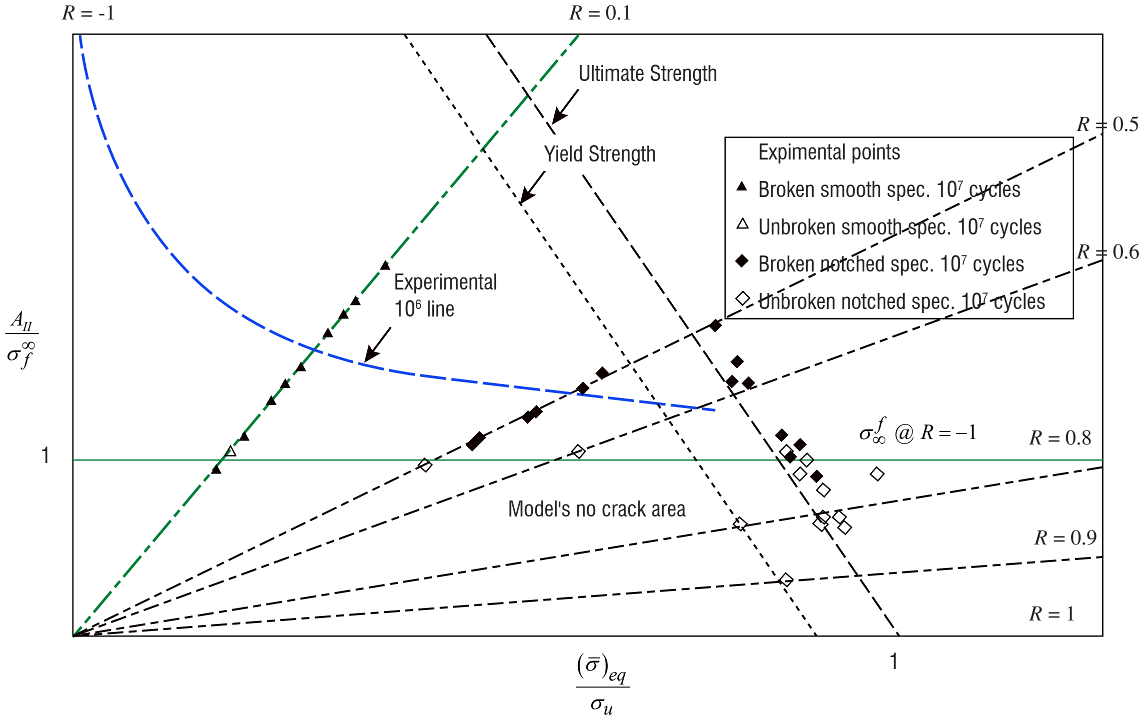

Figure 8 - Experimental multiaxial A_{II} / σ_f^∞ vs. $(\overline{\sigma})_{eq} / \sigma_u$ Haigh diagram of a TA6V alloy at a low temperature

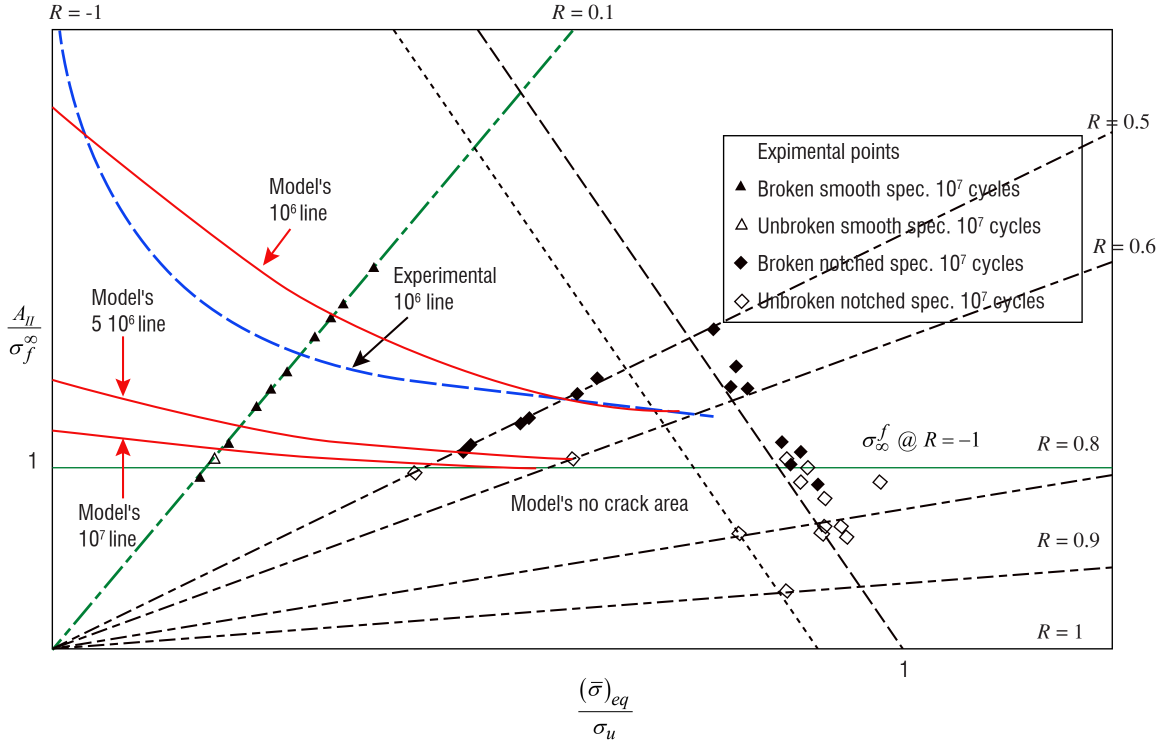

Figure 9 - Multiaxial A_{II} / σ_f^∞ vs. $(\overline{\sigma})_{eq} / \sigma_u$ Haigh diagram with two-scale damage model iso-lifetime lines

point is associated with a number of cycles to crack initiation calculated by DAMAGE EAS. The maximum stress was systematically chosen above the σ_f^∞-fatigue limit identified for the material at R = -1 which is, in this two-scale analysis, the limit below which the model does not announce any crack initiation. With such a network of theoretical points associated with their lifetime prediction, it is then possible to plot both the experimental (here at $N_R = 10^6$ cycles, "Experimental 1E6 line") and the theoretical iso-lifetime curves (using a Box-Cox regression technique). The iso-lifetime curves given by the two-scale damage model for 10^6(1E6), 5 10^6(5E6) and 10^7(1E7) cycles are shown in figure 9, each corresponding to a classical Haigh diagram for this TA6V alloy.

A_{II} vs. $(\overline{\sigma})_{eq}$ multiaxial Haigh diagram

Both the experimental and computational results have been reported in figures 8 and 9 (by means of the two scale damage analysis). The asymptotic fatigue limit and the ultimate stress are respectively denoted by σ_f^∞ and σ_u. The unbroken specimens after 10^7 cycles are represented by white marks, whereas the broken ones are represented by plain black marks. The smooth specimens (R = 0.1) are represented by triangular marks. The notched specimens are represented by diamonds marks. For these, the stress state is 3D so a first multiaxial Haigh diagram can be plotted by replacing the uniaxial stress amplitude (vertical axis) by the octahedral shear $_{II}$, the local equivalent alternated stress,

$$\sigma_a = A_{II} = \frac{1}{2}\sqrt{\frac{3}{2}(\sigma'_{Max}-\sigma'_{min}):(\sigma'_{Max}-\sigma'_{min})} \qquad (21)$$

and by replacing the uniaxial mean stress (horizontal axis) by the Von Mises equivalent stress of the mean stress tensor, the mean local stress is

$$(\overline{\sigma})_{eq} = \frac{1}{2}\sqrt{\frac{3}{2}(\sigma'_{Max}+\sigma'_{min}):(\sigma'_{Max}+\sigma'_{min})} \qquad (22)$$

The horizontal line $A_{II}/\sigma_f^\infty = \sigma_a/\sigma_f^\infty = 1$ or $A_{II} = \sigma_a = \sigma_f^\infty$ corresponds to the infinite alternated fatigue limit (identified from the § "Fast identification" procedure). It is interesting to notice that, for this TA6V at a low temperature, this limit separates the broken specimens (black marks) from the unbroken ones (white marks) quite well. Note that the model theoretical iso-lifetime curves drawn here are rapidly decreasing in the -1 to 0.1 -range. All of the lines converge towards the asymptotic fatigue limit identified at R = -1 (horizontal line $\sigma_a/\sigma_f^\infty = 1$). This line constitutes an asymptote for the iso-lifetime curves when the number of cycles to crack initiation increases. This feature is due to the fact that the equation for the asymptote is $f^\mu = 0$ and that in this case a Von Mises plasticity criterion is considered at the microscale.

In order to directly compare the theoretical iso-lifetime curves to their experimental counterparts, a more detailed study can be carried out on the $N_R = 10^6$ line – which corresponds to the usual Haigh diagram at 10^6 cycles – for both the theoretical predictions and the available experimental data. A non-linear data regression allows the experimental 10^6(1E6) iso-life line (dashed line) to be plotted. It is remarkable that the experimental line fits its theoretical counterpart quite well. The global decreasing shape of the $N_R = 10^6$ computed Haigh diagram is quite similar to that of the experimental one: the two-scale damage model proposes an evolution of the theoretical iso-lifetime curve in good accordance with the experimental $N_R = 10^6$ line evolution for this TA6V alloy at a low temperature.

Finally, the influence of the local plastification on the local true stress ratio can also be observed. Once the yield stress is reached (straight line "Yield Strength" in figure 8), the local stress ratio computed at the notch tip decreases and the corresponding point leaves its original iso-R line. All plastified points accumulate along the 45° "Ultimate Strength" straight line. This phenomenon has already been observed [37] and shows the importance of considering the local stress and strain state when drawing Haigh diagrams for notched specimens.

A_{II} vs. $\mathrm{tr}\overline{\sigma}$ multiaxial Haigh diagram

It is also possible to use another multiaxial extension of the Haigh diagram, the octahedral shear $\sigma_a = A_{II}$ versus the trace of the mean stress tensor,

$$\mathrm{tr}\overline{\sigma} = \overline{\sigma}_{11} + \overline{\sigma}_{22} + \overline{\sigma}_{33} \quad \text{with} \quad \overline{\sigma} = \frac{1}{2}(\sigma_{min} + \sigma_{Max}) \qquad (23)$$

This complementary representation offers the advantage of better taking the stress triaxiality into account (it is consistent with the Sines approach of multiaxial fatigue [59]). The further values of the stress tensor trace are those of the smooth and notched fatigue specimens, computed by Finite Elements.

In figure 10, three different iso-lifetime lines predicted by the two-scale damage model have been plotted: the $5\ 10^5$(5E5), 10^6(1E6) and $5\ 10^6$(5E6) iso-lifetime lines, with the corresponding experimental points. Several fatigue tests carried out on smooth specimens at $R = -1$, $R = 0.1$ and $R = 0.5$ up to 10^6 cycles, allow the shape of the $N_R = 10^6$ cycles line to be confirmed. As mentioned before, the theory and experiments fit quite well.

Figure 11 is the equivalent of figure 9 (with $(\overline{\sigma})_{eq}$ replaced by $\mathrm{tr}\overline{\sigma}$). The level of local triaxiality and yielding for each test is better apprehended (this information was not clear in figure 9, since all plastified points were aligned).

Let us insist once again on the fact that the observations made here only concern locally plastified specimens. It would not have been possible to explore such high stress ratio values and such high plastification levels in the High Cycle Fatigue with uniaxial smooth specimens.

Stronger asymptotic mean stress effect

The mean stress obtained previously in the mean stress range considered was in fact not so important, so that it has been modeled through the dissymmetry of damage growth (by means of a low fatigue limit and a micro-crack closure parameter $h \ll 1$). A more general model is possible, still within the kinetic framework of rate form damage modeling, i.e., still with no need for the notion of cycle or for the Rainflow-type counting cycle method.

Linear mean stress effect

A linear mean stress effect on the fatigue asymptote can be introduced into the two-scale damage model by considering a Drucker-Prager criterion function at the microscale [3, 4], where is a material parameter,

$$\begin{aligned} f^\mu &= \left(\sigma^\mu - X^\mu\right)_{eq} + a\ \mathrm{tr}\sigma^\mu - \sigma_f^\infty \\ &= \left(\sigma^\mu - X^\mu\right)_{eq} + 3a\sigma_H - \sigma_f^\infty \end{aligned} \qquad (24)$$

i.e., by making the fatigue criterion pressure/first invariant dependent, as proposed by many authors [12, 59, 13, 24, 42, 50] for fatigue. From the Eshelby-Kröner scale transition law (5) – as well as from the scale transition law (8) – and incompressible plasticity, $\mathrm{tr}\sigma^\mu = \mathrm{tr}\sigma = 3\sigma_H$ is still obtained. The differences here compared with classical works are: (i) the infinite lifetime domain $f^\mu < 0$ is translated by micro-plasticity, (ii) the current values of the stresses are used (not the maximum or mean values) and the modeling remains incremental. Micro-plasticity and damage are the solution of a kinetic differential equation, so there is no need to define a cycle in order to calculate the time to crack initiation (it is the time at which $D(t) = D_c$, the critical damage).

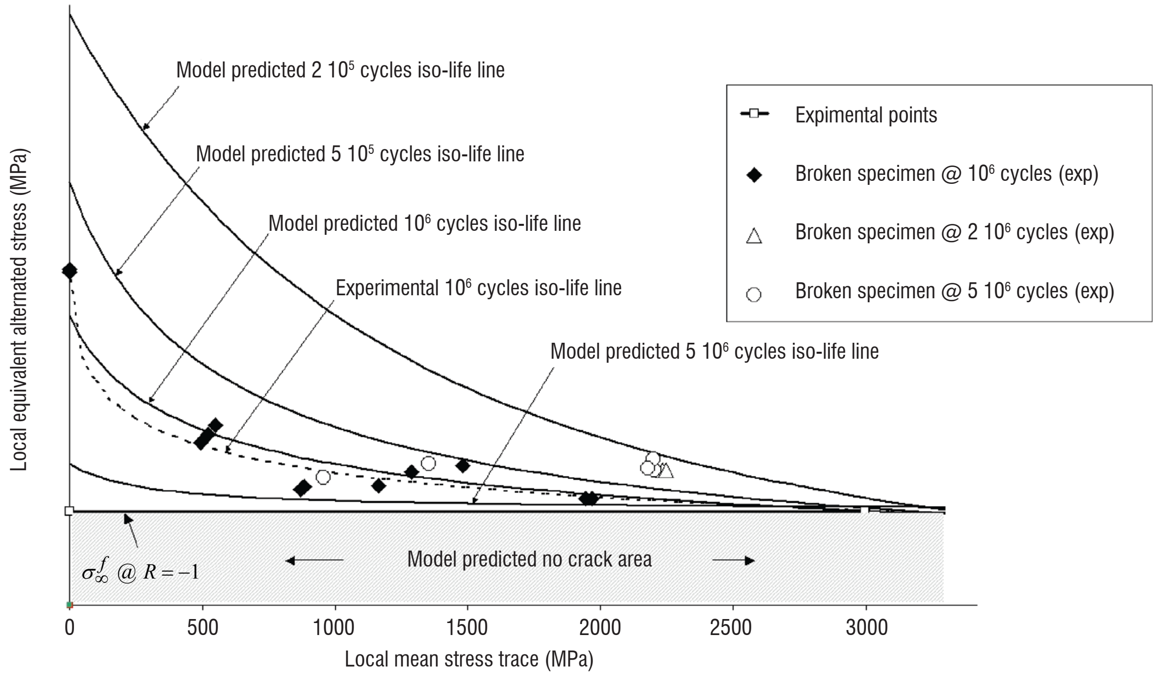

Figure 10 - Partial multiaxial A_{II} / σ_f^∞ vs. $\mathrm{tr}\overline{\sigma}$ Haigh diagram (TA6V alloy at a low temperature).

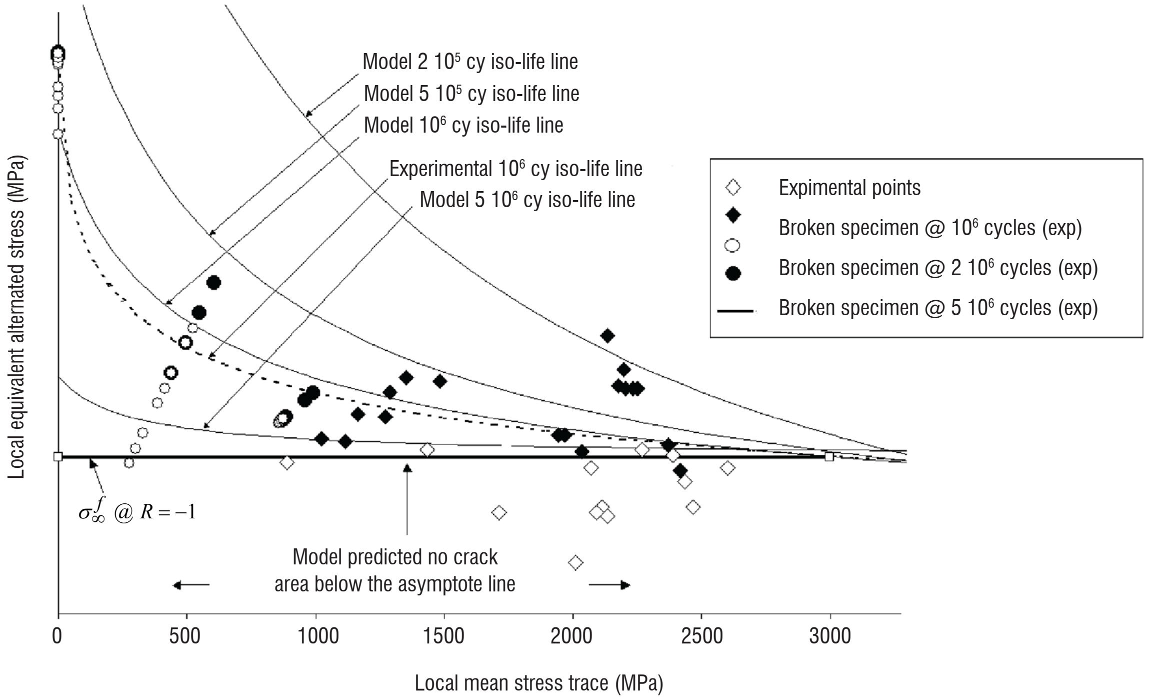

Figure 11 - Multiaxial A_{II} / σ_f^∞ vs. $\mathrm{tr}\,\overline{\sigma}$ Haigh diagram (TA6V alloy at a low temperature).

In box 1, from the two-scale damage model constitutive equations, the asymptotic fatigue limit is shown to be linearly mean stress dependent as at infinite lifetime,

$$\begin{aligned} &\text{in 1D}: \sigma_a = \sigma_\ell = \sigma_f^\infty - a\overline{\sigma} \\ &\text{in 3D, proportional loading}: A_{II} = \sigma_\ell = \sigma_f^\infty - a\,\mathrm{tr}\,\overline{\sigma} \end{aligned} \qquad (25)$$

so that the Sines criterion is retrieved in 3D, under a proportional loading assumption with octahedral stress A_{II} equal to the Von Mises norm of stress tensor amplitude. The fatigue limit in shear is obtained as $\tau_f^\infty = \sigma_f^\infty / \sqrt{3}$ for any mean shear stress $\overline{\tau}$: it is not mean stress dependent, as experimentally observed [59, 42].

Bi-linear mean stress effect

A non-linear or at least bilinear modeling of the mean stress effect is sometimes needed if the applications range from alternated fatigue to high mean stress loading [33, 6].

A bilinear mean stress effect on the fatigue asymptote can be introduced into the two-scale damage model, by considering a bilinear definition of the first invariant term of the criterion function at the microscale, as

$$f^\mu = \left(\sigma^\mu - X^\mu\right)_{eq} + K^\mu(\sigma_H) - \sqrt{3}\tau_f^\infty$$
$$K^\mu(\sigma_H) = \begin{cases} 3a_1\sigma_H & if\,\sigma_H \le \frac{1}{3}\sigma_0 \\ 3a_2\sigma_H + (a_1 - a_2)\sigma_0 & if\,\sigma_H > \frac{1}{3}\sigma_0 \end{cases} \qquad (26)$$

where a_1, a_2 and the mean stress domain transition stress σ_0 are material parameters and $K^\mu(\sigma_H = 0) = 0$ so τ_f^∞ is the fatigue limit mean stress, independent in pure shear. $K^\mu(\sigma_H) = 3a\sigma_H = a\,\mathrm{tr}\sigma = a\,\mathrm{tr}\sigma^\mu$ is recovered and the linear mean stress effect from $a_1 = a_2 = a$.

The dependency of the fatigue limit σ_ℓ on the mean stress is now obtained as follows. For a positive mean stress:

- for $\overline{\sigma} \le \overline{\sigma}_0$ $\quad \sigma_a = \sigma_f^\infty - a_0\overline{\sigma}$
- for $\overline{\sigma} > \overline{\sigma}_0$ $\quad \sigma_a = \sqrt{3}\tau_f^\infty - (a_1 - a_2)\sigma_0 - a_2\overline{\sigma}$

where

$$\begin{aligned} \sigma_f^\infty &= \frac{2\sqrt{3}\tau_f^\infty - (a_1 - a_2)\sigma_0}{2 - (a_1 - a_2)} \\ \overline{\sigma}_0 &= \frac{\sigma_f^\infty - \sqrt{3}\tau_f^\infty + (a_1 - a_2)\sigma_0}{a_0 - a_2} \\ a_0 &= \frac{a_1 + a_2}{2 - (a_1 - a_2)} \end{aligned} \qquad (27)$$

The calculations of an asymptotic multiaxial Haigh diagram (at infinite lifetime) can be found in Appendix A. Note that over the entire range of mean stresses, including the highly negative ones, the Haigh diagram is in fact trilinear.

Conclusion

The computation of two complementary multiaxial Haigh diagrams has been presented by means of an incremental two-scale damage analysis. Damage and failure are considered as part of the material behavior, in High Cycle Fatigue also, and this even if a structure behaves elastically at the macroscopic scale. The time integration, time step by time step, of the plasticity coupled with the damage microscale constitutive equations determines HCF failure, here the microcrack initiation, simply by the reaching of a critical damage, $D = D_c$, in 3D cases, in notch yielding cases, in any general complex fatigue loading cases.

The two scale damage analysis has been carried out on TA6V notched specimens at a low temperature. The TA6V specimens were tested at up to 10^7 cycles at different stress ratios, from $R = 0.5$ up to $R = 0.9$. The advantages of notched specimens have been pointed out as twofold,

- on the one hand, they allow an interesting bi-axial stress state to be obtained in the average proportion of 70% in axial and 30% in hoop stresses,
- on the other hand, they allow high stress ratios and high local plastification levels to be easily explored; these levels are often observed in real structures.

This is often not possible with uniaxial (smooth) specimens.

The model has been identified first by fatigue data for a single population of smooth specimens tested at $R = -1$. It has then been applied, in a post-processing approach, to notched specimens exhibiting plastification at the notch tip (at different stress ratios R). Both the non-rupture events and the numbers of cycles to crack initiation have been correctly predicted. An average factor of 2 has been obtained between the experimental lifetimes and the computed numbers of cycles to crack initiation (over a 21 notched specimen population).

This work also emphasizes a quite good concordance between the experimental iso-lifetime curves and their theoretical counterparts, at least at $N_R = 10^6$ for TA6V at a low temperature: they decrease and seem to converge towards a unique asymptote in Haigh diagrams, as the stress ratio increases. This asymptote corresponds to the infinite alternated fatigue limit, a material parameter also called asymptotic fatigue limit, for the considered titanium alloy – a TA6V optimized for aeronautics applications.

The asymptote may not be horizontal, thus leading to a stronger mean stress effect. A way to obtain a linear or piecewise linear Haigh diagram from the two-scale damage model has been finally addressed.

Finally, note that neither the scale nor the gradient effects have been introduced (nor are they needed) in the modeling. A quantitative study of such effects for this titanium alloy is left for further work. It must be noted that the possibilities of gradient modeling within a two-scale damage model can be found, in [16, 46] ■

Box 1 - Mean stress effect from a two-scale damage model: proof under proportional loading

Under a proportional loading, a time-space multiplicative decomposition can be applied:

$$\sigma = \sigma(t)\Sigma \quad \text{with} \quad \Sigma_{eq} = \sqrt{\frac{2}{3}\Sigma':\Sigma'} = 1 \tag{1-1}$$

where $\sigma = \sigma(t) = sign(\sigma)\sigma_{eq}$ is a scalar function (the signed Von Mises stress) and Σ is a constant tensor, normed, such as $tr\Sigma > 0$, so the stress triaxiality is $\sigma_H / \sigma_{eq} = \frac{1}{3} sign(\sigma) \mathrm{tr}\Sigma$.

At the microscale, due to the Eshelby-Kršner scale transition (5), proportionality is maintained only for deviatoric tensors :

$$\mathrm{e}^{\mu p} = \frac{3}{2}\varepsilon^{\mu p}\Sigma' \quad \text{and} \quad X^{\mu} = X^{\mu}\Sigma' \tag{1-2}$$

where $\dot{X}^{\mu} = C^{\mu}(1-D)\dot{\varepsilon}^{\mu p}$ for the now scalar kinematic hardening law.

The deviatoric part of the scale transition for the deviatoric tensors gives $\tilde{\sigma}^{\mu'} = \sigma' - 2G(1-\beta)\varepsilon^{\mu p} = (\sigma - 3G(1-\beta)\varepsilon^{\mu p})\Sigma'$, so quantities at the microscale can be expressed from the scalar signed Von Mises stress σ:

$$\begin{cases} \mathrm{t}r(\sigma^{\mu}) = \mathrm{t}r(\sigma) = \sigma \mathrm{t}r(\Sigma) \\ (\sigma^{\mu} - X^{\mu})_{eq} = | \sigma - (3G(1-\beta) + C^{\mu})\varepsilon^{\mu p} | \end{cases} \tag{1-3}$$

The expression (24), generalized into Eq. (26) for the yield criterion at the microscale, becomes in proportional loading :

$$f^{\mu} = | \sigma - (3G(1-\beta) + C^{\mu})\varepsilon^{\mu p} | + K^{\mu}(\sigma_H) - \sqrt{3}\tau_f^{\infty} \tag{1-4}$$

The extrema of a cycle at the onset of plasticity $f = 0$ at both the maximum stress σ_{Max} and minimum stress σ_{min} are

$$\begin{cases} f_{Max} = \sigma_{Max} - (3G(1-\beta)\varepsilon^{\mu p} + X^{\mu}) + K^{\mu}(\sigma_{HMax}) - \sqrt{3}\tau_f^{\infty} = 0 \\ f_{min} = -\sigma_{min} + 3G(1-\beta)\varepsilon^{\mu p} + X^{\mu} + K^{\mu}(\sigma_{Hmin}) - \sqrt{3}\tau_f^{\infty} = 0 \end{cases} \tag{1-5}$$

Infinite lifetime (endurance) corresponds to a possible pre-yielding, but then to elastic loading at constant $\varepsilon^{p\mu}$ and X^{μ} at the microscale, to a stress amplitude lower than $\sigma_a = \frac{1}{2}(\sigma_{Max} - \sigma_{min}) = \frac{1}{2}(\sigma_{Max}\Sigma' - \sigma_{min}\Sigma')_{eq} = A_{II}$ (due to $\Sigma_{eq} = 1$) determined from both conditions $f_{Max} = f_{min} = 0$. In any case, it is $A_{II} = \sqrt{3}\tau_f^{\infty} - \frac{1}{2}(K^{\mu}(\sigma_{Hmin}) + K^{\mu}(\sigma_{HMax}))$,

- if a linear Drucker-Prager expression (24) is used $\frac{1}{2}(K^{\mu}(\sigma_{HMax}) + K^{\mu}(\sigma_{Hmin})) = ktr\overline{\sigma}$ so that linear Sines criterion describing the infinite lifetime domain is obtained :

$$A_{II} = \frac{1}{2}(\sigma_{Max} - \sigma_{min})_{eq} = \sqrt{3}\tau_f^{\infty} - a\,\mathrm{tr}\,\overline{\sigma} \qquad (1\text{-}6)$$

- if a bilinear definition of function $K^{\mu}(\sigma_H)$ is used, there are 3 cases :

i) $\mathrm{tr}\sigma_{Max} \le \sigma_0$ or ii) $\mathrm{tr}\sigma_{min} \ge \sigma_0$ or iii) $\mathrm{tr}(\sigma_{Max}) > \sigma_0$ and $\mathrm{tr}(\sigma_{min}) < \sigma_0$.

For cases (i) and (ii) the same parameter a_i acts in f_{min} and f_{min} so that the same calculations as previously hold, therefore the mean stress effect is linear (but with different slopes a_1 or a_2) as

$$\begin{array}{ll} \text{when } \mathrm{tr}\sigma_{\mathrm{Max}} < \sigma_0 & A_{II} = \frac{1}{2}(\sigma_{Max} - \sigma_{min})_{eq} = \sqrt{3}\tau_f^{\infty} - a_1\,\mathrm{tr}\,\overline{\sigma} \\ \text{when } \mathrm{tr}\sigma_{\mathrm{min}} > \sigma_0 & A_{II} = \frac{1}{2}(\sigma_{Max} - \sigma_{min})_{eq} = \sqrt{3}\tau_{f^{\infty}} - (a_1 - a_2)\sigma_0 - a_2\,\mathrm{tr}\,\overline{\sigma} \end{array} \qquad (1\text{-}7)$$

In the last case, the two constants a_1 and a_2 act as in eq. (26)

$$\begin{cases} \mathrm{tr}\sigma_{Max} > \sigma_0 & f^{\mu} = \sigma_{Max} - (3G(1-\beta)\varepsilon^{\mu p} + X^{\mu}) + a_2\sigma_{Max}\,\mathrm{tr}\Sigma + (a_1 - a_2)\sigma_0 - \sqrt{3}\tau_f^{\infty} = 0 \\ \mathrm{tr}\sigma_{min} < \sigma_0 & f^{\mu} = -\sigma_{min} + 3G(1-\beta)\varepsilon^{\mu p} + X^{\mu} + a_1\sigma_{min}\,\mathrm{tr}\Sigma - \sqrt{3}\tau_f^{\infty} = 0 \end{cases} \qquad (1\text{-}8)$$

By adding the two equations, at identical $\varepsilon^{p\mu}$, the amplitude is obtained:

$$\sigma_a = \sqrt{3}\tau_f^{\infty} - (a_1 - a_2)\sigma_0 - (a_2\sigma_{Max} + a_1\sigma_{min})\mathrm{tr}\Sigma \qquad (1\text{-}9)$$

Finally, using $\sigma_{Max} = \overline{\sigma} + \sigma_a$, $\sigma_{min} = \overline{\sigma} - \sigma_a$, $\mathrm{tr}\Sigma = \mathrm{tr}\sigma / \sigma_{eq}$ and $\sigma_a = A_{II}$ in such a proportional cyclic loading a linear mean stress effect is obtained, which is stress triaxiality dependent, with a slope in the Haigh diagram different from parameters a_1 and a_2,

$$\text{when} \begin{cases} \mathrm{tr}\sigma_{Max} > \sigma_0 \\ \mathrm{tr}\sigma_{min} < \sigma_0 \end{cases} \quad A\ II = \frac{2\sqrt{3}\tau_f^{\infty} - (a_1 - a_2)\sigma_0}{2 - 3(a_1 - a_2)\frac{\sigma_H}{\sigma_{eq}}} - \frac{a_1 + a_2}{2 - 3(a_1 - a_2)\frac{\sigma_H}{\sigma_{eq}}}\mathrm{tr}\,\bar{\sigma} \qquad (1\text{-}10)$$

In uniaxial tension-compression $\Sigma = diag[1,0,0]$, there is a diagonal tensor so

$$\sigma_a = \frac{2\sqrt{3}\tau_f^{\infty} - (a_1 - a_2)\sigma_0}{2 - (a_1 - a_2)} - \frac{a_1 + a_2}{2 - (a_1 - a_2)}\overline{\sigma} = \sigma_f^{\infty} - a_0\overline{\sigma} \qquad (1\text{-}11)$$

This last equation defines the mean stress effect at low mean stress, if a parameter σ_0 is identified that is smaller than the uniaxial fatigue limit σ_f^{∞}. It thus defines the fatigue limit at zero mean stress σ_f^{∞} from the fatigue limit in pure shear τ_f^{∞} and the parameters a_1, a_2, σ_0 of the bilinear $K^{\mu}(\sigma_H)$ function.

Acknowledgements

Snecma and LMT-Cachan would like to especially acknowledge the CNES (Direction des Lanceurs) for its support for this study carried out on the TA6V alloy.

References

[1] K. AAS-JACKOBSEN, R. LENSHOW R - *Behavior of Reinforced Columns Subjected to Fatigue Loading*. ACI Journal, 70(3), pp. 199-206, 1973.

[2] O.H. BASQUIN (1910) - *The Exponential Law of Endurance Tests*. Proc. ASTM, 10, 625–630.

[3] G. BARBIER, R. DESMORAT, J.P. SERMAGE, A. DUTERTRE, S. COURTIN, J. DEHOUVE, D. TCHOU-KIEN - *Mean Stress Effect by Incremental Two Scale Damage Model, LCF6*. 6th International Conference on Low Cycle Fatigue, Berlin, Sept. 8-12, 2008.

[4] G. BARBIER, R. DESMORAT, B. RAKA - *Mean Stress Effect and Bi-Axial Fatigue of Structures from Two Scale Damage Model*. ICTAM 2008 -22nd International Congress of Theoretical and Applied Mechanics, Adelaide, Australie, August 25-29, 2008.

[5] A. BENALLAL, R. BILLARDON, I. DOGHRI, L. MORET-BAILLY - *Crack Initiation and Propagation Analyses Taking into Account Initial Strain Hardening and Damage Fields*. Luxmore A. (ed.), Numerical Methods in Fracture Mechanics, Pineridge Press, pp. 337-351, 1987.

[6] V. BONNAND, J.L. CHABOCHE, P. GOMEZ, P. KANOUTÉ, D. PACOU - *Investigation of Multiaxial Fatigue in the Context of Turboengine Disc Applications*. International Journal of Fatigue 33, 1006–1016, 2011.

[7] M.W. BROWN, K.J. ILLER - *A Theory for Fatigue Failure under Multiaxial Stress-Strain Conditions Institution of Mechanical Engineers*. Proceedings. vol. 187, no. 65, pp. 745-755. 1973

[8] J.L. CHABOCHE - *Continuum Damage Mechanics and its Application to Structural Lifetime Predictions*. La Recherche Aerospatiale (English Edition), 4, pp. 37-54, 1987.

[9] J.L. CHABOCHE - *Development of Continuum Damage Mechanics for Elastic Solids Sustaining Anisotropic and Unilateral Damage*. Int. J. Damage Mechanics, Vol. 2, pp. 311-329, 1993.

[10] J.L. CHABOCHE, P.M. LESNE - *A Non-Linear Continuous Fatigue Damage Model*. Fatigue Fract Engng Mater Struc 11, 1-17, 1988.

[11] J.L. CHABOCHE, P.M. LESNE - Fatigue & Fracture of Engineering Materials & Structures, 11, p. 1-17, 1988.

[12] B. CROSSLAND - *Effect of Large Hydrostatic Pressures on the Torsional Fatigue Strength of an Alloy Steel*. Proc. of the Inter. Conf. on fatigue metals Inst. Mech. Engr., pp. 138-149, 1956.

[13] K. DANG-VAN - *Sur la résistance à la fatigue des métaux*. Sciences et Techniques de l'Armement, vol. 3, pp. 647-722, 1973.

[14] K. DANG-VAN - *Macro-Micro Approach in High-Cycle Multiaxial Fatigue, Advances in Multiaxial Fatigue*. ASTMSTP1191, D.L. McDowell and R. Ellis Eds., Americain Society for Testing Materials, Philadelphia, pp. 120-130, 1993.

[15] R. DESMORAT - *Modélisation et estimation rapide de la plasticité et de l'endommagement*. Habilitation à Diriger des Recherches, Université Paris 6, 2000.

[16] R. DESMORAT - *Two Scale Damage Model for Fatigue Representation of Gradient Effects*. 6th National Congress on Mechanics, Thessaloniki, Grèce, Vol. 2, p. 318-327, 19-21 july 2001.

[17] R. DESMORAT, J. LEMAITRE - *Two Scale Damage Model for Quasi-Brittle and Fatigue Damage, Handbook of Materials Behavior Models*. J. Lemaitre Ed., Academic Press, chapter Continuous Damage, Section 6.15, pp. 525-535, 2001.

[18] R. DESMORAT - *Damage and Fatigue : Continuum Damage Mechanics Modeling for Fatigue of Materials and Structures*. European Journal of Environmental and Civil Engineering (Revue Européenne de Génie Civil), 10, p. 849-877, 2006.

[19] R. DESMORAT, F. PAUGET, J.P. SERMAGE - *DAMAGE_2005: a Post-Processor for High Cycle Fatigue under Complex Thermomechanical Loading*. ASME Pressure Vessels and Piping Division Conference, Vancoucer, BC, Canada, july 23-27, 2006.

[20] R. DESMORAT, A. KANE, M. SEYEDI, J.P. SERMAGE - *Two Scale Damage Model and Related Numerical Issues for Thermo-Mechanical High Cycle Fatigue*. Eur. J. Mech A/Solids, Vol. 26, pp. 909-935, 2007.

[21] R. DESMORAT, F. RAGUENEAU, H. PHAM - *Continuum Damage Mechanics for Hysteresis and Fatigue of Quasi-Brittle Materials and Structures*. International Journal of Numerical and Analytical Methods for Geomaterials, vol. 31, p. 307-329, 2007.

[22] R. DESMORAT, S. CANTOURNET - *Modeling Micro-Defects Closure Effect with Isotropic/Anisotropic Damage.* International Journal of Damage Mechanics, vol. 17, pp. 65–96, 2008.

[23] R. DESMORAT, S. OTIN - *Cross-Identification Isotropic/Anisotropic Damage and Application to Anisothermal Structural Failure*. Engineering Fracture Mechanics, 75(11), p. 3446-3463, 2008.

[24] C. DOUDARD, S. CALLOCH, P. CUGY, A. GALTIER, F. HILD - *A Probabilistic Two Scale Model for High-Cycle Fatigue Life Prediction*, Fatigue Fract. Engng Mater Struct, 28, p. 279-288, 2005.

[25] J. DUFAILLY, J. LEMAITRE - *Modeling Very Low Cycle Fatigue.* International Journal of Damage Mechanics, 4, p. 153-170, 1995.

[26] C. ERNY, D. THEVENET, J.Y. COGNARD, M. KÖRNER - *Fatigue Life Prediction of Welded Ship Details*. Marine Structures, 25, p. 13-32, 2012.

[27] J.D. ESHELBY - *The Determination of the Elastic Field of an Ellipsoidal Inclusion, Related Problems*. Proc. Roy. Soc., London, vol. A241, p. 376, 1957.

[28] A. FATEMI, L. YANG - *Cumulative Fatigue Damage and Life Prediction Theories: a Survey of the State of the Art for Homogeneous Materials.* International Journal of Fatigue, vol. 20, pp. 9-34, 1998.

[29] L. FLACELIERE, F. MOREL, A. DRAGON - *Coupling Between Mesoplasticity and Damage in High-Cycle Fatigue*. International Journal of Damage Mechanics, 16, pp. 473-509, 2007.

[30] D. FRANÇOIS, A. PINEAU, A. ZAOUI - *Comportement mécanique des matériaux – élasticité et plasticité*. Hermès Paris, 1992.

[31] F. GALLERNEAU, J.L. CHABOCHE - *Fatigue Life Prediction of Single Crystals for Turbine Blade Applications*. International Journal of Damage Mechanics, 8(4), pp. 404-427, 1999.

[32] A. GANCZARSKI, L. BARWACZ - *Low Cycle Fatigue Based on Unilateral Damage Evolution*. International Journal of Damage Mechanics, 16, pp. 159-177, 2007.

[33] V. GOMEZ - *Etude en fatigue biaxiale à haute température d'alliages métalliques pour disques de turbomachines aéronautiques*. PhD thesis, Univ. Paul Sabatier, 2001.

[34] C.T. HUA, D.F. SOCIE - *Fatigue Damage in 1045 Steel under Constant Amplitude Biaxial Loading*. Fatigue Eng. Mat. Struct., 7, 165–179, 1984.

[35] E. KRÖNER - *On the Plastic Deformation of Polycrystals*. Acta Metall., vol. 9, pp. 155-161, 1961.

[36] P. LADEVÈZE, J. LEMAITRE, 1984 - *Damage Effective Stress in Quasi unilateral Conditions*. 16th International Congress of Theoretical and Applied Mechanics, Lyngby, Denmark.

[37] D.B. LANNING, T. NICHOLAS, G.K. HARITOS - *On the use of Critical Distance Theories for the Prediction of the High Cycle Fatigue Limit Stress in Notched Ti-6Al-4V*. International Journal of Fatigue, vol. 27, pp. 45-57, 2005.

[38] N. LAUTROU, D. THEVENET, J.Y. COGNARD - *A Fatigue Crack Initiation Approach for Naval Welded Joints*. Oceans 2005 - Europe, 2, p. 1163 - 1170, 2005

[39] H.H.E. LEIHOLZ - *On the Modified S-N Curve for Metal Fatigue Prediction and its Experimental Verification*. Engineering Fracture Mechanics, vol. 23, pp. 495-505, 1986.

[40] J. LEMAITRE, J.L. CHABOCHE - *A Non-Linear Model of Creep-Fatigue Damage Cumulation and Interaction*. Symposium IUTAM, Gothenburg, 2-6 september 1974.

[41] J. LEMAITRE, A. PLUMTREE - *Application of Damage Concepts to Predict Creep-Fatigue Failures*. Journal of Engineering Materials Technology, vol. 101, pp. 284–292, 1979.

[42] J. LEMAITRE, J.L. CHABOCHE - *Mécanique des matériaux solides*. Dunod 1985, Mechanics of solid materials (3rd Edition 2009), Oxford University Press, 1991 (english translation).

[43] J. LEMAITRE - *A course on Damage Mechanics*. Springer Verlag, 1992.

[44] J. LEMAITRE, I. DOGHRI - *Damage 90: a Post-Processor for Crack Initiation*. Comp. Methods Appl. Mech. Engrg. 115: 197-232, 1994.

[45] J. LEMAITRE, J.P. SERMAGE, R. DESMORAT - *A two Scale Damage Concept Applied to Fatigue*. International Journal of Fracture, vol. 97, pp. 67-81, 1999.

[46] J. LEMAITRE, R. DESMORAT - *Engineering Damage Mechanics : Ductile, Creep, Fatigue and Brittle Failures*. Springer, 2005.

[47] Z.X. Li, F.F. Jiang, Y.Q. Tang - *Multi-Scale Analyses on Seismic Damage and Progressive Failure of Steel Structures*. Finite Elements in Analysis and Design, 48, p. 1358-1369, 2012.

[48] D.L. MCDOWELL - *Damage Mechanics and Metal Fatigue: A Discriminating Perspective*. International Journal of Damage Mechanics, 8, pp. 376-403, 1999.

[49] S.S. Manson, M.H. Hirschberg 1964 - *Fatigue: An Interdisciplinary Approach.* Syracuse University Press, Syracuse, N.Y.

[50] A. MARMI, A HABRAKEN, L. DUCHENE - *Multiaxial Fatigue Damage Modelling at Macro Scale of Ti6AL4V Alloy*. International Journal of Fatigue, 31, 2031-2040, 2009.

[51] V. MONCHIET, E. CHARKALUK, D. KONDO - *Plasticity-Damage Based Micromechanical Modelling in High Cycle Fatigue*. C. R. Mecanique, 334, p. 129-136, 2006.

[52] F. MOREL - *A Critical Plane Approach for Life Prediction of High Cycle Fatigue under Multiaxial Variable Amplitude Loadingn.* International Journal of Fatigue vol. 22(2), pp. 101-119, 2000.

[53] T. NICHOLAS - *Critical Issues in High Cycle Fatigu*e. International Journal of Fatigue, 21(1), pp. 221-231, 1999.

[54] M.H. PAAS, P.J.G. SCHREURS, W.A.M. BREKELMANS - *A Continuum Approach to Brittle and Fatigue Damage: Theory and Numerical Procedures*. Int. J. Solids Struct., 30, 579–599, 1993.

[55] I.V. PAPADOPOULOS - *A High-Cycle Fatigue Criterion Applied in Biaxial and Triaxial Out-of-Phase Stress Conditions*. Fatigue & Fracture of Engineering Materials & Structures vol. 18(1), pp. 79-91, 1995.

[56] I.V. PAPADOPOULOS, P. DAVOLI, C. GORLA, M. FILIPPINI, A. BERNASCONI - *A Comparative Study of Multiaxial High-Cycle Fatigue Criteria for Metals*. International Journal of Fatigue Vol. 19(3), pp. 219-235, 1997.

[57] J.P. SERMAGE, J. LEMAITRE, R. DESMORAT - *Multiaxial Creep Fatigue under Anisothermal Conditions.* Fatigue and Fracture of Engng Mater. & Struct., 23(3), pp. 241 - 252, 2000.

[58] M. SAUZAY - *Effet de surface en fatigue polycyclique*. PhD thesis Univ. Paris 6, 2000.

[59] G. SINES - *Behavior of Metals under Complex Static and Alternating Stresses*. In: Sines, G., Waisman, J.L. (Eds.). McGraw-Hill, New York, pp. 145–169, 1959.

[60] R. SMITH, P. WATSON, T. TOPPER - *A Stress-Strain Function for the Fatigue of Metals*. Journal of Mat., vol. 5, pp. 767-778, 1970.

[61] K. THEPVONGSA, Y. SONODA, H. HIKISAKA - Journal of Applied Mechanics, 6, p. 1227-1234, 2003.

AUTHORS

Rodrigue Desmorat. A former student of the Ecole Normale Supérieure de Cachan (ENSC) and Research Associate in Mechanics, Rodrigue Desmorat, 47, has been an Assistant Professor at the University Paris 6. Since 2002, he has been a full Professor at ENSC and carries out research at the LMT-Cachan in the field of Damage Mechanics. He is the co-author of two books.

Pierre Gaborit. A graduate from Arts et Métiers ParisTech and Karlsruher Institut für Technologie in Mechanical Engineering, Pierre Gaborit, 27, carried out his PhD research at the LMT-Cachan (Ecole Normale Supérieure de Cachan). This work will be defended in the second half of 2015. Since July 2014 he has been working as a Material Engineer for forged products at Snecma.

Alban du Tertre. A graduate from the ECAM Lyon, Alban du Tertre, 40, joined the Space Engine Division of Snecma at Vernon (F) in 1999. He was successively in charge of thermomechanical computations and of powder metallurgy component development in the cryogenic turbo-pump department. He then managed various research and methodological projects, mainly linked to HCF and LCF fatigue applied to rocket engine components, in cooperation with the LMT Cachan, ONERA, the Pprime Institute, etc. Promoted to Expert status in 2014, he now works as a mechanical development project manager in the combustion device design office.

M. Kaminski, F. Laurin, J.-F. Maire
(ONERA)
C. Rakotoarisoa
(Snecma, Safran Group)
E. Hémon
(Safran Composites, Safran Group)

E-mail: Myriam.Kaminski@onera.fr

DOI : 10.12762/2015.AL09-06

Fatigue Damage Modeling of Composite Structures: the ONERA Viewpoint

The aim of this paper is to present the fatigue damage modeling approach developed at ONERA for the fatigue life prediction of composite materials and structures. This paper is divided into five sections. The first one explains why the already developed and validated methods for fatigue life modeling of metals and alloys cannot be directly applied to composite materials. Thus, the proposal of an efficient fatigue model for composite materials necessitates a good understanding of the specific damage mechanisms that occur under static and fatigue loadings of composites. These damage mechanisms are detailed in the second section. Then, the next section presents the different types of models reported in the literature; among them, the progressive damage models, to which special attention will be paid. Finally, structural simulations and constant-life diagrams will be considered in the last sections.

Introduction

The introduction of composite materials in a wide range of structural components requires engineers and research scientists to reconsider fatigue loading as a factor inducing failure, even for structures where fatigue was not traditionally considered as an issue. Up to now, composite materials were considered as fatigue insensitive and one of the ideas implied behind this statement was that the conventional loading levels applied to components were far too low to initiate any local damage that could induce catastrophic failure under repeated loading. Then, the requirement for no growth of defects, i.e., manufacturing defects and accidental damage, has always been assumed to be sufficient for the design of composite airframes subjected to fatigue loading. However, this assertion has been questioned by the aerospace industrial sector. Indeed, with the continuous improvement of composite design methods during the last decades and the imperative of structural mass minimization for recent airliners, during in-life service composite structures are subjected to loadings increasingly closer to their static strength. To be more specific, increasing the operational loads in the structures by reducing the static strength margins down to their minimum values does not make fatigue critical for composite structures [68]. However, this assumption is likely to lead to situations where more unstable fatigue cracks develop in areas where out-of-plane stresses may be found. Fatigue is also inherently an important issue in rotating composite structures. Applications are as diverse as rotor blades for wind turbines and helicopters, marine propellers, flywheels, paper machine rolls, etc. Matrix fatigue degradation and fiber failure are the main failure modes and they should be avoided through sensitive design. An iterative process for the definition of different prototypes is usually required and, in order to reduce cost and time for product development, accurate fatigue behavior simulation is critical for composite structural components or structures.

Consequently, fatigue of composite structures is of growing interest and leads industrials to develop accurate fatigue modeling, as well as a better prediction of delamination in laminates during fatigue loading. Since fatigue of metallic materials is a well-known phenomenon, first attempts to account for fatigue in composites consisted in adapting to composites, the already existing methods for metallic materials [68]. Unfortunately, the situation regarding the fatigue behavior of composite materials is different from that of metals and alloys. The methods developed for metallics are unsuitable and strongly not recommended for composites, as will be explained in the first section of this paper. Thus, in order to develop fatigue models for composite materials and to achieve a more optimized design and selection of materials, it is first necessary to understand the damage mechanisms and failure modes to propose models suitable for either conventional laminates or woven composite structures. However, as mentioned in [5], it is "difficult to get a general approach of the fatigue behavior of composites materials, including polymer matrix, metal matrix, ceramic matrix composites, elastomeric composites, Glare, short fiber reinforced polymers and nano-composites".

Research on the fatigue performance of advanced composites started at the beginning of the 70s, just after their introduction and first applications. A lot of experimental work has been performed over the last four decades for fiber-reinforced composites and very comprehensive databases have been constructed, particularly concerning wind power applications [34]. Along with these experimental works, theoretical models have been developed to predict damage accumulation and fatigue life for fiber-reinforced composites with various stacking sequences and fiber- and matrix-types under loading conditions that vary from constant-amplitude loading to spectrum loading [4, 20, 28, 38, 57, 58, 77]. A classification of these models will be presented further in this paper. Despite all of these studies, research efforts should be continued to meet the challenge of developing models with a more generalized applicability in terms of loading conditions and of material selection.

How should the issue of fatigue be addressed for composite materials?

Fatigue in materials is caused by repeated loading and unloading cycles to maximum stresses lower than the ultimate tensile strength of the material. Cycling loading and the different loading regimes are characterized by the R-ratio $(R=\sigma_{min}/\sigma_{max})$ as reported in figure 1.

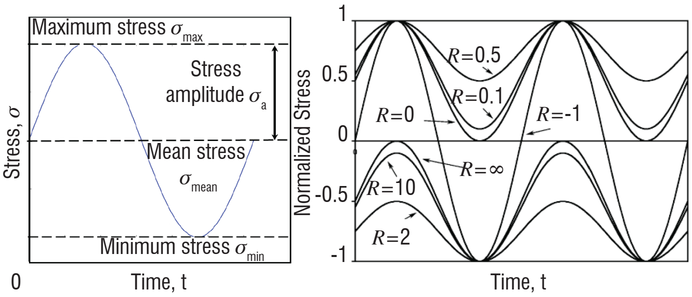

Figure 1 - Sinusoidal loading and relevant terminology of different loading R-ratios from Post et al.[59]

Metals vs. composite materials

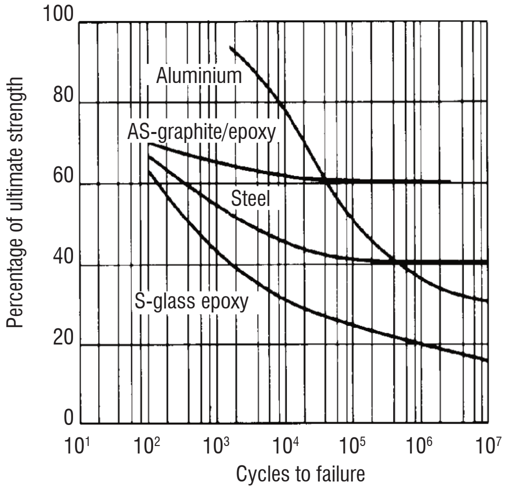

Figure 2 - Comparison of fatigue strengths of graphite/Epoxy, steel, fiberglass/Epoxy and aluminum from Weeton et al. [91]

As mentioned previously, metals and composites behave differently under fatigue loading. Bathias [5] devoted an entire paper to the comparison of fatigue damage between metals and composite materials, and pointed out some important differences between metals and high performance composites. The main differences are summarized as follows. Composite materials exhibit a better resistance to fatigue, compared to metals. The fatigue ratio, S_D/UTS, between the fatigue strength, S_D, in tension-tension $(0<R<1)$ and the ultimate static tensile strength, UTS, is always higher than 0.4 and can reach 0.9 for CFRP (Carbon Fiber Reinforced Polymer). These values are comparable to those found for metals, i.e., less than 0.5, and only 0.3 for aluminum alloys (Figure 2).

However, despite their high fatigue performances, composites are not totally sheltered from fatigue damage, due to, essentially, the variety of configurations (types of fiber, resin and lay-up) that can result in different endurances. Figure 3 shows a comparison of various architectures with regard to fatigue performance.

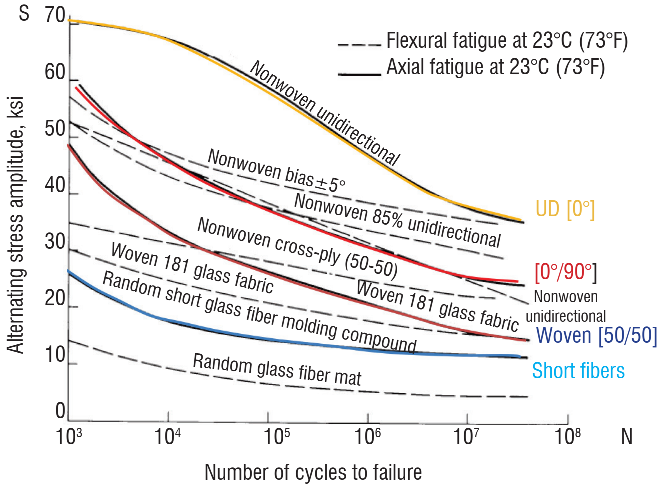

Figure 3 - Comparative fatigue strengths of a same resin/Glass composite with various fiber architectures (UD, woven, laminates) from Weeton et al. [91]

A difficulty with composite materials is that increasing fiber resistance or matrix toughness, or even improving fiber/matrix bonding, does not always result in an improved fatigue performance, i.e., a longer fatigue life and a higher fatigue ratio [40].

The fatigue resistance of composite materials is much lower in compression–compression $(R>1)$ than in tension-tension $(0<R<1)$, whereas it is the contrary for metallic alloys. Tension-compression fatigue is more deleterious than tension-tension fatigue and is the most detrimental loading condition for fatigue of composites. Note that the ratio S_D/UTS under compressive loading can be as low as 0.3 for some composite materials. Under bending, the behavior of composite materials is difficult to determine because of the multitude of types of damage that occur (transverse cracks due to tensile loading, delamination, fiber kinking due to compression loading). As a result, the fatigue of composite materials is a complex phenomenon. For instance, even if the compressive strength of a composite is generally lower than the tensile strength and the composite is less damaged under compression loading, an effect of the tension damage on the compressive strength can be observed.

The comparison between damage accumulation in composite materials and in homogeneous materials, as a function of the number of cycles, is schematically described in figure 4. A relatively large part of the total fatigue life in metals is devoted to the stage of gradual and invisible deterioration (i.e., mesoscopic scale damage, such as: dislocation cells, persistent slip bands (PSB), etc.). There is no significant reduction of stiffness in metals during the fatigue process. The final stage of the process starts with the formation of small cracks, which are the only form of observable damage. These cracks grow gradually and coalesce quickly to produce a large crack leading to final failure of the structural component [86].

During fatigue of composites, damage starts very early, after only a few hundred loading cycles or even during the first loading cycle for a high stress level. This early damage is followed by a second stage of very gradual degradation of the material, characterized by a progressive reduction of the apparent stiffness. More severe types of damage appear in the third stage, such as fiber breaks and unstable delamination growth, leading to an accelerated decline and, finally, to catastrophic failure [86].

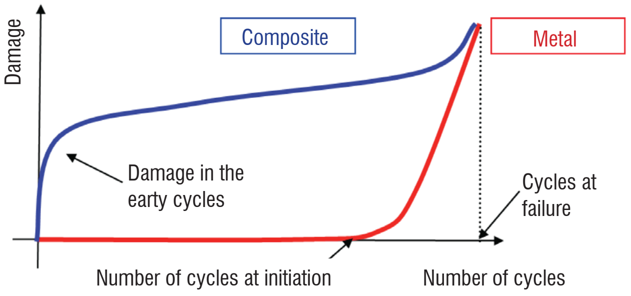

Figure 4 - Comparison of the damage evolution as a function of the number of cycles for composites and metals.

All of these differences between metals and composite materials lead to developing specific methods for modeling the fatigue behavior of each material. Usually, methods for predicting the damage initiation are sufficient for metals, whereas it is necessary to follow the evolution of the different damage mechanisms in composite materials and to be able to estimate the effect of these different damage modes on the material behavior and failure (residual performances). Consequently, methodologies developed for metals are not suitable for composite materials. In order to develop specific methods for composites, it is thus imperative to understand their fatigue damage mechanisms.

Fatigue damage mechanisms in composite materials

Generally, failure of composites under static loading is due to a combination of various interacting mechanisms leading to the final rupture. In the case of laminates, as well as in a single lamina, different kinds of damage mechanisms can be found. Failure usually originates at the interface between matrix and reinforcement (i.e., debonding), especially on defects, which are always present in composites, mainly due to the manufacturing process. Other common types of failure modes are: matrix cracking, fiber rupture, delamination (in laminates) and buckling (in compression).

During fatigue, the first stage of deterioration of continuous fiber-reinforced polymers is characterized by the formation of a multitude of microscopic cracks and other forms of damage, such as fiber/matrix interface debonding and fiber pull-out from the matrix. As mentioned earlier, during fatigue, damage starts very early (Figure 5 a-b). During this initial loading period (Stage 1), there is generally a small drop in stiffness associated with the formation of damage. Then, there is a second stage of very gradual degradation of the material, where the stiffness reduces progressively and where damage seems to increase slowly and linearly. More serious types of damage appear in the third stage, such as fiber breakage and unstable delamination growth, leading to an accelerated decline with an increasing amount of damage and finally catastrophic failure [23]. Schulte et al. [71-73] first reported this three-stage stiffness reduction and it has, since then, been observed in many different types of composite materials, and also in woven composites [22, 93].

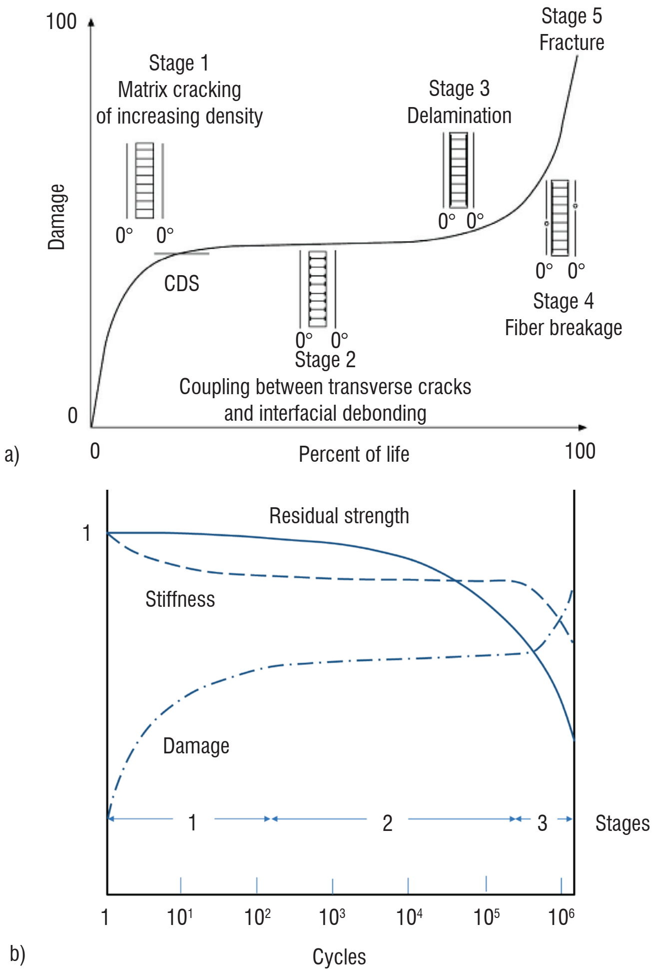

Figure 5 - a) Fatigue crack growth in cross-ply laminates and b) the three characteristic stages of fatigue damage in composites from Reifsnider [62]

Several authors have shown that the observed damage mechanisms are identical for laminates under static and fatigue loadings [66, 85, 90]. However, the crack evolution laws are different and the damage threshold in fatigue is lower than the damage threshold during static loading [7, 8, 42].

Another type of composites, such as woven-fabric composites, is showing growing interest and is used in advanced structural applications due to its inherent advantages. Indeed, the advantages conferred by the woven reinforcements compared to fiber lay-ups are an easier manipulation and ply stacking during composite manufacturing, good drapability properties that allow the use of woven reinforcements in complex mold shapes, increased impact resistance and damage tolerance of the composite material and delamination resistance capability owing to the presence of fibers along the thickness direction. Along with these advantages, composite materials based on woven fabric reinforcements achieve high stiffness and strength, comparable with those obtained through traditional fiber reinforcements.

In 2D woven composites (fabric formed by interlacing the longitudinal yarns (warp) and the transverse yarns (weft)), such as plain, twill or satin), four types of damage mechanisms occur under static and fatigue loadings: intra-yarn cracks in yarns oriented transversely to the loading direction, inter-yarn decohesion between longitudinal and transverse yarns, fiber failure in longitudinal yarns and yarn failures [9, 11, 52, 54, 82, 85].

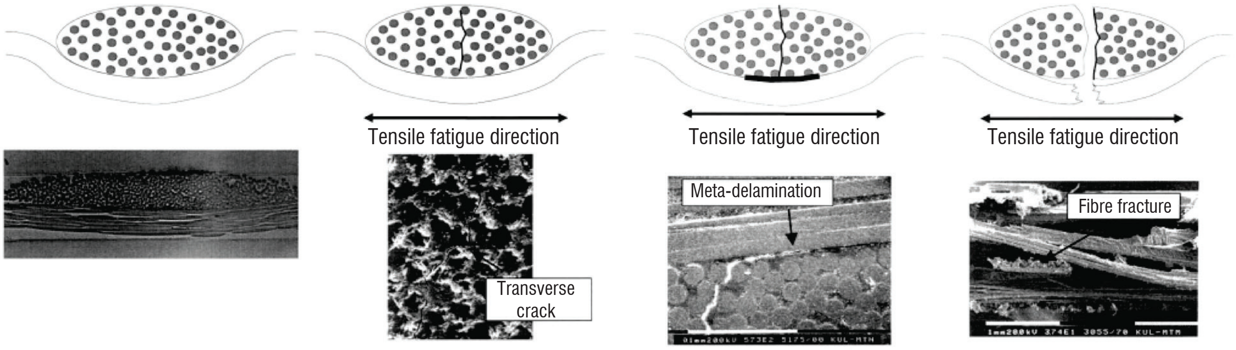

a) No fatigue failure b) Crack in a transverse yarn c) Meta-delamination d) Fibre fracture at longitudinal yarns

Figure 6 - Scheme of the tensile fatigue damage development in woven fabric composites, subjected to a tension–tension fatigue loading in the weft direction from Pandita et al. [54].

A damage scenario consisting in four stages can be deduced from these works (Figure 6) and has been proposed by Pandita et al. [54]. Under fatigue loading, for a plain-weave fabric composite subjected to a maximum tensile fatigue load of 0.5 of the static strength in the on-axis direction, there is no or very little fatigue damage in the first stage (Figure 6a). In a second stage, fatigue damage consists of fiber-matrix debonds and matrix cracks in transverse yarns, leading to a continuous transverse crack (Figure 6b). This transverse crack subsequently grows either into a matrix-rich area or is deflected into the longitudinal fiber bundle within the same layer, a phenomenon called 'meta-delamination' (Figure 6c). It constitutes the third stage, characterized by a saturation of intra-yarn cracks. The propagation of the transverse cracks proceeds very slowly. The fourth stage (Figure 6d) consists in the separation between the longitudinal yarns. Finally, in 2D woven fabrics, static and fatigue damage mechanisms are similar, the only difference concerning the damage evolution laws.

The geometry of 3D or interlock woven composites and composites with braided reinforcement is so complex that it is generally difficult to clearly separate the occurring damage mechanisms: microcracking, interface failure, void initiation and void growth. A major difference, compared to composite laminates or 2D woven composites, is that delamination is impeded. During static loading, the observed damage mechanisms are intra-yarn cracks in transverse yarns, inter-yarn debonding between longitudinal and transverse yarns, fiber failure in longitudinal yarns and failure of the yarns. These 3D woven composites, which have very good mechanical properties - improved through-thickness elastic properties, resistance to delamination and to impact damage - present similar static and fatigue mechanisms, as observed experimentally [31, 69].

To summarize, while damage mechanisms are really different between UD laminates and woven composites, in both cases, these damage mechanisms are comparable under either a static or a fatigue loading. The only change is in the damage evolution laws.

Fatigue damage modeling

State of the art

As mentioned earlier, fatigue studies started mainly with experimental campaigns during the 70s in the aerospace field to demonstrate that fatigue was not a real issue at that time. Some experimental campaigns are still conducted nowadays. For example, an extensive material testing program, the OPTIMAT research program [34], was conducted recently over 3000 individual tests over four years. Testing has been focused on the mechanical properties of the composite materials commonly used in modern wind turbine blades, specifically epoxy GFRP (Glass Fiber Reinforced Composite). However, experimental tests are expensive and it is difficult to cover all of the configurations.

In order to reduce the number of tests for predicting composite fatigue failure, composite fatigue modeling is required. An interesting article written by Degrieck and Van Paepegem [17] focuses on the existing modeling approaches for the fatigue behavior of fiber reinforced polymers and gives a comprehensive survey of the most important modeling strategies for fatigue behavior. A more recent paper written by Sevenois and Van Paepagem [76] gives an overview of the existing techniques for fatigue damage modeling of FRPs with woven, braided and other 3D fiber architectures. The aim of the present paper is not to give an in-depth discussion of the fatigue models; thus, the interested reader will be asked to refer to references [17, 76]. In the first reference, the authors justify the classification, currently made by Sendeckyj et al. [75], concerning the large number of existing fatigue models for composite laminates. This classification consists of three major categories: fatigue life models (empirical/semi-empirical models), which do not take into account the actual degradation mechanisms, but use S-N curves or Goodman-type diagrams and introduce a fatigue failure criterion; phenomenological models for residual stiffness/strength; and, finally, progressive damage models (or mechanistic models), which use one or more damage variables related to observable damage mechanisms (such as transverse matrix cracks, delamination). Note that this classification has been recently slightly modified for fatigue damage modeling techniques for FRP (Fiber Reinforced Polymers) with woven, braided or other 3D fiber architectures [76], but the classification reported in the following refers to [17].

Empirical or semi empirical models quantify failure or determine the composite fatigue life based solely on a fixed loading condition (i.e., the stress state). These experimentally based models are all specific to certain types of composite materials and do not consider specific damage mechanisms in their formulation. They require extensive and expensive experimental campaigns and are difficult to extend towards more general loading conditions. This methodology is traditionally used by industrialists. Various models can be found in the literature [12, 19, 20, 28, 63]. As shown in figure 7, (semi) logarithmical formulations can be used as well as numerous other S-N formulations; some of them are reported in figure 7.

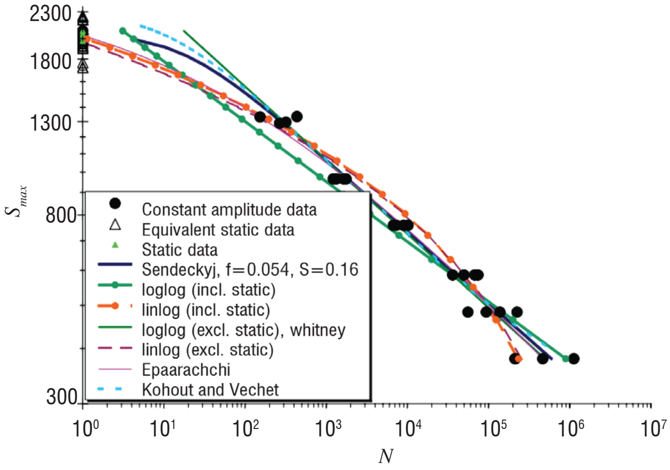

Figure 7 - Various constant amplitude S-N curve fits for $(0°)_8$ glass/epoxy, R=0.1 [50]

Phenomenological models describe the fatigue behavior of the composite through the evolution of macroscopic properties, such as stiffness [39, 56, 81] and strength [16, 36, 65, 78]. The loss of these macroscopic properties is usually described. Residual strength models possess a natural failure criterion (Figure 8): if the residual strength falls to about the same level as the externally applied stress, then, the material fails [26]. However, it necessitates destructive tests. Empirical models and residual strength models cannot be used to simulate the stiffness degradation during fatigue life because both S-N fatigue life methodology and residual strength approach do not take into account the loading history, i.e., the successive damage states, the continuous redistribution of stress and the reduction of stress concentrations that appear during the gradual degradation of a fiber-reinforced composite in a structural component. Residual stiffness models describe the degradation of the stiffness properties due to fatigue damage in terms of macroscopic variables, but they exhibit much less statistical scatter than residual strength models.

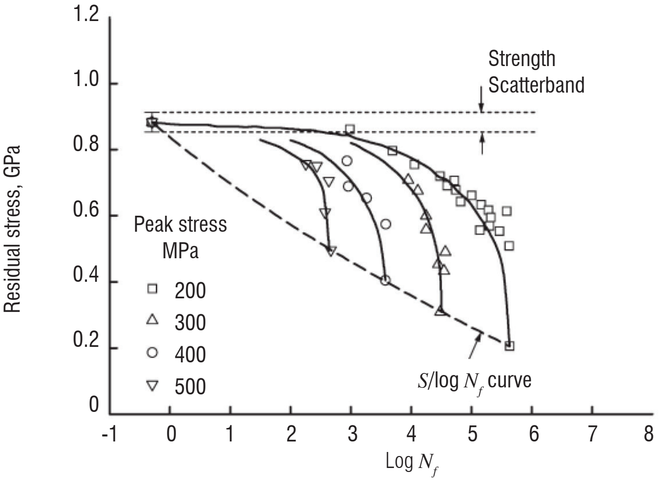

Figure 8 - Residual strength curves for 0/90 GRP laminate samples subjected to fatigue cycling at an R ratio of 0.1 and various stress levels [24]

Progressive damage models, which use one or more damage variables related to measurable effects of damage (interface debonding, transverse matrix cracks, delamination size, etc.), are claimed as the most promising models because they quantitatively account for the damage accumulation in the composite structure. Degrieck and Van Paepegem [17] subdivide progressive damage models into two classes:

- Damage models that predict the damage growth as such (e.g., number of transverse matrix cracks per unit length, size of the delaminated areas). These models consider one specific damage mechanism and determine the physical change in damage with increasing loading cycles. They are typically of the form of the well-known Paris' law for crack propagation in homogeneous materials (i.e., da/dN). References, essentially on fatigue of composite laminates, can be found in [6, 21, 30, 70].
- Models that correlate the damage growth with the residual mechanical properties (stiffness/strength). One of the major causes of the stiffness degradation is distributed matrix cracking, and such a type of progressive damage suggests the use of a continuum damage model to describe the material behavior [41, 43, 46, 83]. These models typically use Finite Element models to simulate the damage progression and some of them have been extended to predict the fatigue life of a structural component. Among the various studies on laminates, different contributions must be quoted: [1, 2, 13, 44, 45, 51, 67, 74, 79, 80, 84]. Most of these works concern fatigue of laminate composites. A few research groups deal with fatigue of woven composites. Among them, Hochard et al. [32, 33] developed a fatigue damage approach as a combination of a static damage model and a cumulative damage evolution law based on a thermodynamic approach. Modeling both static and fatigue loadings with the same model is allowed by the use of a non-linear cumulative law that describes the damage evolution according to the maximal load and the amplitude of the cyclic loading. This model is based on a damage model developed for UD carbon/epoxy laminates [55]. Thanks to the assumption consisting in replacing the woven ply by two stacked unidirectional virtual plies, this generalized model can be used to simulate the mechanical behavior of various unbalanced woven plies, from quasi-unidirectional to balanced woven plies. This model has been applied with success to a 5-harness satin weave glass/epoxy laminate without stress concentration. Nevertheless, a plane stress assumption is made and this model cannot be directly applied to thick 3D woven composites.

A damage model has also been proposed by Van Paepagem et al. [87, 88] and is based on anisotropic damage evolution functions with separate terms for the damage initiation, the damage growth and the final progressive damage evolution. This model can simulate stiffness damage, stress redistribution and accumulation of permanent strain. The use of a modified Tsai-Wu static failure criterion has been proposed. The fatigue damage model has been applied to displacement-controlled bending fatigue experiments of plain-weave glass/epoxy specimens and good agreement was found between predicted and simulated specimen deformation and applied force.

These two models have been developed for 2D woven composites and not for 3D woven interlock composites. The plane stress assumption cannot be applied [61], since these composites are relatively thick.

An important feature of these degradation approaches is that they enable variable amplitude loadings to be dealt with, since they can take into account a change of stress state during loading. Actually, traditionally, fatigue characterization of a material is performed under constant amplitude sinusoidal loading and most experimental studies of variable amplitude loading in composite materials have focused on loading that consists of two or more constant amplitude blocks with two to four stress levels and R-ratios [27, 53, 92]. Nevertheless, the block loading tests are not representative of realistic loading situations and may not even generate the same type of damage state in the material. The majority of the models presented in the literature have only been applied to constant amplitude loading and block loading with a few stress levels. The reader is referred to a comparative study presented in [59] that evaluates different models in terms of their predictive capability under more realistic spectrum loading cases of interest to the wind turbine and naval architecture industries.

ONERA fatigue damage modeling of 3D woven interlock PMC and CMC composites

ONERA has been working for years on progressive damage models under static loading of 3D polymeric and ceramic woven composites (ONERA Damage Model (ODM) [46, 48]). These two models accurately describe the static behavior of either 3D woven polymer matrix composites (PMC) or ceramic matrix composites (CMC). Recently, they have been extended to fatigue loadings [29, 61]. As mentioned previously, in the case of interlock woven PMC, the same damage mechanisms occur during monotonic and fatigue loadings, but their damage evolution laws differ. These damage mechanisms are described using damage variables that describe the effects of damage on the behavior in the three main directions of the woven composite. Then, a cumulative damage d_k, per k mechanism (k=1, 2 or 3), is defined by adding two terms: one part is due to the monotonic loading d_k^{Mon} and the other one is governed by fatigue loading d_k^{Fat}. The monotonic damage law depends on the driving forces y_k which are themselves a quadratic form of strain: $y_k = fct(\varepsilon)$. This leads to a scalar (instead of a tensor) formulation, which is easier to analyze and to generalize to multiaxial loadings. The matrix damage driving forces for monotonic loading are also assumed to drive the matrix damage during fatigue loading:

$$d_k = d_k^{Mon}\left(\sqrt{y_{Max}}\right) + d_k^{Fat}\left(y_{Max},\, R_{yk}\right) \tag{1}$$

The cyclic damage law, where N is the number of cycles, includes the description of the matrix damage evolution during cyclic loading:

$$\frac{\delta d_k^{\ddot{u}}}{\delta N} = \left(d_{\infty(k)} - d_k\right)^{\gamma_k} \left(\frac{\left\langle \left(1 - \ddot{u}_{yk}\right)^{\beta_k} {}_{Max(k)} - {}^{\ddot{u}}_{0(k)} \right\rangle_+}{y_{c(k)}^{\ddot{u}}} \right)^{\delta_k} \tag{2}$$

$$R_{yk} = \begin{cases} \dfrac{y_{min(k)}}{y_{Max(k)}} & if\ y_{Max(k)} > 0 \\ 0 & else\, if \end{cases} \tag{3}$$

R_y evolves between 0 and 1 since the driving forces are always positive. Moreover, this specific ratio definition is very convenient to deal with multiaxial loadings. Note that when the stress ratio is negative $R_\sigma < 0$, the corresponding driving force ratio is null (because $y_{min} = 0$ when $R_\sigma < 0$). Rakotoarisoa [61] does not take into account the behavior for compressive loadings in the model; consequently, the damage evolution is only possible for tension (static or fatigue) loadings (thus, only for positive stress ratios). $y_{0(k)}^{Fat}$ is the fatigue damage threshold, $y_{Max(k)}$ is the maximal driving force (maximum over one cycle) and $y_{c(k)}^{\ddot{u}}$, γ_k, β_k, δ_k are model parameters. At saturation, the damage reaches the saturation value $d_{\infty(k)}$. This model has been validated on smooth specimens and a good agreement was found between experimental data and simulation. Variable amplitude loadings can be described with this model, even creep loading cases, except spectral loading, in which all cycles have a different load evolution. To address these complex loadings, a 3D kinetic damage model for woven PMC composites, i.e. with a rate form written damage evolution laws ($\partial d / \partial t = \ldots$), is currently under development in collaboration with LMT-Cachan [3] based on the ODM-PMC model. A specific feature of the proposed damage law is that it only introduces one damage variable per mechanism, but with two contributions (a monotonic contribution and a fatigue contribution). The kinetic damage evolution law can be applied to different kinds of loading (monotonic, fatigue, random) and is also mean stress dependent [18]. The final damage evolution law recovers the initial cumulative damage ODM-PMC model exactly in cases of monotonic and creep loadings.

Concerning the yarn failure (due to fiber failures), even though the fibers are usually assumed to be insensitive to fatigue loadings [82], matrix damage leads to load transfer to the fiber bundles leading to fiber failure, thus inducing a reduction in the effective strength of the fiber bundles. Finally, fiber bundle fracture is used as a criterion for the evaluation of fatigue lifetime, as well as residual strength. The rupture is induced by a sudden and unstable multiplication of fiber failures in the yarns. These yarns can be considered as the critical element in the sense of Reifsnider [64], since their failure defines the composite failure. There is no first sign of damage for the yarn (loss of modulus) because early failures are limited and spatially dispersed.

Fatigue of CMC woven composites is also a new subject of interest in the community [15, 60]. CMC woven composites can be used in the aerospace industry, because of their low mass density and good mechanical properties at high temperature, since they are protected against oxidation by a self-healing matrix at temperatures higher than 650°C. A fatigue model, based on the ODM model specifically devoted to CMC woven composites (five damage variables, since damage is oriented by the loading [47], instead of three variables for PMC woven composites for which damage is mainly oriented by the microstructure) has been developed at ONERA [29, 49]. The lifetime of the material is determined through a macroscopic mechanical model and a physicochemical model, which is time-dependent. The procedure has been validated considering SiC/SiC specimens under fatigue loadings and subjected to different kinds of environment, i.e., pressure (oxygen and water) and temperature.

Structural simulation

These two models have been implemented in a finite element code (ZeBuLoN), in order to (i) keep track of the continuous stress redistribution (the simulation requires the complete path of damage states to be followed) and (ii) to perform fast and efficient finite element simulations.

Figure 9 presents the modeling strategy to determine the fatigue life and residual strength of interlock woven PMC composites. A first static analysis is performed with the quasi-static model to verify whether the specimen has failed or not. If it is not the case, a first set of cycles is applied. The cumulative damage law allows the resulting matrix damage variables to be calculated. Then, before ensuring that the bundle failure criterion is not attained, in order to perform the next block of cycles, the strain fields, fiber bundle fracture variables and matrix damage driving forces are updated by simulating one cycle (shown in red in figure 9) with the quasi-static model. To reduce the computational costs of the model, the updating is performed at three characteristic load levels only: maximum and minimum load are

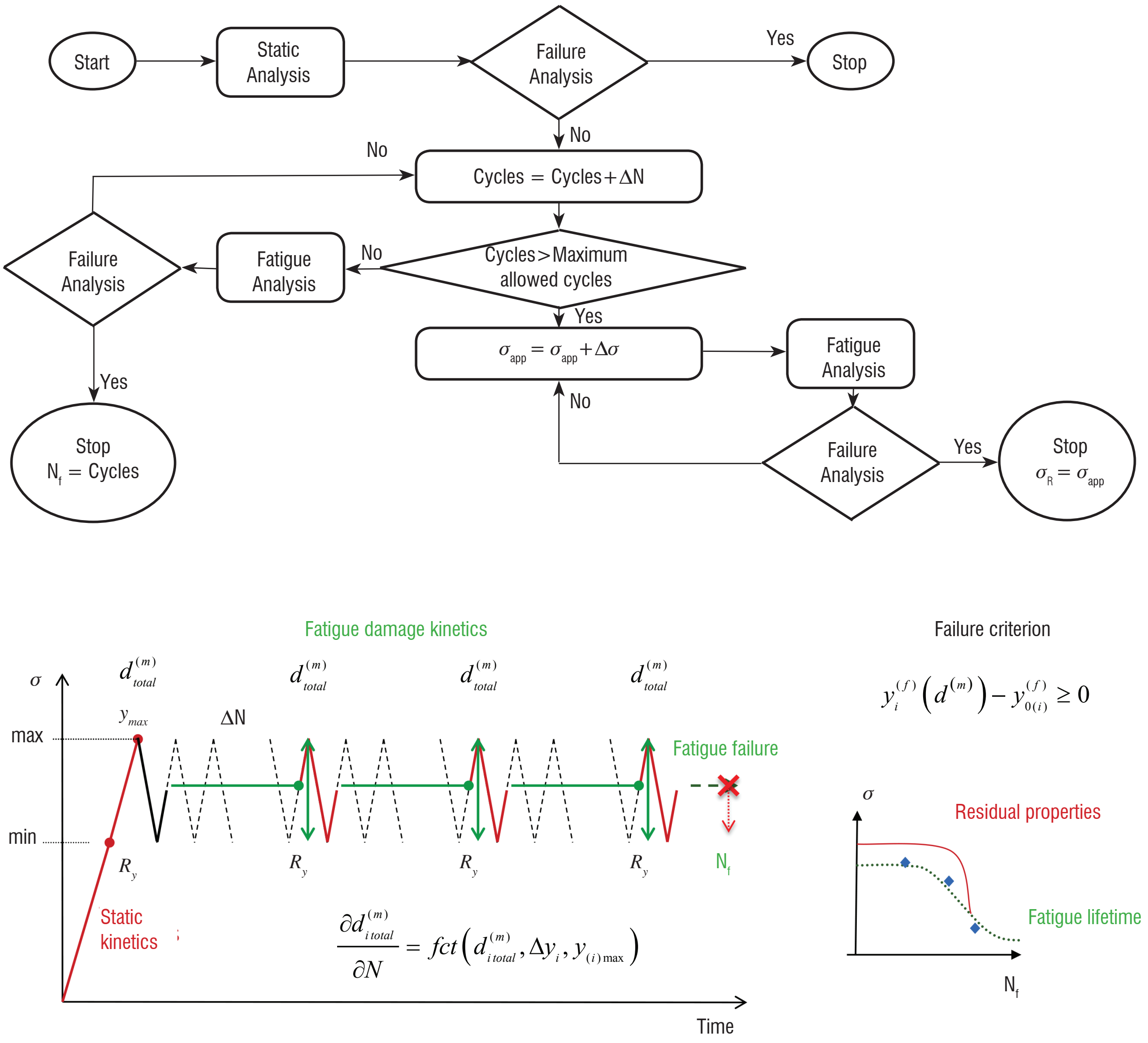

Figure 9 - Modeling strategy for lifetime and residual strength prediction

chosen in order to calculate the parameters required for the failure analysis and the next fatigue analysis. The mean load is chosen in order to estimate the evolution of viscous strain. This method can be considered as an adapted version for composites of a jump-in-cycle procedure. The value of the "cycle jump" can be determined by an automated criterion [45]. The damage variables are used as a measurement for determining the size of the block of cycles. The faster the damage evolution is, the smaller the blocks are and, consequently, the number of cycles per block. Moreover, the larger the number of cycles used to update the driving forces is, the longer the finite element fatigue life simulations are, since the updated cycle needs to be finely discretized. This model has been applied to open-hole specimens, but the simulation results still need to be compared with experimental data.

Constant life diagram

Generating fatigue data for every configuration as a basis for efficient predictive models is not conceivable. Constant life diagrams (CLD) offer a predictive tool for the estimation of the fatigue life of the material under loading patterns for which no experimental data exist. It is a representation of S-N data. The constant-life lines in the CLD connect points with the same estimated lifetime, as a function of mean stress and stress amplitude.

Constant life diagrams for metals are usually observed to be symmetric, whereas for composites they are distinctly not, due to the different tensile and compressive strengths that they exhibit. Actually, in fatigue, there are different damage and failure mechanisms in tension and compression. Under tensile loading, the laminate composite is governed by fiber failures (in a fiber-dominated lay-up). Under compression loading, the composite properties are mostly determined by the matrix and matrix-fiber interaction. As a result, a typical CLD for composite materials is often shifted to the right hand side and the highest point is located away from the $R = -1$, ($\sigma_{mean} = 0$) line, as shown in figure 10.

Vassilopoulos et al. [89] have examined the influence of the formulation of a CLD on the composite lifetime. The predictive accuracy of the constant life formulation is very important because fatigue analysis results are significantly affected by the accuracy of the estimated S-N curve. They assessed the most common and recent formulations considering the ease of application, the need for experimental data and forecast accuracy, as critical evaluation parameters. The main highlights are given in the following.

On the adjustment of non-linearity (Figure 10), several approaches have emerged, i.e., piecewise linear "R-value multiple CFL diagram" [50], power law [25], power law from a single S-N experimental curve [37]and different power laws in tension and compression [10].

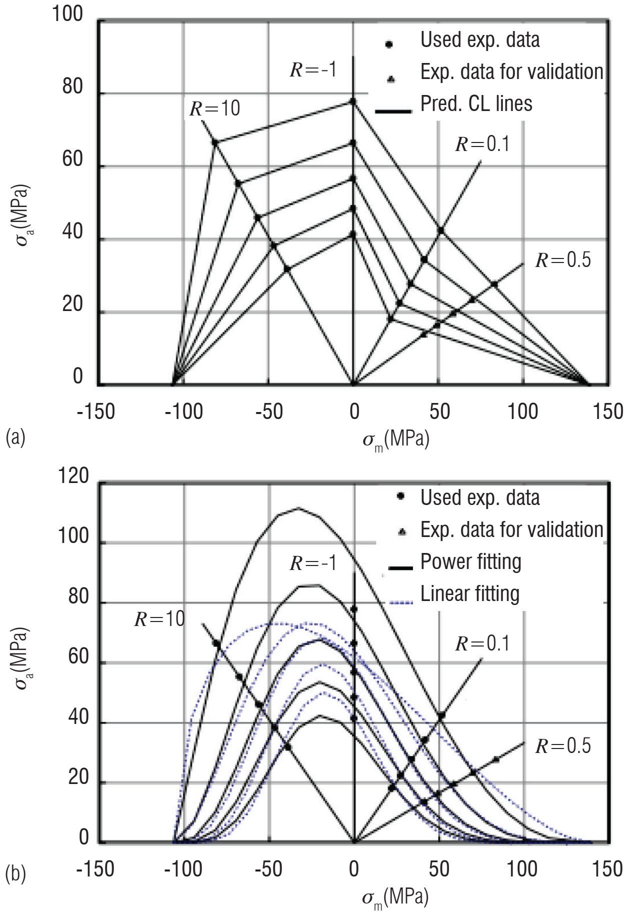

Figure 10 - Different types of CLD:
a - « multiple R-value CFL diagram »[50], b – power law [25]

Concerning the need for experimental data, the most demanding approaches have proven to be the most reliable. This is the case of the piecewise linear approach, which is the most accurate among the various formulations analyzed when a minimum number of three available S-N curves is available. The simplifying assumptions that allow some models to expect only a few fatigue data [37] or none [35] do not lead to a satisfactory accuracy. Moreover, these assumptions do not usually allow new fatigue measures to be incorporated “on the fly”. Finally, it should be noted that all of these approaches raise the question of a joint processing of static and fatigue data.

Uncertainties and variability

An inherent characteristic of composite materials, which must be taken into account, is the variability in strength and fatigue life data. This variability is higher than that observed in metals. The structural reliability provided by the conventional deterministic design approach (using safety factors) is different for composite and metal structures. Composite structures have to be designed with the same level of confidence as metallic structures and, therefore, a probabilistic-based methodology is of interest. In addition to the scatter in strength and life data, the uncertainties of the applied loads also affect the reliability of a structure. To deal with these uncertainties, a safety factor of 1.5, traditionally used in aircraft structural design, generally provides a very high level of reliability although not quantifiable. A probabilistic certification method can provide additional and useful information for a more efficient structural design. Recent works at ONERA have illustrated the implementation of an advanced probabilistic treatment by applying it, as a beginning, to simple empirical models. The approach is based on the SLERA principle (Strength-Life-Equal-Rank Assumption), which considers the static data dispersion as the main source of the whole observed dispersion [14], as presented in figure 11. The tools developed for the statistical identification are well adapted to the available types of data (lifetimes, static / residual strengths) and their structuring. They are based on the innovative use of the EM (Estimation-Maximization) algorithm. This allows the identification to be made more versatile and more effective compared to techniques in the available literature. Its application to purely numerical fatigue models is still in progress and will incorporate the already available numerical techniques for propagating uncertainty.

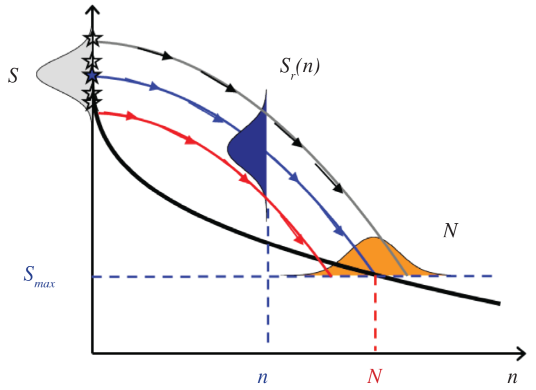

Figure 11 - SLERA principle (Strength-Life-Equal-Rank Assumption)[14]

Conclusion / Perspectives

This paper has attempted to address the problem of fatigue life prediction of composites from the point of view of ONERA. It describes the methodology that ONERA adopted to propose a fatigue life modeling. In this respect, ONERA has taken advantage of years of experience in progressive damage models under monotonic loadings, both for laminates and 3D woven composites. Nevertheless, studies on fatigue of composites are relatively recent at ONERA, less than five years. The first idea was that ONERA would benefit from a good knowledge of fatigue of metallics, in order to propose a fatigue model for composites; however, as reported in the first part of this paper, the fatigue methodologies for metallics cannot be directly applied to composites. It has also been shown that the composite fatigue failure modes are different depending on the type of composites (2D or 3D woven, UD laminates). There is no single method for the modeling of a series of composite materials. To propose a fatigue model for 3D interlock woven composites (PMC or CMC), the initial important step for ONERA consisted in understanding the damage mechanisms occurring in woven composite materials during fatigue. It resulted from this study that the types of damage mechanisms in 3D interlock woven composites resulting from monotonic or fatigue loadings are fairly similar. This then allowed the existing monotonic damage models to be extended to a fatigue model. These models have been applied to simple structures and the next step will consist in applying them to real structures under real loadings. This constitutes a challenging perspective to this study. ■

Acknowledgements

The collaboration with Snecma and Herakles is gratefully acknowledged. This work was partly supported under the PRC Composites, a French research project funded by the DGAC, involving SAFRAN Group, ONERA and CNRS. The authors would like to express their sincere gratitude to Dr. R. Valle for valuable and helpful discussions.

References

[1] D.H. ALLEN, C.E. HARRIS, S.E. GROVES - *A Thermomechanical Constitutive Theory for Elastic Composites with Distributed Damage: I. Theoretical Development*. International Journal of Solids and Structures, 23 (1987) 1301-1318.

[2] D.H. ALLEN, C.E. HARRIS, S.E. GROVES - *A Thermomechanical Constitutive Theory for Elastic Composites with Distributed Damage: II. Application to Matrix Cracking in Laminated Composites*. International Journal of Solids and Structures, 23 (1987) 1319-1338.

[3] L. ANGRAND, R. DESMORAT, M. KAMINSKI, C. RAKOTOARISOA - *Incremental Damage Model for Multiaxial Random Fatigue of Interlock Woven Composite.* Proceedings of the first International Conference on Mechanics of Composites (MECHCOMP 2014), Stony Brook University, Long Island, New York, USA, 2014.

[4] J. AWERBUCH, H. HAHN - *Off-Axis Fatigue of Graphite/Epoxy Composite.* K.N.Lauraitis (Ed.). Fatigue of fibrous composite materials. ASTM STP 723, 243-273. 1981.

[5] C. BATHIAS - *An Engineering Point of View about Fatigue of Polymer Matrix Composite Materials*. International Journal of Fatigue, 28 (2006) 1094-1099.

[6] H.W. BERGMANN, R. PRINZ - *Fatigue Life Estimation of Graphite/Epoxy Laminates under Consideration of Delamination Growth*. Int. J. Numer. Meth. Engng., 27 (1989) 323-341.

[7] J.M. BERTHELOT, J.F. LE CORRE - *Modelling the Transverse Cracking in Cross-Ply Laminates: Application to Fatigue.* Composites Part B: Engineering, 30 (1999) 569-577.

[8] J.M. BERTHELOT - *Transverse Cracking and Delamination in Cross-Ply Glass-Fiber and Carbon-Fiber Reinforced Plastic Laminates: Static and Fatigue Loading*. Applied Mechanics Reviews, 56 (2003) 111-147.

[9] M. BIZEUL - *Contribution à l'étude de la propagation de coupure en fatigue dans les revêtements composites tissés minces.* 2009. Doctorate thesis, Université de Toulouse, France.

[10] G.K. BOERSTRA - *The Multislope Model: a New Description for the Fatigue Strength of Glass Fibre Reinforced Plastic*. International Journal of Fatigue, 29 (2007) 1571-1576.

[11] R. BÖHM, M. GUDE, W. HUFENBACH - *A Phenomenologically Based Damage Model for Textile Composites with Crimped Reinforcement*. Composites Science and Technology, 70 (2010) 81-87.

[12] I.P. BOND - *Fatigue Life Prediction for GRP Subjected to Variable Amplitude Loading*. Composites Part A: Applied Science and Manufacturing, 30 (1999) 961-970.

[13] J.F. CARON, A. EHRLACHER - *Modelling of Fatigue Microcracking Kinetics in Crossply Composites and Experimental Validation,* Composites Science and Technology, 59 (1999) 1349-1359.

[14] P.C. CHOU, C. ROBERT - *Residual Strength in Fatigue Based on the Strength-Life Equal Rank Assumption*. Journal of Composite Materials, 12 (1978) 177-194.

[15] C. CLUZEL, E. BARANGER, P. LADEVEZE, A. MOURET - *Mechanical Behaviour and Lifetime Modelling of Self-Healing Ceramic-Matrix Composites Subjected to Thermomechanical Loading in Air*. Composites Part A: Applied Science and Manufacturing, 40 (2009) 976-984.

[16] I.M. DANIEL, A. CHAREWICZ - *Fatigue Damage Mechanisms and Residual Properties of Graphite/Epoxy Laminates*. Engineering Fracture Mechanics, 25 (1986) 793-808.

[17] J. DEGRIECK, W. VAN PAEPEGEM - *Fatigue Damage Modeling of Fibre-Reinforced Composite Materials: Review*. Applied Mechanics Reviews, 54 (2001) 279-300.

[18] R. DESMORAT, L. ANGRAND, P. GABORIT, M. KAMINSKI, C. RAKOTOARISOA - *On the Introduction of a Mean Stress in Kinetic Damage Evolution Laws for Fatigue.* International Journal of Fatigue, 77 (2015) 141-153.

[19] F. ELLYIN, H. EL-KADI - *A Fatigue Failure Criterion for Fiber Reinforced Composite Laminae*. Composite Structures, 15 (1990) 61-74.

[20] Z. FAWAZ, F. ELLYIN - *Fatigue Failure Model for Fibre-Reinforced Materials under General Loading Conditions*. Journal of Composite Materials, 28 (1994) 1432-1451.

[21] X. FENG, M.D. GILCHRIST, A.J. KINLOCH, F.L. MATTHEWS - *Development of a Method for Predicting the Fatigue Life of CFRP Components*. International Conference on Fatigue of Composites, 1997, pp. 407-414.

[22] T. FUJII, S. AMIJIMA, K. OKUBO - *Microscopic Fatigue Processes in a Plain-Weave Glass-Fibre Composite*. Composites Science and Technology, 49 (1993) 327-333.

[23] R.M. GUEDES - *Time-Dependent Failure Criteria for Lifetime Prediction of Polymer Matrix Composite Structures*. R. M. Guedes (Ed.), Creep and Fatigue in Polymer Matrix Composites, Woodhead Publishing Series in Composites Science and Engineering, Woodhead Publishing, 2011, pp. 366-405.

[24] B. HARRIS - *A Historical Review of the Fatigue Behaviour of Fibre-Reinforced Plastics.* B. Harris (Ed.), Fatigue in Composites, Woodhead Publishing Series in Composites Science and Engineering, Woodhead Publishing, 2003, pp. 3-35.

[25] B. HARRIS - *A Parametric Constant-Life Model for Prediction of the Fatigue Lives of Fibre-Reinforced Plastics.* B. Harris (Ed.), Fatigue in Composites, Woodhead Publishing Series in Composites Science and Engineering, Woodhead Publishing, 2003, pp. 546-568.

[26] B. HARRIS - *Fatigue Behaviour of Polymer-Based Composites and Life Prediction Methods*. A.H.Cardon (Ed.), Durability Analysis of Structural Composite Systems, Balkema, Rotterdam, 1996, pp. 49-84.

[27] Z. HASHIN - *Cumulative Damage Theory for Composite Materials: Residual Life and Residual Strength Methods*. Composites Science and Technology, 23 (1985) 1-19.

[28] Z. HASHIN, A. ROTEM - *A Fatigue Failure Criterion for Fiber Reinforced Materials*. Journal of Composite Materials, 7 (1973) 448-464.

[29] E. HÉMON - *Modèles multi-niveaux de prévision des durées de vie en fatigue des structures composites à matrice céramique pour usage en turbomachines aéronautiques*. 2013. Doctorate thesis, Université de Bordeaux, France.

[30] C. HENAFF-GARDIN, M.C. LAFARIE-FRENOT, I. GOUPILLAUD - *Prediction of Cracking Evolution Under Uniaxial Fatigue Loading in Crossply Composite Laminates*. International Conference on Fatigue of Composites, 1997, pp. 189-196.

[31] J. HENRY - *Mécanismes d'endommagement en fatigue dans les tissus multicouches interlocks*. 2013. Doctorate thesis, Université de Technologie de Compiègne, France.

[32] C. HOCHARD, J. PAYAN, C. BORDREUIL - *A Progressive First Ply Failure Model for Woven Ply CFRP Laminates under Static and Fatigue Loads*. International Journal of Fatigue, 28 (2006) 1270-1276.

[33] C. HOCHARD, Y. THOLLON - *A Generalized Damage Model for Woven Ply Laminates under Static and Fatigue Loading Conditions*. International Journal of Fatigue, 32 (2010) 158-165.

[34] L.G.J. JANSSEN, A.M.V. WINGERDE, C.W. KENSCHE, T.P. PHILIPPIDIS, P. BRØNDSTED, A.G. DUTTON, R.P.L. NIJSSEN, O. KRAUSE - *Reliable Optimal use of Materials for Wind Turbine Rotor Blades.* Final report OPTIMAT BLADES. www.kc-wmc.nl/optimat_blades/index.htm . 2006. ECN Wind Energy. ECN-C-06-023.

[35] C. KASSAPOGLOU - *Fatigue Life Prediction of Composite Structures under Constant Amplitude Loading*. Journal of Composite Materials, 41 (2007) 2737-2754.

[36] C. KASSAPOGLOU, M. KAMINSKI - *Modeling Damage and Load Redistribution in Composites under Tension-Tension Fatigue Loading*. Composites Part A: Applied Science and Manufacturing, 42 (2011) 1783-1792.

[37] M. KAWAI - *A Method for Identifying Asymmetric Dissimilar Constant Fatigue life Diagrams for CFRP Laminates*. Key Engineering Materials, 334 (2007) 61-64.

[38] M. KAWAI - *A Phenomenological Model for Off-Axis Fatigue Behavior of Unidirectional Polymer Matrix Composites under Different Stress Ratios.* Composites Part A: Applied Science and Manufacturing, 35 (2004) 955-963.

[39] M. KAWAI, T. TANIGUCHI - *Off-Axis Fatigue Behavior of Plain Weave Carbon/Epoxy Fabric Laminates at Room and High Temperatures and its Mechanical Modeling*. Composites Part A: Applied Science and Manufacturing, 37 (2006) 243-256.

[40] O. KONUR, F.L. MATTHEWS - *Effect of the Properties of the Constituents on the Fatigue Performance of Composites*. A review, Composites, 20 (1989) 317-328.

[41] P. LADEVEZE, E. LEDANTEC - *Damage Modelling of the Elementary Ply for Laminated Composites*. Composites Science and Technology, 43 (1992) 257-267.

[42] M.C. LAFARIE-FRENOT, C. HENAFF-GARDIN, D. GAMBY - *Matrix Cracking Induced by Cyclic Ply Stresses in Composite Laminates*. Composites Science and Technology, 61 (2001) 2327-2336.

[43] N. LAWS, G.J. DVORAK, M. HEJAZI - *Stiffness Changes in Unidirectional Composites Caused by Crack Systems*, Mechanics of Materials, 2 (1983) 123-137.

[44] J.W. LEE, D.H. ALLEN, C.E. HARRIS - *Internal State Variable Approach for Predicting Stiffness Reductions in Fibrous Laminated Composites with Matrix Cracks*. Journal of Composite Materials, 23 (1989) 1273-1291.

[45] B. LIU, L.B. LESSARD - *Fatigue and Damage-Tolerance Analysis of Composite Laminates: Stiffness Loss, Damage-Modelling, and Life Prediction*. Composites Science and Technology, 51 (1994) 43-51.

[46] J.F. MAIRE, J.L. CHABOCHE - *A New Formulation of Continuum Damage Mechanics (CDM) for Composite Materials*. Aerospace Science and Technology, 1 (1997) 247-257.

[47] J.F. MAIRE, P.M. LESNE, J.L. CHABOCHE - *Modélisation micro-macro du comportement mécanique des tissus SiC-SiC*. Rapport ONERA, No.12/6138 RY 033 R. 1994.

[48] L. MARCIN - *Modélisation du comportement, de l'endommagement et de la rupture des matériaux composites à renforts tissés pour le dimensionnement robuste de structures.* 2010. Doctorate thesis, Université de Bordeaux I, France.

[49] L. MARCIN, J.F. MAIRE, N. CARRERE, E. MARTIN - *Development of a Macroscopic Damage Model for Woven Ceramic Matrix Composites*. International Journal of Damage Mechanics, 20 (2011) 939-957.

[50] R.P.L. NIJSSEN - *Fatigue Life Prediction and Strength Degradation of Wind Turbine Rotor Blade Composites*. 2006. Doctorate thesis, Faculty of Aerospace Engineering, Delft University, Netherlands.

[51] S.L. OGIN, P.A. SMITH, P.W.R. BEAUMONT - *Matrix Cracking and Stiffness Reduction during the Fatigue of a (0/90)s GFRP Laminate*. Composites Science and Technology, 22 (1985) 23-31.

[52] T. OSADA, A. NAKAI, H. HAMADA - *Initial Fracture Behavior of Satin Woven Fabric Composites*. Composite Structures, 61 (2003) 333-339.

[53] W.V. PAEPEGEM, J. DEGRIECK - *Effects of Load Sequence and Block Loading on the Fatigue Response of Fiber-Reinforced Composites*. Mechanics of Advanced Materials and Structures, 9 (2002) 19-35.

[54] S.D. PANDITA, G. HUYSMANS, M. WEVERS, I. VERPOEST - *Tensile Fatigue Behaviour of Glass Plain-Weave Fabric Composites in on- and off-Axis Directions*. Composites Part A: Applied Science and Manufacturing, 32 (2001) 1533-1539.

[55] J. PAYAN, C. HOCHARD - *Damage Modelling of Laminated Carbon/Epoxy Composites under Static and Fatigue Loadings*. International Journal of Fatigue, 24 (2002) 299-306.

[56] T.P. PHILIPPIDIS, A.P. VASSILOPOULOS - *Fatigue of Composite Laminates under Off-Axis Loading*. International Journal of Fatigue, 21 (1999) 253-262.

[57] T.P. PHILIPPIDIS, A.P. VASSILOPOULOS - *Fatigue Strength Prediction under Multiaxial Stress*. Journal of Composite Materials, 33 (1999) 1578-1599.

[58] T.P. PHILIPPIDIS, A.P. VASSILOPOULOS - *Complex Stress State Effect on Fatigue Life of GRP Laminates. Part I, Experimental.* International Journal of Fatigue, 24 (2002) 813-823.

[59] N.L. POST, S.W. CASE, J.J. LESKO - *Modeling the Variable Amplitude Fatigue of Composite Materials. A Review and Evaluation of the State of the Art for Spectrum Loading*. International Journal of Fatigue, 30 (2008) 2064-2086.

[60] L. QUEMARD, F. REBILLAT, A. GUETTE, H. TAWIL, C. LOUCHET-POUILLERIE - *Degradation Mechanisms of a SiC Fiber Reinforced Self-Healing Matrix Composite in Simulated Combustor Environments*, Journal of the European Ceramic Society, 27 (2007) 377-388.

[61] C. RAKOTOARISOA - *Prévision de la durée de vie en fatigue des composites à matrice organique tissés interlock.* 2013. Doctorate thesis, Université de Technologie de Compiègne, France.

[62] K.L. REIFSNIDER - *Fatigue of Composite Materials*. Elsevier, 1991.

[63] K.L. REIFSNIDER, Z. GAO - *A Micromechanics Model for Composites under Fatigue Loading.* International Journal of Fatigue, 13 (1991) 149-156.

[64] K.L. REIFSNIDER - *The Critical Element Model: a Modeling Philosophy*. Engineering Fracture Mechanics, 25 (1986) 739-749.

[65] K.L. REIFSNIDER, W.W. STINCHCOMB - *A Critical-Element Model of the Residual Strength and Life of Fatigue-Loaded Composite Coupons*. Composite materials: fatigue and fracture, ASTM STP, 907 (1986) 298-313.

[66] N. REVEST - *Comportement en fatigue de pièces épaisses en matériaux composites.* 2011. Doctorate thesis, Ecole Nationale Supérieure des Mines de Paris - Centre des Matériaux, France.

[67] N. REVEST, A. THIONNET, J. RENARD, L. BOULAY, P. CASTAING - *Comportement en fatigue de structures épaisses en matériaux composites.* Comptes Rendus des JNC, 16 (2009).

[68] J. ROUCHON - *Fatigue and Damage Tolerance Evaluation of Structures: the Composite Materials Response*. NLR-TP-2009-221. 2009. Nationaal Lucht-en Ruimtevaartlaboratorium NLR, National Aerospace Laboratory, Netherlands.

[69] J. SCHNEIDER - *Mécanismes d'endommagement dans les composites multicouches à renforts interlock.* 2011. Doctorate thesis, Université de Technologie de Compiègne, France.

[70] J. SCHÖN - *A Model of Fatigue Delamination in Composites*. Composites Science and Technology, 60 (2000) 553-558.

[71] K. SCHULTE - *Stiffness Reduction and Development of Longitudinal Cracks during Fatigue Loading of Composite Laminates*. A. H. Cardon and G. Verchery (Eds.), Mechanical characterisation of load bearing fibre composite laminates, 1985, pp. 36-54.

[72] K. SCHULTE, C. BARON, N. NEUBERT - *Damage Development in Carbon Fibre Epoxy Laminates: Cyclic Loading.* Advanced Materials Research and Developments for Transport, (1985) 281-288.

[73] K. SCHULTE, E. REESE, T.W. CHOU - *Fatigue Behaviour and Damage Development in Woven Fabric and Hybrid Fabric Composites.* Proceedings of Sixth International Conference on Composite Materials (ICCM-VI) & Second European Conference on Composite Materials (ECCM-II), 1987, pp. 89-99.

[74] A. SEDRAKIAN, T. BEN ZINEB, J.L. BILLOET, N. SICOT, P. LARDEUR - *A Numerical Model of Fatigue Behaviour for Composite Plates: Application to a Three Point Bending Test*. Proceedings of International Conference on Fatigue of Composites, 1997, pp. 3-5.

[75] G.P. SENDECKYJ - *Life Prediction for Resin-Matrix Composite Materials*. Fatigue of composite materials, 4 (1990) 431-483.

[76] R.D.B. SEVENOIS, W. VAN PAEPEGEM - *Fatigue Damage Modeling Techniques for Textile Composites: Review and Comparison with Unidirectional Composite Modeling Techniques.* Applied Mechanics Reviews, 67 (2015) 020802.

[77] M.M. SHOKRIEH, F. TAHERI-BEHROOZ - *A Unified Fatigue Life Model Based on Energy Method*. Composite Structures, 75 (2006) 444-450.

[78] M.M. SHOKRIEH, L.B. LESSARD - *Multiaxial Fatigue Behaviour of Unidirectional Plies Based on Uniaxial Fatigue Experiments*. *I. Modelling.* International Journal of Fatigue, 19 (1997) 201-207.

[79] M.M. SHOKRIEH, L.B. LESSARD - *Progressive Fatigue Damage Modeling of Composite Materials. Part I: Modeling*. Journal of Composite Materials, 34 (2000) 1056-1080.

[80] M.M. SHOKRIEH, L.B. LESSARD - *Progressive Fatigue Damage Modeling of Composite Materials*. *Part II: Material Characterization and Model Verification*. Journal of Composite Materials, 34 (2000) 1081-1116.

[81] F. SIDOROFF, B. SUBAGIO - *Fatigue Damage Modelling of Composite Materials from Bending Tests*. Proceedings of the Second European Conference on Composite Materials (ECCM2), London, UK, 1987, pp. 432-439.

[82] D.Y. SONG, N. OTANI - *Approximate Estimation of Fatigue Strength of Polymer Matrix Composites by Material Properties*. Materials Science and Engineering: A, 254 (1998) 200-206.

[83] R. TALREJA - *Transverse Cracking and Stiffness Reduction in Composite Laminates*. Journal of Composite Materials, 19 (1985) 355-375.

[84] A. THIONNET, J. RENARD - *Laminated Composites under Fatigue Loading: a Damage Development Law for Transverse Cracking*. Composites Science and Technology, 52 (1994) 173-181.

[85] Y. THOLLON - *Analyse du comportement à rupture de composites stratifiés constitués de plis tissés sous chargements statique et de fatigue.* 2009. Doctorate thesis, Université d'Aix-Marseille - Laboratoire de Mécanique et d'Acoustique, France.

[86] W. VAN PAEPEGEM - *Fatigue Testing Methods for Polymer Matrix Composites*. R. M. Guedes (Ed.), Creep and Fatigue in Polymer Matrix Composites, Woodhead Publishing, 2011, pp. 461-493.

[87] W. VAN PAEPEGEM, J. DEGRIECK - *Coupled Residual Stiffness and Strength Model for Fatigue of Fibre-Reinforced Composite Materials*. Composites Science and Technology, 62 (2002) 687-696.

[88] W. VAN PAEPEGEM, J. DEGRIECK - *Modelling Damage and Permanent Strain in Fibre-Reinforced Composites under In-Plane Fatigue Loading*. Composites Science and Technology, 63 (2003) 677-694.

[89] A.P. VASSILOPOULOS, B.D. MANSHADI, T. KELLER - *Influence of the Constant Life Diagram Formulation on the Fatigue Life Prediction of Composite Materials*. International Journal of Fatigue, 32 (2010) 659-669.

[90] A.T. VU - *Endommagement de stratifiés aéronautiques à fibres de carbone et matrice polymère soumis à des chargements monotones ou cycliques à plusieurs températures.* Essais et modélisation. 2009. Doctorate thesis, Ecole Nationale Supérieure de Mécanique et d'Aéronautique, Poitiers, France.

[91] J.W. WEETON, D.M. PETERS, K.L. THOMAS - *Engineers' Guide to Composite Materials*. American Society for Metals, 1987.

[92] H.A. WHITWORTH - *Cumulative Damage in Composites*. Journal of Engineering Materials and Technology, 112 (1990) 358-361.

[93] J. XIAO, C. BATHIAS - *Fatigue Damage and Fracture Mechanism of Notched Woven Laminates.* Journal of Composite Materials, 28 (1994) 1127-1139.

AUTHORS

Myriam Kaminski graduated (Engineering Diploma) from EPF (Sceaux, France) in 2003. She received her Master Degree from Ecole Centrale Paris in 2004 and her PhD in mechanics from ENSMP (Ecole Nationale Supérieure des Mines de Paris) in 2007. Then, she joined the Composite Materials and Structures Department at ONERA as a research scientist. Her research field is mainly focused on the experimental investigation of fatigue behavior of composite materials and finite element modeling of fatigue damage in these materials.

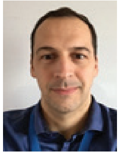

Frédéric Laurin graduated (Engineering Diploma) from Ecole Centrale Marseille (ECM) in 2002 and received his PhD in mechanics from the University of Franche-Comté in 2005. He joined ONERA in 2005 and works as a research scientist in the Composite Materials and Structures Department. His research interest includes the development of damage and failure approaches for composite materials, strength predictions of composite structures through finite element modeling and experimental investigations on the damage and failure mechanisms encountered in such materials.

Jean-François Maire joined ONERA in 1992 after receiving his PhD from Franche-Comté University (Besançon, France). He worked with Prof. Jean-Louis Chaboche for 10 years to develop several damage models for composite materials under static or fatigue loadings. He received the “Daniel Valentin Award” from AMAC in 1996. Since 2011, he is the Director of the Composite Materials and Structures Department at ONERA.

Carole Rakotoarisoa received her Engineering Diploma from ENSEIRB-MATMECA (Bordeaux, France) in Mathematical and Mechanical Modeling (2009) and her PhD in advanced mechanics from UTC (Université de Technologie de Compiègne, France) in 2013. Her PhD was on the development of a fatigue damage model able to predict the lifetime of a woven interlock polymer matrix composite (PMC). Since then, she works as a research scientist in the field of Composite Materials and Mechanics at Snecma (Safran Group). She is mainly involved in the comprehension of the interlock PMCs behavior under different types of loading and she manages the PRC-Composites program, which involves companies of the Safran Group, ONERA – The French Aerospace Lab - and several academic partners.

Elen Hemon received a double Master of Sciences Degree from the University of Bretagne Sud (Lorient, France) in 2009 and a PhD in mechanics from the University of Bordeaux in 2013. Since then, she has joined Safran Composites (Safran Group) as a composite material simulation engineer. She works in the field of springback for the manufacturing of sandwich-structured composites.

J.Cormier, F. Mauget
(Institut Pprime-ISAE ENSMA)
J-B Le Graverend*
(ONERA
Institut Pprime-ISAE ENSMA)
C. Moriconi
(Turbomeca-SAFRAN)
J. Mendez
(Institut Pprime-ISAE ENSMA)

E-mail: jonathan.cormier@ensma.fr

DOI: 10.12762/2015.AL09-07

Issues Related to the Constitutive Modeling of Ni-based Single Crystal Superalloys under Aeroengine Certification Conditions

This paper presents a constitutive modeling approach (the Polystar model) used to compute the viscoplastic behavior and the durability of high pressure turbine blades and vanes of aeroengines during complex thermomechanical histories typically encountered during certification procedures. This model is based on internal variables representing explicitly the microstructure evolutions occurring during very high temperature non-isothermal loading (e.g., dissolution/re-precipitation of the strengthening phase, dislocation recovery mechanisms, etc.) in a crystal viscoplasticity modeling framework. This article shows that the development of such a modeling tool requires a good characterization of fast microstructure evolutions, as well as in-service-type experiments (using burner rigs) able to reproduce the complex thermomechanical loading spectra. The capabilities of the model are illustrated, as well as its potential industrial applications and further developments are commented.

Introduction

Having robust life-prediction methods for the design of aeroengine high temperature components, such as turbine blades and vanes, are today highly desired by engine makers, especially when considering certification procedures. Indeed, the thermomechanical paths encountered by these components during certification are far more complex and severe than during their service life. As an example, the procedures for the certification of turboshaft engines for helicopters consist in mixing different engine regimes and repeated short very high temperature overheatings [1-4]. During these temperature peaks, high pressure turbine blades made of Ni-based single crystal superalloys are exposed to extreme conditions (temperatures close to their melting point). However, since these overheatings are short in duration (typically, from 5 to 150 seconds), the microstructure of the material is left out of equilibrium, leading to a transient mechanical response of the alloy [1, 2, 5-7]. As shown earlier by Cailletaud [8-10], a classical constitutive model in which the temperature dependence is only taken into account by the material parameters identified using isothermal experiments is not able to reproduce out of equilibrium states. Figure 1 illustrates this in the case of the polycrystalline Ni-based alloy IN 100, loaded under stress control non-isothermal LCF conditions [9]. It is especially observed in this figure that the modeling of the hysteresis loop using a classical viscoplastic approach* (dotted line in figure 1) over predicts the hysteresis width compared to the experimental loop (black dots). In order to obtain a better modeling of the behavior and life of the material, the proposed solution is to introduce additional internal variables accounting for microstructure evolutions, such as dissolution/precipitation of strengthening precipitates and their coarsening. This was already done by Cailletaud et al., as illustrated in figure 1, where such a "microstructure-sensitive" model was capable of accurately predicting the hysteresis loop after an overheating (continuous line in figure 1), even if the additional internal variables used by Cailletaud et al. were only tailored to capture the effect of microstructure evolutions at the macroscopic scale, without any actual representation of it (such as, e.g., precipitate size evolutions, volume fraction, or interparticle distances) [8-10].

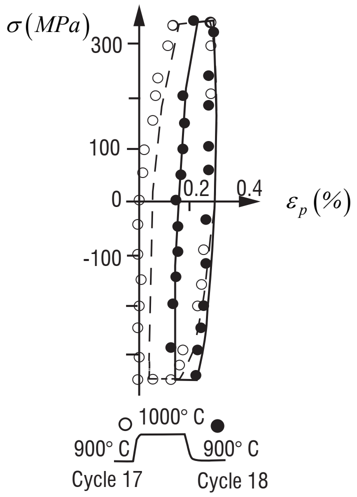

Figure 1 - Measured (circles) and calculated (lines) loops of the IN100 superalloy before and after an overheating at 1000°C lasting 120 s during the course of a fatigue test performed at 900°C, with $\Delta\sigma = 685 MPa$ and $R = -1$ [9]. A decrease in the loop width is observed just after the overheating (black circles). The calculated loop without additional variables (dotted line) is not predictive of the post overheating loop compared to the model with additional variables (continuous line).

---

* Now at Texas A&M University, Department of Aerospace Engineering

Such a modeling approach has been re-used more recently at Institut Pprime, in collaboration with the Centre des Matériaux and ONERA, using a crystal plasticity framework and introducing internal variables accounting more accurately for microstructure evolutions [11-15]. The Polystar model was developed in 2007 to compute the creep elongation and life of Ni-based single crystal superalloys subjected to thermomechanical histories representative of those encountered in the most severely damaged sections of high pressure turbine blades during certification procedures (Accelerated Simulated Mission Endurance Testing - ASMET, or 150 hours engine tests). This model has been identified for different alloys and is currently under evaluation at SAFRAN-Turbomeca for 3D finite element calculations.

The aim of this article is to show that the development of such microstructure-sensitive models is necessarily accompanied by the performance of complex non-isothermal experiments and microstructure characterizations. Hence, after presenting the basic ingredients of the model and the microstructure evolutions occurring during very high temperature jumps, specific microstructure characterizations and burner testing experiments developed at Institut Pprime will be presented. The new burner rig facility developed (the MAATRE burner) to reproduce aeroengine operating conditions with a good control of both the applied temperature and the mechanical loading coupled with a monitoring of sample deformations will be briefly detailed [4, 16]. Then, the model performances under complex thermomechanical histories will be outlined, as well as some illustrative potential uses of the Polystar model in an industrial context. Finally, some on-going activities to improve the modeling approach will be discussed.

Basic ingredients of the model and the microstructural evolutions considered

Basic single crystal model and hardening modifications

The model used for the simulation of the non-isothermal creep behavior through additions of physically motivated internal variables is a crystal plasticity model that has been applied to numerous structural calculations of components, such as tubular testing samples [17] or single crystalline turbine blades made of superalloys [18]. The basic equations of this model under a small strain assumption are recalled below. γ^s is the viscoplastic shear on a given slip system s, v is its accumulated value (the derivative of the second being the absolute value of the first), τ^s is the resolved shear stress on slip system s, v is the accumulated viscoplastic strain and ε^p is the viscoplastic strain tensor. The slip rate is determined (eq.(1)) by means of τ^s, the isotropic hardening r^s and the kinematic hardening x^s. $\underline{\underline{m}}^s$ is the orientation tensor calculated according to eq. (3), knowing the normal to the slip system plane $\underline{n}^s$ and the slip direction in this plane $\underline{l}^s$. Knowing the applied stress tensor $\underline{\underline{\sigma}}$, the resolved shear stress is calculated according to eq. (4) and then the viscoplastic strain tensor is determined using eq. (5). The damage evolution has been considered to occur at the slip system level. The damage scalar d_c^d is therefore introduced in eq. (1) using a concept of effective resolved shear stress. The damage evolution equation will be presented in § " Damage law " of this paper.

$$\dot{\gamma}^s = \left(\frac{\left|\tau^s - x^s\right| - r^s}{K\left(1-d_c^s\right)}\right)^n sign\left(\tau^s - x^s\right) \tag{1}$$

$$\dot{v} = \left(\frac{2}{3}\left(\dot{\underline{\underline{\varepsilon}}}_p : \dot{\underline{\underline{\varepsilon}}}_p\right)\right)^{1/2} \tag{2}$$

$$\underline{\underline{m}}^s = \frac{1}{2}\left(\underline{n}^s \otimes \underline{l}^s + \underline{l}^s \otimes \underline{n}^s\right) \tag{3}$$

$$\tau^s = \underline{\underline{\sigma}} : \underline{\underline{m}}^s \tag{4}$$

$$\dot{\underline{\underline{\varepsilon}}}^p = \sum_s \dot{\gamma}^s \, \underline{\underline{m}}^s \tag{5}$$

As a second assumption, only octahedral slip systems (i.e. <110>{111} slip systems) will be considered (cubic slip - <110>{001} - and stacking fault systems - <112>{111} - systems are ignored).

To introduce the microstructure evolutions occurring during temperature changes [1, 5, 19-21], a new form of the isotropic hardening τ^s is proposed in eq. (6). τ^s depends on the isotropic state variable ρ^s on the slip system s (eq. (7)) and on τ_0^s, the critical resolved shear stress as usually defined. A non-linear saturating form of ρ^s is chosen in eq. 7 to account for the transition from the primary to the secondary creep stage. It represents the increase of the dislocation density in the γ channels and at the γ / γ' interfaces during the early stage of viscoplastic deformation and the critical dislocation density that can enter into γ channels [22, 23]. In addition, two new improvements have been made in the formulation of r^s:

- An Orowan $\tau_{or} = \sqrt{\frac{2}{3}}\frac{GB}{W_{[001]}}$ contribution has been added to account for the structural hardening brought by the γ'-phase, whatever its kind of population (large or fine precipitation). G is the shear modulus ($= C_{44}$ for orthotropic materials, such as single crystal superalloys), B the Burgers vector magnitude (= 0.254 nm), and $W_{[001]}$ the γ-channel width along the [001] direction (i.e., in a (100) or a (010) plane). Since dislocations under high temperature conditions are mainly gliding in the matrix on octahedral slip systems, the $\sqrt{\frac{2}{3}}$ correction factor is added when calculating the Orowan stress, using γ corridor width along the [001] direction [24]. Linking $W_{[001]}$ with the volume fractions of large and fine γ' precipitates (see the next section) then enables the modeling of the γ' dissolution/precipitation effects upon the viscoplastic behavior.

- The second term of eq. (6) represents dislocation hardening through the isotropic state variable ρ^s and cross hardening by means of the interaction matrix [h]. For a given dislocation state, defined by a set of ρ^s on each slip system, the hardening consists of a steady-state contribution, given by Q, and a transient contribution, defined by Q^*. The material parameter Q depends on temperature only, while Q^* is a variable that depends on temperature and aging history (see further on).

$$r^s = \tau_0^s + b\left(Q + Q^*\right)\sum_j h_{sj}\rho^j + \sqrt{\frac{2}{3}}\frac{GB}{W_{[001]}} \tag{6}$$

$$\dot{\rho}^s = \left(1 - b\rho^s\right)\dot{v}^s \tag{7}$$

From a metallurgical point of view, eq. (6) can therefore be described as the sum of, from left to right, the solid solution hardening brought by the matrix ( ), the dislocation hardening and the structural hardening coming from the precipitates.

The evolution of the kinematic hardening x^S is classically defined on each slip system by means of the variable α^s(eq. (8)), which has a non-linear evolution with respect to the plastic slip on system s, γ^s (eq. (17)).

$$x^s = C\alpha^s \tag{8}$$

$$\dot{\alpha}^s = \left(sign\left(\tau^s - x^s\right) - d\alpha^s\right)\dot{v}^s \tag{9}$$

Microstructural evolutions considered

The main microstructure evolutions occurring during high temperature viscoplastic deformation of Ni-based single crystal superalloys are the γ / γ' morphological evolutions (i.e., homothetic coarsening, directional coarsening – so-called γ'-rafting [25-28]) and massive dissolution/re-precipitation processes occurring during temperature changes for a very high temperature domain (T ≥ 950°C). Figure 2 illustrates the γ / γ' morphological evolutions occurring during a high temperature/low stress creep test of a first generation Ni-based superalloy (MC2 alloy). The characterization of the γ / γ' morphological evolutions was performed by analyzing several interrupted creep tests at high temperatures and low applied stresses. These analyzes were devoted to identifying the evolution of $W_{[001]}$ as a function of time. Based on these observations, two different evolutions in the γ channel width $W_{[001]}$ were found, one mainly related to the γ' volume fractions of the different classes of γ' particles [12] (described further on) and one sensitive to the time-temperature-strain rate history [14, 15].

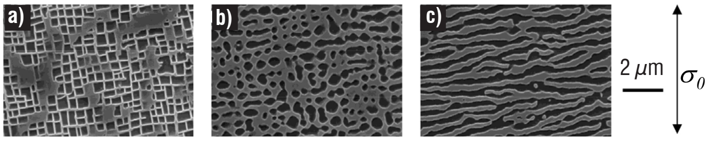

Figure 2 - γ' rafting during a creep test at 1050°C/160 MPa of MC2 alloy: γ / γ' microstructure at the beginning of the experiment (a), after 4.7 h (during primary creep stage) (b) and after 9.4 h (beginning of secondary creep stage) (c). Note that the γ' phase appears as dark areas

The precipitation evolution considered in the Polystar model are the γ' dissolution/precipitation mechanisms occurring during heating/cooling stages in a temperature range inducing pronounced γ' dissolution (T > 950°C for a majority of commercial alloys). Figure 3 illustrates what is happening for a single overheating close to the γ'-solvus of the alloy and figure 4 is an actual γ / γ' microstructure observation after an overheating.

As shown in figure 3, a fast γ' dissolution occurs during a temperature jump in the γ' dissolution domain, leading to a widening of the γ matrix channels (i.e., an increase in), i.e., to an easier viscoplastic flow due to the decrease in the Orowan stress. Such a γ' dissolution mechanism is accompanied by a decrease in the dislocation density at the γ / γ' interfaces, as shown by TEM observations [1] and more recently using in situ non-isothermal creep experiments followed by X-Ray diffraction (XRD) under synchrotron radiation [29, 30]. Cooling down to the nominal temperature entails the precipitation of hyperfine (tertiary) γ' particles in the γ channels, as well as an increase in the dislocation density at the γ / γ' interfaces (see the last column in figure 3). It means that the γ' precipitation during non-isothermal loading is no longer monomodal, but, at least, bi-modal, with two classes of γ' precipitate, as shown in figure 4. The respective volume fractions of coarse and fine (tertiary) γ' precipitates will be denoted as fl and fs in the rest of the paper. It is also worth mentioning that all of the microstructure evolutions occurring during very high temperature changes are highly dependent on the temperature levels, heating/cooling rates and durations of the overheating. Indeed, the microstructure of the material is left out of thermodynamical equilibrium if the temperature changes and the dwell times are respectively fast and short enough, hence leading to transient mechanical responses of the alloy (the new primary creep shown in the second column of figure 3 is a typical illustration of such a transient creep behavior). The microstructure evolutions presented in figure 3 are all taken into account in the Polystar model and their evolution laws are now presented.

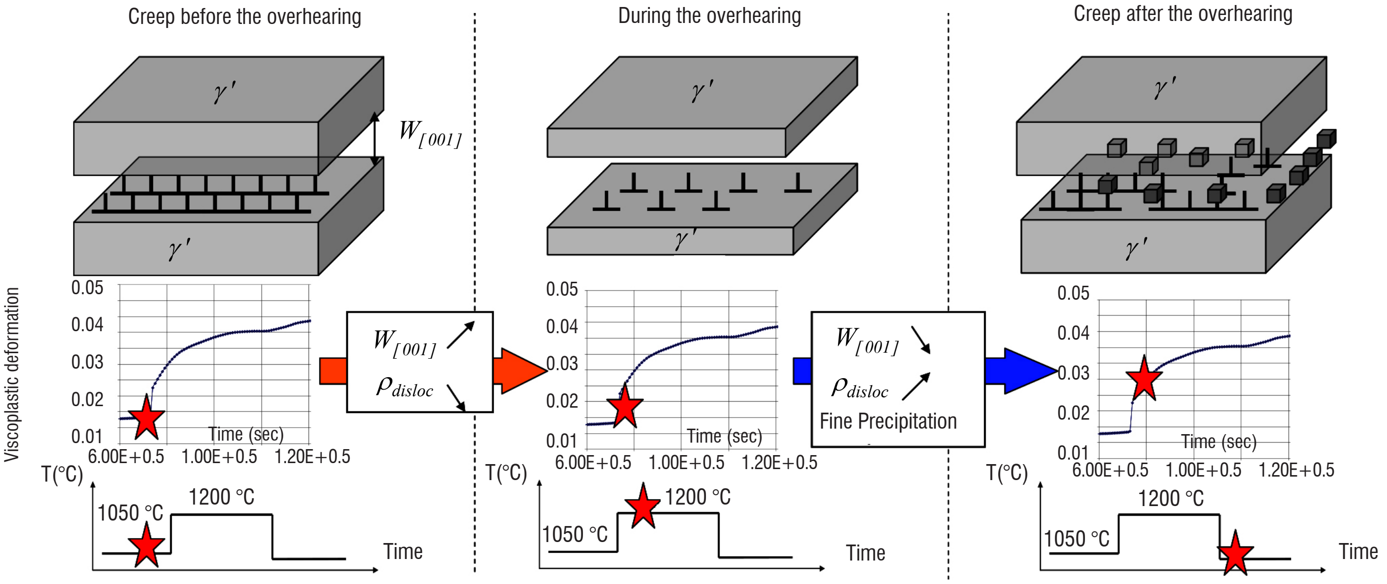

Figure 3 - γ' dissolution/precipitation mechanisms during a single overheating introduced after a given amount of creep deformation. The upper row is a schematic illustration of the γ / γ' microstructure and of the dislocation density evolutions. The middle row shows the evolution of the creep strain and the last row shows the actual position (red star) in the thermal history.

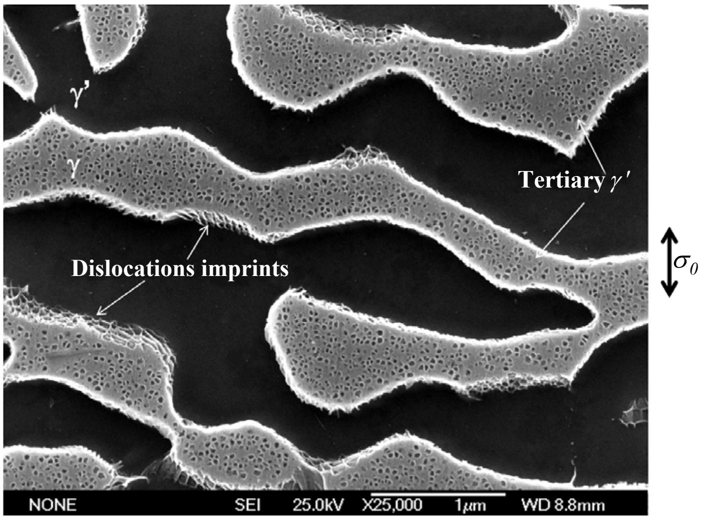

Figure 4 - γ / γ' microstructure obtained after a non-isothermal creep test performed with the CMSX-4 Plus® Mod C single crystal superalloy. The experiment was interrupted after an 1150°C overheating. Note ultrafine (tertiary) γ' precipitates in the γ channels. The γ' phase appears as dark areas.

An exponential type expression has been initially chosen to describe the evolution of the volume fraction of large γ' particles (f_l), as observed in IN100 polycrystalline superalloy [31], or more recently in MC2 alloy [19]. The same kind of evolution was chosen in recent phase field simulations performed by Wang et al to analyze the effect of the initial γ' precipitate size on dissolution kinetics [32]. α_l is the time constant for the dissolution/coalescence process depending on temperature. The temperature-dependent values of α_l and f_{equ} (the γ'-volume fraction at thermodynamical equilibrium) were measured from microstructural investigations performed previously [2, 19, 33].

$$\dot{f}_l = \frac{f_{equ} - f_l}{\alpha_l} \tag{10}$$

However, to obtain a better description of the dissolution/precipitation kinetics of large γ' particles, a modification of eq. (10) has been recently proposed. In fact, an impact of the accumulated plastic deformation on the dissolution kinetics was clearly demonstrated by Giraud et al. for CMSX-4® alloy [21]. Equation 10 was then modified into eq. (11), with   and ecfl being temperature-dependent material parameters:

$$\dot{f}_l = \left[1 - \delta_l \times exp\left(-\frac{\nu}{e_{cfl}}\right)\right]\left(\frac{f_{equ} - f_l}{\alpha_l}\right) \tag{11}$$

A challenging issue was also to model the evolution of the fine γ' precipitation occurring in the γ channels on cooling (see figure 4). Indeed, it would have been easy to assume that $f_l + f_s = f_{equ}, f_s$ being the volume fraction of small precipitates. Nevertheless, this equation is only valid when the tertiary precipitation occurs (cooling after a dissolution time). In fact, the small precipitates may not have the same chemical composition as the largest ones. It was even shown that the kinetics of dissolution or coalescence are different for large and small precipitates [33]. The following evolutions of the fine precipitate volume fractionare f_s then defined, considering isothermal conditions without overheating or during an overheating eq. (12), cooling after an overheating eq. (13) and re-heating after an overheating eq. (14):

if $\left(f_{equ} - f_l\right) \leq 0$, $\dot{f}_s = -\dfrac{f_s}{\alpha_s}$ (12)

if $\left(f_{equ} - f_l\right) > 0$ and $\dot{T} < 0$,

$$\dot{f}_s = -\frac{f_{equ} - f_l - f_s}{\alpha_s}\left(\frac{\dot{T}}{\dot{T}_0}\right) - \left(\frac{f_s}{K_{s_1}}\right)^{m_s} \tag{13}$$

if $\left(f_{equ} - f_l\right) > 0$ and $\dot{T} \geq 0$, $\dot{f}_s = -\left(\dfrac{f_s}{K_{s_2}}\right)^{m_s}$ (14)

Eq. (12) is a phenomenological representation of the dissolution of hyperfine precipitates during a temperature increase and during isothermal dwells. Under continuous cooling conditions after an overheating, both nucleation and dissolution have to be considered. Their respective contributions are taken into account by, respectively, the first and second terms in eq. (13) and both processes are highly dependent on the cooling rate. The last case occurs when the microstructure is out of equilibrium after an overheating (a population of hyperfine particles already nucleated) and a new overheating is occurring. Under such circumstances, a very fast dissolution of tertiary precipitates occurs (even faster than under the first case described by eq. (12)), which is taken into account by equation (14). The time constant α_s is smaller than α_l for the largest precipitates. In particular, the dissolution is quasi-instantaneous for temperatures over 1000 °C. Based on the γ' volume fraction evolutions presented in eqs. (11) to (14) and assuming that $W_{[001]}$ is only γ' volume fraction dependent, the following phenomenological dependence on f_l and f_s has been determined [12]:

$$W_{[001]} = \frac{a_0}{\delta}\left(f_l^{m_l} - d_{tp} f_s\right) \tag{15}$$

where a_0 is the initial average edge length of the γ' cubes (= 0.45 μm) and m_l, d_{tp} and δ are material parameters. This equation has been experimentally validated for both cuboidal and rafted γ' morphologies [12]. A linear dependence of $W_{[001]}$ on f_s has been introduced, since the fine precipitation filling the γ channels on cooling is very effective in narrowing them (the γ channel width can be as small as 10 nm). It should be admitted at this point of the study that the d_{tp} parameter has not yet been determined experimentally, due to difficulties in the stereological characterization of these ultrafine particles. It is also pointed out that an experimental evolution of $W_{[001]}$ on the γ' volume fractions has been chosen rather than physical models based on geometrical considerations [34, 35], since our model should take into account rapid changes of volume fraction under a wide range (from 0 to 0.7) and independently from the precipitate morphology (cuboidal or rafted). The authors also point out that eq. (15) is not able to capture slow morphological evolutions of the precipitates (i.e., γ' directional coarsening) under isothermal conditions. Indeed, this "medium version" of the model is suitable to the simulation of complex certification cycles of turboshaft engines for helicopters presented later in this paper. The durations of such thermomechanical histories (see, e.g., figure 10) are short enough to neglect the contribution of γ'-rafting to the viscoplastic behavior of the alloy. A more refined version of the model published last year takes into account such a time dependence of the γ' morphology of the precipitates [15].

The dislocation density evolutions occurring during temperature changes have been modeled through a decomposition of the work hardening (second term in eq. (6)): Q is a material parameter corresponding to the dislocation pinned at the γ / γ' interfaces, which cannot vanish during overheatings due to recovery processes (dislocation climb or γ'cutting/annihilation process), while Q^* is a variable describing the effect of microstructure changes on the dislocations density recovery. Q^*depends on a state variable $a*$ (eq. (16)) whose evolution range is [0,1]. Q_{S0} is then the maximum recoverable dislocation hardening. The evolution of $a*$ is presented in eq. (17): the metallurgical steady-state (maximum recovery) is obtained for $a* = 0$. The first term of eq. (17) accounts for the recovery effects upon temperature changes, while the second one represents the (re) establishment of dislocation structures after a temperature peak. $\alpha*$ and $\beta*$ are the time constants for those processes with $\alpha* << \beta*$.

$$Q^* = a^* Q_{S0} \tag{16}$$

$$\dot{a}^* = -\frac{a^*}{\alpha^*}\frac{\dot{T}}{\dot{T}_0} - \frac{a^*}{\beta^*} \qquad a^*(t=0) = 1 \tag{17}$$

The Q^* term hence allows a partial recovery of the isotropic hardening, due to thermal changes. The evolution of Q_{S0} as a function of temperature typically allows such recovery processes only at very high temperatures (T > 1100°C).

Damage law

Past non-isothermal creep tests with one single overheating performed on MC2 alloy showed that increasing the overheating duration led to increased creep life [1-3], while a stress-driven damage evolution would have predicted the opposite, since the applied stress remains almost constant. A plasticity driven damage evolution is hence proposed. The damage evolution is formulated at a microscopic level, on each slip system (eq. (18)). This damage evolution has been given a Rabotnov – Kachanov formulation [36]. Nevertheless, instead of using the applied stress, a kinematic variable $\left|x_d^s\right|$ is chosen as the critical variable. The use of x_d^s instead of $\tau^s$is motivated by the fact that a high frequency fatigue loading must not generate creep damage. This is naturally verified if x_d^s is the critical variable, since the plastic strain amplitude remains negligible and so does x_d^s. After a nucleation period defined by a threshold ν_d (the accumulated viscoplastic strain must reach a given value $\nu > \nu_d$ before damage starts), the damage rate is defined as a power function of $\frac{\left|x_d^s\right|}{\left(1-d_c^s\right)}$, which produces a catastrophic softening and tertiary creep on a macroscopic level (eq. (18)).

$$\text{if } \nu > \nu_d,\ \dot{d}_c^s = \left(\frac{\left|x_d^s\right|}{K_x\left(1-d_c^s\right)}\right)^{m_x} \tag{18}$$

This evolution is somehow identical to previous models, where multiplication of mobile dislocations is a softening mechanism [37-39]. Pore growth is also a source of damage in this kind of alloys, but this is a relevant damage mechanism only in the last stage of life for which very steep tertiary creep occurs for creep strains greater than 5 % [40]. This would create a viscoplastic volume change that is not taken into account in our model.

Based on the experimental observations, the macroscopic creep strain threshold ν_d beyond which the damage evolution is activated is typically between 0.5 and 1.5%, depending on the alloys and temperature. As for the viscoplastic behavior (eqs. (8) and (9)), the evolution of x_d^s is classically defined on each slip system by means of the variables x_d^s (eq. (19)), which have a non-linear evolution with respect to the plastic slip on system , γ^s(eq. (20)).

$$x_d^s = C_d \alpha_d^s \tag{19}$$

$$\dot{\alpha}_d^s = \left(sign\left(\tau^s - x_d^s\right) - d_d \alpha_d^s\right)\dot{\nu}^s - M\left|\alpha_d^s\right|^{m_s} \tag{20}$$

A static recovery term $-M\left|\alpha_d^s\right|^{m_s}$has been added in eq. (20) to allow better predictions of progressive tertiary creep stages. The evolution of this backstress is different for the one presented in eqs. (8) and (9), since the damage kinetics under both isothermal and complex thermal cycling conditions cannot be reproduced using x^s. Such a phenomenological formulation has indeed been shown to take into account in a reasonable way the effect of the thermal cycling frequency on the non-isothermal creep life (not shown here). A further improved version of the damage evolution has been recently used by Ghighi et al to account for long tertiary creep stages at low temperatures/medium to high applied stresses [13].

Identification of the model

Three different versions of the Polystar model exist, with different degrees of refinement. The version of the model presented in this paper, which can be qualified as the “medium version”, has been identified for two alloys (MC2 and CMSX-4®) in the 750 °C-1300 °C temperature range, while only the microstructural part was identified for AM1 alloy. This version of the model only considers γ' volume fraction evolutions and recovery processes during complex thermomechanical histories. The most refined version of the model, which takes into account morphological evolutions of the precipitates (such as γ' rafting) in addition to the microstructure evolutions already taken into account in the medium version of the model, was identified only for MC2 alloy in the 950 °C – 1200 °C temperature range. The less refined version of the model is almost identical to the medium version of the model, without considering kinematic hardening (eqs. (8) and (9)) and static recovery in the damage evolution. It also neglects the coupling between the accumulated creep strain and the dissolution kinetics of the γ' phase (i.e., eq. (10) is used instead of eq. (11)). It is hence only useful for the modeling of the uniaxial creep behavior without a better numerical efficiency. The simplest version requires 28 material parameters (9 of these directly given by microstructure characterizations) to be identified per temperature [12], the medium one (the one presented here) requires 36 parameters per temperature (11 of these given by microstructure analyzes) while the most complex one requires 45 parameters to be identified (17 of these given by microstructure analyzes) [15]. Among all of these parameters, those characterizing the microstructure evolutions can be determined separately through microstructure investigations and specific XRD experiments detailed hereafter.

In the rest of the paper, all of the simulations presented in the figures result from the use of the medium version of the model, except in figure 14 where the most refined version of the model has been used. It has been chosen not to detail this refined version in this article, since this most refined model has been identified in a narrower temperature domain (and it is not applicable to large temperature variations like the ones presented in figures. 11 and 15. The interested reader is referred to le Graverend et al for further details [15].

Microstructure evolutions

The identification of the dissolution/precipitation kinetics of the γ' phase is typically performed using heat treatments and subsequent image analysis techniques [41]. This procedure has been used several times for MC2 and CMSX-4® alloys in the past [12, 19, 42]. figure 5 illustrates such a direct identification of eq. (11) using several short thermal treatments at 1250°C after different amplitudes of creep deformation (in the 0% - 0.5% range) introduced at high temperature (1050°C in the case presented in figure 5). The γ' volume fraction at equilibrium (at 1250 °C here) can be directly determined by using the horizontal asymptote, while the other parameters of eq. (11) (e_{cfl} , δ_l and α_l) are determined through an inverse method.

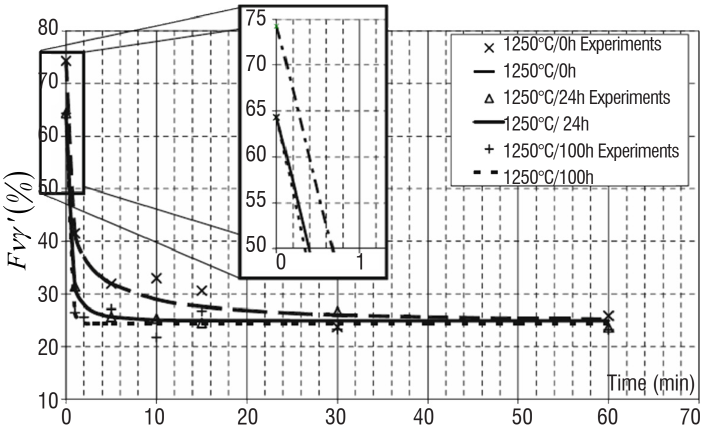

Figure 5. γ' volume fraction evolution in CMSX-4® as a function of the dwell time at 1250 °C without and with a prior creep deformation at 1050°C of 24 hours and 100 hours [42].

Despite the robustness of this method, it has to be reproduced for various temperatures of interest in the γ' dissolution domain (typically above 950 °C, by 50 °C steps) and this method is hence very time consuming. In addition, the fundamental assumption of such a method is that the microstructure evolutions, likely to occur during heating and cooling from/to room temperature, do not affect the microstructure obtained at the end of the heat treatment before final cooling. More recently, a new method has been proposed in close collaboration with Institut Jean Lamour / *Ecole des Mines de Nancy* to calibrate the equations accounting for the γ' volume fraction evolutions. It consists in a quasi-continuous monitoring of the actual γ' volume fraction during a non-isothermal creep test, using XRD characterizations under a synchrotron beam [43]. With such a method, uncertainties in microstructure characterizations due to heating/cooling to room temperature are suppressed. This method has been used for AM1 and CMSX-4® alloys and it is illustrated in figure 6 for AM1 alloy [29, 30, 44]. A very good modeling of the experimental evolution of the large γ' volume fraction (f_l) using the Polystar model is observed in figure 6. Hence, by varying the temperatures reached during overheatings, the heating/cooling rates and the positions of temperature changes in the creep life of the alloy (i.e., the amount of creep deformation), all of the material constants presented in eqs. (11) to (14) can be identified using at the most two to three experiments.

Mechanical behavior and damage law

The material parameters governing the mechanical behavior and the damage evolution have been identified on a large database composed of both isothermal experiments (tensile, low cycle fatigue and creep tests) and non-isothermal creep tests mainly performed on [001] oriented samples. An optimization process using the optimizer module *Z-opt* of the ZéBuLoN software suite [45] was performed to identify the flow rule parameters (n,K), as well as $\tau_0^S ,b; C,d$ and $(Q+Q_{S0})$. These parameters were identified from a set of tension tests at high temperatures with different strain rates (typically, 1.10^{-3} s^{-1}, 1.10^{-4} s^{-1}, 1.10^{-5} s^{-1}), LCF tests with various strain amplitudes (two to three tests) and at least four isothermal creep experiments per temperature. Subsequently, non-isothermal creep experiments with various single overheating lengths and positions in the isothermal creep life under a high temperature/low stress condition were carried out to identify $a^*, \alpha^*, b^*, and\ \beta^*$. The experiments used for the identifications were chosen so that the temperature jumps were always performed once a rafted microstructure had been generated before the overheating. The damage evolution parameters $(K_X ,C_d ,D_d ,M,m_x ,m_s)$ were manually identified from both isothermal and non-isothermal creep tests using the same procedure.

Figure 7 illustrates the model predictions of the non-isothermal creep behavior and durability of the first generation Ni-based single crystal superalloy MC2. Various overheatings close to the γ' solvus of the alloy (overheatings at 1200°C in figure 7) were introduced somewhere in the creep life of the alloy at 1050°C/140 MPa using the burner rig Thalie developed at Institut Pprime [5]. Very good performances of the model are observed, both in terms of elongation and creep life. Indeed, as observed in figure 7, all of the creep stages are properly taken into account, including the new primary creep stage after the overheating and the change in creep strain rate after the overheating resulting from the microstructure evolutions during the overheating.

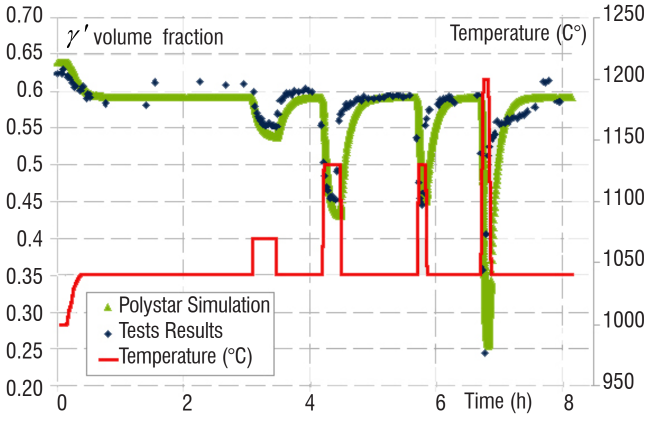

Figure 6 - γ' volume fraction evolution in AM1 alloy (blue dots) as a function of time for a complex non-isothermal creep test [29]. The temperature history appears in red and the model simulation is represented by the green continuous line. The applied stress maintained constant during this experiment.

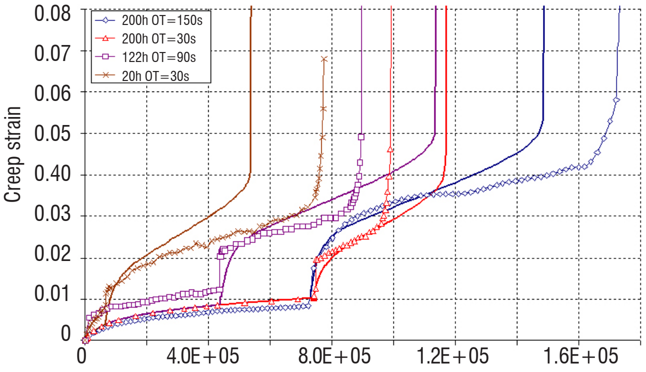

Figure 7 - Comparison between Polystar simulations (continuous curves) and experimental creep elongations (dotted curves) during non-isothermal creep experiments using MC2 alloy [1, 2]. These experiments included a single overheating at 1200 °C of different durations (OT = Overheating Time) ranging from 30 to 150 seconds, introduced somewhere in the creep life at 1050 °C/140 MPa of the alloy. Note that the actual positions of the overheating are included in the legend.

Complex thermomechanical history simulations and industrial applications

Presentation of the MAATRE burner

The evaluation of the Polystar model performances has been performed using very complex thermomechanical histories characteristic of those encountered by the high pressure turbine blades of turboshaft engines in helicopters during certification procedures. As has already been mentioned in the introduction, such procedures consist of a mixture of different engine regimes, including repeated over-temperature events. The use of classical laboratory test benches has already been shown to be excessively conservative (i.e., too low creep lives, too high amount of creep elongation during overheatings) to be representative of the in-service mechanical behavior of Ni-based single crystal superalloys during these events, since heating/cooling rates with a good temperature control are usually too slow [5]. Hence, 150h or ASMET engine tests have been reproduced using a very unique burner rig (the MAATRE burner) developed at Institut Pprime. A schematic illustration of its working principle is shown in figure 8.

As observed in figure 8, a burner based on the combustion of natural gas with air supplies hot gases that are blown onto the sample lying in the testing section. To reach higher temperatures for some very specific conditions, the combustion could be doped with oxygen. These hot gases are accelerated using a convergent located in the exhaust section of the burner, hence allowing a sufficient gas velocity in the testing section and a subsequently high heat exchange at the sample surface to allow very fast heating and cooling rates. Samples are also mechanically loaded (under monotonic or cyclic loading paths) with an electromechanic testing machine or a creep frame and they could be internally cooled by compressed air. Monitoring and controlling all of these equipment parameters (gas and sample temperatures, gas flow, cooling flow and temperatures, sample displacements, applied load of the sample, etc.) as well as managing security are ensured using a central computer. Gas temperatures up to 1650°C can be reached in the testing section, with hot gas velocities up to 400 m.s-1. Controlled heating/cooling rates as high as 150°C/s can be obtained within this equipment, which is essential for the engine tests presented in this paper. The mechanical loading, during the tests presented in this article, was applied with a creep testing machine using dead weights. An illustration of the test bench equipped with this creep testing machine is presented in figure 9.

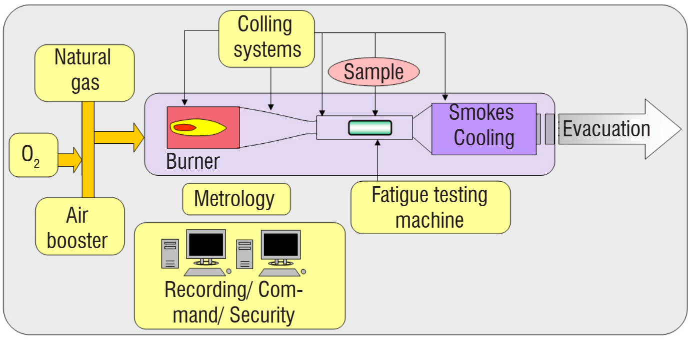

Figure 8 - Working principle of the MAATRE test bench

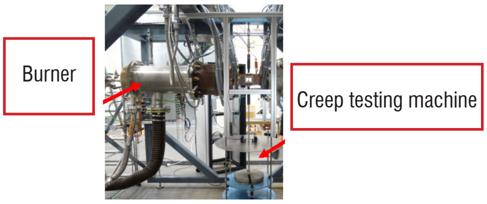

Figure 9 - MAATRE test bench equipped with the creep testing machine

A specific metrology has been developed for measuring both the displacement and temperature of the sample, in order to perform accurate interpretations of the tests. During the subsequently presented tests, the temperature of the sample was measured with a spot welded S type thermocouple. The diameter of this thermocouple must be large enough to ensure a sufficient mechanical resistance to the aerothermal drag generated by the hot gas flow and small enough to avoid thermal perturbations from the thermocouple wire. A 0.35 mm in diameter thermocouple was used. The combustion in the burner section was directly controlled with a closed loop using this temperature measurement. During experiments, elastic, thermal and creep strain were measured using a videoextensometry technique. Strain measurements are performed using markers deposited in the central part of the gage length of the samples, where the temperature is spatially homogeneous (with a +/-3°C accuracy). The interested reader is referred to two previous papers from the authors for further details [4, 16].

Testing conditions

Two kinds of engine tests were performed, namely a “150h” and “ASMET” (Accelerated Simulated Mission Endurance Testing). These tests comprise different stages. These stages can be divided into “long term” temperature steps or successive temperature peaks. The details of these testing conditions are presented in figure 10.

A tensile stress is applied to the specimen during the test. It is worth mentioning here that overheatings around 1220 and 1240 °C are very close to the γ'-solvus (Tsolvus = 1265 °C) of the alloy used for this study, namely, the first generation MC2 alloy [12, 19].

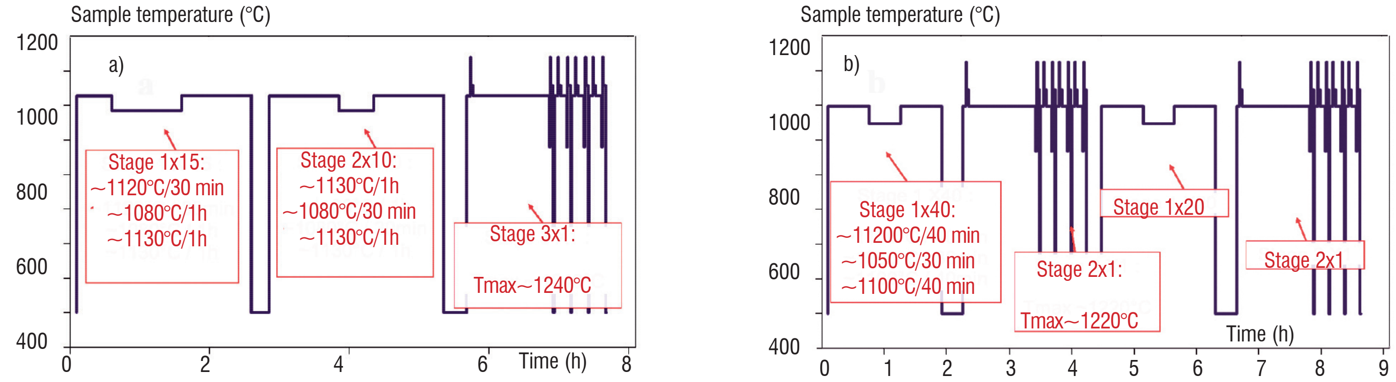

Figure 10 - Testing conditions for the 150h test (a) and the ASMET test (b)

Experimental results and performances of the Polystar model

The evolutions of the viscoplastic strain and measured temperature as a function of time are given in figure 11 for both the ASMET and 150h tests. Under such conditions of strain measurements for a sample loaded under the impact of a gas flow, the creep strain measurement can be considered to be very satisfying. It must be pointed out that the absence of strain measurements between 75 and 100h for the ASMET test (figure 11b) is due to a computer data overflow. According to figure 11, a progressive decrease in the creep rate during the two first stages of the 150h test is observed (figure 11a), and, as expected, a steep increase in the creep rate during the last stage containing the overheatings. Indeed, each temperature peak involves a fast creep strain jump. This fast increase in the strain rate has also been observed in [4]. The ASMET test is less damaging than the 150h one, based on a creep strain criteria (figure 11b). In addition, the creep strain increase during the overheatings is less pronounced compared to that observed during the overheatings of the 150h test. This is consistent with the fact that the overheatings performed during the 150h test are closer to the γ'-solvus of MC2 alloy (see figure 10).

The Polystar performances have been evaluated using these complex experiments performed under combustion environment. The simulations have been performed considering a homogeneous spatial distribution of the temperature at each time. Using such an assumption, a simulation at one Gaussian point can be directly compared to the experimental result. A rather good agreement between the experimental result and the simulation can be observed in figure 12. In addition, it is observed that the model predicts in a reasonable way the creep strain jumps entailed by the overtemperatures. This is more clearly observed in figure 13, where it is observed that the calculated jumps' amplitude is increasing while, experimentally, the amplitude of the creep strain jumps remains almost constant. This difference results from a non-negligible damage increase in the model while, according to microstructural observations performed elsewhere, only limited evidences of creep damage in the form of deformation pores and submicron crack initiation at casting pores were observed [4]. According to the simulation, the material should have failed a few minutes before the end of the test.

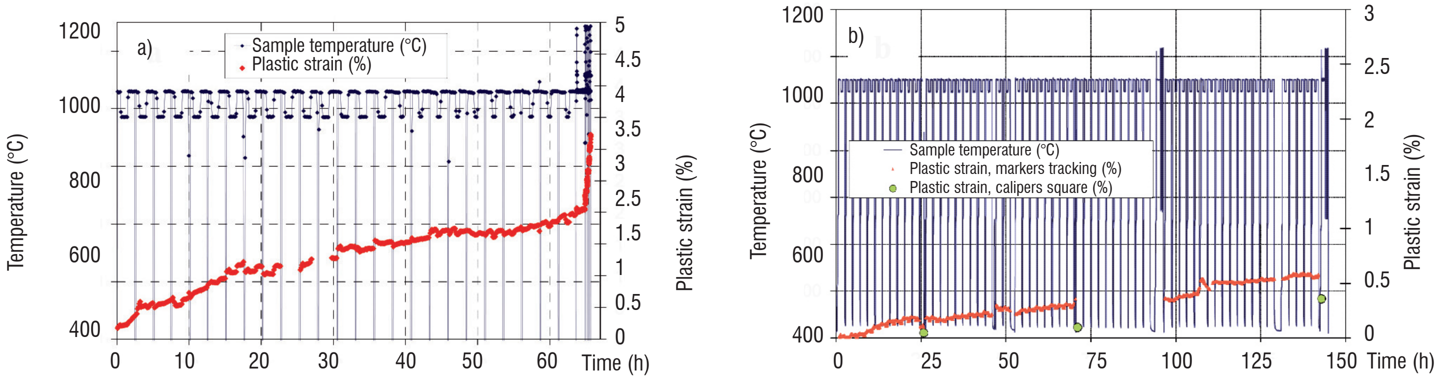

Figure 11 - Evolution of plastic strain (red curves) and sample temperature (blue curves) as a function of time for the 150h (a) and ASMET (b) tests.

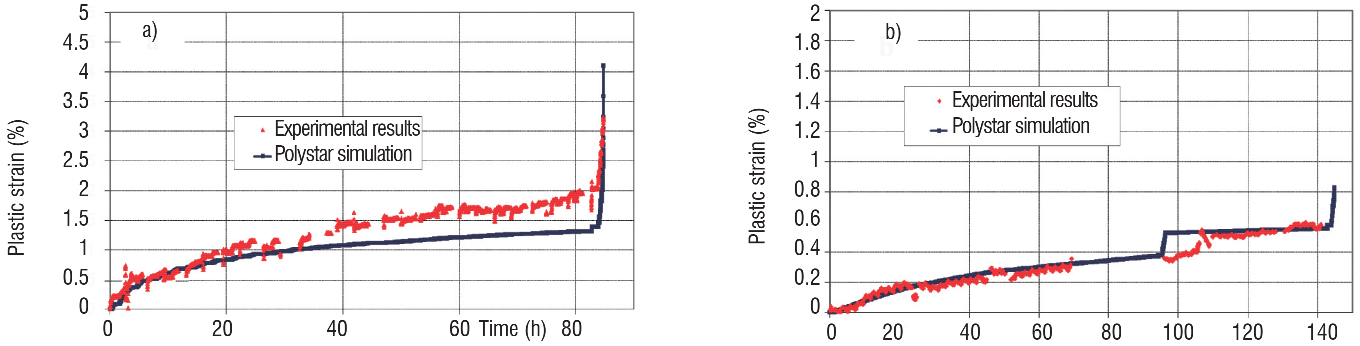

Figure 12 - Comparison between the experimental and simulated creep strain evolutions for the 150h (a) and ASMET (b) engine-like tests.

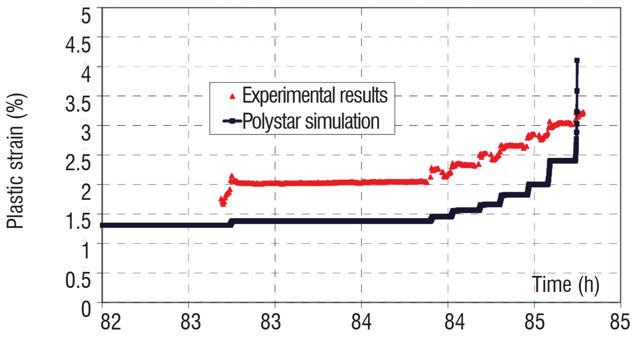

Figure 13 - Comparison between the experimental and simulated creep strain evolutions for the 150h engine-like test during the last stage.

Evaluation of the model under complex mechanical field and industrial applications

The two simulations presented in the previous section showed the Polystar capabilities for estimating the plastic strain monitored during complex tests representative of in-service thermomechanical conditions. The model seems to be very accurate in the lowest temperature range of testing, but it can overestimate the creep strains in the highest ones (T > 1200 °C). This may come from a poorer precision in the model calibration at very high temperature levels. Nevertheless, this model with its additional internal variable is the only one able to capture complex microstructural phenomena, such as dissolution/precipitation of strengthening particles, dislocation recovery processes and their impact on the mechanical behavior. Under very intricate conditions, such as those presented in this article, this model performs better than any other model where the temperature dependence is only taken into account through the temperature dependence of the material coefficients.

As a further evaluation of the model performances, a complex non-isothermal experiment using a bi-notched specimen has been used and compared to a 3D finite element simulation using the Polystar model as a constitutive material behavior. The sample geometry can be observed in figure 14. This experiment under constant

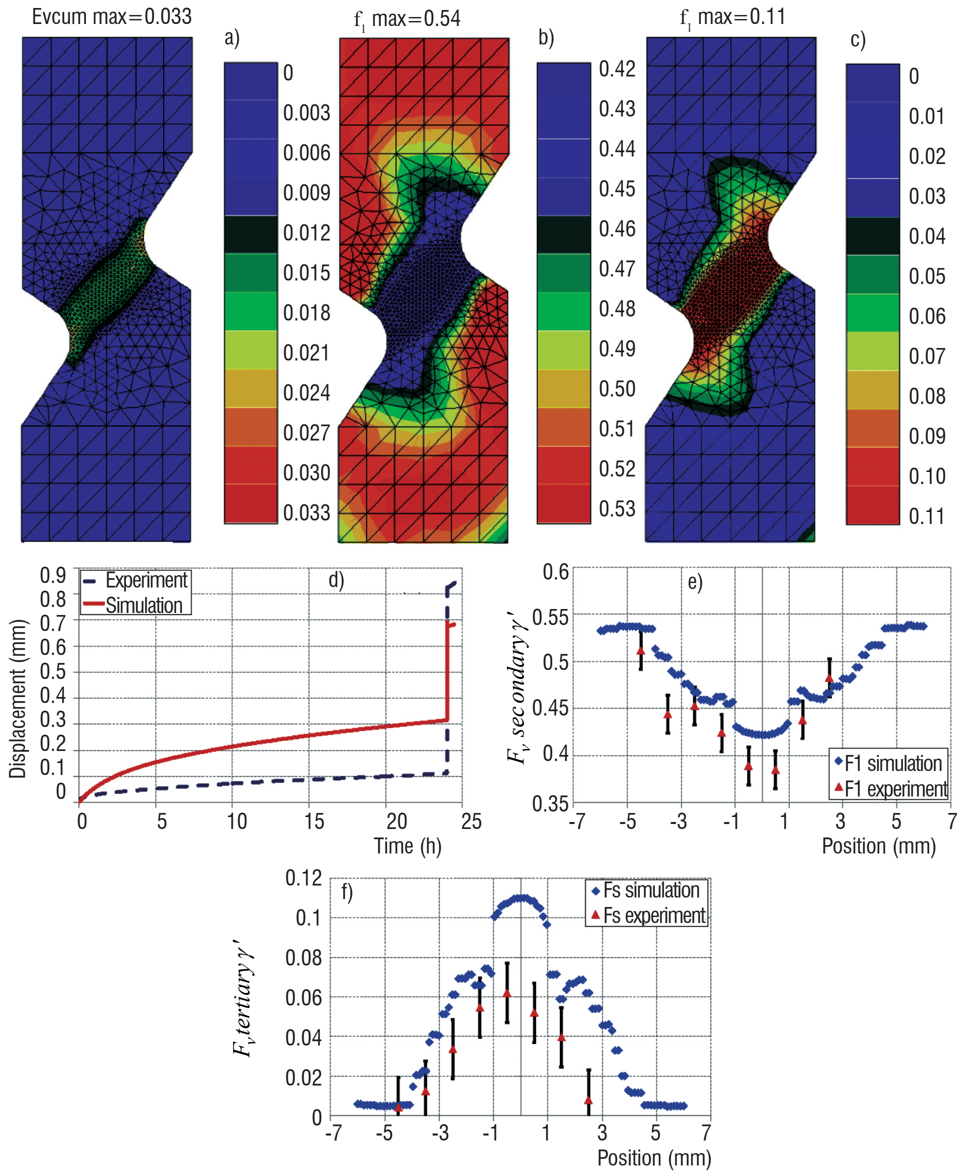

Figure 14 - Prediction of (a) the accumulated plastic strain (ν or evcum), (b) the volume fraction of secondary γ' precipitates (f_l) and (c) the volume fraction of tertiary γ' precipitates (f_s). (d) Comparison between the elongation predicted by the model and the experimental elongation. (e) and (f) correspond respectively to the evolution of the volume fractions of secondary and tertiary γ' precipitates presented in (b) and (c) along a vertical central path shown in (a).

load consists of 24h at 1050 °C, followed by a short temperature spike of 20 seconds at 1200 °C and 30 additional minutes at 1050 °C after the overheating. After testing, microstructure observations were done and volume fraction measurements of secondary (f_l) and tertiary $(f_l)\,\gamma'$ precipitates were performed. Further details about this experiment can be found in [15].

As expected, a greater creep strain at the end of the test is predicted between the two notches (figure 14a). Such a difference in local creep strain greatly affects the evolutions of secondary and tertiary γ' particles. This effect is properly considered by the model (figures. 14a and 14b respectively for fl and fs) through eqs. 11 and 12 to 14. Comparing γ' volume fraction measurements with the simulation along the path defined in figure 14a, a good agreement is observed (figures. 14e and 14f), despite huge difficulties in the experimental characterization of the tertiary γ' evolutions (dissolution/precipitation) [12]. A comparison between the longitudinal creep displacement (along the vertical in figure 14a) monitored during the experiment and the computed one has also been performed. A quite pronounced difference is observed in figure 14d, both during the isothermal part before the overheating and during the overheating itself. Indeed, an overestimation of the creep elongation by the model is observed before the overheating and an underestimation of the creep accumulation is observed during the overheating. Such differences were partly attributed to crystal lattice rotations, where the multi-axial state of stresses are the largest [15].

After such laboratory evaluations/validations of the model under complex thermomechanical histories using smooth specimens or notched ones (technological samples), the model has been introduced in the SAFRAN – Turbomeca Methods Department. The model performances are presently evaluated at Turbomeca using 1D beam-like calculations, each slice of the beam being assigned the spatial average stress and temperature histories of one section of an HP blade profile. Moreover, 3D finite element simulations using Z-Ansys as software and the Polystar model have been performed. A complex thermomechanical history (presented at the bottom of figure 15) representative of a certification test has been chosen as an input loading. Figure 15 shows the evolution of the von Mises stress, of the accumulated creep strain (ν) and of the secondary γ' volume fraction (fl) distributions in an HP blade profile after one, five and ten missions. It is observed in this figure that the hottest areas close to the leading edge, where the γ' volume fraction turns to blue, do not correspond necessarily to the most severely creep-deformed areas. In addition, it is observed that even if the von Mises stress distribution hardly evolves, a creep strain accumulation is observed and an even lower γ' volume fraction at the leading edge is obtained thus increasing the mission number, due to a higher creep strain, which accelerates the γ' dissolution (see eq. 11). Such calculations are presently used to predict the elongation and the durability of HP blades during complex certification engine tests. It is especially useful to evaluate the safety margins that can be used during the certification of new turboshaft engines for helicopters. According to Turbomeca practices, this model may also reduce the design durations/costs with a closer-to-reality prediction of the creep behavior (in terms of elongation and durability) of an HP blade made of Ni-based single crystal superalloys.

Limitations of the model, on-going activities and additional potential use

According to various previous studies, several limitations listed hereafter were already observed in the model:

- A poor description of the cyclic ratcheting was observed by le Graverend [46] under uniaxial high temperature dwell-fatigue conditions. No solution has been found up to now and one possible solution would be the introduction of a second kinematic hardening term in the yield function in the octahedral slip systems.

- The model was observed to provide poor predictions of the elongation/shear strain under isothermal and non-isothermal multiaxial loadings (e.g., tension-torsion tests using single crystalline tubes, tension tests on notched samples) [46]. This was especially observed when large shear stresses were introduced. Figure 14d is a good illustration of this. Some on-going investigations by A. Mattiello in the context of a collaboration between LMT Cachan, SAFRAN – Turbomeca and Institut Pprime are devoted to the formulation of the model in a large strain context, to account for the crystal lattice rotations observed under such conditions [47]. In addition, a better identification of the interaction matrix between slip systems and the introduction of cube slips will further be evaluated. Taking into account lattice rotations should also allow a better modeling of the tertiary creep stages when considering the tensile creep acceleration for misoriented samples [12, 13].

- Even if the model was initially devoted to the modeling of very high temperature ($T > 1000$ °C) non-isothermal creep conditions, low temperature creep under a large applied stress condition remains a critical issue for cooled components, especially in the web sections [48, 49]. Under such conditions, the <112>{111} slip activity has to be considered for various alloys, since it can contribute to large primary creep strains of up to 10 pcts [49]. The associated question is how the identification of the materials parameters characterizing such a slip activity on <112>{111} systems must be done, since the slip activity on these systems results from a classical <110>{111} slip activity (i.e., both slip systems are co-existent) and is highly dependent on the crystal orientation and applied stress. This work is presently in progress for the case of CMSX-4® alloy [47].

- Finally, due to the large number of internal variables introduced in the model, computation times are rather long, especially for industrial perspectives. A reduced model (i.e., suppressing some second-order internal variables) or more efficient calculation schemes must be made.

In regard to the potential additional uses of the model, it has been shown in the previous sections that the Polystar model provides good evaluations of the microstructure evolutions, especially in terms of secondary γ' precipitate volume fraction f_l (see for example figures 6 and 14). In addition to the computation of the mechanical behavior and durability of Ni-based single crystal superalloys used for the components of the hot sections of gas turbines, the microstructure module of the model can also be used as an expert assessment tool for the estimation of local metal temperature histories. Indeed, knowing the T41 temperature evolution in an engine (T41 being the gas temperature at the exhaust of the combustion chamber), the resulting true metal temperature history can be computed by an inverse method, using a final microstructure inspection of a component. This microstructure part of the model can even be considered as a potential tool for validating thermal calculation methodologies used in design departments.

Finally, since the model is sensitive to some initial microstructure features, such as the γ' size or the γ' volume fraction at thermodynamical equilibrium, this model is also, by nature, sensitive to some microstructural differences from the "standard state" likely to result from the elaboration processes. As an example, an evaluation of the impact of a small variation in the as-received γ' content on the mechanical response can be done easily with this model, as has already been shown in the pioneering paper on this model [12]. A more systematic study would be required to obtain a good estimation of scatter bands around the average mechanical behavior resulting from such small variations of the parameters representing the initial microstructure. All of this work remains, however, to be done.

Concluding remarks

A microstructure sensitive model (the Polystar model) has been developed within the framework of crystal plasticity, in order to be predictive of the non-isothermal viscoplastic behavior of Ni-based single crystal superalloys, especially when rapid microstructure evolutions are likely to occur, such as γ' strengthening phase dissolution, dislocation recovery processes, or hyperfine precipitation in the γ matrix. Such rapid microstructure evolutions are encountered during the certification procedure of aeronautic gas turbines and they lead to transient mechanical behaviors that cannot be reproduced with standard constitutive modeling approaches without any additional internal variables. This model, mainly developed since 2007 at Institut Pprime – ISAE-ENSMA (among other partners), is based on the introduction of new internal variables, such as the γ' volume fraction of coarse

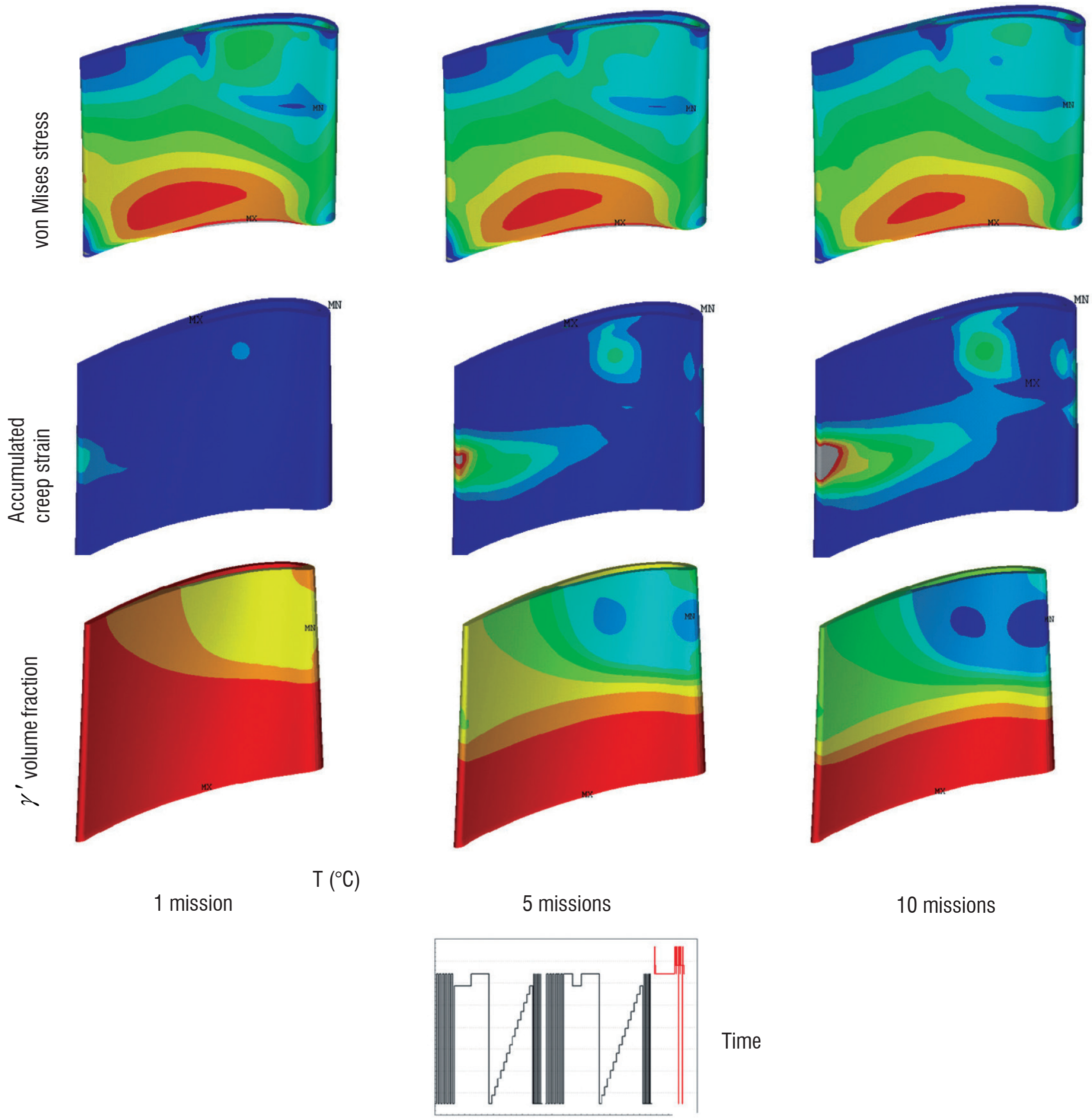

Figure 15 - Evolutions of the von Mises stress, of the accumulated creep strain (ν) and of the γ' volume fraction (f_l) spatial distributions in an HP blade profile, as a function of the number of certification missions. The mission used for the simulation is presented at the bottom of this figure and is typical of a 150h engine test. Color code: higher von Mises stresses, higher accumulated creep strain and lower γ' volume fraction fl from blue to red.

and small particles or a temperature dependent aging variable, to account for dislocation recovery. Various versions of the model have been tailored with a more or less refined description of microstructure evolutions.

It is shown in this paper that the model provides good predictions of the non-isothermal viscoplastic behavior of Ni-based single crystal superalloys under complex thermomechanical loading histories. It is also shown that the identification and validation of this model can be improved and eased by the use of very specific experiments, such as in situ XRD creep experiments under a synchrotron beam to accurately evaluate microstructure evolutions, as well as by performing very unique experiments with fast heating and cooling rates up to extreme temperatures. Such unique experiments are recreated at Institut Pprime with the large scale facility MAATRE, a specific burner rig fully developed internally to be able to achieve representative testing conditions of the hottest sections of gas turbines, with an excellent metrology.

After the validation of the Polystar model in a laboratory context, this model has been implemented in the SAFRAN – Turbomeca lifing chain for a deeper evaluation within an industrial context in the Methods Department. Full-scale 3D calculations were successfully performed and, despite all of its remaining deficiencies presented in this paper, the Polystar model is the set of constitutive equations that provides the best estimations of the HP blade elongation and durability during engine certification procedures ■

Acknowledgements

Financial support from the French Ministry of Defense (DGA) and SAFRAN-Turbomeca is gratefully acknowledged. The authors are also grateful to SARGI S.A. for their help and efficiency in the design of the very unique burner used in MAATRE. The financial support from the CPER and FEDER (Poitou-Charentes Region, Vienne Department, European Community, Poitiers Agglomeration and French Education and Research Ministry) for the construction of MAATRE is also gratefully acknowledged.

JC, JM and FM are grateful to SAFRAN-Turbomeca for the continuous collaboration on superalloys for over 12 years: Dr. Elisabeth Ostoja-Kuczynski, Dr. Zéline Hervier, Dr. Antoine Organista, Dr. Sandrine Lesterlin and Dr. François Vogel are especially thanked for their continuous interest and encouragement. Former PhD students at Institut Pprime and SAFRAN-Turbomeca (Dr. Julien Ghighi and Dr. Rémi Giraud) who used the Polystar model and who participated to its development are also gratefully acknowledged for their contribution. Dr. Serge Kruch and Dr. Franck Gallerneau (ONERA/DMSM) are gratefully acknowledged for their help in improving the most refined version of the Polystar model. Dr. Alain Jacques, Dr. Thomas Schenk and Olivier Ferry (Institut Jean Lamour, Ecole des Mines de Nancy) are acknowledged for their valuable experimental contributions (XRD during non-isothermal creep experiments using a synchrotron beam) and for stimulating discussions. The Cannon Muskegon Corporation (Dr. Jacqui Wahl and Dr. Ken Harris) is gratefully acknowledged for providing several Ni-based single crystal samples. Stimulating discussions and exchanges with Dr. Farida Azzouz (Centres des Matériaux, MinesParistech) have been highly appreciated.

JC is indebted to Pr. Georges Cailletaud (Centres des Matériaux, Mines Paristech) who shared all of his experience in the pioneering developments of the Polystar model and for all of the stimulating discussions. Finally, JC is very grateful to Dr. Serge Kruch and Dr. Esteban Busso for their continuous encouragement in the preparation of this article

References

[1] J. CORMIER, X. MILHET and J. MENDEZ - Acta Materialia, 2007. 55(18): p. 6250-6259.
[2] J. CORMIER, J., X. MILHET, F. VOGEL, and J. MENDEZ - Superalloys 2008. Seven Springs, Champion, PA, USA.
[3] J.-B. LE GRAVEREND, , J. CORMIER, F. GALLERNEAU, S. KRUCH and J. MENDEZ - Materials and Design. 2014. 56(April): p. 990-997.
[4] F. MAUGET, D. MARCHAND, G. BENOIT, M. MORISSET, D. BERTHEAU, J. CORMIER, J. MENDEZ, Z. HERVIER, E. OSTOJA-KUCZYNSKI and C. MORICONI - Eurosuperalloys 2014. 2014. Presqu'île de Giens, France: Matec Web of Conferences.
[5] J. CORMIER, X. MILHET, J.-L. CHAMPION and J. MENDEZ - Advanced Engineering Materials. 2008. 10(1-2): p. 56-61.
[6] J. CORMIER, X. MILHET and J. MENDEZ - Materials Science and Engineering A, 2008. 483-484: p. 594-597.
[7] J.-B. LE GRAVEREND, J. CORMIER, M. JOUIAD, F. GALLERNEAU, P. PAULMIER and F. HAMON - Materials Science and Engineering, 2010. A527(20): p. 5295-5302.
[8] G. CAILLETAUD - 1979, Doctoral Thesis, University of Paris VI.
[9] G. CAILLETAUD and J.-L. CHABOCHE - Third International Conference on Mechanical Behaviour of Materials (ICM-3). 1979. Cambridge (G.B.): Pergamon Press.
[10] G. CAILLETAUD, J.P. CULIE and H. KACZMAREK - 1983. Stockholm: Tiré à part ONERA T.P. n° 1983-86.
[11] J. CORMIER and G. CAILLETAUD - Technische Mechanik, 2010. 30(1-3): p. 56-73.
[12] J. CORMIER and G. CAILLETAUD - Materials Science and Engineering, 2010. A527(23): p. 6300-6312.
[13] J. GHIGHI, J. CORMIER, E. OSTOJA-KUCZYNSKI, J. MENDEZ, G. CAILLETAUD and F. AZZOUZ - Technische Mechanik, 2012. 32(2-5): p. 205-220.
[14] J.-B. LE GRAVEREND, J. CORMIER, S. KRUCH, F. GALLERNEAU and J. MENDEZ - Advanced Materials Modelling for Structures H. Altenbach and S. Kruch, Editors. 2013, Springer. p. 189-199
[15] J.-B. LE GRAVEREND, J. CORMIER, F. GALLERNEAU, P. VILLECHAISE, S. KRUCH and J. MENDEZ - International Journal of Plasticity, 2014. 59: p. 55-83.
[16] F. MAUGET, F., D. MARCHAND, M. MORISSET, D. BERTHEAU, J. CORMIER and J. MENDEZ - Matériaux & Techniques, 2012. 6/7: p. 541-545.
[17] L. MÉRIC AND G. CAILLETAUD - Journal of Engineering Materials and Technologies, 1991. 113: p. 171-182.
[18] G. CAILLETAUD, J.-L. CHABOCHE, S. FOREST and L. RÉMY - La Revue de Métallurgie, 2003(Feburary): p. 165-172.
[19] J. CORMIER, J., X. MILHET and J. MENDEZ - Journal of Materials Science, 2007. 42(18): p. 7780-7786.
[20] J. CoRMIER, J., M. JOUIAD, F. HAMON, P. VILLECHAISE and X. MILHET - Philosophical Magazine Letters, 2010. 90(8): p. 611-620.
[21] R. GIRAUD, R., Z. HERVIER, J. CORMIER, G. SAINT-MARTIN, F. HAMON, X. MILHET and J. MENDEZ - Metallurgical and Materials Transactions A, 2013. 44A: p. 131-146.
[22] A. DLOUHY, M. PROBST-HEIN and G. EGGELER - Material Science and Engineering, 2001. A309-310: p. 278-282.
[23] M. PROBST-HEIN, A. DLOUHY and G. EGGELER - Acta Mater, 1999. 47(8): p. 2497-2510.
[24] M. BENYOUCEF, N. CLEMENT and A. COUJOU - Material Science and Engineering, 1993. A164: p. 401-406.

[25] B. FEDELICH, A. EPISHIN, T. LINK, H. KLINGELHÖFFER, G. KÜNECKE and P.D. PORTELLA - Superalloys 2012. 2012. Seven Springs, PA, USA: TMS.
[26] B. FEDELICH, B., A. EPISHIN, T. LINK, H. KLINGELHÖFFER, G. KÜNECKE, and P.D. PORTELLA - Computational Materials Science, 2012. 64: p. 2-6.
[27] R.C. REED, D.C. COX and C.M.F. RAE - Materials Science and Engineering, 2007. A 448: p. 88-96.
[28] J.K. TIEN and S.M. COPLEY - Met. Trans., 1971. 2: p. 215-219.
[29] J.-B. LE GRAVEREND, L. DIRAND, A. JACQUES, J. CORMIER, O. FERRY, T. SCHENK, F. GALLERNEAU, S. KRUCH and J. MENDEZ - Metallurgical and Materials Transactions A, 2012. 43A: p. 3946-3951.
[30] J.-B. LE GRAVEREND, A. JACQUES, J. CORMIER, O. FERRY, T. SCHENK and J. MENDEZ - Acta Materialia, 2015. 84: p. 65-79.
[31] H. HUFF and H. PILLHOFER - Superalloys 1988. 1988: TMS, Warrendale, PA.
[32] S. WANG, D.S. XU, N. MA, N. ZHOU, E.J. PAYTON, R. YANG, M.J. MILLS and Y. WANG - Acta mater, 2009. 57: p. 316-325.
[33] J. CORMIER - Phd Thesis, 2006, University of Poitiers - ISAE-ENSMA, Poitiers, France.
[34] W. CHEN and J.-P. IMMARIGEON - Scripta Materiala, 1998. 39(2): p. 167-174.
[35] B. FEDELICH, G. KUNECKE, A. EPISHIN, T. LINK and P. PORTELLA - Materials Science and Engineering, 2009. A 510-511: p. 273-277.
[36] L.M. KACHANOV - Isv. Akad. Nauk. SSR. Otd. Tekh. Nauk., 1958. 8: p. 26-31.
[37] N. MATAN, D.C. COX, P. CARTER, P.A. RIST, C.M.F. RAE and R.C. REED - Acta mater, 1999. 47(5): p. 1549-1563.
[38] M. MCLEAN and B.F. DYSON - Journal of engineering Materials and Technology, 2000. 122: p. 273-278.
[39] N.X. HOU, Z.X. WEN and Z.F. YUE - Materials Science and Engineering, 2009. A 510-511: p. 42-45.
[40] J. KOMENDA and P.J. HENDERSON - Scripta Materiala, 1997. 37(11): p. 1821-1826.
[41] J.-R. VAUNOIS, J. CORMIER, P. VILLECHAISE, A. DEVAUX and B. FLAGEOLET - 7th International Symposium on Superalloy 718 and Derivatives. 2010. Pittsburgh, PA, USA: TMS.
[42] R. GIRAUD, J. CORMIER, Z. HERVIER, D. BERTHEAU, K. HARRIS, J. WAHL, X. MILHET, J. MENDEZ and A. ORGANISTA - Superalloys 2012. 2012. Seven Springs, PA, USA.
[43] A. JACQUES and P. BASTIE - Phil. Mag., 2003. 83(26): p. 3005-3027.
[44] T. SCHENK, T., A. JACQUES, J.-B. LE GRAVEREND and J. CORMIER - in TMS 2015 Annual Meeting. 2015. Orlando, Fl, USA.
[45] J. BESSON, R. LE RICHE, R. FOERCH and G. CAILLETAUD - Revue Européenne des Eléments Finis, 1998. 7: p. 567-588.
[46] J.-B. LE GRAVEREND - PhD. Thesis 2013, ISAE-ENSMA & ONERA, Chatillon, France.
[47] A. MATTIELLO - PhD. Thesis, 2017, ISAE-ENSMA & ENS Cachan, Cachan, France.
[48] D. DYE, A. MA and R.C. REED - Superalloys. 2008. Seven Springs, Champion, PA, USA: TMS.
[49] C.M.F. RAE and R.C. REED - Acta mater, 2007. 55: p. 1067-1081.

AUTHORS

Jonathan Cormier received his Engineering diploma and his Doctoral degree in Mechanics of Materials both from ISAE-ENSMA in 2003 and 2006 respectively. Since 2002, he has been involved in various experimental and numerical studies on the deformation and damage processes of high temperature materials, with a special focus on the role of microstructure evolutions on the mechanical resistance of cast (SX/DS) and wrought superalloys and on the durability of TBC coatings under close-to-reality loading conditions (using unique burner rig experiments). Since 2007, he works as an Associate professor at ISAE-ENSMA in 2007 (Institut Pprime, UPR CNRS 3346, Futuroscope-Chasseneuil). He authored/co-authored over 50 international publications in these fields and he acts as a member of the Metallurgical and Materials Transactions A Board of review.

Florent Mauget received his engineering diploma in 2007 from Polytech'Orléans. He has worked at Institut Pprime since 2007 as an engineer. He designed and developped a new burner rig facility called MAATRE used to perform thermomechanical fatigue tests under hot gas flow. He is involved in studies on Ni-based superalloys behavior in close to realistic conditions as well as studies on the dammage mechanisms of thermal barrier coatings systems.

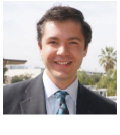

Jean-Briac le Graverend received his Engineering diploma from ISAE-ENSMA in 2009 and his PhD in Mechanics of Materials from ISAE-ENSMA and ONERA in 2013 during which he studied the anisothermal deformation and damage of Ni-based single crystal superalloys under conditions representative of in-service operation. After his graduation, he did a post-doc at Caltech during which he worked on characterizing the viscoelastic properties of electromechanical composites under temperature and electric field control. Since 2014, he works as an Assistant Professor within the department of Aerospace Engineering at Texas A&M University. His research goals are to predict the mechanical behavior of materials (metallic and ceramic) at high temperature by means of a multi-scale approach using experimental (high temperature mechanical testing, microstructure observation, tomography, and synchrotron radiation), theoretical (crystal plasticity, phase field, and incremental variational principle), and computational (FE simulation) tools.

Clara Moriconi received her Engineering diploma from ISAE-ENSMA in 2009 and her PhD in Mechanics of Materials from ISAE-ENSMA in 2012 during which she worked on modelling of fatigue crack propagation in gaseous hydrogen using cohesive zone elements and a specifically-designed material law. Since 2013, she has been working as a numerical methods engineer at TURBOMECA - a French manufacturer of gas turbine turboshaft engines for helicopters, in the field of creep and fatigue life prediction of turbine components. Her mission is to constantly strive to improve methods used for life prediction of TURBOMECA structures.

José Mendez, Doctor of Sciences from ENSMA and Director of Research at CNRS. He is involved in experimental studies on the fatigue damage mechanisms of metallic materials. His current fields of interest are: 1) Damage mechanisms of structural materials under monotonic and cyclic loading; 2) Relation between microstructure and mechanical properties (fatigue, creep-fatigue); 3) Aging effects; 4) Effect of temperature and environment (air, high vacuum) on fatigue properties; 5) Improvement of fatigue resistance by thin coatings or other surface treatments; 6) Microstructure optimisation of advanced materials: titanium alloys, nickel base superalloys, stainless steels, high strength steels. He authored or co-authored more than 120 publications in these fields.

S. Kruch, P. Kanouté, V. Bonnand
(ONERA)

E-mail: serge.kruch@onera.fr

DOI : 10.12762/2015.AL09.08

ONERA's Multiaxial and Anisothermal Lifetime Assessment for Engine Components

This paper presents the calculation methods developed at ONERA to assess the lifetime of aeroengine structures subjected to multiaxial thermo-mechanical loadings. The complexity of the steps required in this process has grown over the past years, in order to take advantage of extremely accurate observations in materials and more precise experimental results. The research activities in the field of fatigue are presented within a framework that covers microstructural observations, mechanical testing, the development of constitutive equations and fatigue damage models associated with numerical calculations. All of these steps are today closely interrelated in the complex analysis of lifetime predictions. A fundamental aspect is highlighted: the simultaneous consideration of multiaxial and anisothermal loadings, which requires specific developments. These points are detailed, illustrated by many examples of applications and positioned with respect to research works in the literature.

Introduction

The lifetime prediction of complex structures, such as the high temperature components of aircraft engines is a critical step in the design process. Despite the number, the complexity and the effectiveness of existing lifetime assessment models in the literature (see the reviews of [32, 76, 66, 47 and 8]), none of them is far from unanimous. Effectively, these models must be integrated into a lifetime analysis workflow and require a consistency between the determination of mechanical fields in the component and the use of these fields in the fatigue model.

This workflow, schematically detailed in figure 1, is divided into several sequential steps, as generally admitted for metallic materials. It starts with the observation and the characterization of the material microstructure at the finest scales (grains, dislocations, precipitates etc.).

This first stage, conducted in parallel with some mechanical characterization tests, is essential to propose constitutive equations reproducing the observed phenomena. This formalism can be described by a purely phenomenological macroscopic approach [11] or by some multi-scale approaches [46], whose complexity will depend on the local phenomena to be taken into account regarding the effects of the microstructure and the dissipation mechanisms observed at this local scale. The third step consists in computing the component using the constitutive equations by the finite element method, in order to determine all of the stabilized mechanical fields (stresses, strains and internal variables) and then to predict the lifetime with the adequate fatigue damage model. In our analysis, the lifetime is related to the number of cycles before the detection of the macroscopic crack initiation with a conventional experimental device. Once the crack initiates, further analysis consists in following the crack propagation as a function of the applied loads and the stress concentrations, using classical tools within the Linear Fracture Mechanics framework [69, 26, 48], or more sophisticated ones taking into account the generalized plasticity [17, 1, 25, 42, 54].

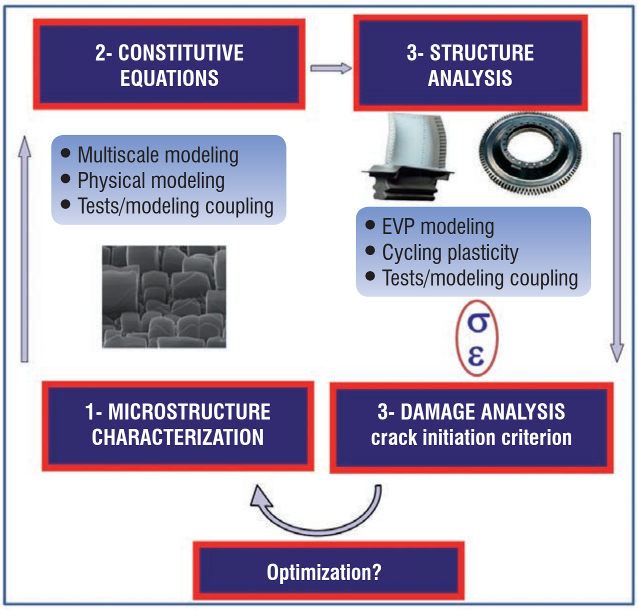

Figure 1 – Lifetime analysis workflow used as an optimization loop

In the near future, it will be possible to propose an optimization loop consisting in finding the best microstructures in the component, in order to delay the crack initiation and then improve the lifetime of the structure.

Generally, this dimensioning process for metallic structures involves at least the steps 2 to 4 which are the most critical and require the consistency cited above. The damage model must be adapted to the complexity of the performed calculation (elasticity, with reduced models, viscoplasticity taking into account strong non-linearities, only to mention growing complexities) or, conversely, the constitutive equations must be consistent with the fatigue damage model, depending on the availability of the models in the computational codes and/or the degree of sophistication of the analysis.

This consistency is the key to achieving correct results and reducing the scatter that is often observed.

In this paper, we focus our analysis on the more complex methods, based on calculations taking into account the non-linear behaviors linked to the cyclic hardening or softening of the material, the relaxation of the mean stress or the ratcheting, to name only the phenomena that are commonly observed. These computations of the material behavior are therefore associated with the fatigue damage models able to integrate all of this available information. Two fundamental issues are addressed: the loading multiaxiality and the temperature effects. However, this modeling step cannot be achieved without the development and validation of experimental tests. Again, the complexity of the test increases with the phenomena that we want to highlight, starting with "conventional" isothermal tests and achieving complex multiaxial anisothermal fatigue tests. The goal is to get closer to the operating conditions of the component, reproducing the temperature maps and the mechanical loads with regard to the geometrical stress concentrations in the best way possible.

The paper is divided into four sections. The first one is devoted to the presentation of constitutive equations developed at ONERA to model the non-linear behavior in cyclic elasto-viscoplasticity of metallic superalloys used in the hot parts of engine aircrafts. The second section presents an extensive literature review on fatigue damage models with respect to the position of our models. In the third section, particular emphasis is placed on the description of multiaxiality and mean stress effects, together with the development of sophisticated experimental tests. The last section of this paper presents some applications of this workflow analysis performed on increasingly complex structures, ranging from classical characterization tests up to real operating ones.

Cyclic inelastic analysis

The development of constitutive equations within the general thermodynamics framework of the continuum media and specifically in elasto-viscoplasticity is the core activity of the Metallic Materials and Structures Department at ONERA. This modeling stage is fundamental to properly reproduce the anisothermal viscoplastic cyclic behavior of the material, which can be complex regarding the several phenomena observed in service. For this purpose, thermo-mechanical tests have been developed, together with the modeling approach, allowing to observe and to characterize the dissipative mechanisms, in order to identify the material parameters of the constitutive equations and, finally, to validate these models on structural specimens representative of aeroengine parts in terms of stress/strain fields.

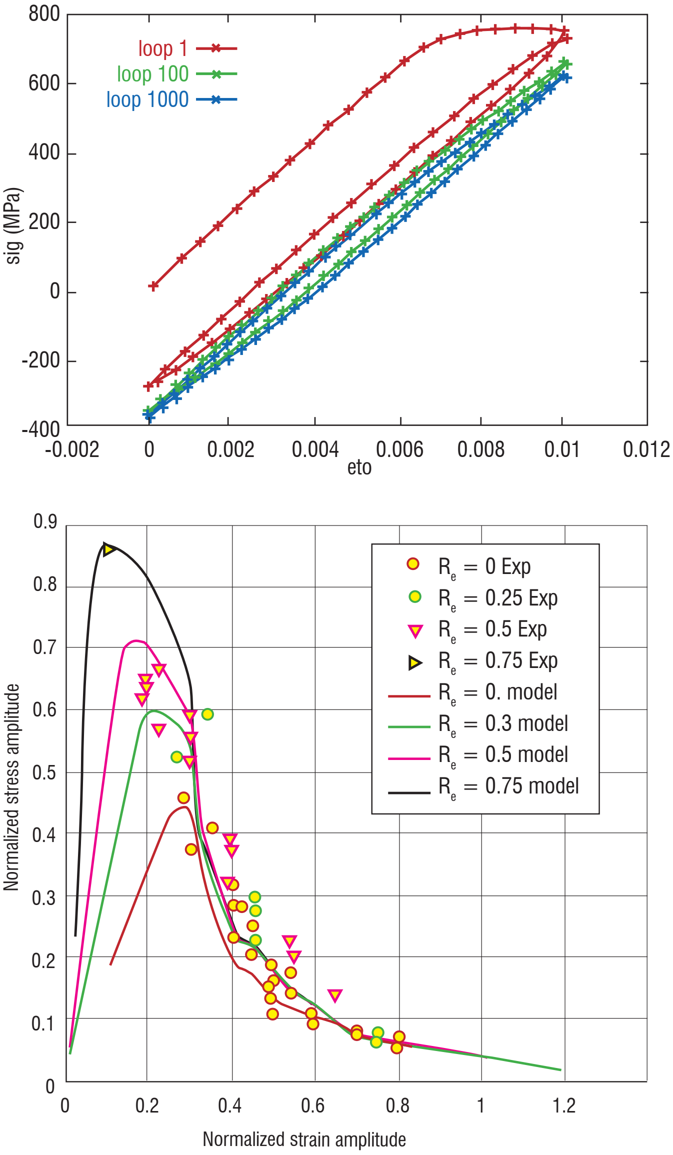

Figure 2 – Ti64, cyclic softening (up) and mean stress relaxation (down)

The observation of experimental results of the Ti64 superalloy cyclic behavior in figure 2 shows a cyclic softening when the material is loaded under constrained strain. Also, for a strain ratio ($\varepsilon_{min}/\varepsilon_{max}$) equal to 0 and a strain amplitude lower than 1%, the mean stress does not relax to 0 as presented in figure 2 (right). It is therefore essential that the constitutive equations representative of the material behavior take into account these phenomena, in order to correctly predict the stress and strain fields at the stabilized state in the structural component, i.e., their levels and also their amplitudes. For this purpose, the formalism adopted to correctly represent the cyclic behavior of metallic materials is characterized by:

- A criterion for the flow rule based on the octahedral shear stress invariant,
- Non-linear isotropic hardenings (to describe the cyclic softening or hardening),
- Non-linear kinematic hardenings (to describe the Bauschinger effect), or more complex relations, in order to reproduce the partial relaxation of the mean stress for dissymmetric strain loading conditions, as observed experimentally (see figure 2) [10].
- This characterization being performed for high temperatures, the viscosity of the material is described by a Norton law, or more recently by a hyperbolic sine law, in order to be able to simulate the behavior in a wider range of strain rates, namely a saturation of the strain rate effects for high plastic strain rates.

These constitutive equations are the basis of the model for isotropic materials. Based on the same formalism but performed at the scale of the grain, a crystal plasticity model has been proposed by [56] and recently improved at ONERA by the introduction of a recovery term in the back stress, to allow a better description of the secondary creep in metals. In this model, internal variables related to the isotropic and kinematic hardenings are introduced on each crystallographic slip plane. The model takes the anisotropic behavior of metallic materials implicitly into account and it has been successfully applied to model the non-linear behavior of a f.c.c. Ni-based single crystal superalloy. In [5] authors investigated torsion tests of a single crystal superalloy at 950°C. These tests were performed under torque control and show the structural effect due to the crystal viscoplasticity (figure 3). This peculiar case requires Finite Element calculations, due to the appearance of zones with higher strains depending on the material secondary direction and obviously to the complex redistribution of stresses. This work highlighted the importance and the impact of crystal anisotropy (octahedral and cubic slip systems) on mechanical behavior.

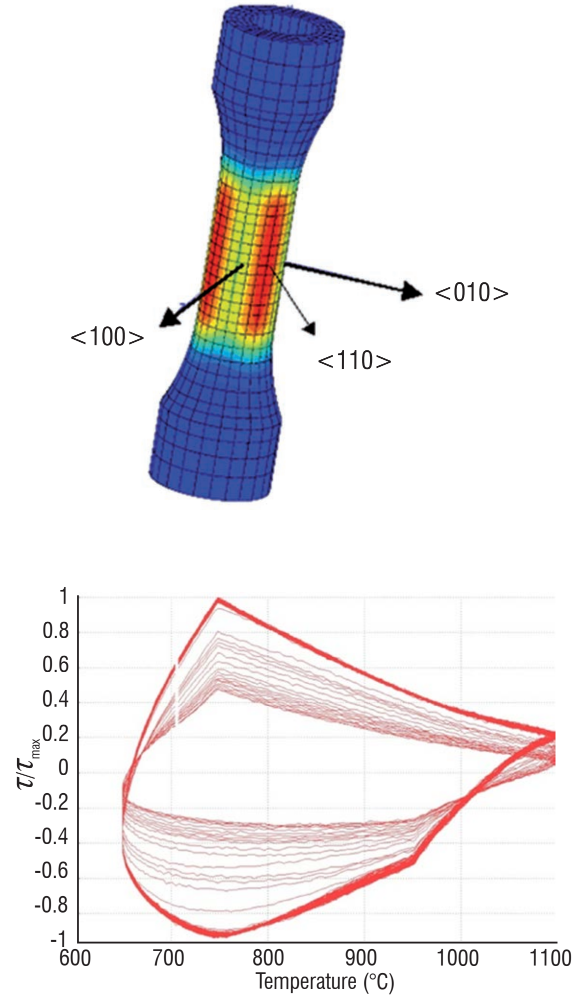

Figure 3 – Torsional fatigue at 950°C of a single crystal superalloy

This work has been recently improved by [33] and [39], who have investigated the influence of the evolution of the microstructure on the mechanical properties of this single crystal superalloy. When the material is subjected to creep at high temperatures, its microstructure evolves and precipitates lose their initially cuboidal shape to reach a rafted pattern. This rafting process has a strong influence on the macroscopic behavior. Some additional internal variables have been introduced in the constitutive equations, in order to describe the evolution of the shape of the precipitates as a function of the load history and its impact on the material parameters. The result of this analysis is shown in figure 4, which presents a comparison between cyclic tests performed on both the reference material and the modified microstructure. In this figure it is possible to see the influence of the rafted microstructure on the overall behavior, inducing a softer macroscopic response that is qualitatively well represented by the proposed model. Work is in progress to improve the results of the modeling.

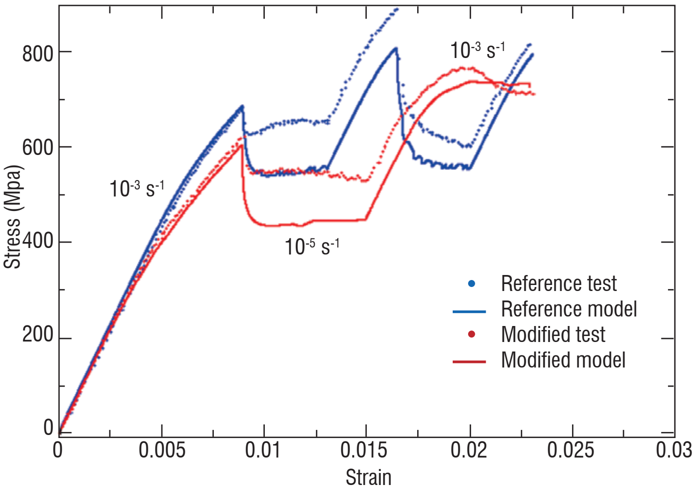

Figure 4 – Tension tests and simulations at two different strain rates, taking into account ageing effects

A similar approach has been proposed for a polycrystalline Nickel based superalloy, N18, [4]. A precipitation model [68] was improved to predict the evolution of the size and the volume fraction of γ' secondary and tertiary precipitates as a function of the thermal history. The influence of the precipitate distribution on the mechanical response of the material is then introduced in the plastic threshold of the viscoplastic model. More specifically, Boittin [4] used, to account for the precipitate distribution, relations based on approaches considering the resolved shear stress necessary to move a dislocation through a glide plane containing precipitates as Orowan: for dislocations bypassing the precipitates, or Hüther and Reppich [41]: for strongly coupled dislocations shearing the precipitates or Brown and Ham [6]: for weakly coupled dislocations shearing the precipitates. The proposed model provided a good description of the cyclic behavior of several different γ' particle distributions obtained through various cooling paths and/or aging treatments in coarse grain size superalloy N18, as shown in figure 5.

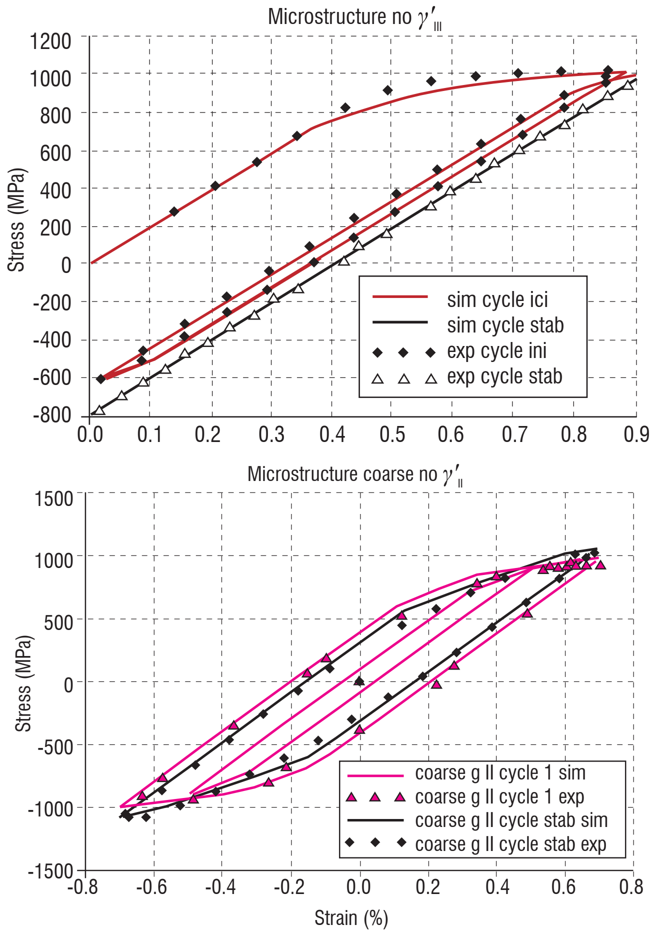

Figure 5 – Influence of the precipitate distribution on the cyclic behavior of coarse grain size superalloy N18 - Comparison of the model and the experimental response in the first and stabilized cycle

On the other hand, experimental observations have shown that Nickel-based or Cobalt-based superalloys could present very complex viscoplastic behavior, depending on the applied temperature and related to the dynamic strain aging phenomena [12]. In an intermediate temperature range (from 300°C to 800°C), a very important hardening process that depends on the applied plastic strain can be observed in the material. Other crucial phenomena are the inverse strain rate dependency and serrations occurring in the strain-stress curve induced by the propagation in the material of strain rate localization bands. Other effects can also be observed, like static recovery of kinematic hardening, even at temperatures around 600°C. The classical macroscopic formalism presented before has been enriched to account for these phenomena and to allow an accurate description of the observed experimental behavior.

Figure 6 summarizes the possibilities of the viscoplastic constitutive equations, including cycling hardening and dynamic strain aging, to accurately estimate the material behavior under complex thermo-mechanical cyclic loads. As can be observed, the model prediction (solid black line) is very close to the experimental data (red points).

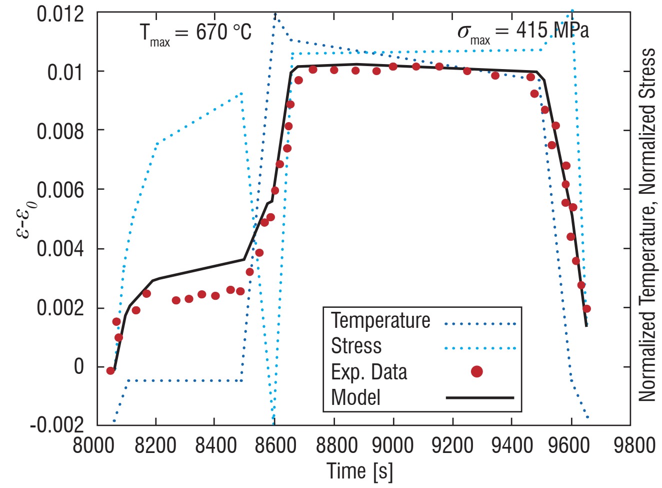

Figure 6 – Anisothermal cyclic behavior identification of a cobalt based superalloy

Another important step of this analysis (as proposed previously) is the validation of the model under anisothermal conditions. Once the model parameters are identified from a set of isothermal characterization tests, it is validated on cyclic thermo-mechanical tension/compression tests with in-phase or out-of-phase load paths interacting time/strain /temperature, as presented in figure 7 for the load path and figure 8 for the comparison between experimental results and the model, in the case of the AM1 single crystal superalloy. A more complex validation case concerns tension/torsion Thermo-Mechanical Fatigue, as represented in figure 9. It is worth noting that the main difficulty of these TMF tests is the application of the mechanical strain obtained by the control of the total strain during the thermal cycle. The structural effect in torsion requested to develop a specific algorithm to control the imposed displacement of the crosshead using Finite Elements simulations. This numerical scheme is based on a perturbation method, in order to impose the proper displacement to obtain locally the desired strain measured by the extensometer.

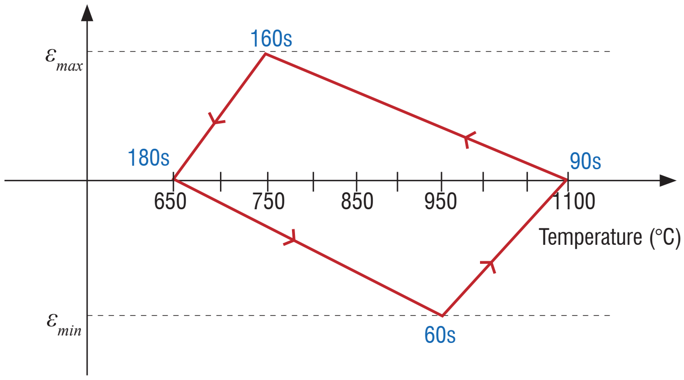

Figure 7 – Thermo-mechanical applied load on cylindrical specimens

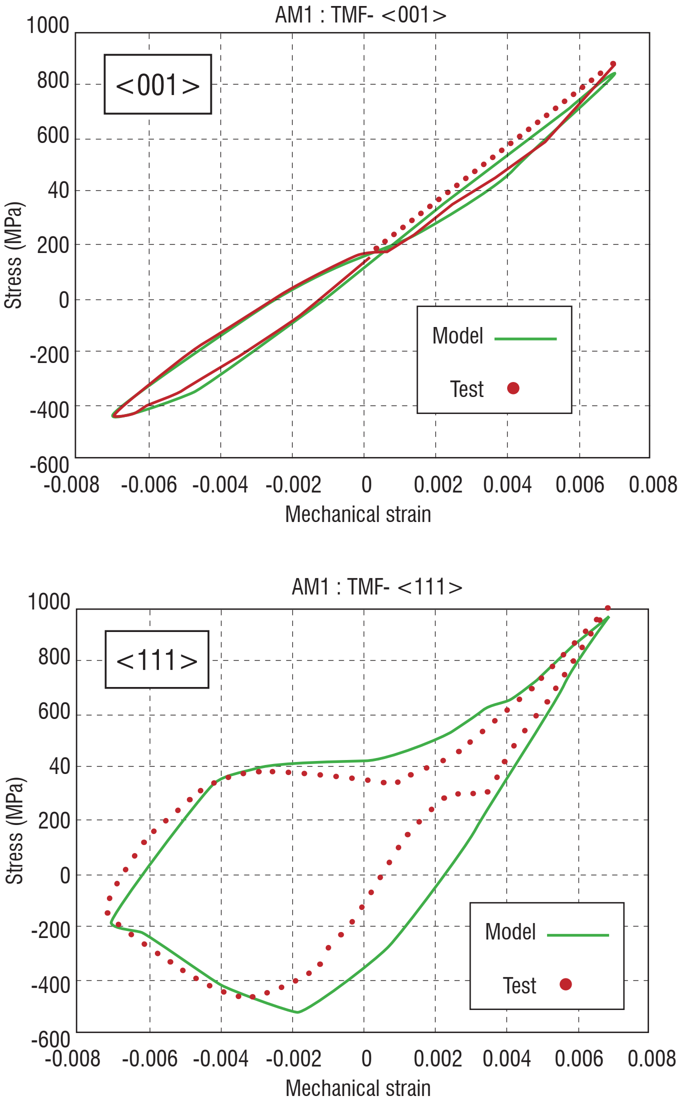

Figure 8 – Stress/mechanical strain behavior in two directions of the single crystal superalloy AM1

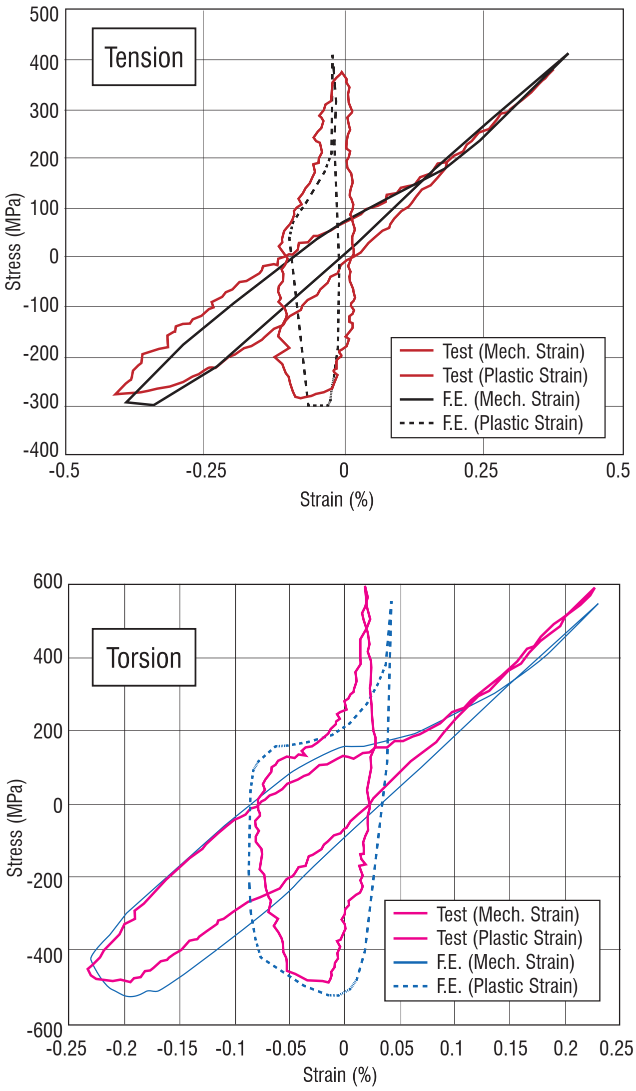

Figure 9 – Stabilized mechanical stress-strain behavior of <001>-oriented single crystal superalloy AM1 under axial-torsional Thermo-Mechanical Fatigue (TMF cycle defined in figure 7)

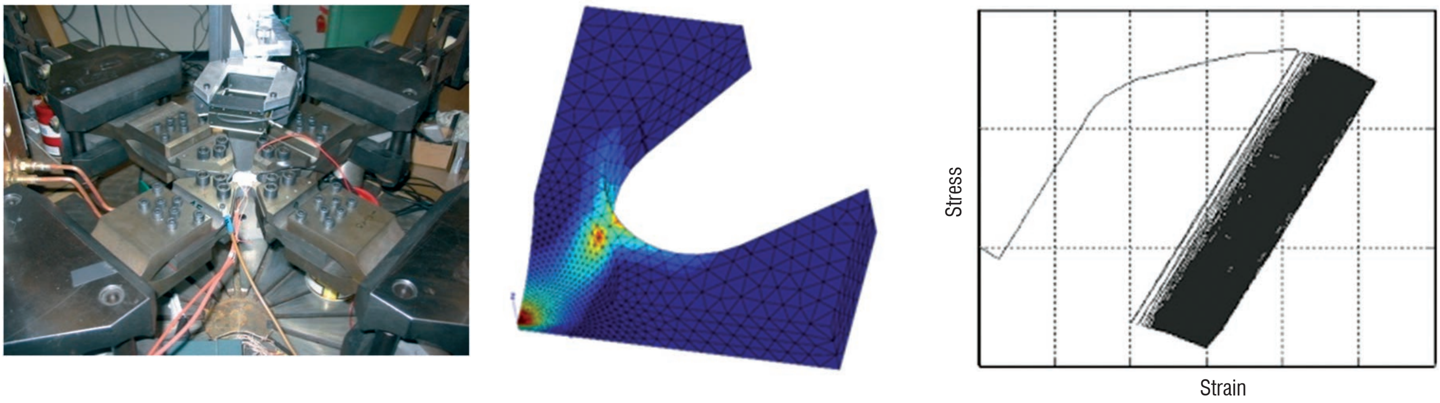

Figure 10 – Biaxial tensile tests device (left) and the finite element simulation (cumulative plastic strain (middle)) on a nickel based specimen up until the stabilized stress/strain state (right)

Finally, once the model has been identified and validated, it is used in the finite element analysis of the structure, as presented in figure 10 (left), for the simulation of the cyclic behavior of a cruciform specimen, on which it is possible to impose multiaxial (tension/tension) loads.

Figure 10 (right) presents the contours of the cumulative plastic strain stress obtained for an equibiaxial tension finite element simulation and the cyclic response on a point in the critical region (the center of the specimen), showing that the stabilized cycle is reached after more than 100 cycles. This important evolution of the stresses and strains is a key point for the fatigue damage analysis.

Multiaxial and anisothermal fatigue modeling

Critical aeroengine components, such as cooled turbine blades, turbine and compressor discs or combustion chambers, are submitted to complex thermo- mechanical loadings that can induce multiaxial stress states. The interaction between low cycle fatigue and high cycle fatigue, combined with high biaxialities and mean stresses, is one of the main topics of concern in fatigue. The exposure to high temperatures will additionally induce various mechanisms, such as creep and oxidation. For turbine discs, the microstructure of the constitutive material and the equibiaxial state play a significant role, while for turbine blades, high service temperatures involve a more important influence of creep and oxidation interacting with geometrical singularity effects induced by the cooling channels.

Also, it is important to specify that, despite the variety of the approaches, the fatigue damage remains closely linked to the effects of the material microstructure in connection with the applied mechanical load, for instance, the multiaxial state and the level of an equivalent mean stress. This is a major difficulty for correctly modeling the fatigue behavior taking into account this multiaxiality, the influence of time and temperature dependent phenomena, and the mean stress effects in a very complex geometry.

Multiaxial models

As has already been mentioned in the introduction, many multiaxial criteria can be found in the literature. From Garud's paper [32], a trend has emerged to classify the models according to several categories:

The empirical models, mainly based on experimental observations, are the oldest ones and began to be developed in the late nineteenth century with the rise of railways. These multiaxial criteria, often based on bending-torsion tests, offer endurance curves (ellipse quadrant). This category includes the work of [37, 63, 64] and extensions of the Manson-Coffin model for low cycle fatigue, taking into account the influence of plasticity.

The next category concerns criteria based on critical plane approaches, which have received great attention in the literature. These criteria were developed from experimental observations showing that, in fatigue, the crack initiates in a critical crystallographic plane and then propagates perpendicular to the direction of the maximum principal stress. The various proposed formulae are different, but the process to follow is merely the same. Firstly, one must find the critical plane and secondly check whether the criterion is met on this plane. It is possible to classify these approaches as stress-based, generally developed for HCF [29, 51, 52, 24, 53, 21, 14, 67, 9], strain-based, which are also valid in LCF ([7, 45] and its variants, the criterion of [28]) and energy-based, discussed hereafter.

Energy-based approaches use the product of the stress and strain to quantify the fatigue damage. Various energy parameters are available and can be divided into three groups, depending on the strain energy density per cycle chosen as a damage parameter: criteria based on elastic strain energy density [65], valid for high cycle fatigue, criteria based on plastic strain energy density, [59, 32] valid for low cycle fatigue and finally criteria based on elastoplastic strain density energy [27, 70] with the aim of covering both high and low cycle fatigue. The most recent works on multiaxial fatigue proposed models based on critical plane approaches using an energy damage parameter, such as the criterion of Liu [49, 50], which describes the crack initiation in three modes, one in the normal direction and two modes in the plane perpendicular to the normal direction (see also [18, 34, 35]). One can also mention the well-known SWT model [74], which uses the product of the maximum normal stress by the strain amplitude in a chosen critical plane for multiaxial applications.

The last more popular category concerns equivalent effective stress or strain models. Based on the invariants of the mechanical fields, such models are essentially extensions of static yield criteria and often combine the hydrostatic pressure to take into account the mean-stress effects and the octahedral shear stress amplitude. This framework includes the models proposed by Sines [73] and Crossland [19] (which generalizes [38]). Chaudonneret [15, 16] proposed in 1993 a multiaxial extension of the ONERA fatigue damage model [13], which has the particularity of describing, in accordance with experimental observations, non-linear damage accumulation for complex variable amplitude loadings. This model was based on a compilation of many two-level fatigue test results and has the capability of reproducing sequence effects and more complicated loading sequences. In particular, it is able to take into account the damage effects of loading cycles performed below the initial fatigue limit. A new formulation is thus proposed to describe multiaxial loadings, providing a better overall adjustment through a new material parameter that allows, for specific values, to obtain Sines, Crossland or results close to the Dang-Van criterion. Using [71], the influence of the hydrostatic pressure was also introduced for the static fracture. In addition, to account for non-proportional loadings, she introduced the concept of stress path and defined a weighted octahedral shear amplitude.

Such a general formalism has served to develop life assessment tools for high temperature applications by coupling the fatigue damage with other damaging mechanisms, such as creep [72, 57, 70, 23] or oxidation [62, 61, 2].

The ONERA creep-fatigue damage model has been applied with success on several materials in various applications (gas turbine blade polycrystalline superalloys, turbine disc materials and waspaloy during the initial design of some components of the Vulcain engine of Ariane V). For complex thermo-mechanical loadings, a multiaxial extension based on the multisurface plasticity theory [60] of the commonly uniaxial rainflow technique has been proposed, together with a calculation of an equivalent temperature, as proposed by Taira [75] over the thermo-mechanical cycle using a simplified incremental model. However, for high temperature applications, as for turbine blade applications, Gallerneau [31] shows insufficiencies of the creep-fatigue damage model, namely due to oxidation effects. A new formulation is then proposed, based on the separation between microinitiation and micropropagation stages and incorporating environment enhanced damage effects into the framework of a creep-fatigue-oxidation model. He also proposed an extension of the Hayhurst criterion [40] to describe multiaxial creep loadings, in order to account for the anisotropy in creep resistance of single crystal superalloys.

Despite several other formulations having been proposed in the literature to describe the interaction between fatigue, creep and eventually oxidation damages, few authors [43, 55, 57, 2, 70, 77, 20, 3] address the case of anisothermal multiaxial loadings.

Figure 11 shows the ability of Gallerneau's model to correctly predict lifetimes for different anisothermal conditions. The material considered is again AM1 single crystal superalloy. The critical cycling mentioned in this figure is relative to the anisothermal load path presented in figure 7, while other cycling is more relative to proportional loadings. Another feature is the accurate description of torsional loading under isothermal and anisothermal conditions, taking into account crystal plasticity and isotropic damage.

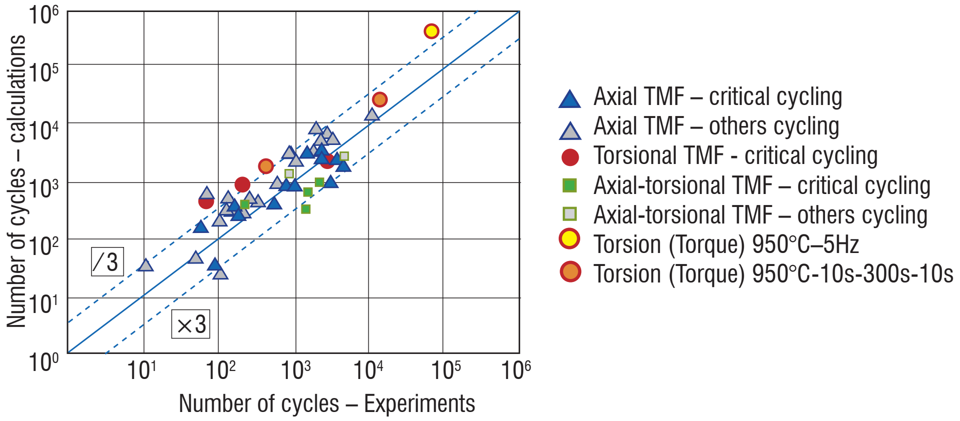

Figure 11 – Lifetime predictions for several anisothermal and multiaxial tests

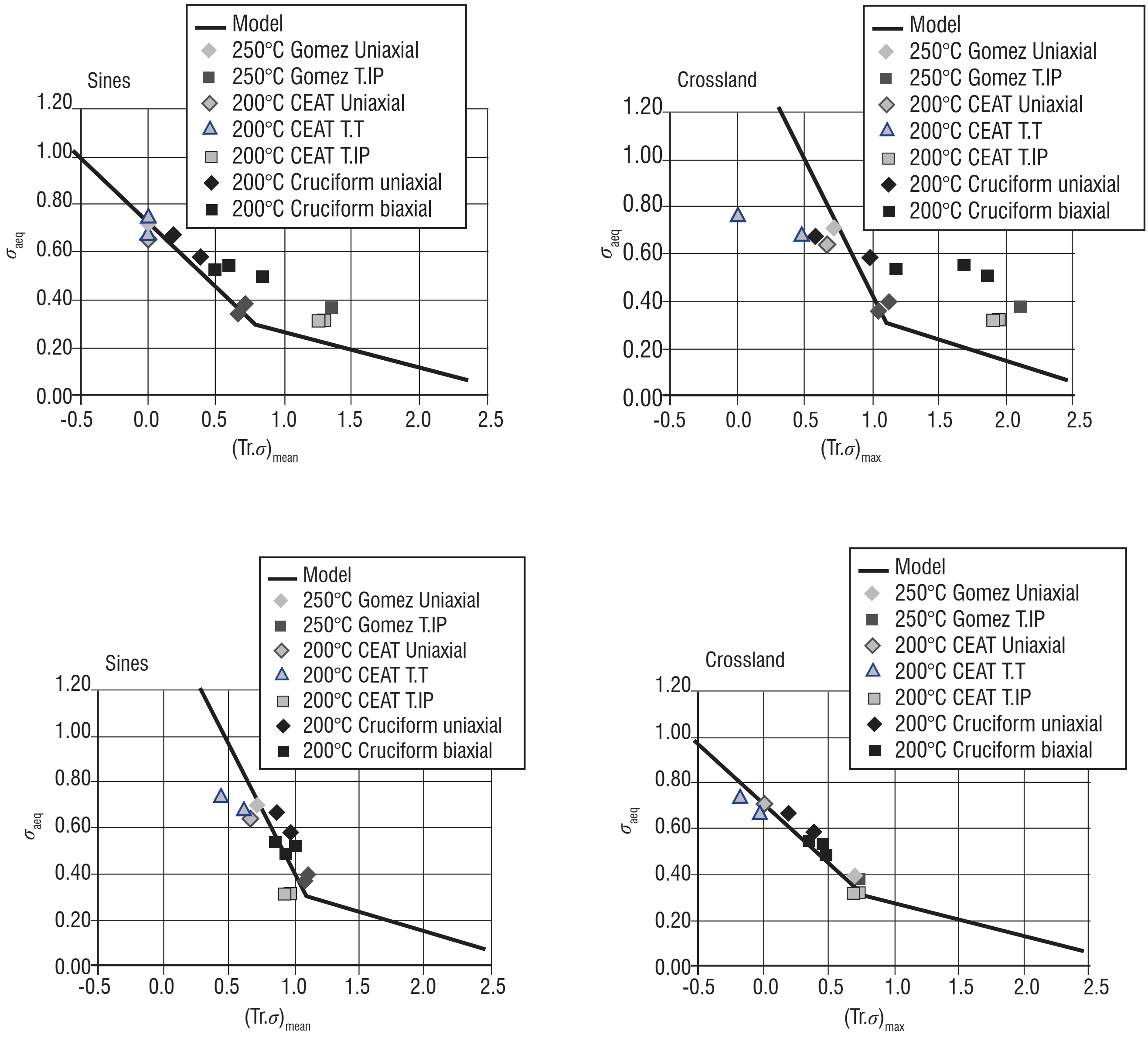

Figure 12 – Comparison of Sines, Crossland, Gonçalves and the ONERA criteria on Ti64 superalloy

A new multiaxial criterion

The majority of the aforementioned models often failed to accurately predict the lifetime for complex loads involving an important contribution of the mean stress and multiaxiality. Recently Bonnand [5] proposed a new multiaxial formulation for low temperature fatigue that can correctly reproduce experimental results obtained in tests involving both high multiaxiality and significant mean stress effects. This model has been formulated with the objective of accurately estimating the shear and equibiaxial conditions. The effective stress is written as

$$\sigma_{a_{eff}} = \sigma_{a_{eq}} \left(1 + b\,\sigma_{D_0} t_{eq}\right) \qquad (1)$$

with the following expression for the triaxiality factor:

$$t_{eq} = \xi \frac{s_F\ t_F}{1+\left|t_F\right|} + (1-\xi)\left(s_F - 1\right) \qquad (2)$$

where $t_F = \frac{\left(Tr\sigma\right)_{mean}}{\sigma_{a_{eq}}}$ and $s_F - 1 = \frac{\sigma_{p\max} - \sigma_{a_{eq}}}{\sigma_{a_{eq}}}$, $\sigma_{a_{eq}}$ is the octahedral shear stress amplitude, $\left(Tr\sigma\right)_{mean}$ is the mean value of the first stress invariant during the cycle and finally $\sigma_{p_{\max}}$ is the maximum stress Eigen. The term σ_{D0} represents the fatigue limit for a reversed cycle at 10^7 cycles and b is a material parameter that will be identified from uniaxial tests with mean stress effects. Finally ξ is a material parameter. This new model gives results similar to the Sines one when t_F tends towards zero and similar to a model with $t_{eq} = s_F$ for high values of t_F.

This new formalism has been compared with models in the literature ([73, 19, 36] for instance) and give very accurate results, as presented in figure 11 (from [5]), which can be seen as a multiaxial extension of Haigh's diagram.

Lifetime analysis of critical components

In order to validate or disprove the existing models and to propose a new formalism, a wide experimental campaign was conducted on aeronautical superalloys, such as Ti64 and INCO718 for discs or the AM1superalloy developed for turbine blades, on a set of test specimens ranging from a classical geometry used for characterization, up to technological specimens approximating real geometries.

The laboratory of complex tests at ONERA has several experimental devices dedicated to multiaxial and anisothermal fatigue tests. Each device has its own specificity to enrich the experimental database, especially in poorly explored areas (loads, geometries,, etc.). It is possible to perform uniaxial characterization tests, as well as biaxial tests under tension/torsion or tension/internal pressure on tubular specimens, with in-phase or out-of-phase temperature evolutions and biaxial tests (tension/tension) on cruciform specimens for various applied loads ratios. For all of these tests, the temperature is imposed by induction, which, regarding its compactness, enables mechanical and optical measurements to be performed to instrument the test as well as possible.

To illustrate these developments and the complexity of experimental tests and modeling performed within this framework, the developments around the fatigue analysis of the single crystal superalloy AM1 are presented hereafter. This application example is part of recent PhD work [22].

The purpose of the study was to investigate the lifetime of single crystal high pressure turbine blades. The geometry of these blades is very complex, with areas involving cooling channels inducing significant mechanical and thermal gradients, which are essential to evaluate. For this purpose, two geometries were tested: the smooth cylindrical specimen heated outside and cooled inside by forced air circulation and the same cylindrical specimen but with a network of cooling holes. These specimens are loaded with the real thermal gradients observed in operating blades. The geometry of the perforated specimen is shown in figure 13 (the perforated area is magnified), together with the high temperature experimental device (from [46]).

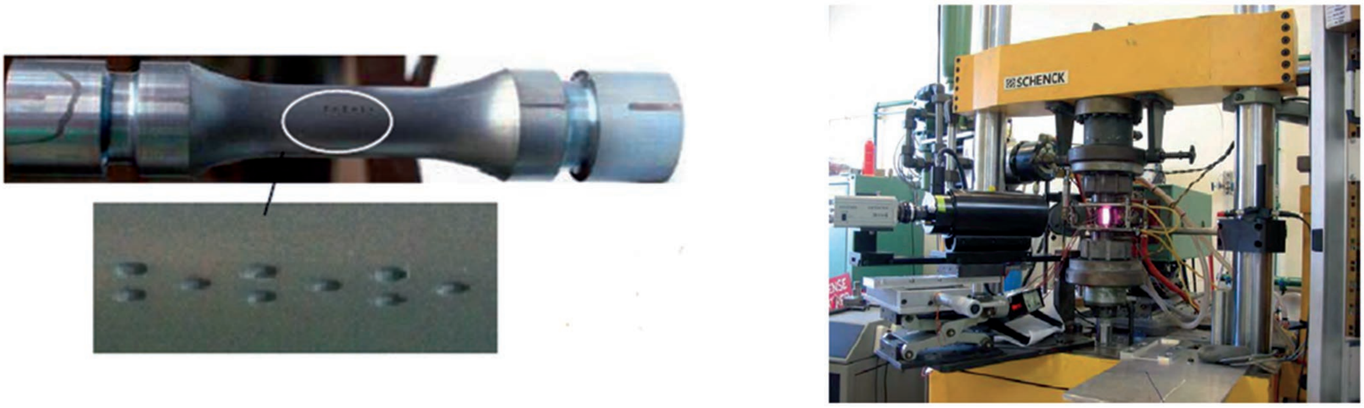

Figure 13 – Perforated tubular specimen (left) and the high temperature tension/torsion/internal pressure experimental device (right)

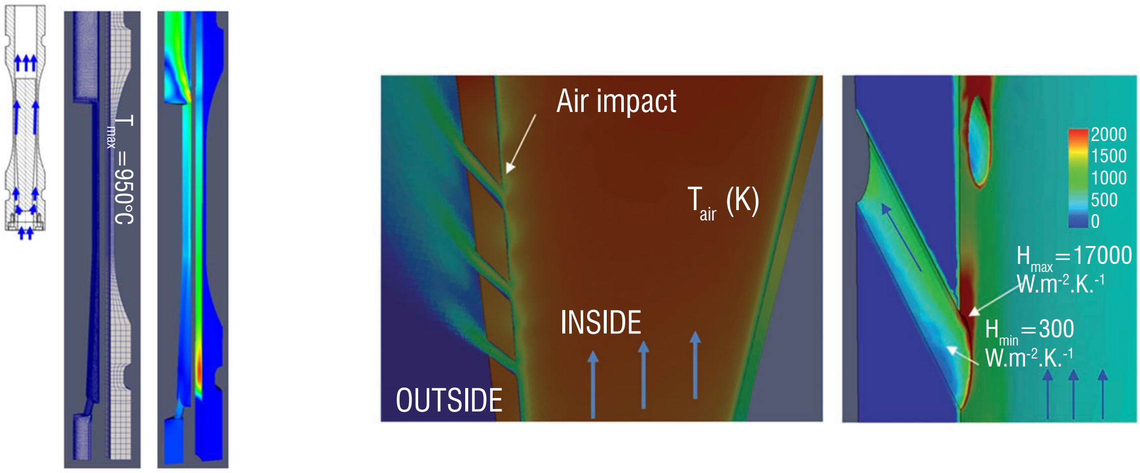

Figure 14 – Thermal/Solid/Fluid coupled calculation: smooth specimen (left) and perforated specimen (right). Temperature contours and the convective heat transfer coefficient h governed by the fluid velocity

This progressive approach validated the experimental device and the associated measures developed to properly assess the thermo-mechanical fields (temperature gradient and strain gradient). In addition, an analysis of such complexity cannot be derived only from experimental results, it is also necessary to perform a numerical analysis in order to adequately catch fields that are not measurable, such as the temperature inside the cooling channels. For this purpose, fully coupled calculations in Thermal/Solid/Fluid mechanics (Zset and Cedre codes from ONERA) have been carried out on these complex geometries. The thermal gradient over the specimen wall was estimated at 68°C for a 1mm thickness. Complex thermo-mechanical cycles were applied to simulate a real engine mission, as presented in figure 14. Heating and cooling rates were up to 50°C/s with a good reproducibility and stability over lots of cycles. In this configuration, copper coils make it possible to avoid the use of classical extensometers with fixed gage length. This is the reason why Digital Image Correlation (DIC) was extended to the high temperature range by treating the loss of optical contrast due to Planck's law. This image methodology allows "strains" to be measured by means of a virtual extensometer, which is used together with finite element calculations. Under these conditions, the proposed strain must be considered as a relative displacement integrating the temperature inhomogeneity into the gage length. The fatigue life prediction is performed as a post calculation, using the fatigue-creep interaction damage model presented previously.

Another main difficulty arising during the fatigue damage analysis of a structure or a specimen containing holes is linked to the gradient effect. It has been well established that the crack will initiate faster for low stress concentration gradients than for higher ones for the same maximum local stress. This is related to the volume of matter affected by the gradient and the potential defects present in this volume. A specific procedure has been developed [46] in order to take into account this fact, consisting in proposing a non-local damage approach, averaging the damage parameter, or the variables that govern the damage, over a spherical volume. The radius of this sphere is a new parameter of the model.

Figure 14 is an illustration of this application on the tubular specimen using the anisothermal fatigue damage model proposed by [31]. Two sets of tests and their simulations are presented: isothermal fatigue (TF) (with a steady state temperature gradient) and thermo-mechanical fatigue (TMF) performed on smooth specimens and perforated ones subjected to relatively complex cyclic loads.

The comparison between experimental results and life prediction is quite satisfactory. The slight over-estimation observed on smooth specimens was shown by DIC to result from the ratcheting effect not precisely described during the hold time. It is important to notice that this agreement has only been possible by taking into account in the modeling the true thermal gradient in the thickness of the tubular specimen and around the holes, the stress gradient and the size effect close to the holes, the multiaxiality and the mean stress effects in the specimen.

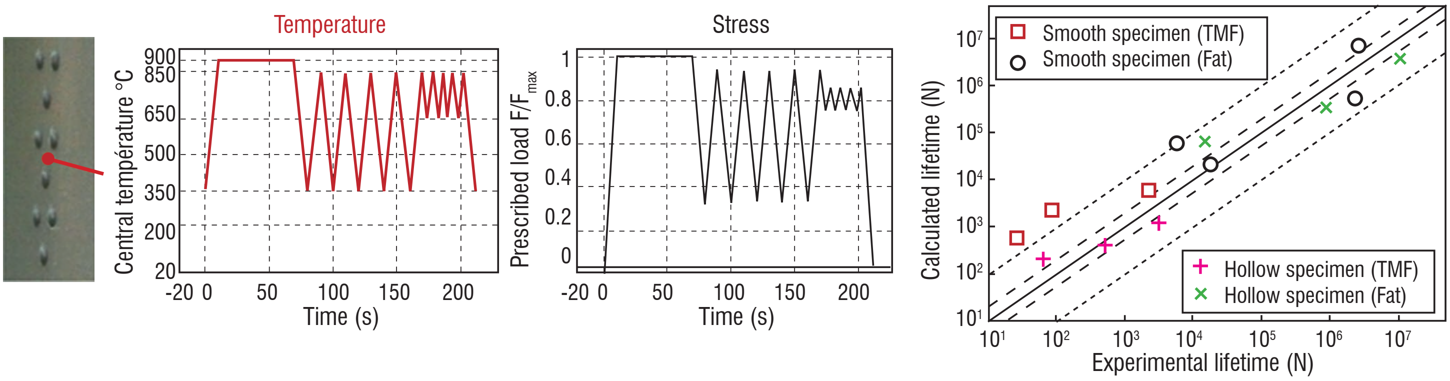

Figure 15 – Lifetime predictions for complex geometries combined with complex cyclic loads

Conclusion and perspectives

The purpose of this paper was to make an assessment of the fatigue damage modeling taking into account the effects induced by the temperature and multiaxial loadings. It showed the strong influence induced by a non-zero mean stress on the lifetimes observed in experimental results obtained on standard specimens, as well as on technological ones representative of real structures. The main findings can be summarized as follows:

It is necessary to develop consistent approaches in the lifetime analysis workflow, which includes the three main stages from the material experimental characterization (microstructure, behavior, fatigue,, etc.) and the development of constitutive equations, up to the fatigue damage model.

While it is possible, for the modeling of the constitutive equations, to define a general framework based on a given approach that will be enhanced according to the phenomena taken into account and the degree of sophistication that we want to introduce, this kind of framework does not exist for fatigue damage modeling and requires the approach to be adapted according to the observed experimental results. For example, for a given material, a strain invariant based approach will be sufficient, whereas for another material (or for the same one under different conditions), an energy-based or critical-plan approach will be more appropriate. This is induced particularly by the physical phenomena involved in the analysis, which are not only numerous but also very distinct and directly linked to the material microstructure, its defects and the stress/strain states. It is therefore necessary to distinguish the modeling of the microstructure for the constitutive equations from the modeling of the microstructure for the fatigue damage models, since the physical phenomena do not develop necessarily at the same scales.

In the case of severe thermo-mechanical loads, as in the example of the cooled blade, it is necessary to reproduce the applied loads as precisely as possible from the experimental point of view, as well as from the numerical point of view. In the latter case, multi-physics coupled approaches must be developed to approximate the real in-service conditions and to be able to expect predictive results to be produced.

These points define the main research topics that we will follow over the next decade ■

Acknowledgements

The financial support of DGAC (Délégation Générale de l'Aviation Civile) is gratefully acknowledged. The authors are also grateful to Snecma and Turboméca for their constant collaboration. We would like also to acknowledge the PhD students that contributed to the results presented in this paper and our colleague Jean-Louis Chaboche for its contribution and the fruitful discussions.

References

[1] M. ANDERSSON, C. PERSSON and S. MELIN – *High-Temperature Fatigue Crack Growth in Inconel 718 Subjected to High Strain Amplitudes*. Fatigue & Fracture of Engineering Materials & Structures, 29, pp. 863–875, 2006.
[2] S. ANTOLOVICH and A. SAXENA – *Thermomechanical Fatigue: Mechanisms and Practical Life Analysis*. Ed. by W. T. BECKER and R. J. SHIPLEY, ASM Handbook 11, Failure Analysis and Prevention, ASME International, Materials Park, Ohio, pp. 738-745, 2002.
[3] L. BERTINI – *Life Predictions by Three Creep-Fatigue Interaction Models: Influence of Multiaxiality End Time-Variable loadings*. Mater. High Temp., 9 (1), pp. 23-29, 1991.
[4] G. BOITTIN – *Expérimentation numérique pour l'aide à la spécification de lamicrostructure et des propriétés mécaniques d'un superalliage base Ni pour des applications moteurs*. PhD Ecole Nationale Supérieure des Mines de Paris, 2011.
[5] V. BONNAND, J.L. CHABOCHE, P. GOMEZ, P. KANOUTÉ and D. PACOU – *Investigation of Multiaxial Fatigue in the Context of Turboengine Disc Applications*. International Journal of Fatigue, Vol.33, Issue 8, pp. 1006-1016, 2011.
[6] L. BROWN and R. HAM – *Strengthening Methods in Crystals*. Ed. by A. KELLY and R. B. NICHOLSON, Elsevier, pp. 30-33, 1971.
[7] M.W. BROWN and K.J. MILLER – *A Theory for Fatigue Failure under Multiaxial Stress-Strain Conditions*. Proc. Inst. Mech. Engrs, 187, pp. 745-755, 1973.
[8] M.W. BROWN and K.J. MILLER – *Two Decades of Progress in the Assessment of Multiaxial Low-Cycle Fatigue Life*. In: C. AMZALLAG, B. LEIS and P. RABBE editors, *Low-Cycle Fatigue and Life Prediction*, ASTM STP 770, Philadelphia: ASTM, pp. 482–499, 1982.
[9] A. CARPINTERI and A. SPAGNOLI – *Multiaxial High-Cycle Fatigue Criterion for Hard Metals*. International Journal of Fatigue, 23, pp. 135-145, 2001.
[10] J.L. CHABOCHE and O. JUNG – *Application of a Kinematic Hardening Viscoplasticity Model with Thresholds to the Residual Stress Relaxation*. International Journal of Plasticity, 13(10), pp. 785-807, 1997.
[11] J.-L. CHABOCHE, P. KANOUTÉ and F. AZZOUZ – *Cyclic Inelastic Constitutive Equations and their Impact on the Fatigue Life Predictions*. International Journal of Plasticity, Vol. 35, pp. 44-66, 2012.
[12] J.-L. CHABOCHE, A. GAUBERT, P. KANOUTÉ, A. LONGUET, F. AZZOUZ and M. MAZIÈRE – *Viscoplastic Constitutive Equations of Combustion Chamber Materials Including Cyclic Hardening and Dynamic Strain Aging*. International Journal of Plasticity, Vol. 46, pp. 1-22, 2013.
[13] J.-L. CHABOCHE – *A Differential Law for Non Linear Cumulative Fatigue Damage*. Materials and Building research, Annales de l'ITBTP, HSNr.39, pp. 117-124, 1977.
[14] E. CHARKALUK, A. CONSTANTINESCU, H. MAÏTOURNAM and K. DANG VAN – *Revisiting the Dang Van Criterion*. Procedia Engineering, 1 (1), pp. 143-146, 2009.
[15] M. CHAUDONNERET – *A Simple and Efficient Multiaxial Fatigue Damage Model for Engineering Applications of Macro-Crack Initiation*. J. Eng. Mater. Technol., 115, pp. 373-379, 1993.
[16] M. CHAUDONNERET and M. ROBERT – *Fatigue Lifetime Prediction Methods: An Analysis of the Different Approximations Involved in Local Approaches*. International Journal of Pressure Vessels and Piping; 66, pp.113-123, 1996.
[17] J. CHEN, S. TAKEZONO, K. TAO and T. HAZAWA – *Application of Fracture Mechanics to the Surface Crack Propagation in Stainless Steel at Elevated Temperatures*. Acta Materialia, 45, pp. 2495–5000, 1997.

[18] C. CHU – *Fatigue Damage Calculation Using the Critical Plane Approach*. Trans. ASME, J. Engng Mater. Technol., 117, pp. 41-49, 1995.
[19] B. CROSSLAND – *Effect of Large Hydrostatic Pressures on the Torsional Fatigue Strength of an Alloy Steel*. Proceedings of the International Conference on Fatigue of Metals, Institution of Mechanical Engineers, London, pp. 138–149, 1956.
[20] L. CUI and P. WANG – *Lifetime Prediction of Steam Turbine Components under Multiaxial Thermo-Mechanical Fatigue Loading*. Applied Mechanics and Materials, 151, pp. 255-259, 2012.
[21] K. DANG VAN – *Macro-Micro Approach in High-Cycle Multiaxial Fatigue*. In: D.L. MCDOWELL and R. ELLIS (Eds.) – *Advances in Multiaxial Fatigue*. American Society for Testing and Materials, STP 1191, Philadelphia, pp. 120–130, 1983.
[22] R. DEGEILH – *Développement expérimental et modélisation d'un essai de fatigue avec gradient thermique de paroi pour application aube de turbine monocristalline*. PhD Thesis Ecole Normale Supérieure de Cachan, 2013.
[23] R. DESMORAT and R. MARULL – *Non-Quadratic Kelvin Modes Based Plasticity Criteria for Anisotropic Materials*. International Journal of Plasticity, 27 (3), pp. 328-351, 2011.
[24] H. DIETMANN, T. BHONGBHIBHAT and A. SCHMID – *Multiaxial Fatigue Behaviour of Steels under In-Phase and Out-Of-Phase Loading, Including Different Wave Forms and Frequencies*. In: K. KUSSMAUL, , D. MCDIARMID and D. SOCIE (Eds.) – *Fatigue Under Biaxial and Multiaxial Loading*. Mechanical Engineering Publications, London, pp. 449-469, 1976.
[25] N. DOWLING and N. IYER – *Fatigue Crack Growth and Closure at High Cyclic Strains.* Materials Science Engineering, 96, pp. 99–107, 1987.
[26] R. DONATH, T. NICHOLAS and L. FU – *An Experimental Investigation of Creep Crack Growth in Es100*. Fracture Mechanics: Thirteenth Conference. ASTM-STP 743, pp. 186-206, 1981.
[27] F. ELLYIN – *A Criterion for Fatigue Under Multiaxial States of Stress*. Mechanics Research Communications 1, pp. 219 – 224, 1974.
[28] A. FATEMI and D.F. SOCIE – *A Critical Plane Approach to Multiaxial Fatigue Damage Including Out-Of-Phase Loading*. Fatigue of Engineering Materials and Structures, 11, pp. 149-165, 1988.
[29] W.N. FINDLEY, W.I. MITCHELL and D.D. STROHBECK – *Effect of Range of Stress in Combined Bending and Torsion Fatigue Tests of 25S-T6 Aluminium Alloy*. Trans Am Soc Mech Engrs.,78, 1956.
[30] W.N. FINDLEY – *A Theory for the Effect of Mean Stress on Fatigue of Metals under Combined Torsion and Axial Load or Bending*. J. Eng. Ind., Trans ASME, 81, pp. 301–306, 1959.
[31] F. GALLERNEAU and J.L. CHABOCHE – *Fatigue Life Prediction of Single Crystals for Turbine Blade Applications*. International Journal of Damage Mechanics, Vol. 8, n° 4, pp. 404-427, 1999.
[32] Y.S. GARUD – *Multiaxial Fatigue: a Survey of the State of the Art*. J. test Evaluat, 9, pp. 165-178, 1981.
[33] A. GAUBERT – *Modélisation des effets de l'évolution microstructurale des superalliages monocristallins sur le comportement mécanique pour des applications aux chargements de très longue durée*. PhD thesis, Ecole nationale Supérieure des Mines de Paris, 2010.
[34] G. GLINKA, G. SHEN and A. PLUMTREE – *A Multiaxial Fatigue Strain Energy Density Parameter Related to the Critical Fracture Plane*. Fatigue of Engineering Materials and Structures,18, pp. 37-46, 1995.
[35] G. GLINKA, G. SHEN and A. PLUMTREE – *Mean Stress Effects in Multiaxial Fatigue*. Fatigue of Engineering Materials and Structures, 18, pp. 755-764, 1995.
[36] C.A. GONÇALVÈS, J.A. ARAUJO and E.N. MAMIYA – *Multiaxial Fatigue: a Stress Based Criterion for Hard Metals*. Int J Fatigue, 27, pp. 177–87, 2005.
[37] H. GOUGH and H. POLLARD – *The Strength of Metals under Combined Alternating Stress*. Proc Inst Mech Engrs, 131, pp. 3–18, 1935.
[38] H. GOUGH and H. POLLARD – *Properties of Some Materials for Cast Crankshafts with Special Reference to Combined Alternating Stresses*. Proc. Inst. Automobile Engrs, 31, pp. 821-893, 1937.
[39] J.-B. LE GRAVEREND – *Étude et modélisation des effets d'incursion à très haute température sur le comportement mécanique d'un superalliage monocristallin pour aubes de turbine*. PhD Ecole Nationale Supérieure de Mécanique et d'Aérotechnique, 2013.
[40] D. HAYHURST – *Computational Continuum Damage Mechanics: Its Use in the Prediction of Creep in Structures – Past, Present and Future*. Proc. 5th IUTAM Symp. On Creep in Structures, Nagoya, Kluwer Academic Press, 2001.
[41] W. HUTHER and B. REPPICH – *Interaction of Dislocation with Coherent, Stress-Free, Ordered Precipitates*. Z. Metall., 69(19), pp. 628–634, 1978.
[42] L. JACOBSSON, C. PERSSON and S. MELIN – *Thermo-Mechanical Fatigue Crack Propagation Experiments in Inconel 718*. International Journal of Fatigue, 31, pp. 1318–1326, 2009.
[43] S. KALLURI and P. BONACUSE – *In-Phase and Out-Of-Phase Axial-Torsional Fatigue Behavior of Haynes 188 At 760°C*. NASA Technical Memorandum 105765, 1991.
[44] M. KAMINSKI – *Modélisation de l'endommagement en fatigue des superalliages monocristallins pour aubes de turbines en zone de concentration de contrainte*. PhD thesis Ecole Nationale Supérieure des Mines de Paris, 2007.
[45] F.A. KANDIL, M.W. BROWN and K.J. MILLER – *Biaxial Low Cycle Fatigue Fracture of 316 Stainless Steel at Elevated Temperatures*. The Metal Society, London, 280, pp. 203-210, 1982.
[46] P. KANOUTÉ, D. BOSO, J.-L. CHABOCHE and B. SCHREFLER – *Multiscale Methods for Composites: A Review, Archives of Computational Methods in Engineering*. 16, pp. 31-75, 2009.
[47] A. KAROLCZUK and E. MACHA – *A Review of Critical Plane Orientations in Multiaxial Fatigue Failure Criteria of Metallic Materials*. Int. J. of Fracture, Vol. 134, Issue 3-4, pp 267-304, 2005.
[48] S. KRUCH, P. PRIGENT and JL. CHABOCHE – *A Fracture Mechanics Based Fatigue-Creep-Environment Crack Growth Model for High Temperature*. International Journal of Pressure Vessels and Piping, Vol. 59, pp. 141-148, 1994.
[49] K.C. LIU – *A Method Based on Virtual Strain-Energy Parameters for Multiaxial Fatigue Life Prediction*. In: D.L. MCDOWELL and R. ELLIS (Eds.) – *Advances in Multiaxial Fatigue*. American Society for Testing and Materials STP 1191, Philadelphia, pp. 67–84, 1993.
[50] K.C. LIU and J.A. WANG – *An Energy Method for Predicting Fatigue Life, Crack Orientation, and Crack Growth under Multiaxial Loading Condition*. International Journal of Fatigue, 23, pp. S129-S134, 2001.
[51] D.L. MCDIARMID – *Failure Criteria and Cumulative Damage in Fatigue under Multiaxial Stress Conditions*. Ph.D. thesis, The City University, London, 1972.
[52] D.L. MCDIARMID – *A General Criterion for High Cycle Multiaxial Fatigue Failure*. Fatigue Fract Eng Mater Struct., 14, pp. 429–453, 1991.
[53] T. MATAKE – *An Explanation on Fatigue Limit under Combined Stress*. Bulletin of The Japan Society of Mechanical Engineers, 20, pp. 257-263, 1977.

[54] V. MAUREL, L. RÉMY, F. DAHMEN and N. HADDAR – *An Engineering Model for Low Cycle Fatigue Life Based on a Partition of Energy and Micro-Crack Growth*. International Journal of Fatigue, Vol. 31, Issue 5, pp. 952-961, 2009.
[55] V. MAUREL, A. KOSTER and L. RÉMY – *An Analysis of Thermal Gradient Impact in Thermal–Mechanical Fatigue Testing*. Fatigue & Fracture of Engineering Materials & Structures, 33(8), pp. 473 – 489, 2010.
[56] L. MÉRIC and G. CAILLETAUD – *Single Crystal Modelling for Structural Calculations. Part 2 - Finite Element Implementation*. J. Eng. Mater. Technol. 113(1), pp. 171-182, 1991.
[57] M. METZGER, B. NIEWEG, C. SCHWEIZER and T. SEIFERT – *Lifetime Prediction of Cast Iron Materials Under Combined Thermomechanical Fatigue and High Cycle Fatigue Loading Using a Mechanism-Based Model*. International Journal of Fatigue, 53, pp. 58-66, 2013.
[58] N. MILHET-GAYRAUD – *Etude expérimentale et modélisation de la précipitation γ' dans le superalliage N18*. Ph.D. thesis, Institut National Polytechnique de Grenoble, France, 1994.
[59] J. MORROW – *Fatigue properties of metals, section 3.2*. In: *Fatigue Design Handbook*, Pub. No. AE-4. SAE, Warrendale, PA., 1968.
[60] Z.MROZ – *On The Description of Anisotropic Workhardening*. Journal of Mechanics and Physics of Solids, 15(3), 163-175, 1967.
[61] G. MURTAZA and R. AKID – *Empirical Corrosion Fatigue Life Prediction Models of a High Strength Steel*. Engineering Fracture Mechanics, 67 (5), pp. 461-474, 2000.
[62] R. NEU and H. SEHITOGLU – *Thermomechanical Fatigue, Oxidation and Creep: Part I And II*. Metallurgical transactions A 20 (9), pp. 1755-1783, 1989.
[63] T. NISHIHARA and M. KAWAMOTO – *The Strength of Metals under Combined Alternating Bending and Torsion*. Memoirs of the College of Engineering, Kyoto Imperial University, 10, 6, 1941.
[64] T. NISHIHARA and M. KAWAMOTO – *The Strength of Metals under Alternating Bending and Torsion with Phase Difference*. Memoirs of the College of Engineering, Kyoto Imperial University, 11, 6, 1954.
[65] T. PALIN-LUC and S. LASSERRE – *An Energy Based Criterion for High Cycle Multiaxial Fatigue*. Eur. J. Mechanics, A/Solids, 17(2) :237–251, 1998.
[66] I.V. PAPADOPOULOS, P. DAVOLI, C. GORLA, M. FILLIPPINI and A. BERNASCONI – *A Comparative Study of Multiaxial High-Cycle Fatigue Criteria for Metals*. Int J Fatigue, 19, pp. 219–35, 1997.
[67] I.V PAPADOPOULOS – *Long Life Fatigue under Multiaxial Loading*. International Journal of Fatigue, 23: pp. 831-849, 2001.
[68] J. PARK and D. NELSON – *Evaluation of an Energy-Based Approach and a Critical Plane Approach for Predicting Constand Amplitude Multiaxial Fatigue Life*. Int. J. Fatigue 22, pp. 23 – 39, 2000.
[69] P. PÉDRON and A. PINEAU – *Crack Growth Behavior of Inconel 718 At 650°C Under Fatigue, Creep and Combined Loading. Effect of Microstructure and Environment*. Materials Science Engineering, 56, pp. 143–156, 1982.
[70] L. REMY – *Fatigue and Thermomechanical Fatigue at High Temperature*. In: K.H. JÜRGEN BUSCHOW *et al.* (Eds.) – *Encyclopedia of Materials: Science and Technology.* Second Edition, Elsevier, Oxford, pp. 2866-2877, 2001.
[71] J. RICE and D. TRACEY – *On the Ductile Enlargement of Voids in Triaxial Stress Fields*. Journal of the Mechanics and Physics of Solids, 17, pp. 201-217, 1969.
[72] P. SERMAGE, J. LEMAITRE and R. DESMORAT – *Multiaxial Creep-Fatigue under Anisothermal Conditions*. Fatigue & Fracture of Engineering Materials & Structures, 23, pp. 241–252, 2000.
[73] G. SINES – *Behaviour of Metals under Complex Stresses*. In: G. SINES and J.L. WAISMAN (Eds.) – *Metal fatigue*. New York: McGraw-Hill, pp. 145–169, 1959.
[74] K.N. SMITH, P. WATSON and T.H. TOPPER – *A stress-strain function for the fatigue of metals*. Journal of Materials JMLSA, 5, pp. 767-778, 1970.
[75] S. TAIRA – *Relationship Between Thermal and Low Cycle Fatigue at Elevated Temperatures*. Fatigue at Elevated Temperatures, ASTM STP 520, American Society for Testing and Materials, pp. 80-101, 1973
[76] Y.Y. WANG and W.X. YAO – *Evaluation and Comparison of Several Multiaxial Fatigue Criteria*. Int. J. Fatigue, 26, pp. 17-25, 2004.

AUTHORS

Serge Kruch received his PhD in Theoretical Mechanics from the University *Pierre et Marie Curie*, Paris 6, in 1988 and his Habilitation à Diriger des Recherches in 2007 from Paris 6. He was hired at ONERA in 1989. He is now Maître de Recherche 2 and Special Advisor in the Metallic Materials and Structures Department. His research interests mainly include non-linear modeling and multiscale approaches for metallic materials

Pascale Kanoute received her PhD in Solids, Structures and Mechanical Systems from the University *Pierre et Marie Curie*, Paris 6, in 1999. She has been working at ONERA since 1999 in the Metallic Materials and Structures Department. Since 2010, she is also a part-time associate professor at the Université de Technologie de Troyes. Since 2013, she is the head of the Behavior and Damage Mechanics research unit at ONERA. Her main research topics are non-linear and multiscale modeling, fatigue-creep interaction and lifetime assessment.

Vincent Bonnand received his PhD in Materials Science and Engineering from the *Ecole des Mines* de Paris in 2006. He has worked at ONERA since 2007 in the Metallic Materials and Structures Department lab. His research topics concern the experimental mechanics at the intersection of different fields, such as solid and fluid mechanics, thermal analysis, associated measurements and non-destructive technologies.

E. Andrieu
(CIRIMAT, ENSIACET/INP)
B. Max
(IRT Saint Exupéry)
B. Viguier
(CIRIMAT, ENSIACET/INP)

E-mail: bertrand.max@irt-saintexupery.com

DOI : 10.12762/2015.AL09-09

Oxidation Assisted Intergranular Cracking in Alloy 718: Effects of Strain Rate and Temperature

Alloy 718 is the most widely used superalloy in industry due to its excellent mechanical properties, as well as its oxidation and corrosion resistance over a wide range of temperatures and solicitation modes. Nevertheless, it is a well-known fact that this alloy is sensitive to oxidation assisted intergranular cracking under loading in the temperature range encountered in service. The mechanisms resulting in such degradation are not well-understood, but it has been well established that a relation exists between a change in fracture mode and the apparition of plastic instability phenomena over a wide range of temperatures. Quantification and characterization of the damaging process provide important information leading to a better understanding of the degradation mechanisms involved in the oxidation assisted intergranular cracking of this alloy. These observations allow various domains to be defined in the strain rate - temperature plane, where the damaging process characteristics are different: a high strain rate / low temperature domain in which instabilities occur and where the fracture mode is systematically transgranular ductile, an intermediary domain where numerous intergranular crack initiations can be observed, and a slow strain rate / high temperature domain where crack propagation is enhanced. These results lead to the proposal of consistent scenarii to explain grain boundary opening due to applied intergranular normal stress and critical decohesion stress changes.

Introduction

A large number of studies dealing with mechanical properties in relation to microstructure and environment have been carried out with alloy 718 [1, 4, 6-9, 13]. Depending on the industrial applications, the microstructure of this Ni-based superalloy can be designed to fulfill service property requirements. Thus, a great variety of microstructures have been explored, together with some slight changes in chemical composition. However, whatever the microstructure may be, this alloy remains sensitive to oxidation assisted intergranular crack initiation or propagation [12]. Studies on the effect of the environment on the crack propagation rate and the cracking path have shown that the occurrence and kinetics of the local intergranular oxidation involved in the damaging process do not vary following classical oxidation laws, but rather depend on the type of oxide formed during the first steps of the oxidation process [2, 3, 11]. A critical oxygen partial pressure was evidenced, relating the type of oxide and the type of crack propagation path. This coupling effect between the local mechanical behavior and the oxidation process give rise to an abrupt change in the fatigue or creep fatigue crack propagation rates when crossing the critical oxygen partial pressure.

At a much lower temperature (340°C), when exposed to simulated pressurized water reactor testing conditions, without irradiation effects, a similar intergranular fracture process occurs during slow strain rate tests [14]. Typical fracture surfaces corresponding to high and low temperature oxidation assisted intergranular fracture are shown in figure 1 [5, 15].

In order to achieve a better understanding of this type of coupling between the mechanical behavior, oxidation and metallurgical state, further studies were performed. A transition between intergranular crack initiation and growth to transgranular ductile fracture is evidenced over the entire temperature range 300°C -700°C under air testing conditions when Portevin-Le Chatelier (PLC) type flow instabilities appear. Given that this boundary between the Dynamic Strain Ageing (DSA) without serrations and the PLC sub-domain is related to microscopic and macroscopic mechanical aspects and mechanisms, studies were continued and the results have been the subject of an earlier publication [10]. A great number of tensile tests have been carried out in an air atmosphere, in order to characterize the plastic instabilities (PLC effect) resulting from a DSA phenomenon in this alloy. The results of these tests are plotted in figure 2, showing the absence or occurrence of plastic instabilities and the rupture mode exhibited by the fracture surface.

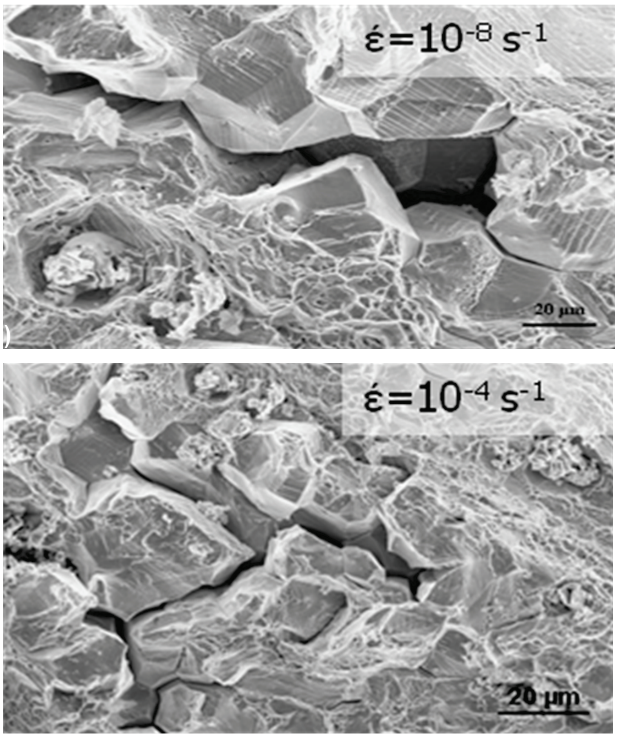

Figure 1 - Typical fracture surface SEM micrographs for (a) a tensile test under simulated PWR testing conditions and (b) a tensile test at 650°C in air

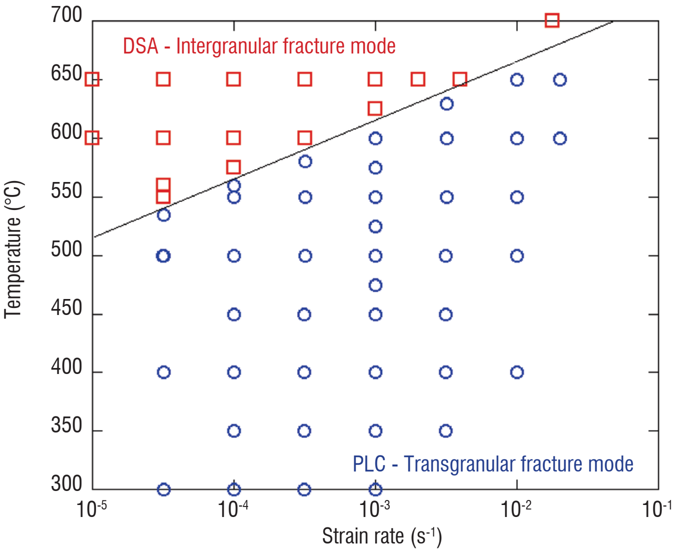

Figure 2 - Representation of the plastic instability occurrence or absence domains (PLC: denotes the domain where serrations were observed; DSA: denotes the domain where no serration was observed, often called the dragging domain) and of the associated rupture modes on the temperature – strain rate plane

This paper mainly focuses on the effect of strain rate on both the mechanical properties and the sensitivity to Oxidation Assisted Intergranular Cracking (OAIC) of alloy 718, during tensile tests in an air environment for a temperature 650°C. The purpose is to propose a realistic scenario concerning the mechanisms responsible for oxidation assisted intergranular crack initiation in alloy 718.

Materials and experimental procedure

The specimens used in this study were machined from a single heat, whose chemical composition is given in table 1. The material was hot rolled and then cold rolled up to a final thickness of 0.64 mm. The as-received material is in a solid solution state. Typical solution annealing heat treatment can be achieved through a standard route (1040°C-0.5h-Water Quench). Tensile specimens and coupons were cut through spark machining. A standard heat treatment (720°C-8h; cooling rate 50°C/h down to 620°C-8h) was then applied to these samples. After being heat treated, all of the samples were mechanically polished in order to eliminate the spark machining affected zone. The tensile specimen geometry is presented in figure 3. The microstructure of the material was then characterized, using usual observation tools (optical and Scanning Electron Microscopes (SEM)). An average grain size of 10 to 20 μm was measured. As expected from the annealing heat treating conditions, the delta phase was not observed. Primary carbide alignments were evidenced, due to the hot and cold rolling steps. Representative micrographs of the microstructure are given in figure 4.

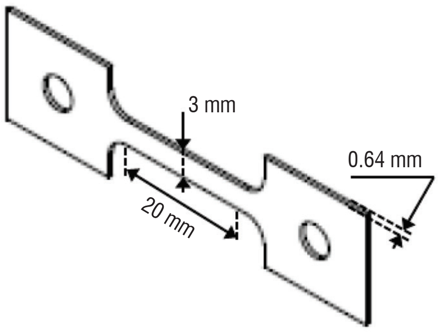

Figure 3 - Geometry of the tensile specimens used in this study

Tensile tests were performed on a low capacity (10kN) MTS tensile machine equipped with a radiation furnace and an environmental control chamber. Care was taken to limit the thermal gradients along the tensile specimens to less than +/- 5°C. Tensile tests were carried out under displacement rate control. Due to the weak strain hardening of this alloy and the in situ measurement of strain by a laser extensometer, different quasi constant strain rates could be explored from $10^{-5}s^{-1}$ to $10^{-1}s^{-1}$. Tensile tests were performed in the temperature range 300°C - 700°C. Initial mechanical properties at room temperature, 300°C and 650°C determined with a strain rate close to $10^{-3}s^{-1}$ are presented in table 2.

Element	Ni	Fe	Cr	Nb	Ta	Ti	Al	Mo	Mn	Si	Cu	Co	C	B	P	S
Composition (weight %)	53.6	18.3	18.4	4.94	0.01	0.95	0.56	3.0	0.06	0.04	0.02	0.02	0.033	0.002	0.01	0.0002

Table 1 - Chemical composition in weight percent of alloy 718 used in this study, as determined by Glow Discharge Mass Spectrometry (GDMS) / Instrumental Gas Analysis (IGA)

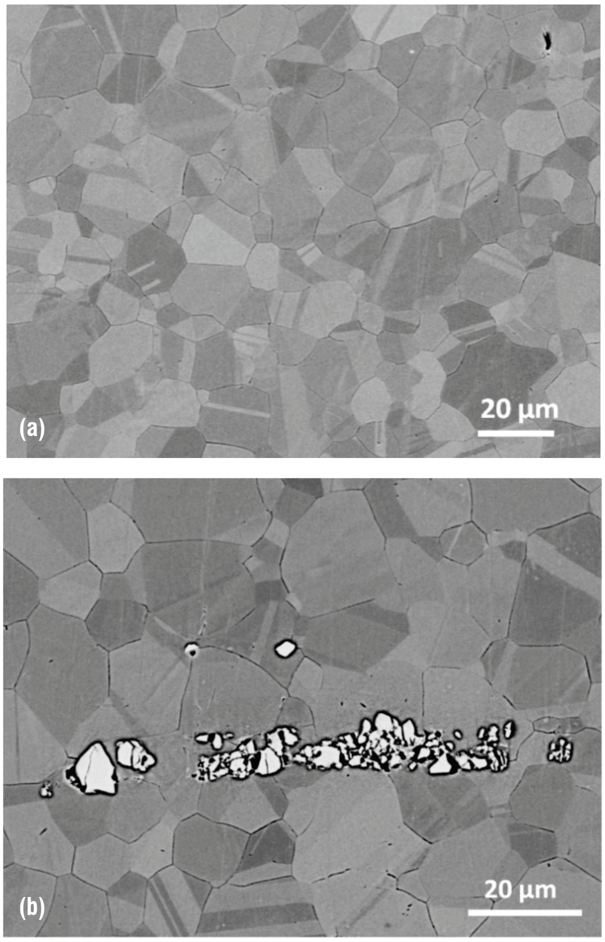

Figure 4 - Typical SEM micrographs of alloy 718 used in this study:
(a) fully recrystallized equiaxed microstructure
(b) typical carbide alignment in the rolling direction

	$\sigma_{0.2}$ (MPa)	σ_{m} (MPa)	E_f (%)	U_e (%)
RT	1200	1600	19	18.2
300°C	1200	1600	16	15.2
650°C	1000	1280	19	18.3

Table 2 - Typical mechanical properties of alloy 718 used in this study for different temperatures: Room Temperature (RT), 300°C and 650°C. Yield stress ($\sigma_{0.2}$), Ultimate tensile stress (σ_m), Elongation to failure (E_f) and Uniform elongation (U_e)

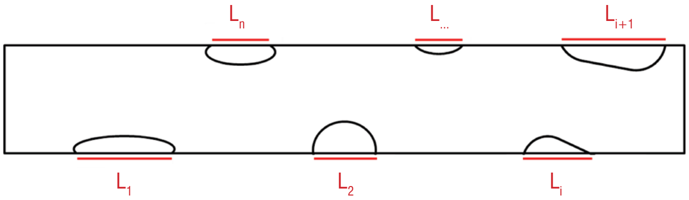

Figure 5 - Diagram of the fracture surface of a sample, with determination of the intergranular brittle fracture length

In this study, two indexes were used to characterize the effects of OAIC: a linear index and an areal index. These indexes can be calculated from quantitative SEM observations of the fracture surfaces of the tensile samples. The linear index is given by the cumulated length of intergranular brittle areas (ΣL_i) over the total perimeter length of the fracture surface ratio, as represented in figure 5 and defined by equation (1). To be taken into account, intergranular brittle areas must be extended over more than one grain. The areal index is given by the ratio of intergranular brittle areas over the total surface of the fracture surface, as defined by equation (2). The linear index is well suited to characterize crack initiation, while the areal index is suited to characterize crack propagation. Calculations of both indexes were carried out for all air tested samples.

$$I_{\text{OAIC}}^{linear} = \frac{\sum_{i=1}^{i=n} L_i}{L_{tot}} \tag{1}$$

$$I_{\text{OAIC}}^{areal} = \frac{\sum_{i=1}^{i=n} S_i}{S_{tot}} \tag{2}$$

Results

Inert environment

In order to assess the effect of the strain rate on the mechanical behavior, tensile tests were carried out in an inert environment. In this case, a dynamic vacuum equal to 10^{-5} mbar was used. The results of these tests at 650°C are presented in figure 6. As expected, a positive effect of the strain rate on the flow stress is found. Flow instabilities appeared for an applied strain rate of 10^{-2} s^{-1}, as well as low noise emissions. This phenomenon is clearly related to the triggering of PLC instabilities. The fracture surface was observed for each test. All of the specimens exhibited a typical ductile fracture with dimples, mostly initiated on primary carbides, whatever the strain rate, independently from the occurrence or not of plastic instabilities. That is to say that flow instabilities in an inert atmosphere do not generate a change in the fracture mode.

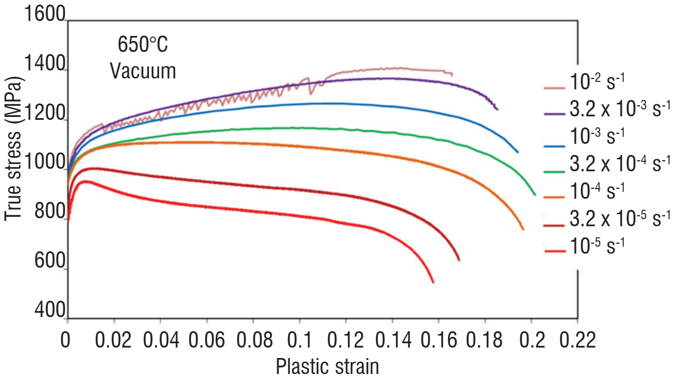

Figure 6 - Evolution of the flow stress for 650°C tensile tests in a vacuum (10^{-5} mbar), as a function of the strain rate

Oxidizing environment

A new set of experiments with the same thermal and mechanical testing conditions but under laboratory air conditions was performed. Some of the corresponding tensile curves are plotted in figure 7. The strain rate sensitivity was confirmed to be unaffected by environmental testing conditions. However, when dealing with elongation to rupture, the results are quite different. figure 8 gathers the results obtained for the two sets of tests, i.e., in a vacuum and under laboratory air testing conditions. The results obtained show that elongation to rupture is much smaller when the tests are carried out in air, except after the triggering of flow instabilities. When the strain rate is greater than the threshold strain rate, the elongation to fracture does not depend on the environment. However, due to the strain localization in the PLC regime, the strain to failure decreases [16]. It is worth noting here that the modification of the fracture behavior between the two environments is associated with a change in the fracture mode. At low strain rates under air testing conditions the fracture mode is intergranular. On the contrary, when the strain rate is greater than the strain rate threshold the fracture surface is ductile, whatever the environment.

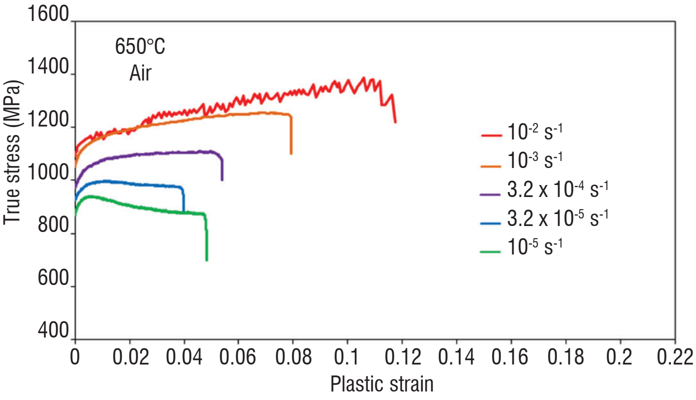

Figure 7 - Evolution of the flow stress for 650°C tensile tests in laboratory air as a function of strain rate

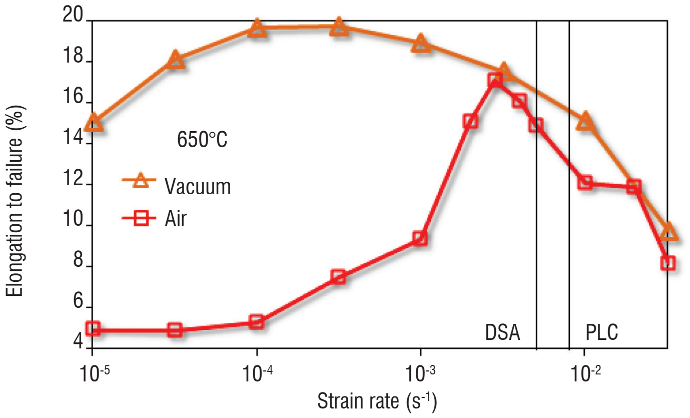

Figure 8 - Elongation to failure for tensile tests at T=650°C for different types of atmosphere: dynamic vacuum (10^{-5} mbar), or air

It is worth noting that tensile properties, such as Yield Stress (YS) and Ultimate Tensile Stress (UTS), are strongly dependent on strain rate. A representation of their evolution as a function of strain rate is plotted in figure 9. The stress experienced by the sample can reach various levels as a function of the strain rate.

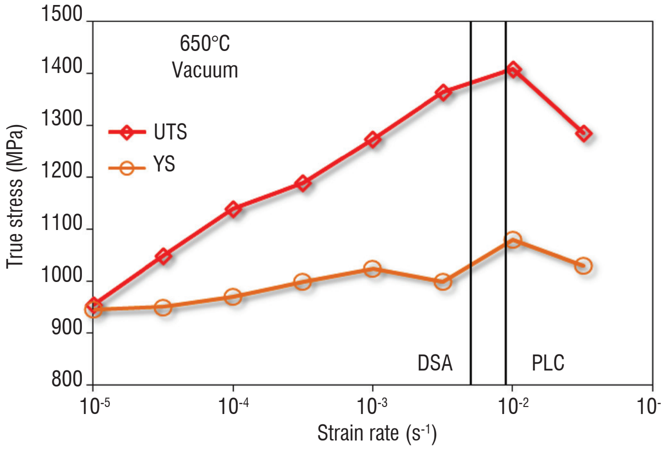

Figure 9 - Evolution of the yield stress and ultimate tensile stress for tensile tests at T=650°C in a dynamic vacuum (10^{-5} mbar)

Discussion

In order to better understand the OAIC mechanism, we compare macroscopic mechanical behavior with microstructural features. This is done through the graphical representation in figure 10, which shows the evolution of rupture elongation and both (linear and areal) indexes for OAIC sensitivity, as defined in a previous section of this paper, versus the strain rate. The plot also contains two complementary scales. The first corresponds to the duration of a tensile test, which varies both with the strain rate and the elongation to failure. The second one corresponds to the maximum crack length, determined using the maximum intergranular propagation rate in alloy 718 CT samples during creep-fatigue tests. This fastest crack propagation rate of a crack in alloy 718 has been evidenced in [12], it corresponds to the propagation of an initiated crack on a CT sample, during creep-fatigue tests (10s-300s-10s) in a high oxygen partial pressure environment (PO_2=0.2 bar) and a high stress intensity factor $\left(\Delta K = 40MPa\sqrt{m}\right)$. More precisely, these loading conditions have proven to lead to an average crack propagation rate of the order of 2 μm.s^{-1}.

Crack propagation in alloy 718 is still a controversial issue; nevertheless, under these assumptions, the maximum crack propagation length related to the tensile test duration can be evaluated, which provides important information on the operating damaging mechanism associated with the applied strain rate.

Something that must be pointed out is first of all that when tensile test parameters, namely the temperature and strain rate, trigger plastic instabilities, i.e., in the PLC domain, the fracture surface is entirely ductile. This experimental fact is due to the strong localization of plastic deformation within macroscopic bands resulting from the PLC effect. Hence, in this case, the fracture cannot be intergranular for two main reasons: the first is that the tensile tests do not last enough for the deleterious process of intergranular oxidation to occur; the second is the localization of the deformation into bands, which tends to enhance the mechanical damaging process.

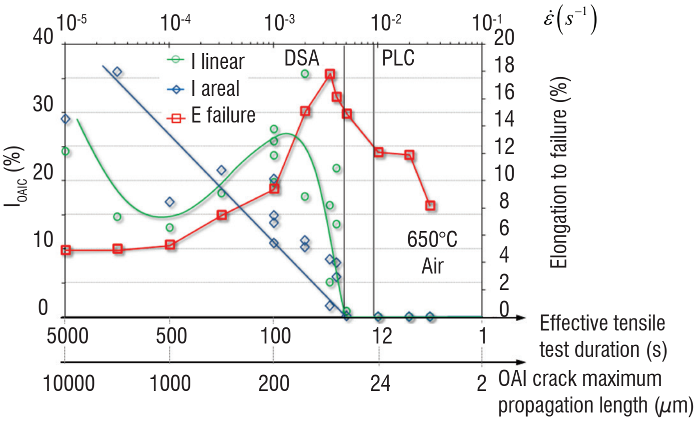

Figure 10 - Evolution of the elongation to failure and OAIC sensitivity indexes as a function of the strain rate for tensile tests at 650°C in an air environment

When entering the DSA domain from the fastest strain rate side, the damage characteristics are as follows: the indexes are rather scattered; crack initiations are numerous, but propagation is inoperative; the bearing section of the sample is, in this case, nearly unaffected by the cracking phenomenon. This strain rate domain enables the crack initiation behavior of the alloy to be characterized. This is the domain of interest for alloy 718, for which sensitivity is the key point regarding in-service lifetime.

When reaching the lowest strain rates in the DSA domain, the damage characteristics are the following: the indexes are weakly scattered; intergranular crack initiation sites are few, but cracks propagate widely. In this case, the bearing section of the sample is strongly affected by the cracking phenomenon and the elongation to failure is significantly reduced and nearly constant in this domain. Thus, this strain rate domain tends to be crack propagation controlled.

It is worth noting that these features, reported in this paper at the fixed temperature of 650°C, were also observed at different temperatures within the 300 - 700°C range. Indeed, OAIC indexes vary similarly versus a decrease in the strain rate or an increase in the temperature [15]. Also, for lower temperatures, PLC instabilities are observed in a systematic way to be associated with ductile fracture surfaces, confirming that the higher local strain rate does not allow OAIC to take place.

For a given grain boundary, crack initiation occurs when the intergranular normal stress σ_{app} reaches a critical value that corresponds to the grain boundary decohesion stress (GBDS), σ_c. Both stresses have a temporal evolution depending on the strain rate distribution in the policrystal, which can be related to various parameters that will be discussed herein.

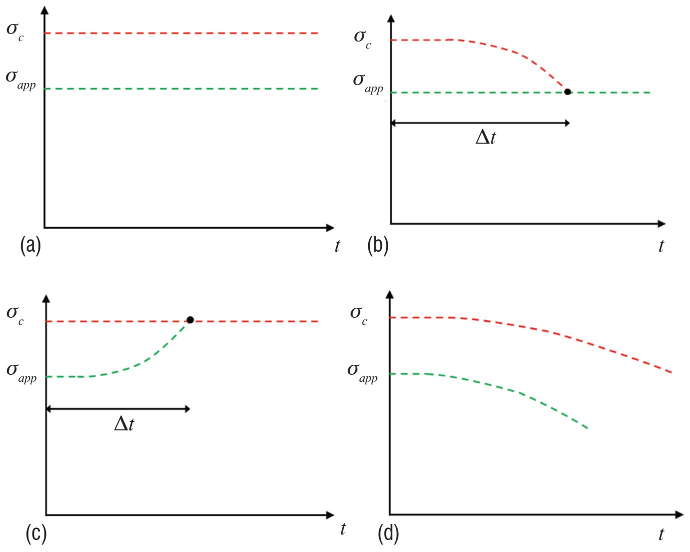

Figure 11 - Graphs of (a) applied intergranular stress and critical decohesion stress of grain boundaries, (b,c) some possible temporal evolutions of applied normal stress and critical bonding stress leading to grain boundary opening and (d) typical evolutions of both stresses in an inert atmosphere

It is relevant to note that the intergranular applied stress is unable to reach the GBDS (d) without an environmental coupling effect, which weakens the grain boundary, since the fracture surface of tensile samples tested at the same temperature in a dynamic vacuum atmosphere never exhibit intergranular brittle areas. It is only when the GBDS is lowered (b), or when the applied stress to a grain boundary increases (c), that intergranular brittle fracture can occur. The question is: how do σ_c and σ_{app} evolve respectively during the tensile test?

The decohesion stress of a grain boundary can be affected by several parameters, which can lead it to evolve during the tensile test. Oxygen penetration, vacancy injection due to the surface oxidation process, cavity formation and alloying element deformation assisted segregation to the favorably oriented grain boundaries are factors that are able to modify the decohesion resistance of the grain boundaries. It is worth mentioning here that intergranular oxidation provides a well-suited means to test interface toughness. This process, which corresponds to crack propagation jumps, might explain the high crack growth rate observed under severe loading conditions, assuming crack arrest due to bifurcation when the crack reaches a triple line.

The intergranular normal stress can evolve during the tensile test due to various phenomena, such as dislocation accumulation at the grain boundary neighborhood or creep of the surrounding grain structure, which leads a grain boundary to endure an evolving normal stress during policrystal deformation. A competition exists between the relaxation kinetics of the grain boundary internal stresses and the weakening kinetics of the grain boundary.

A previous study [15] carried out on a heat of alloy 718 within the 550°C to 700°C temperature range and within the 3x10^{-5}s^{-1} to 10^{-1}s^{-1} strain rate range showed the necessity to accumulate a given amount of plastic strain before crack initiation can occur. This study based on interrupted tensile tests and SEM observations showed that the amount of accumulated plastic strain before crack initiation can be observed on the gage length of the sample ranges from 1.8 to 3%. The existence of this threshold highlights the effect of strain and stress redistribution in the policrystal, occurring at the early stages of the strain hardening process.

Conclusion

For a given microstructure of the alloy, oxidation assisted intergranular cracking in alloy 718 is still an open and important topic. Results and observations obtained within the framework of this study bring to light some new elements, allowing a better understanding of the coupling processes involved in the intergranular crack initiation damaging mechanism. Two types of indexes were defined in order to characterize both crack initiation and crack propagation on tensile specimens. The evolution of these indexes depending on temperature, strain rate and environmental testing conditions enabled three domains to be determined. In the first, characterized by a high strain rate and/or low temperatures, flow instabilities (PLC) and short test durations, intergranular crack initiation never occurs whatever the environment. In the second, for intermediate strain rates, crack initiation occurs solely in an air environment and the elongation to failure remains unaffected by the damaging process. In the third, associated to slow strain rates and high temperatures, intergranular crack propagation is enhanced in an air environment and, consequently, the elongation to failure is significantly reduced. Finally, it would be useful to reexamine the evolution and localization of the damage using EBSD imaging during in-situ interrupted tests, in order to validate the proposed coupling mechanisms, which are suspected to depend on microstructural state ■

References

[1] E. ANDRIEU, R. COZAR, A. PINEAU - *Effect of Environment and Microstructure on the High Temperature Behavior of Alloy 718.* Superalloy 718-Metallurgy and Applications, 1989: p. 241-256.

[2] E. ANDRIEU, A. PINEAU, H. GHONEM - *Two-Stage Crack Tip Oxidation Mechanism in Alloy 718*. Elevated temperature crack growth, 1990: p. 25-29.

[3] E. ANDRIEU, R. MOLINS, H. GHONEM, A. PINEAU - *Intergranular Crack Tip Oxidation Mechanism in a Nickel-Based Superalloy*. Materials Science and Engineering: A, 1992. 154(1): p. 21-28.

[4] A. DIBOINE, A. PINEAU - *Creep Crack initiation and Growth in Inconel 718 alloy at 650°C.* Fatigue & Fracture of Engineering Materials & Structures, 1987. 10(2): p. 141-151.

[5] V. GARAT, J.-M. CLOUÉ, D. POQUILLON, E. ANDRIEU - *Influence of PLC Effect on Rupture Mode of Alloy 718 Specimens*. Journal of Nuclear Materials, 2008. 375: p. 95-101.

[6] H. GHONEM, T. NICHOLAS, A. PINEAU - *Elevated Temperature Fatigue Crack Growth in Alloy 718 - Part I : Effects of Mechanical Variables*. Fatigue and Fracture of Engineering Materials and Structures, 1993. 16(5): p. 565-576.

[7] H. GHONEM, T. NICHOLAS, A. PINEAU - *Elevated Temperature Fatigue Crack Growth in Alloy 718 - Part II : Effects of Environmental and Material variables*. Fatigue and Fracture of Engineering Materials and Structures, 1993. 16(6): p. 577-590.

[8] L.A. JAMES - *Effect of Temperature upon the Fatigue-Crack Growth Behavior of Two Nickel-Base Alloys*. J. Eng. Mater. Technol., no. 4, 1973. 95(4): p. 254-256.

[9] S. LYNCH, T. RADTKE, B. WICKS, R. BYRNES - *Fatigue Crack Growth in Nickel-Based Superalloys at 500-700° C. II: Direct-Aged Alloy 718.* Fatigue & Fracture of Engineering Materials & Structures, 1994. 17(3): p. 313-325.

[10] B. MAX, B. VIGUIER, E. ANDRIEU, J.M. CLOUE - *A Re-Examination of the Portevin-Le Chatelier Effect in Alloy 718 in Connection with Oxidation-Assisted Intergranular Cracking*. Metallurgical and Materials Transactions A, 2014. 45(12): p. 5431-5441.

[11] R. MOLINS, G. HOCHSTETTER, J. CHASSAIGNE, E. ANDRIEU - *Oxidation Effects on the Fatigue Crack Growth Behaviour of Alloy 718 at High Temperature*. Acta Materialia, 1997. 45(2): p. 663-674.

[12] J. PEDRON, A. PINEAU - *The Effect of Microstructure and Environment on the Crack Growth Behaviour of Inconel 718 Alloy at 650 C Under Fatigue, Creep and Combined Loading.* Materials Science and Engineering, 1982. 56(2): p. 143-156.

[13] K. SADANANDA, P. SHAHINIAN - *Crack Growth Under Creep and Fatigue Conditions.* Creep - Fatigue - Environment Interactions, 1979: p. 86-111.

[14] B. TER-OVANESSIAN, J. DELEUME, J.-M. CLOUÉ, E. ANDRIEU - *Quantitative Assessment of Intergranular Damage Due to PWR Primary Water Exposure in Structural Ni-Based Alloys*. Corrosion Science, 2012. 67: p. 11-19.

[15] B. TER-OVANESSIAN, D. POQUILLON, J.-M. CLOUÉ, E. ANDRIEU - *Influence of Local Mechanical Loading Paths on the Oxidation Assisted Crack Initiation of Alloy 718*. Materials Science and Engineering: A, 2012. 533: p. 43-49.

[16] H.D. WANG, C. BERDIN, M. MAZIÈRE, S. FOREST, C. PRIOUL, A. PARROT, P. LE-DELLIOU - *Experimental and Numerical Study of Dynamic Strain Ageing and its Relation to Ductile Fracture of a C-Mn Steel*. Materials Science and Engineering, 2012. A 547: p. 19-31.

Acronyms

CIRIMAT	(Centre Inter-universitaire de Recherche et d'Ingénierie des Matériaux)
ENSIACET	(Ecole Nationale Supérieure des Ingénieurs en Arts Chimiques et Technologiques de Toulouse)
DSA	(Dynamic Strain Ageing)
GDMS	(Glow Discharge Mass Spectrometry)
IGA	(Instrumental Gas Analysis)
OAIC	(Oxidation Assisted Intergranular Cracking)
PLC	(Portevin-Le Chatelier)
SEM	(Scanning Electron Microscope)
UTS	(Ultimate Tensile Stress)
YS	(Yield Stress)

AUTHORS

Eric Andrieu Doctor-Engineer ENSMP, 1990-1996 : Associate Professor at the Materials Center Pierre Marie Fourt-ENSMP. Head of a research group dealing with Mechanical Behaviour of metallic alloys and Environment. Since 1996: Professor at INP Toulouse / ENSIACET / CIRIMAT Head and now member of a research group studying couplings between mechanical (behavior and damage), microstructure (metallurgical states), reactivity (oxidation, corrosion) on metallic materials.

Bertrand Max Doctor-Engineer INPT-ENSIACET, Post-Doctoral position at IRT Saint-Exupéry, Toulouse Dynamic strain aging, Couplings between mechanical and oxidation, Impact of thermomechanical processes on microstructures.

Bernard Viguier Engineer in Physics from INSA Toulouse (1991), PhD degree from EPFL (1995), University Professor at INP Toulouse / ENSIACET / CIRIMAT Head of the Materials engineering department at ENSIACET and Deputy Director of the Doctorate School in Materials Sciences from the University of Toulouse. Experimental characterization of plastic deformation and phase transformations.

M. Perrut
(ONERA)

E-mail: mikael.perrut@onera.fr

DOI : 10.1276212015.AL09.10

Thermodynamic Modeling by the CALPHAD Method and its Applications to Innovative Materials

Among the different steps leading to a multi-scale lifetime prediction for aero-engine components and other industrial components, one seems to be apart from the other mechanical engineering concerns: thermodynamic and microstructural modeling. Here is given an introduction to the CALPHAD method [19, 27], explaining how it actually models the thermodynamic properties of multicomponent systems. Then, a number of applications are described, while emphasizing the relevance of using the CALPHAD method for the purpose of developing integrated engineering methods. Finally, the importance of building thermodynamic databases creates a high need for the development of *ab initio* calculations, as well as high-throughput experiments and, generally speaking, combinatorial materials science.

Introduction

There have recently been many incentives or ideas for new methods to accelerate the development and maturation of innovative materials: the DARPA-AIM program [45], the Materials Genome Initiative [36], the Integrated Computational Mechanical Engineering (ICME) approach [1] and European programs [16]. Numerical modeling is a key tool within this context and in particular multi-scale modeling, in order to achieve virtual optimizations of new materials and their associated processes as fast as possible. The final purpose of the ICME approach is to be able to model the entire chain, from the elaboration of a material to the in-service behavior of the industrial component, covering the full range of process / structure / property / performance relationships.

However, the first step in this chain – or the first floor of the building – is to model microstructures. This step is crucial, since microstructures have very strong impacts on the local mechanical properties, for example through precipitation hardening. This requires, at least, a relevant thermodynamic model for the various phases in relationship with the alloy composition. Therefore, this thermodynamic model represents the foundations of our building. By the term “relevant”, we mean both the efficiency (or precision) and the tractability of this thermodynamic model, since both are highly necessary in multi-scale modeling. The CALPHAD method has proven to be capable of both efficiency and simplicity: it is in fact the only known method to calculate the thermodynamics of multicomponent alloys in a simple way. This is why both academic and industrial uses of the CALPHAD (CALculation of PHAse Diagrams) method are strongly developing nowadays. Many microstructural models have, or become modified to have, CALPHAD-based thermodynamic inputs [2,9,20]; so do commercial software applications like MICRESS [38] or TC-PRISMA [42].

This article will give a theoretical introduction to the CALPHAD method, showing how the various data from experiments or numerical simulations can be collected and translated into a simple and consistent thermodynamic description, called a thermodynamic database. Then, a brief overview of CALPHAD industrial applications will be given. Finally, the importance of supporting the development and optimization of thermodynamic databases will be stressed, with examples of original dedicated experiments.

CALPHAD method basics

The simplest way to have a complete description of the thermodynamic behavior of a system at fixed temperature, pressure and chemical composition, is to know – i.e. to be able to calculate – its Gibbs energy G (also called free energy), as a function of these state variables. Once G is known, the thermodynamic equilibrium is calculated by minimizing G. Then, it is possible to have access to any phase diagram, any chemical potential (or activity), or any chemical composition of the stable phases. The main idea of the CALPHAD method is to evaluate the free energy of every phase by simple polynomials, called Redlich-Kistler polynomials. There are two main advantages of this solution: data storage is easy, since a polynomial is fully described by the list of its coefficients, and minimization is “not so hard” because a polynomial and its derivatives are easily calculated. These polynomial coefficients are the fitting parameters for the CALPHAD thermodynamic database optimization; hence, they are very often called “parameters” by the CALPHAD community.

How approximate descriptions of G give rise to polynomial expressions with physical relevance is now explained. The first step is to investigate the Gibbs energy of a pure element. The Gibbs-Helmholtz equation gives:

$$G(T_0) = H_{298} + \int_{298}^{T_0} C_p dT - T_0 \left(S_{298} + \int_{298}^{T_0} \frac{C_p}{T} dT \right) \qquad (1)$$

where H_{298} and S_{298} are the standard enthalpy and the standard entropy of the pure element at atmospheric pressure and at a temperature of 298 K. Contrary to the entropy S, the enthalpy H (and hence G) has no absolute value: by convention, H_{298} is chosen to be equal to zero. C_p is the heat capacity of the element at constant pressure. Equation (1) is highly important, because it is the source of our formulation for the expression of the Gibbs energy of a pure element, that is :

$$G^0(T) = a + bT + cT\ln T + \sum_2^n d_n T^n \qquad (2)$$

where a, b, c and the d_n are user-defined coefficients, called parameters, that drive the temperature dependence of the Gibbs energy of the pure element in a particular phase. Equation (2) must be fitted for each stable phase of the investigated element, the parameters being associated to the temperature range where the phase is stable. Moreover, differentiating equation (1) gives a very interesting result, since we obtain the following expression for the heat capacity:

$$C_p(T) = -c - \sum (n-1) d_n T^{n-1} \qquad (3)$$

Equation (3) means that, given the heat capacity, there are only two parameters (a and b) missing from the Gibbs energy expression. The next step is to develop an expression for single-phased alloys. When no interaction takes place between atoms of a different nature, it is easy to add the $x_i \ln(x_i)$ term corresponding to the configuration entropy in the case of ideal mixing. However, it is necessary to add an excess Gibbs energy, due to the interactions between the different atoms. Assuming the absence of ternary interactions, the molar Gibbs energy G_m is written as:

$$G_m = \sum_i x_i G_i^0 + RT \sum_i x_i \ln x_i + \sum_i \sum_{j>i} x_i x_j \Omega_{ij} \qquad (4)$$

where x_i and G_i^0 are, respectively, the mole fraction and the Gibbs energy of the i^{th} pure element, R is the ideal gas constant and Ω_{ij} is the excess Gibbs energy associated with the interaction between the i^{th} and the j^{th} pure element. It must be noted that the excess Gibbs energy contribution in equation (4) is automatically canceled when x_i or x_j is zero. Eq. (4) is called the regular solution theory. Given that this excess energy Ω_{ij} has no physical relevance, it may vary with temperature, as well as with x_i and x_j. In order to be able to break the symmetry between the ith and jth element, Ω_{ij} is developed in powers of $x_i - x_j$. This development of Ω_{ij} in the expression (4) of G_m is called the Redlich-Kistler (RK) polynomial. The various expressions of the Gibbs energy are not limited by RK polynomials, and far more complex analytical expressions can be written, including contributions due to pressure, magnetism, etc. [7].

In ternary and higher-order systems, ternary interactions L_{ijk} (ternary Gibbs excess energy) can be added, but there is no need to model quaternary interactions in common systems. This is a crucial remark: it implies that the thermodynamic model for a system of n elements can be approximately considered as an extrapolation of various ternary systems. These ternary systems can be modeled separately, the extrapolation being performed through the use of Kohler's rule or Muggianu's rule [14], as shown in figure 1. Gathering these ternary systems, containing data for each of the above parameters, produces what is called a thermodynamic database. Gathering systems supposes that the same description is made for shared pure elements, shared binary systems and any shared subsystems. Namely, the CALPHAD community shares a public pure element database [7].

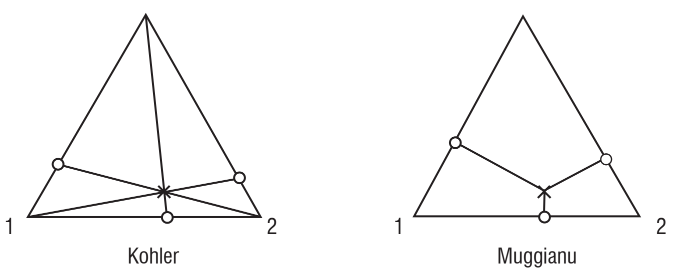

Figure 1 – Kohler's and Muggianu's rules illustrated in the example of a ternary system [14]

This is why the thermodynamic databases are said to be best described as a brick assembly, where the “unit” bricks are the pure elements, whose CALPHAD models allow binary models to be built, then ternary models and so on. This is also why there is research activity about very accurate calculations of the Gibbs energy and heat capacity of pure elements, to be compared with the CALPHAD unary database [10, 28].

The way in which the database can be built and optimized is far beyond the scope of this article. In brief, the relevance of the database parameters is tested by calculating the discrepancy between the thermodynamic data that the database produces and the corresponding experimental (or numerical) data. Optimization loops are performed and this is the know-how of the expert researchers in the field, to be able to optimize the numerous parameters of a database, with the aid of the special algorithms included in the thermodynamic software (Thermo-Calc PARROT [42], PanOptimizer [39], FactSage Optisage [35], etc.). It must be highlighted that there are many different models that can reproduce a particular binary phase diagram. The accuracy of the CALPHAD assessment will be revealed when the extrapolation into higher order systems is performed. This accuracy depends strongly on the accumulation of reliable experimental results concerning: phase diagram, calorimetric measurements and activity measurements.

Another set of data comes from what is called *ab initio* calculations, or first-principle calculations, which means that the calculation directly solves the Schrödinger equation and obtains the well-known wave functions of the quantum mechanics for the desired system. These calculations have become popular since the DFT method [23] became readily available *via* commercial software (VASP [46], Wien2k [47], ABINIT [34], etc.) and personal computers are able to solve simple systems in moderate CPU times. The accuracy of the results is often discussed, because various approximations lead to significant differences in the obtained results and, also, because unskilled researchers will very easily get irrelevant *ab initio* results.

In any case, these calculations are an appreciated help for temperature ranges that are difficult to reach, metastable or unstable phases, or for dangerous elements such as actinides. However, they have a strong limitation in regard to the number of atoms that they are able to simulate, so that – most of the time – only a unit cell of the crystalline structure is considered. For this reason, it is not possible to simulate disordered alloys, where the position of alloying atoms is not always in the same place within the unit cell, but rather random. The point is that there are specific CALPHAD models for the Gibbs energy of ordered phases that will be able to incorporate these *ab initio* calculations.

Box 1 - Regular solution theory and topological features of the binary phase diagrams

In order to understand the topology of phase diagrams, Pelton and Thompson modeled in 1975 a basic binary phase diagram and added constant excess Gibbs energies Ω in the solid and in the liquid phase [24]. This corresponds to the regular solution theory. The figure B1-1, taken from [27], has been created in the same way, starting from the red-framed reference A-B binary diagram. If Ω is negative in the liquid or in the solid phase, this means that A and B "like" to be mixed together, so nothing complicated happens. Conversely, if Ω is positive, it means that A and B "dislike" to be mixed together. Two-phased domains appear and become larger. For example, adding an excess mixing energy in the solid phase leads to an eutectic diagram. The liquid alloy may also demix, if Ω is positive in the liquid. The upper-right corner of figure B1-1 shows that almost no single-phased domain remains when large amounts of excess energies are added in both the liquid and solid phases. In conclusion, the regular solution theory gives many different topological features for phase diagrams, even with the two-phase simplest binary diagram.

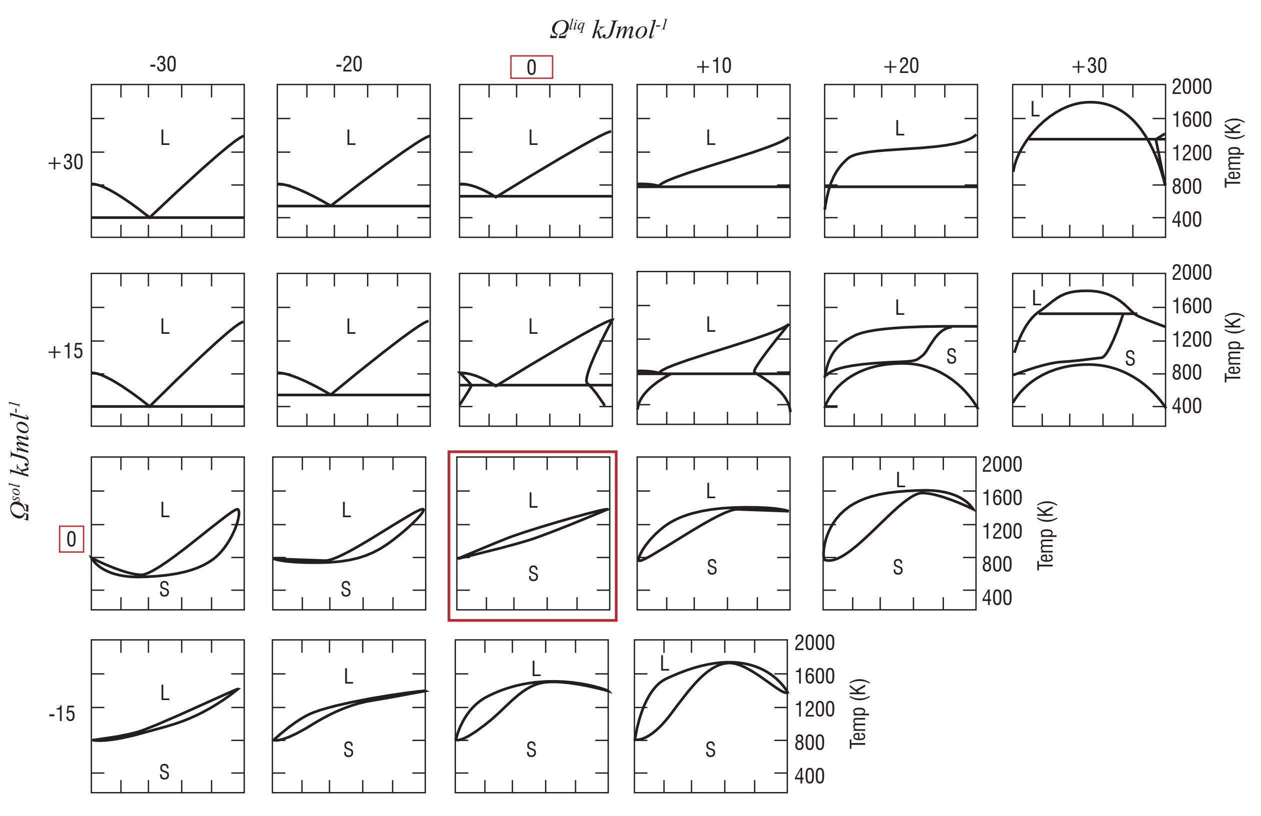

Figure B1-1 – Topological features of phase diagrams calculated using the regular solution theory [27]

In order to model ordered phases, the CALPHAD formulation should discriminate between the various sublattices occupied by the system elements. These sublattice models had a tremendous influence on the development and success of the CALPHAD method, because it is able to model not only line compounds, but also, through the associated defects (substitutions, vacancies and interstitials), interstitial phases, complex intermetallic compounds and order/disorder transformations [27]. Assuming two sublattices S1 and S2 in a binary system A-B, there are now four reference states: A:A (pure A), A:B (A occupying S1 and B occupying S2), B:A (B occupying S1 and A occupying S2), B:B (pure B). These four reference free enthalpies, known as the end-members, are very important in CALPHAD modeling. The excess Gibbs energy also has a new formulation, taking into account the sublattices through different contributions [19,27].

The phases corresponding to the end-members are very often thermodynamically (or dynamically) unstable, except for the ordered compound investigated, that is, only one among the four phases. However, each end-member must be evaluated, even though only one is experimentally available. Here, it should be understood that the *ab initio* calculations are mandatory to provide these values, which are necessary for the construction of a relevant thermodynamic database. Results are, in general, more accurate if the CALPHAD sublattices come closer to the real crystallographic sublattices.

However, given that modeling a phase with m sublattices in an n-element thermodynamic system does require the calculation of nm end-members, there is actually a high demand for ab initio calculations from the CALPHAD community. For example, the work of Yaqoob *et al.* [30] details a 5 sublattice model for the σ phase in the Ni-Mo-Re system. This phase has a complex crystallography, which is shown on the left in figure 2. However, this is highly relevant to model this phase, because it is known to deteriorate the behavior of Ni-based superalloys, which are widely used in the high pressure turbines of aeroengines. Due to the 5 sublattice combination, the authors of [30] had to perform calculations for $3^5 = 243$ different structures, representing 90 different chemical compositions, but the results are very satisfactory. It should be emphasized that there is a recent trend towards accumulating the results of *ab initio* calculations in the form of databases, which are growing very quickly [37].

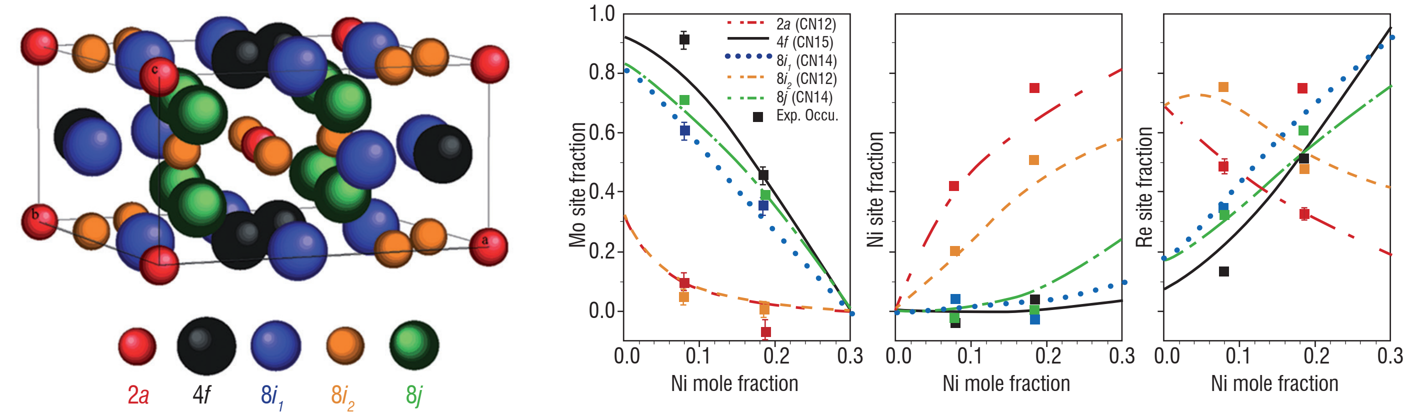

Figure 2– Crystal structure of the σ phase (left); comparison between experimental (squares) and calculated (lines) site occupancies of the Ni-Mo-Re σ phase at 1873 K along a line of the ternary diagram [30]

Once the thermodynamic model has been completed, equilibrium calculations may be performed by minimizing the Gibbs energy. The classical method for obtaining the minimum of the Gibbs energy is the use of Lagrange multipliers μ_i and λ^φ related to the $N_{el} + N^\varphi$ physical constraints (mass balance equation for each of the N_{el} elements, sum of the molar fractions equal to unity in each of the N^φ phases), as described in [15]. The Lagrange function, noted as L, is written as:

$$L = \sum_{\phi=1}^{N^\phi} n^\phi G_m^\phi + \sum_{i=1}^{N_{el}} \mu_i \left(n_i - \sum_{\phi=1}^{N^\phi} n^\phi x_i^\phi \right) + \sum_{\phi=1}^{N^\phi} \lambda^\phi \left(1 - \sum_{i=1}^{N_{el}} x_i^\phi \right) \qquad (5)$$

where $G_m^{\ \varphi}$ is the molar Gibbs energy of the phase φ, n^φ is the number of moles of the phase φ and $x_i^{\ \varphi}$ is the mole fraction of the i^{th} element in the phase φ. Then, a non-linear system of $N_\varphi\ (N_{el} + 1)$ Lagrange-type equations (6a) and (6b) must be solved, usually using a Newton-Raphson algorithm, in addition to the $N_{el} + N_\varphi$ initial constraints (6c) and (6d).

$$\frac{\partial L}{\partial n^\phi} = G_m^\phi - \sum_{i=1}^{N_{el}} \mu_i x_i^\phi = 0 \qquad (6a)$$

$$\frac{\partial L}{\partial x_i^\phi} = n^\phi \left(\frac{\partial G_m^\phi}{\partial x_i^\phi} - \mu_i \right) - \lambda^\phi = 0 \qquad (6b)$$

$$1 - \sum_{\phi=1}^{N_{el}} x_i^\phi = 0 \qquad (6c)$$

$$n_i - \sum_{\phi=1}^{N^\phi} n^\phi x_i^\phi = 0 \qquad (6d)$$

The final result gives the values of the initially unknown quantities: the amount n^φ of the various phases, their composition given by the $x_i^{\ \varphi}$ and the Lagrange multipliers λ^φ and μ_i, these μ_i being considered as the chemical potentials of the i^{th} element. All information regarding the thermodynamic equilibrium has been calculated.

Industrial applications

Outside ONERA

The domains of application of the CALPHAD method are so numerous that it is impossible to list them here. The list of thermodynamic databases proposed by the TCS-AB company for the Thermo-Calc software gives an idea of the number of material classes that have been assessed with the CALPHAD method [42]. It includes metallic materials (steels, Ni-based superalloys, titanium alloys and aluminum alloys), ceramics, cemented carbides, intermetallics, nuclear fuels, cermets, solders, etc. Some striking examples will be given here, showing what can be expected in the future for alloy design and optimization.

The Ford company has developed the ability to perform so-called “virtual castings” [1]. Using the Procast [40] and Abaqus [33] software applications, the sole inputs for the calculation are: the complex die geometry, the alloy composition and the required properties. The castability, phase transformations and resulting mechanical properties (tensile strengths, as well as low-cycle fatigue properties) are simulated together in the same 3D virtual object. The Ford company claimed that this new approach reduced time from 15-20% for the design of new engine blocks and hence saved millions of dollars. This required state-of-the-art calculations and experiments. As an example, they investigated how to calibrate heat-transfer coefficients for the solidification simulation. Moreover, solid-state diffusion was coupled to the dendrite structure evolution, with the entire calculation being actually coupled with the CALPHAD software Pandat [39]. The influence of each length scale in their multi-scale simulation is summed up in figure 3.The acceleration effort for the ultrahigh-strength steel design, such as Ferrium S53 and M54,

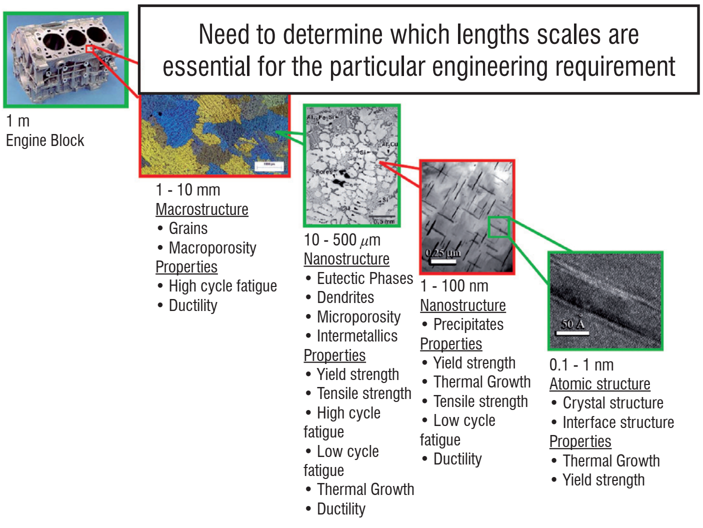

Figure 3 – Relevant length scales behind the multi-scale modeling from atoms to engine that was developed by Ford company to simulate so-called “virtual castings” [1]

is a very good illustration of the success of Accelerated Insertion of Materials [45] (see figure 4). The microstructural modeling was performed by the Precipicalc software, which uses the Thermo-Calc and DICTRA software as engines for the calculation of equilibrium and diffusion [42]. The most surprising fact may lie in the ability to predict the manufacture variation. Big simulation datasets have allowed designers to evaluate the 1% minimum ultimate tensile strength and to compare it to the material requirement. This proved the necessity of additional process optimization before starting the material evaluation at a larger production scale, saving approximately one year in time and a half million dollars. Finally, the evaluation of the 1% minimum ultimate tensile strengths (over 10 heat values and 600 observations) showed only a 7 MPa difference between the calculation results and the experiments, revealing how relevant this approach has been.

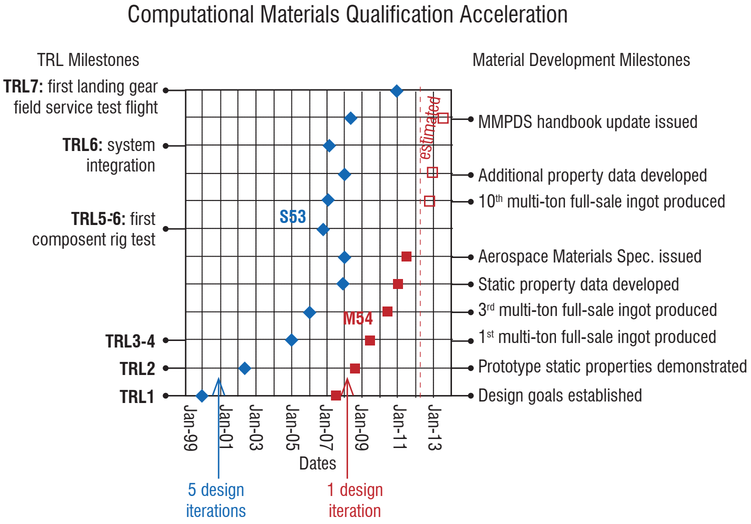

Figure 4 – Accelerated insertion of materials.
Example from American steel-making industry given by G.B. Olson [22]

The European contribution to advanced material design is of course very significant, namely by the very high level of knowledge in terms of quantum mechanics modeling, microstructural or process modeling, although the full integration of the various length scales remains a challenge. The CALPHAD method is widely used in Europe: the SGTE group in Grenoble France, founded by E. Bonnier, laid the foundations for this method since the 1970s, with a crucial role played by H. Ansara [11]. There has been a strong presence of CALPHAD developers and users in Europe: the Thermo-Calc Software in Sweden, the Thermotech company in England, the MatCalc project in Austria, the MICRESS team in Germany coupling phase-field methods with CALPHAD and the Zircobase project (development of a thermodynamic database for Zr-based alloys) in France thanks to the CEA. Only two examples are detailed below, illustrating the microstructural modeling of Ni-based superalloys: the first concerns oxidation behavior and the second concerns microsegregation and its influence on γ' precipitation.

An English research team succeeded in predicting the formation of an alumina layer during the oxidation of Ni-based superalloys at high temperature [2]. Not only does the model calculate the evolution of the oxide thicknesses at the surface, but also the γ' fraction as a function of the distance to the outer surface. The authors use a combined model: the parabolic growth of the oxides is coupled with a DICTRA multi-element diffusion calculation, focusing mainly on the Al content evolution (see figure 5). The input parameters are few and mainly used to describe the parabolic-type behavior of the superalloy oxide growth.

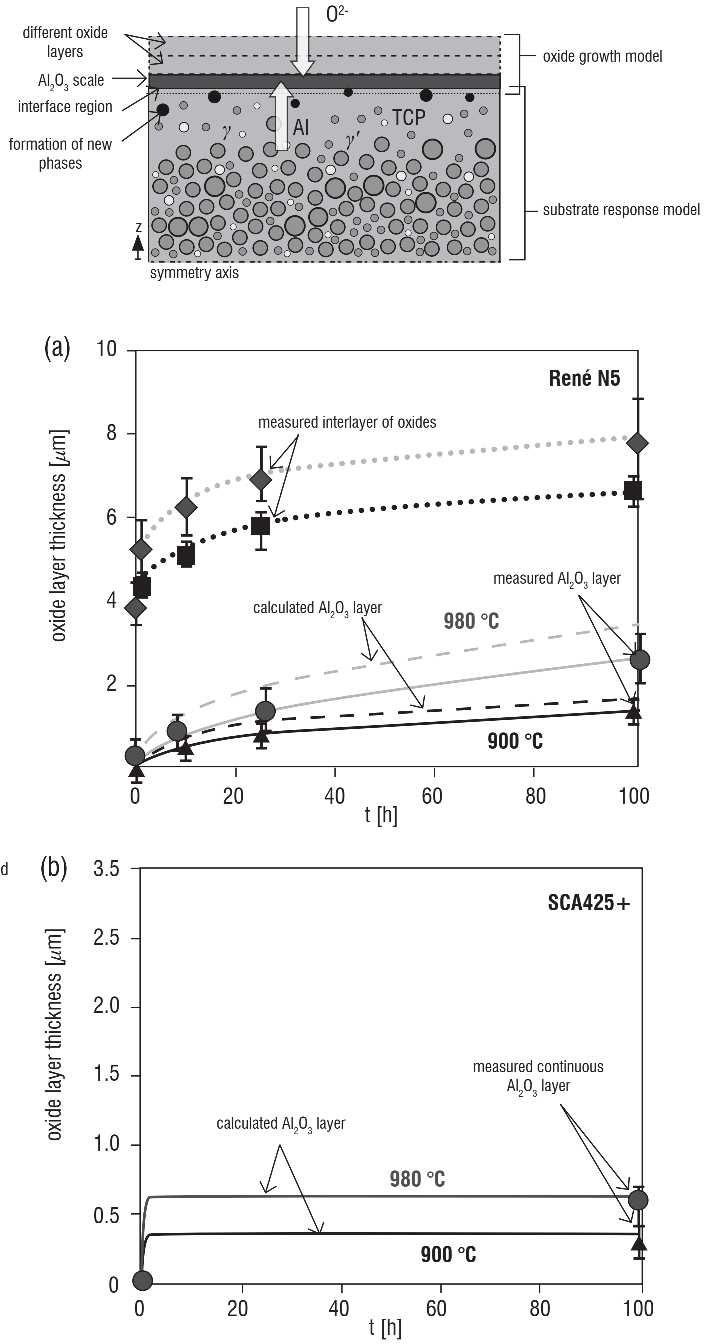

Figure 5 – Coupling an oxide growth model to a multi-element diffusion calculation: scheme of the physical process (top) and simulation results concerning two different alloys (a and b) [2]

An example of French research that strives to achieve the integration of multi-scale process modeling is the PhD work of Luc Rougier [26]. Its aim was to model successively the solidification, homogenization heat treatment and quench of cast Ni-based superalloys. In fact, the main goal was to model the γ' precipitation occurring during the quench. However, the precipitate mean size (for one, two, or more different populations) depends on the quench rate and on the local chemical composition. The latter can only be calculated by modeling the micro-segregation processes of the solidification step and the following solid-state diffusion during the homogenization heat treatment. Satisfying results were obtained, showing in particular the great influence of cross diffusion on the final microstructure, in the case of a Ni-Al-Cr ternary alloy. This means that the diffusion of an element in the Ni-based γ matrix should be known, not only in relationship with its own mole fraction gradient (classical diffusion), but also with the mole fraction gradients of all of the other elements (cross diffusion), leading to a need for the knowledge of the entire diffusion matrix with sufficient precision.

Within ONERA

There has been a lot of work within ONERA concerning powder metallurgy Ni-based superalloys for high-pressure turbine disks. An example of the ICME approach has been applied to the N18 superalloy used in the Snecma M88 engine. The size distribution of its γ' precipitates was first modeled in the late 1980s using a binary alloy model [21]. The precipitation model has been recently revised at ONERA, upgraded in a pseudo-binary alloy model and finally used in a multi-scale mechanical model for the calculation of the fatigue life under low cycle fatigue conditions [3]. These calculations were able to successfully predict the lifetime of the disk and also to guess its dangerous locations due to cycling deteriorations of the material.

The new calibration of the precipitation model for the N19 superalloy has been accelerated through the use of the Thermo-Calc software, its TCNI5 thermodynamic database [43] and its MOBNI2 mobility database [44]. We give a brief reminder here of the approach, the main assumptions and the input parameters associated with the model. This is a particle size distribution model, based on classical nucleation and Lifshitz-Slyozov-Wagner (LSW) coarsening theory [17], where precipitates are distributed in size classes. It calculates the size distribution of intragranular γ' precipitates over time, depending on the material thermal history (which is supposed to be given as an input of the model). The distribution obtained is bimodal most of the time, or even n-modal ($n > 2$). This results in the knowledge of relevant parameters for the microstructure at the end of the heat treatment: mean sizes and volume fractions of each mode of the distribution (i.e., secondary and tertiary γ' precipitates for $n = 2$). Primary precipitates do not interact directly with the calculated intragranular precipitation, but their existence strongly modifies the matrix chemical composition inside the grains, which is taken into account in the model.

Given that this kind of calculation is performed at each Gauss point of a mesh, it is necessary to simplify the problem. It is therefore assumed that the precipitates are isolated spheres (no interaction between precipitates), that the influence of elasticity is neglected and that the precipitate/matrix interfaces are at local equilibrium. A pseudo-binary approach is used to calculate the equilibrium mole fractions: the Al, Ti and Nb γ'-forming element mole fractions are summed, in order to deduce a "solute" mole fraction, like in the PhD work of J. Mao [20]. A single "effective" energy-activated diffusion coefficient is used to match the precipitation kinetics. The driving force is taken from [29] and consists in a simple analytical expression of the matrix supersaturation and is not specific to the material.

The list of the material-dependent input parameters is: initial solute mole fraction, interfacial energy, pseudo-binary phase diagram, effective diffusion coefficient and its activation energy, volume fraction of primary γ' precipitates. The molar volume of the γ' phase is also needed, but its slight variation has only slight impact on the kinetics, since the elasticity influence is not taken into account. The interfacial energy is assumed to be constant, whatever the temperature or the size of the precipitates. This simple model has few material-dependent input parameters, but it was successfully used to describe N18 precipitation kinetics. However, experimentally determining the N18 pseudo-binary phase diagram and in addition evaluating the effective diffusion coefficients by investigating the isothermal long-time microstructural dynamics at several temperatures was time consuming. It was thus decided to test, for the calibration of N19 precipitation kinetics, a Calphad-based calibration with even fewer experiment-based input parameters.

at.%	Ni	Cr	Co	Mo	Ti	Al	W	Nb	Zr	Hf	B	C	γ' solvus	γ' frac.
N18	bal.	12.3	14.8	3.8	5.1	9.1	/	/	.018	.16	.083	.075	1195°C	55-60%
N19	bal.	14.6	12.0	2.9	4.6	5.5	1.0	1.0	.038	.1	.08	.1	1145°C	40-45%

Table 1 – Chemical compositions (at. %),γ' solvus temperature and typical γ' fraction at room temperature of N18 and N19 alloys [25]

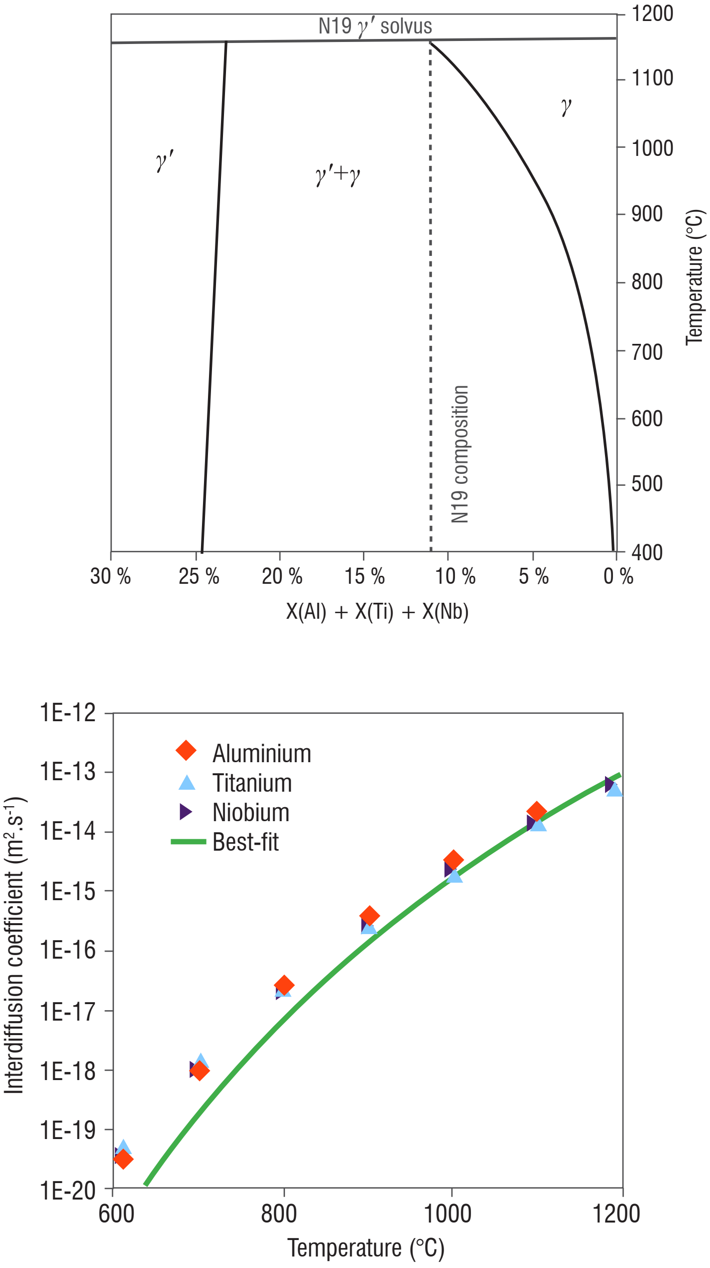

Figure 6 – Pseudo-binary phase diagram of the N19 alloy obtained by the Thermo-Calc software (top); Interdiffusion coefficients of Al (red squares), Ti (blue triangles) and Nb (purple triangles) in the N19 γ phase for various temperatures, obtained with the DICTRA software and compared with the effective diffusion coefficient (green line), which better fitted the experimental results (bottom)

Figure 6 shows the phase diagram obtained and the diagonal interdiffusion coefficients for the elements Al, Ti and Nb in the γ phase at its temperature-dependent equilibrium composition [25]. It must be noted that no coupling between the Thermo-Calc (or DICTRA) and Z-set is performed, but rather only a priori calculations for the input parameters.

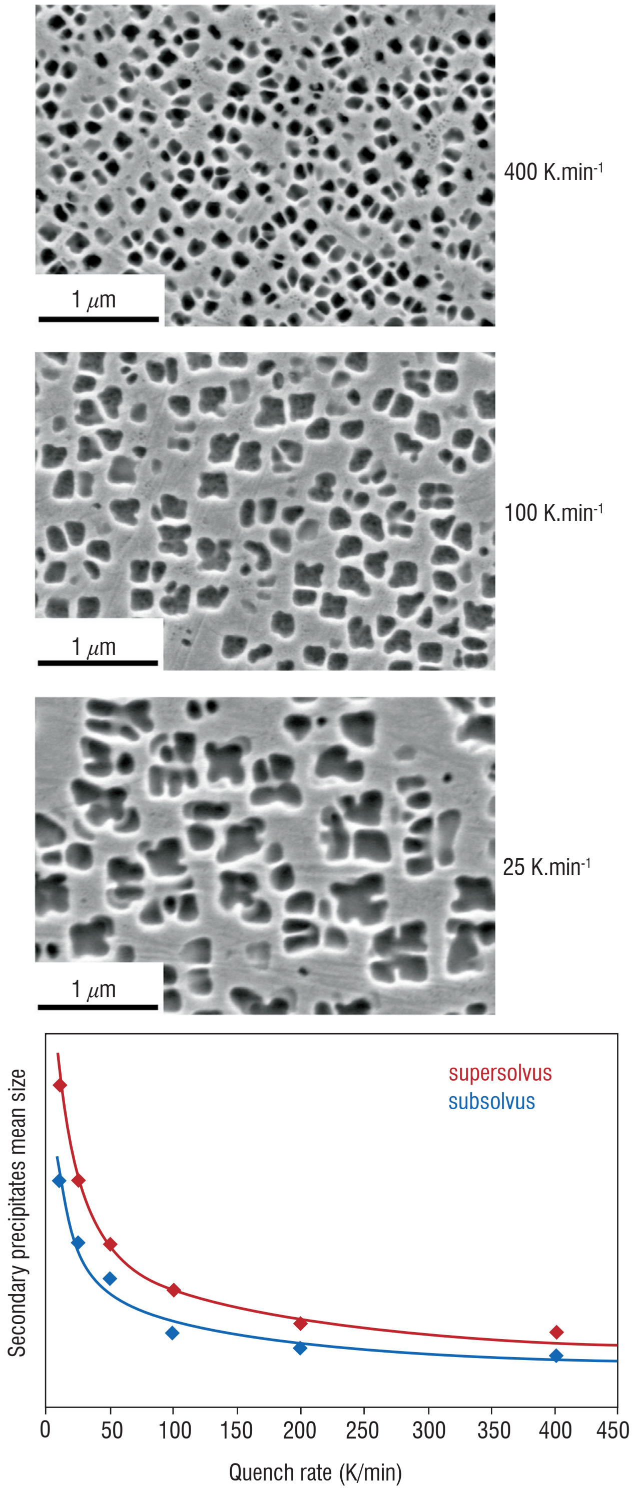

Figure 7 – Influence of the quench rate on the precipitate mean size: experimental microstructures (top) and comparison between numerical simulations and experimental measurements (bottom) [25]

The phase diagram obtained allows the calculation of polynomial fits of the equilibrium molar fraction evolution in γ'-forming elements of the γ phase and of the γ' phase, from room temperature up to the calculated γ' solvus temperature (1153°C). There is no need to optimize these calculated fractions. Concerning diffusion coefficients, it can be noted that the three elements investigated have similar diffusion coefficients, which greatly simplifies the problem. However, we had to optimize the effective diffusion coefficient by comparison with our experimental results. The calculated interdiffusion coefficients give a good initial estimate, especially at high temperatures, but the activation energy must be taken slightly higher to fit the experimental values of the precipitate mean sizes. The last input parameter that strongly influences the precipitation kinetics is the energy of the $\gamma - \gamma'$ interface. It was determined by fitting the experimental results, while keeping it within a relevant range (1 to 100 mJ.m^{-2}).

The validation of this approach was carried out by comparison with experimental mean sizes of secondary precipitates and corresponding surface fractions. Micrograph examples are shown in figure 7 (bottom), where the microstructures are very different due to the variation in the applied cooling rates. A very satisfying agreement was found between the calculations and the experimental results, as shown in figure 7 (right), for both the subsolvus and supersolvus heat treatments. When considering air cooling or oil quenching, the effects of the precipitation latent heat will not be counteracted, which has been discussed in [25].

These encouraging results open the path to extending our integrated approach for the calculation of a turbine disk lifetime to the N19 alloy and to many other Ni-based superalloys.

Enriching the databases

Outside ONERA

The impressive success of the CALPHAD method for various applications poses the question of how the scientific community can efficiently construct all of the thermodynamic data needed by industries in all fields. This is a difficult problem to address. The high demand for numerous and reliable ab initio calculations might not be met, due to the need for huge computational resources and the corresponding skilled materials scientists. The rapid progress in terms of supercomputing performances may greatly help. However, it is more difficult to imagine how phase diagrams could be experimentally assessed at a high speed and with high precision. There are 61 commercially available metals, resulting in around 1,800 binary systems that are not completely known (even some with much scientific or technological interest present still unclear areas), and 90% of the 36,000 ternary systems are said not to have been explored in any way [16].

The necessity of creating thermodynamic experimental data at a higher speed can be solved in two different ways: accumulating numerous experiments, at a very high rate, with the help of automated routines or performing experiments that yield, at once, a great amount of data. A combinatorial materials science project, called ACCMET (ACCelerated METallurgy), has been recently funded by the European Commission through a FP7 research program [16]. The main idea is to cast small samples of metallic alloys by mixing pure elements, producing a sample in only 30s, offering the opportunity to screen large compositional landscapes. Automated characterizations may follow, including micro-hardness, RX diffraction and resistivity measurements as a function of temperature. This is enough to reveal intermetallic phases and to evaluate the ability of these new phases to maintain their strength at high temperatures.

A famous high-throughput experimental method was reported in 1970 by Hanak, who prepared composition-spread films of metal alloys by sputtering mixed-material targets [12]. Since 1970, this method has unfortunately not been extensively used, but, more recently, Cui et al [6] have used co-deposition techniques to discover new shape-memory alloys and to rapidly assess the compositional domain of these (see figure 8). A serious concern is that these as-cast microstructures and as-coated microstructures may be very far from equilibrium and no accurate thermodynamic data can be deduced before a relevant thermal treatment.

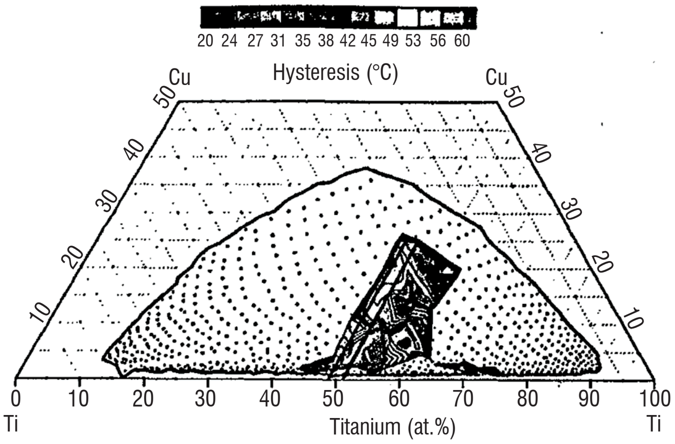

Figure 8 – Shape-memory hysteresis measured for many different compositions of the Ni-Ti-Cu ternary system with the help of high-throughput experiments [6]. The figure shows at a glance the interesting composition ranges to obtain the desired shape-memory effect

Another example of an interesting technique is the diffusion triples [8,13,31]. Diffusion couples are commonly used to determine interdiffusion kinetics between two materials. This technique could be extrapolated to three pure elements that are welded or bonded together. Long-term heat treatment leads this ternary system to thermodynamic equilibrium. As the three elements diffuse throughout the entire sample, most of the ternary phase diagram is explored and Electron Probe MicroAnalysis (EPMA) profiles are able to measure the compositions of the stable phases and the tie-lines that are associated with the interfaces between the phases. Zhao et al [31,32] provided many insights in regard to this experimental technique. The special interest is that the technique can explore, in one single experiment, a ternary diagram at a chosen temperature. The Zhao team has evaluated many ternary systems for the company General Electric during the 2000 s.

However, some phases that have slow kinetics never appear during these diffusion experiments and – once again – there is a strong concern about the out-of-equilibrium nature of the microstructure. A well accepted assumption is that the mole fractions of the various elements at the interface between two phases correspond to the stable tie-lines of the phase diagram, but this is only an approximation. It is also not possible to determine the crystalline structures of the observed phases, only their chemical composition.

Within ONERA

Diffusion couple experiments were performed at ONERA in order to determine composition-dependent interdiffusion coefficients in the intermetallic compound β-(Ni,Pt)Al by numerical inverse analysis [4]. The intermetallic compound β-(Ni,Pt)Al is used as a high temperature protective coating for superalloys and a bondcoat for thermal barrier coatings. In this context, it is especially relevant to estimate the diffusion kinetics of the Al element, which has a high influence on the lifetime of coated Ni-based superalloy turbines in an oxidizing environment. It was possible to derive relevant interdiffusion coefficients from these experiments and to prove the consistency of the method [4].

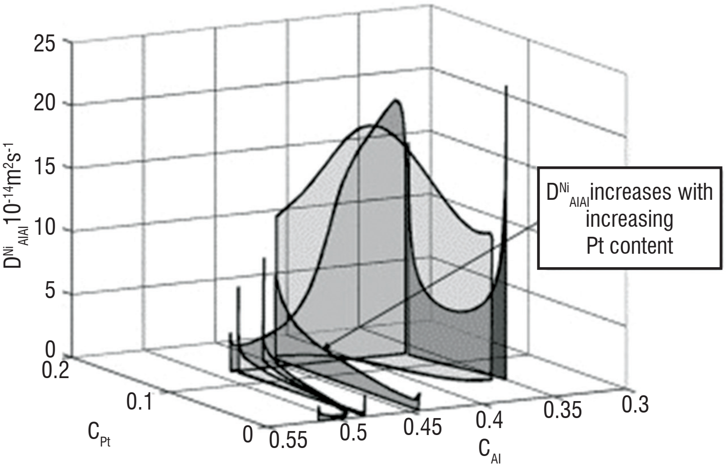

Figure 10 – Influence of the composition of the β-(Ni,Pt)Al phase on the interdiffusion coefficient of Al with respect to the gradient of the Al mole fraction [4]

More recently, inspired by the work of J.C. Zhao and based on our experience in diffusion couples, diffusion multiple experiments have been performed at ONERA. Our main idea was to perform quick and simple experiments, needing only common laboratory devices and quick chemical characterization. Contrary to Zhao's team, the hot isostatic press (HIP) was not used, but rather only a laboratory furnace with sufficient volume and a flat base, where two pure metals can be bonded according to the scheme in figure 11. The solid-solid bonding can be repeated on the obtained couple with a third metal. In most cases, it is helpful to use a melting process to build the triple, for example by cutting a hole in the first couple and using it as a crucible [8]. It is important to inspect the binary diagrams in order to predict how the liquid pure element will react with both other elements.

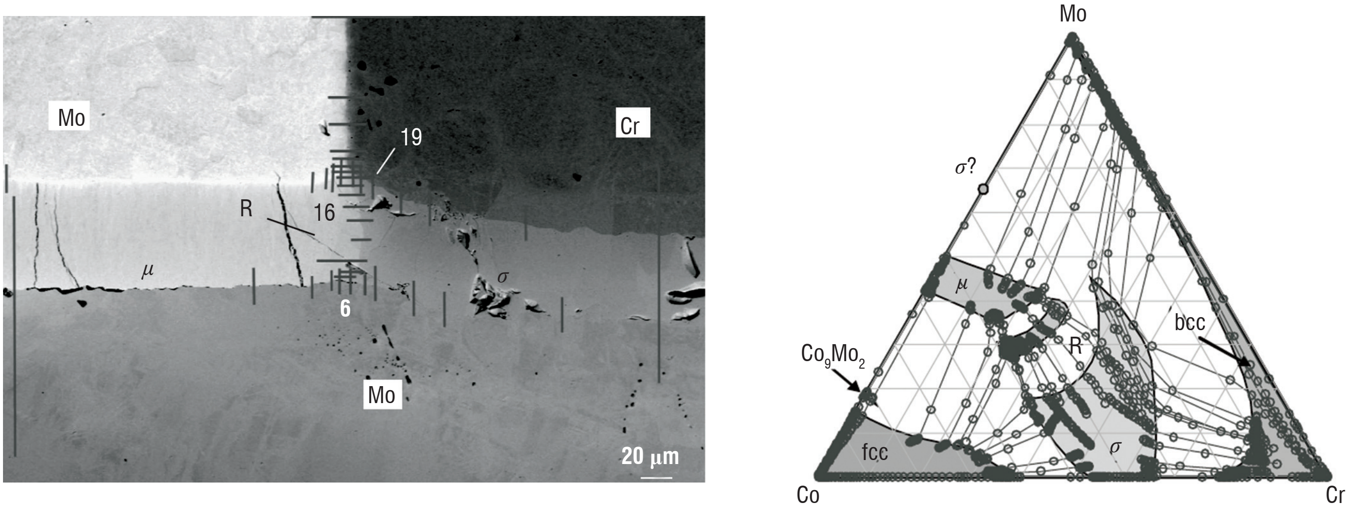

Figure 9 – EPMA profiles after the diffusion of a Cr-Co-Mo triple for 40 days at 1100°C (left) and the corresponding phase diagram data (right) [32]

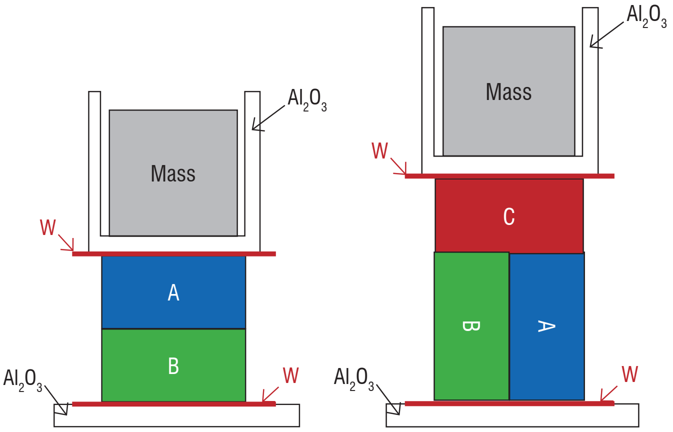

Figure 11 – Simple solid-solid bonding method that can be used with conventional laboratory furnaces

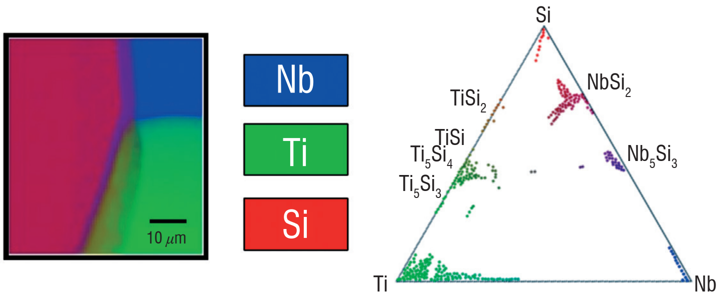

Figure 12 – Quantitative chemical imaging of a Nb-Ti-Si diffusion triple at 1200°C for 5 days (left); example of results given by an automated "image processing" of EDS maps for two different triples

In fact, eutectic reactions often occur, preventing the system from maintaining the presence of the pure elements, which limits the width of the compositional exploration of the ternary system. For example, in the case of the Nb-Ti-Si system, considering that Si (Liq) → 0.94 Si (diamond) + 0.06 $NbSi_2$ (hexagonal), it is interesting to use pure Nb as a crucible for Si. Conversely, testing a pure Ti (or even a Ti/Nb couple) crucible led to the L → Ti + Ti_5Si_3 eutectic reaction, with no pure Si left in the sample. Some wetting problems could also occur. If the liquid metal wets the crucible completely, it escapes through the hole and, again, a very small quantity of the third metal is left.

The longest step in the experiment is due to the long-term diffusion heat treatment that is needed to explore the diagram, ranging from a duration of one day (high temperatures) to several months (intermediate or low temperatures). There are several ways to shorten the duration: downsizing the samples to thin layers, performing a diffusion treatment on an initial couple before bonding the third element, or performing a dual anneal diffusion multiple approach [5].

The last step is the chemical characterization of the obtained microstructure, which should reveal the ternary diagram properties. It usually consists in performing EPMA profiles around the triple point and perpendicularly to planar interfaces, so that the positions of the various ternary diagram tie-lines are evaluated [32]. We are now developing a new method at ONERA that is less reliable but very quick and does not need any EPMA. The EDS mapping technique is used around the triple point with a refined mesh, so that the EDS spectra are automatically acquired, typically overnight. The advantage is that all of the data can be post-processed, keeping the scanning electron microscope available for other experiments during the daytime. An automated quantification procedure has been specially developed by the company SAMx [41] in order to obtain a quantitative chemical composition at each pixel of the map, with the option of grouping several spectra into one larger pixel if the EDS spectrum quality must be improved. This is the recent technological progress in terms of X-ray detection (SDD detectors) that makes this current approach possible.

The evaluation of ternary phase diagrams can be easily derived. It is even possible to obtain an automated "image processing" of the EDS map that gives a quick evaluation, if not a reliable assessment of the phase diagram. In any case, due to the EDS limitations compared to the EPMA, the method cannot be considered as precise enough to perform a proper assessment. Note that this approach is only beginning and is still under development. We believe that it offers a chance to obtain quick answers about the structure of a ternary phase diagram, i.e., about the zones of the diagram where ternary phases do appear or not, for intermediate temperatures: not too high (without liquid phase) and not too low (too long diffusion times). This can be of a great help when exploring some of the 32,000 unknown ternary diagrams.

Conclusions and outlook

The CALPHAD method was presented and its high relevance for the microstructural modeling of multi-component systems was highlighted. The great number of fields in materials science where the CALPHAD method is already used strengthens the present and future impacts of CALPHAD in the processes for accelerated design and optimization of new materials and components. Nevertheless, the need for enriching thermodynamic databases must be met, which demands a very high number of experiments and ab initio calculations. In this perspective, high-throughput experiments, such as diffusion multiples, are a very relevant topic to be explored by the scientific community ■

References

[1] J. ALLISON, M. LI, C. WOLVERTON and X.M. SU – *Virtual Aluminum Castings: An Industrial Application of ICME*. JOM, Vol. 58, n°11, 28-35, 2006.

[2] M. BENSCH, A. SATO, N. WARNKEN, E. AFFELDT, R.C. REED and U. GLATZEL – *Modelling of High Temperature Oxidation of Alumina-Forming Single-Crystal Nickel-Base Superalloys*. Acta Materialia, Vol. 60, 5468–5480, 2012.

[3] G. BOITTIN, D. LOCQ, A. RAFRAY, P. CARON, P. KANOUTE, F. GALLERNEAU and G. CAILLETAUD – *Influence of γ' Precipitate Size and Distribution on LCF Behavior of a PM Disk Superalloy*. Superalloys 2012, edited by E.S. Huron *et al.*, TMS, Warrendale, USA, 167–176, 2012.

[4] R. BOUCHET and R. MEVREL – *Calculating the Composition-Dependent Diffusivity Matrix along a Diffusion Path in Ternary Systems: Application to β-(Ni,Pt) Al*. CALPHAD, Vol. 27, n°3, 295-303, 2003.

[5] S. CAO – *Determination of the Fe-Cr-Ni and Fe-Cr-Mo Phase Diagrams at Intermediate Temperatures using a Novel Dual-Anneal Diffusion-Multiple Approach*. PhD of the Ohio State University, Columbus, Ohio, USA, 2013.

[6] J. CUI, Y.S. CHU, O.O. FAMODU, Y. FURUYA, J. HATTRICK-SIMPERS, R.D. JAMES, A. LUDWIG, S. THIENHAUS, M. WUTTIG, Z. ZHANG and I. TAKEUCHI – *Combinatorial Search of Thermoelastic Shape-Memory Alloys with Extremely Small Hysteresis Width*. Nature Materials, Vol. 5, 286-290, 2006.

[7] A.T. DINSDALE – *SGTE Data for Pure Elements*. CALPHAD, Vol. 15, n°4, 317-425, 1991.

[8] R. DUCHER, R. KAINUMA, I. OHNUMA and K. ISHIDA – *Phase Equilibria and Stability of B2 and L21 Ordered Phases in the Co–Fe–Ga Heusler Alloy System*. Journal of Alloys and Compounds, Vol. 437, n°1–2, 93–101, 2007.

[9] S.G. FRIES, B. BÖTTGER, J. EIKEN and I. STEINBACH – *Upgrading Calphad to Microstructure Simulation: the Phase-Field Method*. International Journal of Materials Research, Vol. 100, n°2, 128–234, 2009.

[10] B. GRABOWSKI, L. ISMER, T. HICKEL and J. NEUGEBAUER – *Ab Initio up to the Melting Point: Anharmonicity and Vacancies in Aluminum*. Physical Review B, Vol. 79, 134106, 2009.

[11] K. HACK (Editor) – *The Sgte Casebook. Thermodynamics at Work*. 2nd Edition, Woodhead Publishing, 2008.

[12] J.J. HANAK – *The "Multiple-Sample Concept" in Materials Research: Synthesis, Compositional Analysis and Testing of Entire Multicomponent Systems*. Journal of Materials Science, Vol. 5, n°11, 964–971, 1970.

[13] S.M. HAO, T. TAKAYAMA, K. ISHIDA and T. NISHIZAWA – *Miscibility Gap in Fe-Ni-Al and Fe-Ni-Al-Co Systems*. Metallurgical Transactions A, Vol. 15, n°10, 1819-1828, 1984.

[14] M. HILLERT – *Empirical Methods of Predicting and Representing Thermodynamic Properties of Ternary Solution Phases*. CALPHAD, Vol. 4, n°1, 1–12, 1980.

[15] M. HILLERT – *A Discussion of Methods of Calculating Phase Diagrams*. Bulletin of Alloy Phase Diagrams, Vol. 2, n°3, 265-268, 1981.

[16] D. JARVIS – *Metallurgy Europe. A Renaissance Programme for 2012-2022*. European Science Foundation, printed by Ireq in Strasbourg, France, June 2012.

[17] I.M. LIFSHITZ and V.V. SLYOZOV – *The Kinetics of Precipitation from Supersaturated Solid Solutions*. Journal of Physics and Chemistry of Solids, Vol. 19, n°1/2, 39-50, 1961.

[18] A. LUDWIG, R. ZARNETTA, S. HAMANN, A. SAVAN and S. THIENHAUS – *Development of Multifunctional Thin Films Using High-Throughput Experimentation Methods*. International Journal of Materials Research, Vol. 99, n°10, 1144–1149, 2008.

[19] H. LUKAS, S.G. FRIES and B. SUNDMAN – *Computational Thermodynamics: the Calphad Method*. Cambridge University Press, UK, 2007.

[20] J. MAO – *γ' Precipitation Modeling and Strength Responses in Powder Metallurgy Superalloys.* PhD thesis, West Virginia University, 2002.

[21] N. MILHET-GAYRAUD – *Etude expérimentale et modélisation de la précipitation de la phase γ' dans le superalliage N18*. PhD thesis, Institut National Polytechnique de Grenoble, France, 1994.

[22] G.B. OLSON – *Genomic Materials Design: the Ferrous Frontier*. Acta Materialia, Vol. 61, 771–781, 2013.

[23] R.G. PARR and Y. WEITAO – *Density-Functional Theory of Atoms and Molecules*. International Series of Monographs on Chemistry, Oxford University Press, USA, 1994.

[24] A.D. PELTON and W.D. THOMPSON – *Phase Diagrams.* Progress in Solid State Chemistry, Vol. 10, n°3, 119–155, 1975.

[25] M. PERRUT and D. LOCQ – *γ' Precipitation Kinetics in the Powder Metallurgy Superalloy N19 and Influence of the Precipitation Latent Heat*. MATEC Web of Conferences Vol. 14, 09004, 2014.

[26] L. ROUGIER, A. JACOT, C.A. GANDIN, P. DI NAPOLI, D. PONSEN and V. JAQUET – *Numerical Simulation of Am1 Microstructure*. MATEC Web of Conferences, Vol. 14, 11003 (2014).

[27] N. SAUNDERS and A.P. MIODOWNIK – *CALPHAD (Calculation of Phase Diagrams): a Comprehensive Guide*. Pergamon Materials Series, University of Cambridge, UK, 1998.

[28] Y. WANG, S. CURTAROLO, C. JIANG, R. ARROYAVE, T. WANG, G. CEDER, L.Q. CHEN and Z.K. LIU – *Ab Initio Lattice Stability in Comparison with Calphad Lattice Stability*. Computer Coupling of Phase Diagrams and Thermochemistry, Vol. 28, 79-90, 2004.

[29] H. WENDT and P. HAASEN – *Nucleation and Growth of γ'-Precipitates in Ni-14 at.% Al*. Acta Metall. Mater. Vol. 31, n°10, 1649–1659, 1983.

[30] K. YAQOOB, J.C. CRIVELLO and J.M. JOUBERT – *Comparison of the Site Occupancies Determined by Combined Rietveld Refinement and Density Functional Theory Calculations: Example of the Ternary Mo–Ni–Re σ Phase*. Inorganic Chemistry, Vol. 51, n°5, 3071–3078, 2012.

[31] J.C. ZHAO, M.R. JACKSON, L.A. PELUSO and L.N. BREWER – *A Diffusion Multiple Approach for the Accelerated Design of Structural Materials*. Materials Research Society Bulletin, Vol. 27, n°4, 324–329, April 2002.

[32] J.C. Zhao – *Methods for Phase Diagram Determination*. Elsevier Science, Great Britain, 2007.

[33] Abaqus official website – http://www.simulia.com.

[34] ABINIT official website – http://www.abinit.org.

[35] FactSage official website – http://www.factsage.com.

[36] Materials Genome Initiative – http://www.whitehouse.gov/mgi.

[37] Materials Project official website – http://www.materialsproject.org.

[38] Micress official website – http://www.micress.de.

[39] Pandat official website – http://www.computherm.com.

[40] ProCAST official website – http://www.esi-group.com.

[41] SAMx official website – http://www.samx.com.
[42] Thermo-Calc Software official website – http://www.thermocalc.com.
[43] Thermo-Calc Software TCNI5, March 2011.
[44] Thermo-Calc Software MOBNI v2.4, Sept 2012.
[45] US Defense Advanced Research Projects Agency: Accelerated Insertion of Materials – http://www.darpa.mil.
[46] VASP official website – http://www.vasp.at.
[47] Wien2k official website – http://www.wien2k.at.

AUTHORS

Mikael Perrut earned his *Ecole Polytechnique* diploma in 2004 and his doctoral degree in Physics at the University Pierre and Marie Curie (Paris VI) in 2007. He joined ONERA in 2009 and is now a scientist in the Metallic Materials and Structures Department. He is mainly interested in microstructure modeling, namely for Ni-based superalloys, in phase diagrams and in the metallurgy of intermetallics, such as titanium aluminides.

S. Pommier
LMT(ENS Cachan, CNRS, UPSaclay)

E-mail: Sylvie.pommier@universite-paris-saclay.fr

DOI : 10.12762/2015.AL09-11

Development of an Incremental Model for Fatigue Crack Growth Predictions

This paper presents an incremental approach for modeling fatigue crack growth with history effects. This approach is being developed at LMT since 2003, in collaboration with several industrial partners, mainly with Snecma, the SAFRAN Group, EDF and AREVA, and the SNCF. The first part of this paper presents the context, objectives and key assumptions on which the model is based. The second part presents some examples of applications of the model, fatigue crack growth under Mode I conditions, with variable amplitude loading; non-isothermal situations; crack growth under coupled environmental and fatigue loading conditions; extension of the model to non-proportional mixed mode loading conditions and to short cracks. The last part presents the ongoing work, the possible developments and the scientific challenges that remain to be overcome.

Introduction

Industrial sectors of public transportation (air, ground or naval) and of energy production (especially nuclear energy) implement an approach, called damage tolerance, to ensure that any damage located in a critical component will have limited consequences and will cause neither catastrophic failure in operating conditions nor fatalities. To do so, assumptions must first be made about the location, the geometry and the size of possible flaws in critical components. These assumptions depend on the resolution of non-destructive inspection techniques used before putting the system in operation or during preventive maintenance operations. If no damage has been detected, then the component is assumed to contain a non-detectable flaw. The design of the system and its preventive maintenance plan must ensure that this flaw will be harmless under operating conditions during the lifetime of the system. In order to do so, the most detrimental configuration is also assumed, i.e., the flaw is assumed to be a crack, located in the most critical zone of the component, with the worst possible orientation and with a size just below the detection threshold of the non-destructive inspection techniques used. At this point, models are needed to predict the growth of this potential crack, so as to predict the safe life of the component under operating conditions, to plan preventive maintenance operations, or the replacement of critical components or of the entire system. For a fail-safe approach, models are also needed to determine the crack path and the size of the fragments in the event of a sudden break, to predict the damage that they can cause and the consequences of the failure of a component on the behavior of the entire system.

However, accurate prediction of fatigue crack propagation and of the service life of critical components under operating conditions remains difficult for the following reasons:

- **2D / 3D**: Critical areas, where cracks are initiated, are usually stress concentration areas (notches, holes, contact areas, interfaces, thermal gradients, etc.), where the stress field usually exhibits a spatial gradient and may be multiaxial. This gives a three-dimensional character to the fatigue crack growth problem (short cracks, curved crack front, non-planar crack, or mixed mode loadings) [35,26]. However, the crack propagation models used to predict the growth of these 3D cracks usually use 2D experiments (Mode I, long and planar cracks).

- **Non-linear material behavior**: The materials used for critical components are, as far as possible, ductile materials and display a non-linear behavior. The non-linear nature of the behavior of the materials is at the origin of history or memory effects in fatigue crack growth. The importance of these history effects on fatigue crack growth has been demonstrated and explained [2, 16, 17, 18, 19, 20, 23, 28, 36, 40, 41, 47, 52, 53, 55, 56, 60, 61, 67, 68]. Various crack propagation models (NASGRO, PREFFAS, Strip Yield, etc.) have been developed to account for these history effects. If the material is non-linear, the loading path (not only the peak loads) is to be considered to predict the fatigue crack growth rate. However, since most models predict a fatigue crack growth rate per cycle, they require the use of a cycle counting method (e.g., rainflow) to be applied to load sequences under operating conditions that might be quite far from being cyclic. When the load sequence stemming from the cycle reconstruction differs significantly from the original one, the life prediction may be questionable. The incremental approach, which we have developed at LMT, avoids the use of a cycle reconstruction method by predicting a crack growth rate per second.

- **Other non-linear effects**: If any non-linear mechanism is involved, questions arise about cycle counting, damage accumulation, load path effects, etc. Aside from the non-linear material behavior, the primary source of nonlinearity is the interference between the crack faces, the plasticity or roughness induced crack closure problem in Mode I and the friction between the crack faces in Mode II and Mode III [4, 7, 8, 6, 12, 13, 14, 15, 21, 22, 24, 30, 39, 43, 51, 57]. Time dependent damage mechanisms may also contribute to crack growth (creep, corrosion, oxidation, etc.) and be coupled with pure fatigue crack growth. An incremental approach makes it possible to consider and to model independently the effects of each mechanism in each time step [1, 3, 5, 25, 29, 31, 34, 42, 49, 59, 65, 69, 70].

- **Complex loading conditions**: Loading sequences under actual operating conditions can be rather complex. The mechanical loadings can be uniaxial or multiaxial, varying in space and time (variable amplitude loading in Mode I, in-phase or out-of-phase loadings under mixed mode conditions, etc.). Similarly, it may be non-isothermal in space and time (thermal fatigue, etc.).

Since 2003, an incremental approach has been developed at LMT, step by step [9, 10, 11, 13, 21, 22, 27, 28, 38, 52, 53, 54, 55, 56, 59, 62], to predict fatigue crack growth under complex loading conditions and in non-linear materials. The approach is based on the assumption that "pure" fatigue crack growth stems from crack tip plasticity [37, 44, 45, 48]. With such an assumption, an incremental model for "pure" fatigue crack growth could be derived from an incremental plasticity model for the crack tip region. The crack growth rate per second can be predicted from the crack tip plasticity measurement. Various authors have derived successful predictions of the fatigue crack growth rate under complex loading conditions, from the analysis of the plastic strain field around the crack front obtained from non-linear finite element simulations. However, non-linear finite element simulations remain unusable in an industrial context, where cracks are usually 3D. A simplified model is required, but the finite element method can be used to develop a simplified model and to verify its capabilities.

The simplified model that has been developed at LMT is aimed at condensing all of the non-linear behavior effects of the material in the crack tip region into a set of constitutive equations based on the minimum number of variables necessary to reasonably represent the crack tip plasticity problem. Moreover, the simplifying assumptions in the model are chosen to be suitable with a use in mixed mode conditions.

Hypotheses

The model is based on some considerations that are briefly recalled below.

- Infinitesimal strain conditions are considered.

- The local solution is assumed to be dominated by the local geometry of the crack. The remote boundary conditions and their history are hence expected to control the intensity of the crack tip fields but not their spatial distribution, which is assumed to be given once for all, and to be associated with the local crack geometry.

- A curvilinear coordinate system R_T, defined with respect to a suitable characteristic scale, can be attached to the local crack front and the local crack plane. In this coordinate system R_T, the crack is assumed to be locally planar and under generalized plane strain conditions along the local straight crack front. This assumption allows the crack tip fields to be partitioned into Mode I (symmetric), Mode II (anti-symmetric) and Mode III (anti-planar) local components.

$$\underline{v}(P,t)_{R_0} = \underbrace{\underline{v}(T,t)_{R_0} + \omega(R_T/R_0)\wedge\underline{TP}}_{growth} + \underbrace{\underline{v}(P,t)_{R_T}}_{behaviour} \qquad (1)$$

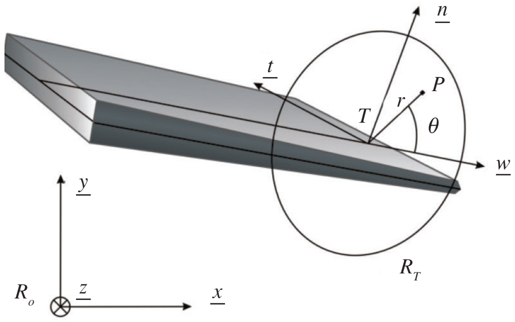

Figure 1 - Local coordinate system attached to the crack front (T) and plane

- With respect to the local coordinate system attached to the local crack plane and crack front, the geometry of the crack is locally scale invariant. This implies that, in each time step, the solution of the problem can be expressed (at least locally, in the vicinity of the crack front) as the product of an intensity factor and of a spatial distribution, which is scale invariant. It implies, in addition, that this spatial distribution can be expressed as the product of a function $f(r)$ of the scale (the distance to the crack tip r) and of a function $\underline{g}(\theta)$ of the angular position with respect to the crack plane. With this approach, the spatial distribution $f(r)\underline{g}(\theta)$ is given once for all and the intensity factor $I(t)$ can be considered as a degree of freedom.

$$\underline{v}(P,t)_{R_T} = \underline{v}(\underline{x},t) = I(t)f(r)\underline{g}(\theta) \text{ , where } f(\alpha r) = \beta f(r) \qquad (2)$$

- Since it is always possible, at least transiently during a time step, to obtain a linear elastic behavior by reversing the loading direction (and assuming infinitesimal strain conditions), the elastic behavior of the crack tip region requires, for each mode, an independent degree of freedom even if elastic-plastic conditions are considered. In such a case, the hypotheses listed above apply independently to elastic and inelastic behaviors. If crack tip plasticity is well confined, the elastic bulk constrains the development of the crack tip plastic zone and this also drastically limits the number of useful degrees of freedom required to represent reasonably well the plastic flow obtained in the crack tip region.

This last property is illustrated in figure 2, for example. The accumulated plastic strain field obtained by elastic-plastic FE simulation under out-of-phase I+II mixed mode conditions was plotted in a logarithmic scale, for different points of a circular loading path in a KI-KII plane. At each point A, B, C or D, the angular distribution of P_{cum} is obviously the same whatever the distance r to the crack tip, so that $P_{cum} \propto f(r)\underline{g}(\theta)$. In addition, it can be seen in figure 2 that P_{ti} decays exponentially from the crack tip, with the same decay rate throughout the mixed mode loading cycle.

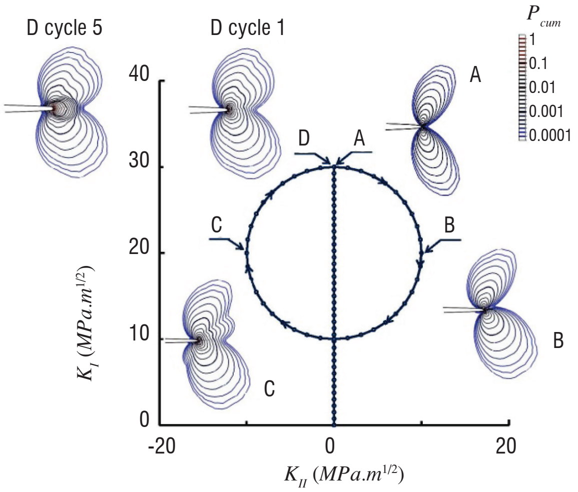

Figure 2 - Illustration : Five out-of-phase Mixed Mode I + II loading cycles (A-B-C-D) were simulated under non-linear conditions using the finite element method. The iso-values of the equivalent plastic strain P_{cum} are plotted in a logarithmic scale, during the first cycle in points A, B, C and D of the load path and at the end of the fifth cycle (D).

As a consequence, under elastic plastic conditions, the velocity field in a reference frame attached to the local crack tip and crack front can be approximated as the superposition of three modes, denoted by i. Each mode requires a degree of freedom $\dot{\tilde{K}}_i$ for the elastic response and another degree of freedom $\dot{\rho}_i$ for the inelastic one. Both the elastic and the inelastic part are expressed as the product of a spatial distribution and an intensity factor used as a degree of freedom and which can be calculated by post-processing elastic-plastic finite element results. The spatial distribution is constructed a priori and is the result of the various constraints (local crack geometry, symmetry, scale independence, etc.).

$$\underline{v}(P,t)_{R_T} = \sum_{i=1}^{3} \underbrace{\dot{\tilde{K}}_i(t).\underline{\varphi}_i^e(P)}_{\underline{v}_i^e(P,t)} + \underbrace{\dot{\rho}_i(t).\underline{\varphi}_i^c(P)}_{\underline{v}_i^c(P,t)} \tag{3}$$

$\underline{v}_i^c(P,t)$ represents the non-elastic part of the velocity field, while $\underline{v}_i^e(P,t)$ represents the elastic part.

If the material behavior is linear elastic, then the intensity factor $\dot{\tilde{K}}_i$ of the elastic part of the velocity field is equal to the nominal applied stress intensity factor $\dot{K}_i^\infty$. Otherwise, these two quantities are slightly different, because elastic strain may arise from applied stresses (and therefore from $\dot{K}_i^\infty$), but also from internal stresses arising from crack tip plasticity and from the confinement of the plastic zone. The difference ($\dot{\tilde{K}}_i - \dot{K}_i^\infty$) can be interpreted as the shielding effect of th plastic zone [58]. As expected, ($\dot{\tilde{K}}_i - \dot{K}_i^\infty$) was observed to be directly proportional to $\dot{\rho}_i$ by post-treatment of FE simulations.

The elastic reference fields $\varphi_i^e(\underline{x})$ are obtained from a linear FE computation for each mode with $\dot{K}_i^\infty = 1MPa\sqrt{m}$ and fit the Westergaard solutions [66].

The non-elastic reference field $\varphi_i^c(P)$ is obtained from elastic-plastic FE computations, using a model-reduction technique [32], as being the best possible field to approximate by Equation 3 the velocity field evolution calculated for each mode for a loading ramp from zero to 0.8 K_{Ic}. According to the model simplifying hypotheses, $\varphi_i^c(P)$ can be locally represented by $f_i^c(r)g_i^c(\theta)$ where $f_i^c(\alpha r)\beta f_i^c(r)$.

Assuming that the plastic zone is confined, this implies that $f_i^c(r) \xrightarrow[r\to\infty]{} 0$. And since $\varphi_i^c(P)$ is the spatial distribution of the inelastic part of the velocity field at the crack tip, it should be discontinuous across the crack faces and maximum at the crack front, which implies that it should decay exponentially and which was observed in FE computations.

$$\begin{cases} f_i^c(\alpha r) = \beta f_i^c(r) \\ \quad f_i^c(r) \underset{r\to\infty}{\aleph} 0 \qquad\qquad f_i^c(r) \quad e^{-kr} \\ \quad f_i^c(r) \xrightarrow[r\to 0]{} 1 \end{cases} \tag{4}$$

$f_i^c(r)$ was rescaled to 1 when $r \to 0$, by convention. In addition, $\underline{g}_i^c(\theta)$ is discontinuous across the crack faces and was rescaled so that:

$$\left[\underline{g}_i^c(\theta)(\theta=\pi) - \underline{g}_i^c(\theta)(\theta=\pi)\right]_\theta = 1 \tag{5}$$

In practice, this post treatment is used to rescale each reference field $\underline{\varphi}_i^c(\underline{x})$ by a constant scalar value, so that the limit when r tends to zero of its discontinuity across the crack plane is equal to 1:

$$\left[\underline{\varphi}_i^c(\theta=\pi, \mathrm{r}\to 0) - \underline{\varphi}_i^c(\theta=-\pi, \mathrm{r}\to 0)\right]_\theta = 1 \tag{6}$$

In other words, the intensity factor $\dot{\rho}_I$ of $\underline{\varphi}_i^c(\underline{x})$ can now also be viewed as the CTOD, the intensity factor $\dot{\rho}_{II}$ of $\underline{\varphi}_{II}^c(\underline{x})$ as the Mode II CTSD and $\dot{\rho}_{\ddot{u}}$ as the Mode III CTSD.

Details about the reference fields $\underline{\varphi}_i^e(P)$ and $\underline{\varphi}_i^c(P)$ and their construction for each mode can be found in previous papers [21, 54, 11].

With these assumptions, the crack tip field under non-linear mixed mode conditions can be fully characterized by only six independent degrees of freedom $\dot{K}_I^\infty$, $\dot{K}_{II}^\infty$, $\dot{K}_{III}^\infty$, and $\dot{\rho}_I$, $\dot{\rho}_{II}$, $\dot{\rho}_{III}$ and $\underline{\dot{\rho}} = (\dot{\rho}_I, \dot{\rho}_{II}, \dot{\rho}_{III})$ represents the discontinuity vector of the plastic velocity field across the crack face.

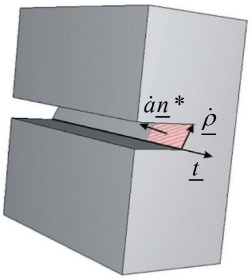

Figure 3 - Schematics of the process of creation of a new cracked area by crack tip plasticity (Neuman model [44, 45], Li model [37])

With such an approximation, following the approaches of Neuman [44, 45] and Li [37], the crack growth rate due to the geometric process of cracked area creation by plasticity can be estimated roughly as follows :

$$\dot{a}\underline{n}^* \propto \left(\underline{t} \wedge \underline{\dot{\rho}}\right) \Rightarrow \dot{a} \propto \sqrt{\dot{\rho}_I^2 + \dot{\rho}_{II}^2} \tag{7}$$

Where $\underline{t}$ is the unit orientation vector of the crack front, $\underline{n}*$ is the unit vector normal to the cracked face oriented outward and $\dot{a}$ is the rate of cracked area creation per unit length of the crack front. It is worth emphasizing that, with such an assumption, Mode III plastic flow in the crack tip region has no effect on the crack growth rate. This point is discussed in § "Mixed mode loading conditions", since Mode III is known to contribute to fatigue crack growth [50, 63].

Once the basis of the reference field has been determined, it can be used to post-process velocity fields obtained from finite element simulations or from experimental field measurements from digital image correlation [11].

The velocity field $\underline{\ddot{u}}^{\ddot{u}}\ (\ ,\ )$ recorded at each time step is projected onto the six reference fields, in order to retrieve the intensity factors related to the elastic and the inelastic parts for each mode:

$$\dot{\tilde{K}}_i(t)=\frac{\int \underline{v}^{rec}(P,t).\underline{\varphi}_i^e(P)\mathrm{dP}}{\int \underline{\varphi}_i^e(P).\underline{\varphi}_i^e(P)\mathrm{dP}}\ ,\quad \dot{\rho}_i(t)=\frac{\int \underline{v}^{rec}(P,t).\underline{\varphi}_i^c(P)\mathrm{dP}}{\int \underline{\varphi}_i^c(P).\underline{\varphi}_i^c(P)\mathrm{dP}} \tag{8}$$

In order to quantify the quality of the approximation in equation 3, the error $C_{2R}(t)$ is also determined in each time step:

$$C_{2\mathrm{R}}(t)=\sqrt{\frac{\int\left(\underline{v}^{rec}(P,t)-\dot{\tilde{K}}_i(t)\underline{\varphi}_i^e(P)-\dot{\rho}_i(t)\underline{\varphi}_i^c(P)\right)^2\mathrm{dP}}{\int\left(\underline{v}^{rec}(P,t)\right)^2\mathrm{dP}}} \tag{9}$$

This error is usually below 10% but increases drastically when the crack is no longer under small scale yielding conditions or when contact occurs between the crack faces. In order to quantify the importance of the plastic part of the approximated velocity field, the error $C_{1R}(t)$ is also determined in each time step:

$$C_{1\mathrm{R}}(t)=\sqrt{\frac{\int\left(\underline{v}^{rec}(P,t)-\dot{\tilde{K}}_i(t)\underline{\varphi}_i^e(P)\right)^2\mathrm{dP}}{\int\left(\underline{v}^{rec}(P,t)\right)^2\mathrm{dP}}} \tag{10}$$

If $\left|C_{1R}(t)-C_{2R}(t)\right|$ is very small, it means that adding a plastic part to the approximation in Equation 3 does not improve it; the behavior of the crack tip region is thus essentially elastic during the time step. This criterion was used to define the frontier of the elastic domain under mixed mode conditions.

Applications and ongoing work

A very small number of degrees of freedom can hence be used to represent the kinematics of the crack tip region reasonably well. Numerical simulations (or experiments with full field measurement) can be used to determine the velocity field and to track the evolution of $\dot{\rho}_i$ for various loading conditions $\dot{K}_i^\infty$, so as to derive a constitutive model of the non-linear behavior of the crack tip region.

The approach used to develop the model is analogous to that used for many years by the Mechanics of Materials community to develop material laws with internal variables within a thermodynamic framework. However, it should be noted that:

- The constitutive law applies to a region and not to a material point. The approach is hence non-local and is tailored for the crack tip region through the use of the reference fields $\underline{\varphi}_i^e(P)$ and $\underline{\varphi}_i^c(P)$ that include a discontinuity across the crack faces.

- Internal variables are introduced to account for the existence of internal stresses, of material hardening and more generally of any other effect related to the non-linear behavior of the material that could be at the origin of significant memory effects in fatigue crack growth. However, the constitutive law for the crack tip region, and hence the internal variables of this constitutive law, are inherent to the crack front, not to the material. Consequently, the internal variables of the constitutive model of the crack tip region will not only have to evolve with plastic flow within the crack tip region, but also as a result of the crack front displacement.

- Due to the presence of the crack in the crack tip region, plastic flow is localized from the beginning and must remain localized in the same manner, as long as the plastic zone is confined by the elastic bulk. Thus, we are spared many difficulties related to the issue of accounting for the localization process or the post-peak transition in the constitutive model.

- From a thermodynamic point of view, the driving force associated with $\dot{\rho}_i$ is not the nominal applied stress intensity factors, but rather $\varphi_{\ddot{u}}=\frac{1-v^2}{E}sign\left(K^\infty\right)K^{2\infty}$. Nevertheless, for ease of reading, the model equations are written in terms of K_i^∞.

The constitutive model for the plasticity of the crack tip region is then associated with a crack propagation model to obtain the incremental model. In "pure" fatigue, the rate $\dot{a}$ of production of cracked areas per unit length of crack front is given by the plastic flow rate $\dot{\rho}_i$: $\dot{a}=\alpha\sqrt{\dot{\rho}_I^2+\dot{\rho}_{II}^2}$.

Mode I fatigue crack growth

Early work was carried out on modeling fatigue crack growth in Mode I at room temperature under variable amplitude loading [55, 56] for aircraft engine applications and then for railway applications [27, 28, 53]. Then, the model was extended to modeling fatigue crack growth under non-isothermal conditions and in the presence of an active environment [59].

Attempts have also been made to extend the model to elastic-viscoplastic materials, with promising results. Studies in this direction have been conducted as part of a collaboration with the University of Sao Paulo, Brazil (PhD thesis of M. Angeloni) and during the Masters internship of P. Nam Wong (Snecma).

A set of constitutive equations was defined that allows $d\rho_I$, the plastic flow in Mode I in the crack tip region, to be determined as a function of the Mode I nominal applied stress intensity factor dK_I^∞.

The model is based on two elastic domains, one for the cyclic plastic zone and the other for the monotonic plastic zone. Each of them is characterized by two internal variables that represent, respectively, the center $\left(K_x^{cpz}\,\text{and}\,K_x^{mpz}\right)$ and the size $\left(K_x^{cpz}\,\text{and}\,K_x^{mpz}\right)$ of each elastic domain.

Results such as that plotted in figure 4 can be obtained using the finite element method, either for a fixed position of the crack front to obtain $\frac{\partial V_{\text{int}}}{\partial \rho_I}$, or after numerically "growing" the crack without allowing plastic strain, so as to obtain $\frac{\partial V_{\text{int}}}{\partial \rho_a}$. This allows an evolution equation to be determined independently for each internal variable, due to plasticity $\frac{\partial V_{\text{int}}}{\partial \rho_I}$ or due to crack propagation $\frac{\partial V_{\text{int}}}{\partial \rho_a}$. The evolution equations introduced for each internal variable are empirical.

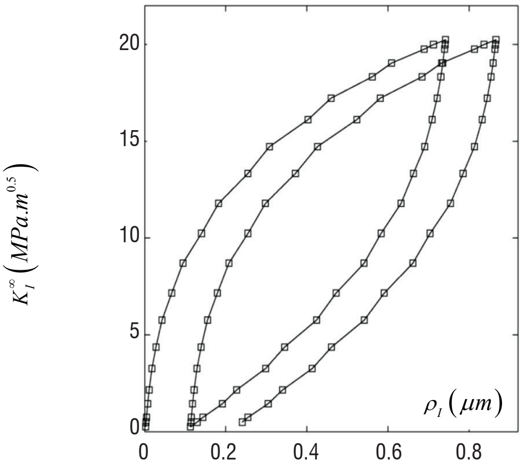

Figure 4 - Illustration of the evolution of the Mode I plastic intensity factor as a function of the Mode I nominal applied stress intensity factor K_I^∞ [10]

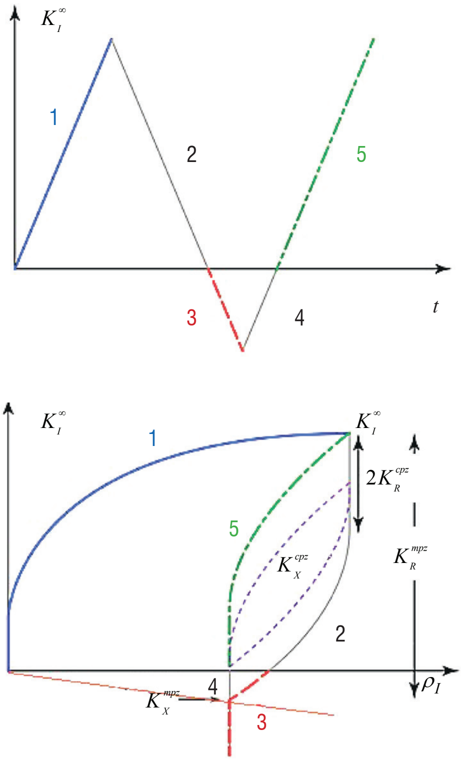

Figure 5 - Illustration of the evolution of the role of each internal variable used in the model

Cyclic plastic zone - K_R^{cpz}

For the cyclic plastic zone, the size of the elastic domain K_R^{cpz} was assumed to be constant. The material constitutive laws that were used for most simulations (Figure 4) included both non-linear kinematic and isotropic hardening [36]. However, the effect of isotropic hardening that is expected to be produced and the evolution of K_R^{cpz} were usually observed to be small and neglected up to now.

Fatigue crack growth is assumed to be the result of crack tip plasticity, through the crack growth model $\dot{a} = \alpha\sqrt{\dot{\rho}_I^2}$, therefore the fatigue threshold ΔK_{th} predicted by the model is equal to $2K_R^{cpz}$.

Cyclic plastic zone - K_x^{cpz}

The evolution law of the center of the elastic domain K_x^{cpz} due to plasticity $\frac{\partial K_x^{\ddot{u}}}{\partial \rho_I}$ is determined from numerical results, such as those depicted in figure 4, for example.

We first proposed an equation that fits the numerical results as well as the numerical results (a power low function with a threshold), but then we preferred to make sure that a unique set of material parameters could be identified, so that we could be able to interpolate the parameters identified for different temperatures, for example. Finally, we also added the constraint that the evolution equations of each internal variable, with respect to plastic flow $\left(\partial \rho_I\right)$ or with respect to the displacement of the crack front $\left(\partial a\right)$, would be consistent, so that:

$$\frac{\partial}{\partial a}\left(\frac{\partial K_x^{cpz}}{\partial \rho_I}\right) = \frac{\partial}{\partial \rho_I}\left(\frac{\partial K_x^{cpz}}{\partial a}\right)$$

Once $\frac{\partial K_x^{cpz}}{\partial \rho_I}$ and K_x^{cpz} are identified from finite element computations (including the constitutive law of the material), the amplitude $\Delta\rho_I$ per fatigue cycle can be predicted as a function of ΔK_I^∞ for a given material. Since we also assume that $\dot{a} = \alpha\sqrt{\dot{\rho}_I^2}$, the fatigue crack growth rate can hence be determined $\frac{da}{dN} = 2\alpha\Delta\rho_I$. It is worth noting that a fatigue crack growth experiment is necessary to adjust the coefficient. In a Paris diagram, this coefficient α allows the position of the Paris law to be adjusted, but not its slope. The slope of the Paris law and the predicted fatigue threshold ΔK_{th}, stem from the relation between ΔK_I^∞ and $\Delta\rho_I$, which are identified, using the finite element method on the basis of the elastic-plastic constitutive behavior of the material.

Monotonic plastic zone - K_R^{mpz}

The size ^{mpz} of the elastic domain in Mode I is directly related to the size of the plastic zone. As a matter of fact, the intensity factor of the plastic part of the velocity field is $\dot{\rho}_I$. It decays exponentially with the distance from the crack tip. Therefore, for a monotonic loading ramp the evolution of ρ_I as a function of K_I^∞ is directly related to the growth of the plastic zone size with K_I^{∞}. In addition, an exponential decay is chosen for $\frac{\partial K_R^{mpz}}{\partial a}$.

Monotonic plastic zone - K_x^{mpz}

The center K_x^{mpz} of the elastic domain in Mode I is also defined as the contact point between the crack faces, whose evolution with crack tip plasticity $\frac{\partial K_x^{mpz}}{\partial \rho_I}$ can be determined using the finite element method. When crack tip blunting occurs $(d\rho_I>0)$, the crack opening level decreases.

The evolution of K_x^{mpz} with the crack length allows the crack closure effect to be accounted for. As the crack propagates through the plastic zone, the internal stresses stored in the plastic zone are transferred from the ligament to the crack faces, resulting in an increase of K_x^{mpz} that is modeled as being proportional to the internal stresses stored in the crack tip region and hence to the plastic zone size. Then, once internal stresses have entirely been transferred to the crack wake, their distance to the crack tip increases with the extent of the crack, producing a decrease in the crack opening level. This yields the empirical equation 11:

$$\frac{\partial K_X^{mpz}}{\partial a}=k_b K_R^{mpz}-k_a K_X^{mpz} \tag{11}$$

Applications – variable amplitude fatigue

The equations were implemented and their coefficients identified using the finite element method for a low carbon steel, by Rami Hamam [27, 28, 53]. The coefficient α of the crack propagation law $\dot{a}=\alpha\sqrt{\dot{\rho}_I^2}$ was adjusted using a Mode I fatigue crack growth experiment in constant amplitude fatigue at $R=0$.

Then, the model was used to simulate the stress ratio effect, the overload effect and the effects of various block loadings on fatigue crack growth [27, 28, 53]. The simulations were compared to experimental results giving satisfactory results. It was shown that the model is capable of representing the stress ratio effect, the overload effect, the overload retardation effect, the higher retardation effect after 10 overloads than after one single overload, etc.

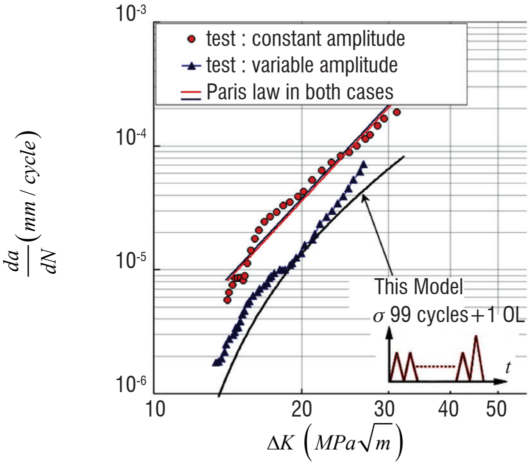

Figure 6 - Illustration of the capability of the model to predict the retardation effect of one overload, with an overload factor of 1.3, in a block of 100 cycles

Applications – non-isothermal conditions and environmental effect

In order to extend the model to non-isothermal conditions, Juan Antonio Ruiz Sabariego [59] identified the parameters of the constitutive model for the N18 nickel base superalloy at various temperatures between 450°C and 650°C. Finite element computations were then performed, in order to identify the parameters of the constitutive law of the crack tip region as a function of the temperature. The parameters obtained for each temperature were interpolated so as to obtain a plasticity model for the crack tip region under non-isothermal conditions [59].

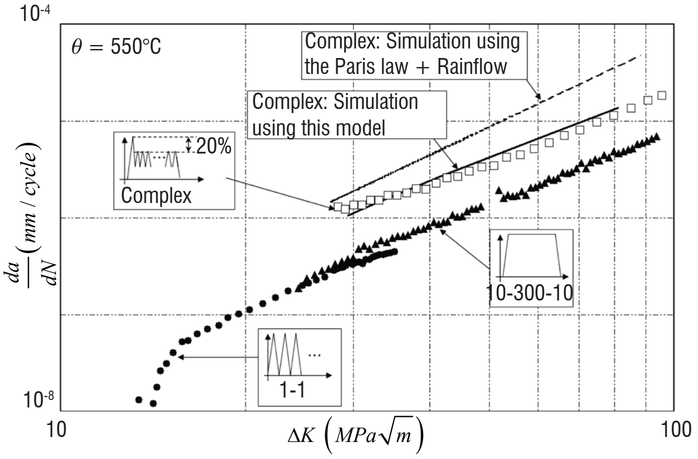

Figure 7 - Fatigue crack growth rate in CT specimens at 550°C in the N18 nickel base superalloy. Symbols correspond to experiments and lines to predictions [59]

In addition, the phenomenon of oxidation that assists fatigue crack growth at high temperatures [49, 3, 33, 31, 70, 64, 29] must also be considered. This mechanism is responsible, for instance, for the detrimental effect of dwell times at temperatures above 550°C [29, 5, 69, 34] in the N18 nickel base superalloy. The grain boundaries are embrittled by oxidation ahead of the crack tip. This mechanism is thermally activated. In addition, the material is designed to develop a passivation layer of oxides, which protects the material against grain boundary oxidation. However, if the crack tip is stretched, the passivation layer breaks and a competition between grain boundary embrittlement and the growth of a passivation layer takes place. Therefore a coupling effect between fatigue and oxidation is observed. This explains, in particular, why the crack growth rate is not only sensitive to the duration of the fatigue cycle, but also to its shape.

These phenomena are modeled as follows. The crack growth rate is now the sum of two terms, the first term is due to crack tip plasticity (Eq. 3), while the second term accounts for the contribution of the time during which grain boundary oxidation takes place:

$$\frac{da}{dt}=\frac{\partial a}{\partial \rho_I}\frac{d\rho_I}{dt}+\frac{\partial a}{\partial t}=\underbrace{\alpha\left|\frac{d\rho_I}{dt}\right|}_{pure\ fatigue}+\underbrace{\frac{\partial a}{\partial t}}_{oxydation} \tag{12}$$

The cyclic elastic-plastic constitutive model for the crack tip region, which provides $\frac{d\rho_I}{dt}$, is a function of the temperature through the dependency of the material cyclic elastic-plastic behavior on the temperature. In addition, the adjustable parameter α was determined using fatigue crack growth experiments at rather high frequency, for which the contribution of the environment is assumed to be negligible (1-1 cycles).

The second term of this equation (Eq. 12) corresponds to the contribution of grain boundary embrittlement by the chemical environment to the fatigue crack growth. Simple partial derivative equations were used to represent the mechanisms of embrittlement identified by other authors [29, 5, 69, 34]. Since grain boundary embrittlement stems from a diffusion process, it was assumed to be thermally activated (Eq. 13).

$$\frac{\partial a}{\partial t} = m\beta_o exp\left(-\frac{Q}{kT}\right) \qquad (13)$$

The crack growth rate $\beta_0 exp\left(-\frac{Q}{KT}\right)$ by grain boundary embrittlement, in the absence of any passivation layer, is modulated by the variable m, which represents the state of that passivation layer. When $m=1$, the passivation layer is broken and the crack growth rate by grain boundary embrittlement is maximum. When $m=2$, the passivation layer is thick enough to fully protect grain boundaries against oxidation. Two adjustable parameters are introduced, in order to control the variations of m. The parameter R_G is introduced, to represent the growth rate of that passivation layer versus time; the parameter R_F is introduced so as to model how the rupture of the oxide layer increases the crack growth rate by grain boundary embrittlement. It is assumed that the oxide layer breaks when the crack tip is stretched, because of crack tip plasticity. This happens only at the opening, when $d\rho_I$ is positive.

$$\begin{cases} \dfrac{\partial m}{\partial t} = -R_G m \\ \dfrac{\partial m}{\partial \rho_I} = -R_F\left(1-m\right), \quad with\ d\rho_I > 0 \end{cases} \qquad (14)$$

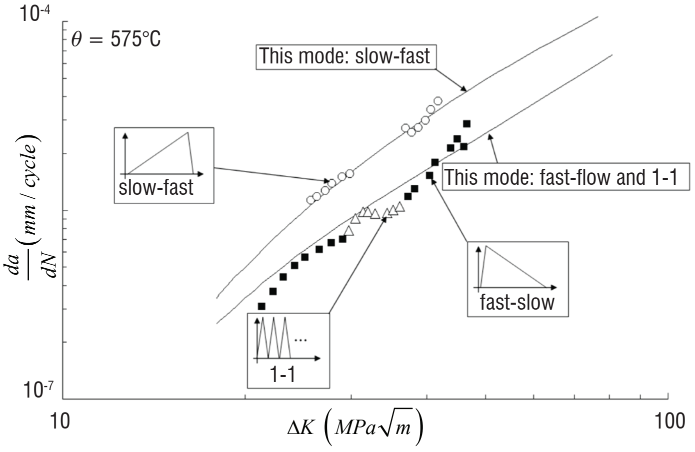

Figure 8 - Fatigue crack growth rate in CT specimens at 575°C in the N18 nickel base superalloy. Symbols correspond to experiments conducted by Hochstetter et al [29] and lines correspond to predictions by the incremental model [59].

This model was validated using complex isothermal fatigue crack growth experiments. For instance, it was possible to reproduce the difference between fast-slow and slow-fast fatigue crack growth experiments (figure 7) [29, 59]. This result was also satisfactory because the parameters were identified at 450°C, 550°C, 600°C and 650°C. 575°C is an intermediate temperature that was not used for the identification. It also successfully reproduces the effect of the shape of the fatigue cycle that was observed in the experiments, though this type of cycle was never used during the identification phase.

Mixed mode loading conditions

The model was then extended to the case of fatigue crack growth under Mixed Mode I + II, loading conditions [10, 11, 54] and for the general case of mixed-mode (I + II + III) loading conditions [21, 22]. P.Y Decreuse [10, 11, 54] and Flavien Fremy [21, 22] have clearly demonstrated, through fatigue crack growth experiments for Mixed Mode I + II and I + II + III on the Astree platform of the LMT, the importance of the load path effect in steel alloys to predict both the crack growth rate and the crack path.

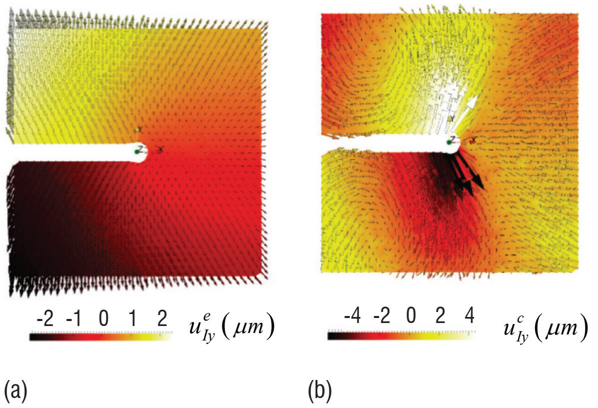

(a) (b)

Figure 9 - Mode I reference fields constructed using DIC. Intensity of the component normal to the crack plane. (a) Elastic reference field, (b) Non-elastic reference field.[10]

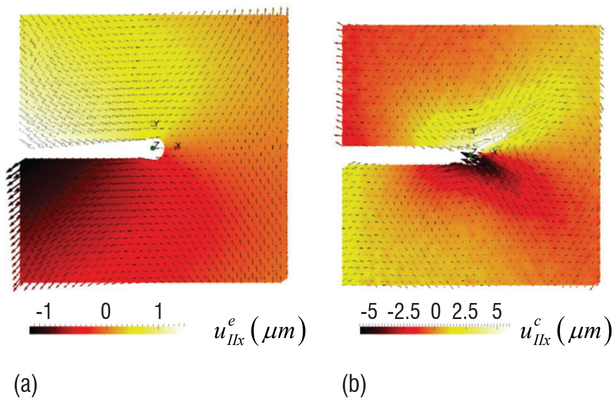

(a) (b)

Figure 10 - Mode II reference fields constructed using DIC. Intensity of the component parallel to the crack plane. (a) Elastic reference field, (b) Non-elastic reference field.[10]

Experimental velocity fields recorded using digital image correlation were post-treated, as explained in Section 2. The experimental reference fields are consistent with those obtained by FE simulations under mixed mode conditions.

It was also possible to determine the evolution $\dot{\rho}_I$ and $\dot{\rho}_{II}$ of the plastic intensity factors as a function of the nominal applied stress intensity factor rates $\dot{K}_I^\infty$ and $\dot{K}_{II}^\infty$. The experimental results confirmed the hypotheses of the model.

Experiments were conducted under Mode I+II and Mode I+II+III non-proportional loading conditions, in order to characterize the load path effect in fatigue crack propagation in 316L stainless steel and the contribution to fatigue crack growth of Mode III loadings [21, 22]. The same maximum, minimum and mean values of the stress intensity factors were used for each loading path in the experiments. Since the same maximum, minimum and mean values of the stress intensity factors were applied in each experiment, the load paths are all considered to be "equivalent" with respect to most of the fatigue crack growth criteria, in particular with respect to those based on $\Delta K_{eq} = \left(\Delta K_I^n + \beta \Delta K_{II}^n + \gamma \Delta K_{III}^n\right)^{1/n}$.

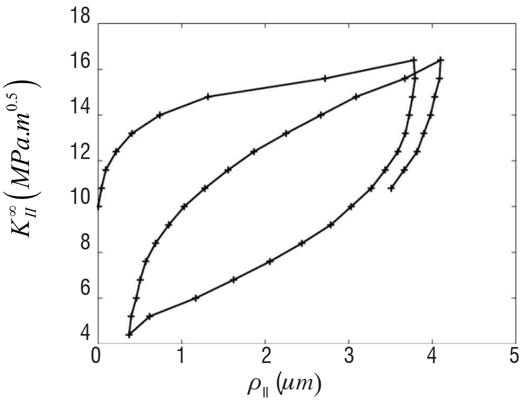

Figure 11 - Evolution of the CTSD as a function of the Mode II nominal applied stress intensity factor. Measurement performed using digital image correlation (DIC), during a Mode II loading phase $\Delta K_{II}^{\infty} = 12MPa\sqrt{m}$ around a mean value $\left(K_{I}^{\infty} = 30MPa\sqrt{m}, K_{II}^{\infty} = 0\right)$.[10]

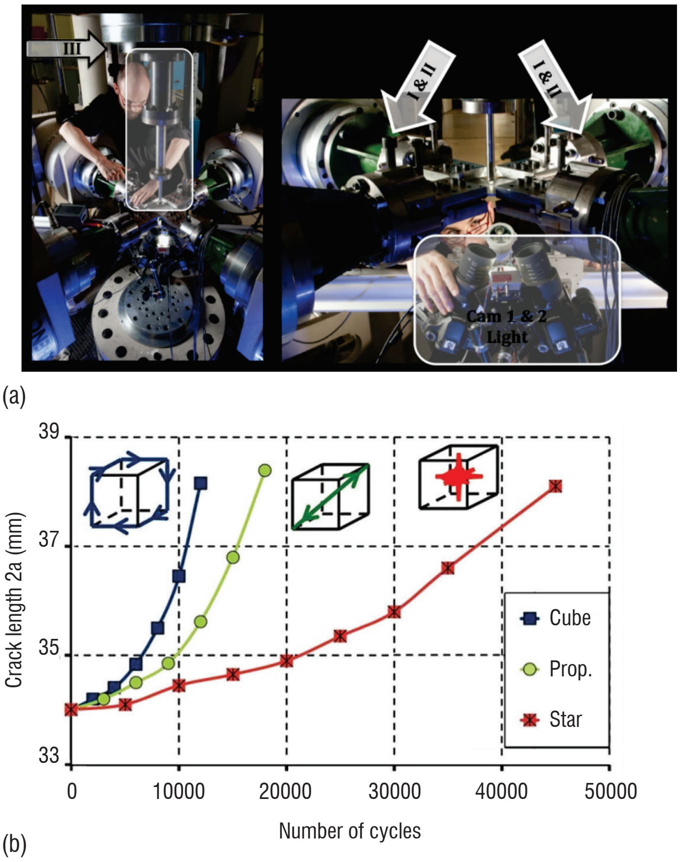

(a)

(b)

Figure 12 - (a) Experimental set-up -Six actuator servo-hydraulic testing machine ASTREE, (b) crack length evolution for three Mixed Mode I+II+III cases for which $\Delta K_I = \Delta K_{II} = \Delta K_{III}$. The three modes were either applied simultaneously (circles), or sequentially (cube), or one after the other (star). [21, 22]

The experiments were conducted on the multiaxial servo-hydraulic testing machine ASTREE, available at LMT. Six actuators were used simultaneously to perform the tests (figure 12). Three pairs of actuators were used to load the specimen along three orthogonal axes and to keep the intersection of the three loading axes fixed. Each horizontal loading axis was load controlled.

The main result of this set of experiments is that very different crack growth rates are observed even though the extreme values and the mean values of the stress intensity factors are the same in each test. A variation by up to a factor of three for the crack growth rate according to the loading path was observed in these experiments, even when the crack path remained macroscopically coplanar. In addition, it was shown that the crack path is also significantly dependent of the load path. For instance, the crack path remains coplanar for the "square" load path, while a tilt is observed for the "proportional" load path in Mixed Mode I+II. In these two cases, the extreme values of the Mode I and Mode II stress intensity factors are attained simultaneously.

Elastic plastic finite element analyses were conducted, in order to analyze, at the scale of the crack tip region, the load path effect on plastic flow under Mixed Mode I+II+III conditions (i.e. $\underline{\dot{\rho}} = \left(\dot{\rho}_I, \dot{\rho}_{II}, \dot{\rho}_{III}\right)$). The load paths tested in these simulations were identical to those used in experiments. By considering that the crack growth rate could be roughly estimated from the Mode I+II parts of the plastic flow rate within the crack tip region, it was possible to show that different load paths displaying the same stress intensity factors for each mode would nevertheless produce different plastic flow amplitudes and hence different crack growth rates.

The finite element simulations were consistent with the experiments, since it was possible to discriminate between the most and the least detrimental load paths and to predict the order of magnitude of the load path effect.

Finally, it was also shown that the mode mixity of the plastic flow rate within the crack tip region does not coincide with the mode mixity of the nominal applied stress intensity factor rate (figure 13). In particular, the addition of a Mode III stress intensity factor amplitude to a Mode I+II cycle increases the Mode I+II plastic flow amplitude in the cycle.

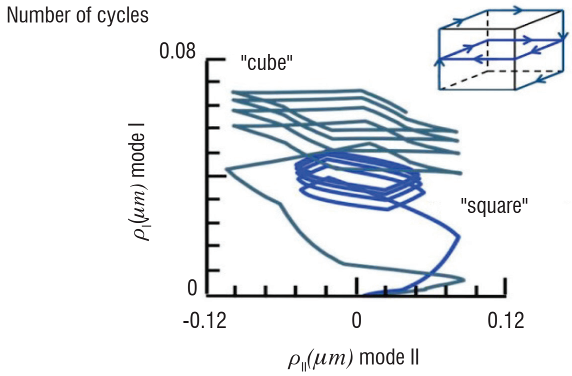

Figure 13 - Mode I+II plastic flow, as calculated from FE analyses, for the "square" and "cube" load paths. The plastic flow amplitude in Mixed Mode I+II is increased when a Mode III stress intensity factor amplitude is added to a Mode I+II load cycle. [22]

A model for mixed mode plasticity was introduced and was the subject of the PhD thesis of F. Fremy in Mode I+II+III [21, 22] and of P. Y. Decreuse in Mode I+II [10, 11, 54]. The model predicts the evolutions of the plastic intensity factor under variable amplitude and non-proportional mixed mode conditions, and the plasticity rates predicted by the model under complex conditions are consistent with crack growth rates obtained in the experiments.

At the moment, the model under Mixed Mode I+II+III conditions contains only one elastic domain for the cyclic plastic zone. It was able to successfully predict the load path effect in constant amplitude fatigue (in phase / out of phase, proportional versus square versus star cycles). However, in order to predict the overload effect, for example, a second elastic domain for the monotonic plastic zone would be useful.

The plasticity model for the crack tip region under Mixed Mode I+II+III conditions contains three components:

- A yield function
- A normality flow rule
- A kinematic hardening rule

The yield criterion was obtained by considering that the yield condition is reached under mixed-mode conditions for the same critical distortional elastic energy as in Mode I. It is then analogous to the Von Mises criterion, except that instead of being applied to a material point, it is applied to the entire crack tip region. To some extent, it is a non-local Von Mises criterion tailored to cracks. To do so, the distortional elastic energy density was calculated under mixed mode conditions using the Westergaard stress functions [66] and then integrated over a domain with a radius D around the crack tip. Given that the Westergaard stress functions [66] of each mode depend on the distance to the crack tip in the same way, the critical distortional elastic energy criterion is not dependent on D and can be reduced to:

$$f = \frac{\left(K_I^{\infty} - K_I^X\right)^2}{\left(K_I^Y\right)^2} + \frac{\left(K_{II}^{\infty} - K_{II}^X\right)^2}{\left(K_{II}^Y\right)^2} + \frac{\left(K_{III}^{\infty} - K_{III}^X\right)^2}{\left(K_{III}^Y\right)^2} - 1$$

where $K_{II}^Y = K_I^Y \sqrt{\frac{7-16\nu(1-\nu)}{19-16\nu(1-\nu)}} \approx 0.48\, K_I^Y$

and $K_{III}^Y = K_I^Y \sqrt{\frac{7-16\nu(1-\nu)}{24}} \approx 0.39\, K_I^Y$

or

$$f\left(G_I, G_{II}, G_{III}\right) = \frac{\left|G_I\right|}{G_I^Y} + \frac{\left|G_{II}\right|}{G_{II}^Y} + \frac{\left|G_{III}\right|}{G_{III}^Y} - 1$$

where $G_i^Y = \frac{1-\nu^2}{E}\left(K_i^Y\right)^2$

and $G_i = signe\left(K_i^{\infty} - K_i^X\right)\frac{1-\nu^2}{E}\left(K_i^{\infty} - K_i^X\right)^2$

This criterion was shown to be consistent with finite element computations and also, in Mixed Mode I+II, with results obtained using digital image correlation.

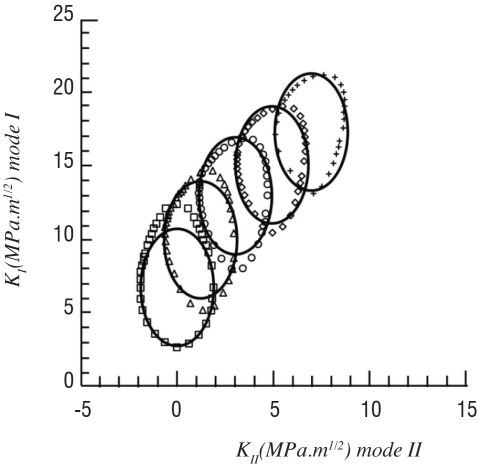

Figure 14 - Evolution of the yield surface during a Mixed Mode I+II loading ramp. The symbols corresponds to the yield points determined from FE computations using the C_{1R}-C_{2R} numerical criterion (Eqs. 9 & 10), the solid lines correspond to the yield function based on a critical distortional energy [54].

The size of the elastic domain is still assumed to be a constant and the shape of the elastic in a K_I, K_{II}, K_{III} diagram is an ellipsoid, whose aspect ratios are a function of the Poisson ratio of the material.

The center of the elastic domain is allowed to be displaced along the plastic flow direction $\underline{\dot{\rho}} = \left(\dot{\rho}_I, \dot{\rho}_{II}, \dot{\rho}_{III}\right)$. In addition, the plastic flow direction is assumed to be normal to the yield function in terms of G_i.

The model was shown to be able to reproduce the evolution of the plastic flow intensity factors calculated using mixed mode elastic plastic FE computations, when complex loading conditions where applied.

Conclusions and future work

An approach was proposed to model the non-local elastic-plastic behavior of the crack tip region. This approach is based on an approximation of the kinematics of the crack tip region. To some extent, it is a non-local elastic plastic constitutive model, tailored to a crack tip region.

The use of this model makes it possible to enrich the usual linear elastic fracture mechanics functions by additional terms that are capable of accounting for the cyclic elastic-plastic behavior of the material, including history effects. The model is valid only under small scale yielding conditions and is dedicated to predicting fatigue crack growth under complex loading conditions (variable amplitude loading, non-isothermal conditions, etc.).

The model provides a scalar measurement of the amount of plastic flow for each mode during a time step, as a function of the loading step (given in terms of the stress intensity factors for each mode). The parameters of the model can be identified using the constitutive law of the material and finite element computations of the behavior of the crack tip region. This model is a non-linear constitutive law for the crack tip region, with internal variables to account for memory effects. A temperature dependency of its parameters can be defined, in order to use it under non-isothermal conditions.

Thus, the rate of production of cracked areas during a time step, due to pure fatigue, is assumed to be directly proportional to the amount of plastic flow predicted by the model. Other mechanisms (oxidation, corrosion) can be also considered and added to the crack propagation law if necessary.

The constitutive model for the crack tip region and the crack propagation law, together, are an incremental model for fatigue crack growth.

In Mode I, the model was completely identified for predicting fatigue crack growth under mixed mode conditions and validated using a large set of experiments. It was extended to non-isothermal conditions and the crack propagation law was completed to include a contribution of oxidation to crack growth. The model simulations were compared to experimental results giving satisfactory results.

Under mixed mode conditions, the model was partially developed and was shown to be able to predict the load path effect successfully under mixed mode conditions. It also provides a framework to analyze mixed mode fatigue tests, in particular the role of Mode III on fatigue crack growth.

The model requires additional development to be able to predict the overload effect under mixed mode conditions. This would not require extensive numerical or modeling work, but the validation by means of experiments would require significant effort. In addition, the prediction of the crack path under mixed mode conditions requires further work. Ongoing work is aimed at extending the validity domain of the model to short cracks by including the T-stresses and to large scale yielding conditions ■

Acknowledgements

I would like to warmly acknowledge the PhD students and Post Doctorates who contributed directly to the development of this model, or that are developing it, Marion Risbet, Rami Hamam, Juan Antonio Ruiz Sabariego, Pablo Lopez Crespo, Pierre-Yves Decreuse, Sophie Dartois, Flavien Fremy, François Brugier and Wen Zhang. Also, I would like to acknowledge our industrial partners for their constant support and interest, Snecma, EDF and AREVA, SNCF and the DGA. In addition, I would also like to acknowledge all of my colleagues for fruitful discussions, Veronique Doquet, François Hild, Ahmed Benallal, Rodrigue Desmorat, Antony Gravouil, Bertrand Burgardt, Didier Soria, Marie Christine Baietto and many others.

References

[1] M.R. HTER, G.J.DANEK, H.H. SMITH - *Effect on Fatigue of Gaseous Environments Under Varying Temperature and Pressure.* Trans. Metall. Soc. AIME, 227(December), 1296–1301, 1963

[2] D. ALIAGA - *Prevision de la fissuration en fatigue sous chargements d'amplitude variable*. Modele PREFFAS, Aerospatiale, Laboratoire Central Doc. PV. No. 47.904, (1985).

[3] J-L. BOUVARD - *Modélisation de la propagation de fissures dans les aubes de turbine monocristallines.* Thesis of ENSMP, Paris, 2006

[4] M.W.B. BROWN, S. L. WONG, et al. (2000) - *Fatigue Crack Growth Rates under Sequential Mixed-Mode I and II Loading Cycles.* Fatigue & Fracture of Engineering Materials & Structures 23(8): 667-674.

[5] J-C. CHASSAIGNE - *Fissuration à hautes temperatures du superalliage base nickel N18 élaboré par métallurgie des poudres, étude du couplage mécanique-environnement en pointe de fissure.* Thèse de l'Ecole Nationale Supérieure des Mines de Paris, 1997

[6] B. H. CHOI, J. M. LEE (2009) - *Experimental Observation and Modeling of the Retardation of Fatigue Crack Propagation under the Combination of Mixed-Mode Single Overload and Constant Amplitude Loads.* International Journal of Fatigue 31(11-12): 1848-1857.

[7] P. DAHLIN, M. OLSSON (2004) - *Reduction of Mode I Fatigue Crack Growth Rate Due to Occasional Mode II Loading.* International Journal of Fatigue 26(10): 1083-1093.

[8] P. DAHLIN, M. OLSSON (2006) - *Mode I Fatigue Crack Growth Reduction Mechanisms After a Single Mode II Load Cycle.* Engineering Fracture Mechanics 73(13): 1833-1848.

[9] P.Y. DECREUSE, S. POMMIER, M. PONCELET, B. RAKA(2011) - *A Novel Approach to Model Mixed Mode Plasticity at Crack Tip and Crack Growth. Experimental Validations Using Velocity Fields from Digital Image Correlation.* International Journal of Fatigue

[10] P.Y. DECREUSE, S. POMMIER, L. GENTOT, S. PATTOFATTO - *History Effect in Fatigue Crack Growth under Mixed Mode Loading Conditions.* Int. J. Fatigue, vol. 31, pp. 1733–1741, (2009)

[11] P.Y. DECREUSE, S. POMMIER, M. PONCELET, B. RAKA - *A Novel Approach to Model Mixed Mode Plasticity at Crack Tip and Crack Growth. Experimental Validations Using Velocity Fields from Digital Image Correlation.* Int Jal of Fatigue. 2011 http://dx.doi.org/10.1016/j.ijfatigue.2011.11.021.

[12] V. DOQUET, G. BERTOLINO (2008) - *Local Approach to Fatigue Cracks Bifurcation.* International Journal of Fatigue 30(5): 942-950.

[13] V. DOQUET, S. POMMIER (2004) - *Fatigue Crack Growth under Non-Proportional Mixed-Mode Loading in Ferritic-Pearlitic Steel.* Fatigue & Fracture of Engineering Materials & Structures 27(11): 1051-1060.

[14] V. DOQUET, Q.H. BUI, A. CONSTANTINESCU (2010) - *Plasticity and Asperity-Induced Fatigue Crack Closure under Mixed-Mode Loading.* International Journal of Fatigue, Vol. 32, pp. 1612-1619.

[15] V. DOQUET, M. ABBADI, et al. (2009) - *Influence of the Loading Path on Fatigue Crack Growth under Mixed-Mode Loading.* International Journal of Fracture 159(2): 219-232.

[16] K.D. DUGDALE - *Yielding of Steel Sheets Containing Slits.* J. Mech. Phys. Solids, 8, pp. 100- 104 (1960).

[17] W. ELBER (1971) - *The Significance of Fatigue Crack Closure.* ASTM STP 486: 230-242

[18] W. ELBER - *Fatigue Crack Closure under Cyclic Tension.* Engineering Fracture Mechanics. 2, pp.37-45 (1970).

[19] N.A. FLECK (1988) - *Influence of Stress State on Crack Growth Retardation.* American Society for Testing and Materials 1: 157-183.

[20] R.G. FORMAN, V.E. KEARNEY, R.M. ENGLE - *Numerical Analysis of Crack Propagation in Cyclic-Loaded Structures.* J. Basic Engng., Trans. ASME D89, pp.459-464, (1967).

[21] F. FREMY, S. POMMIER, E. GALENNE, S. COURTIN, J.C. LE-ROUX - *Load Path Effet on Fatigue Crack Propagation in I+II+III Mixed Mode Conditions - Part 2 : Finite Element Analyses.* Int Jal of Fatigue. Vol 62. Pages 113-118. 2014 DOI

[22] F. FREMY, S. POMMIER, M. PONCELET, B. RAKA, E. GALENNE, S. COURTIN, J.C. LE ROUX - *Load Path Effect on Fatigue Crack Propagation in I + II + III Mixed Mode Conditions – Part 1: Experimental Investigations*. Int Jal of Fatigue. Vol 62. Pages 104-112. 2014

[23] H. FUEHRING, T. SEEGER - *Dugdale Crack Closure Analysis of Fatigue Cracks under Constant Amplitude Loading*. Engng. Fracture Mech. 11, pp. 99-122 (1979).

[24] H. GAO, S. UPUL(1996) - *Effect of Non-Proportionnal Overloading in Fatigue Life.* Fat. Fract. Eng. Mat. Struct. 19: 1197-1206.

[25] R. GERVAIS-MOLINS - *Oxydation de superalliages à base nickel.* Thèse de l'Ecole Nationale Supérieure des Mines de Paris, 1995

[26] A. GRAVOUIL, N. MOËS, T. BELYTSCHKO (2002) - *Non-Planar 3D Crack Growth by the Extended Finite Element and Level Sets - Part II: Level Set Update.* International Journal for Numerical Methods in Engineering 53(11): 2569-2586.

[27] R. HAMAM, S. POMMIER, F. BUMBIELER - *Mode I Fatigue Crack Growth Under Biaxial Loading*. Int Jal of Fatigue. Vol 27. Num 10. Pages 1342-1346. 2005

[28] R. HAMAM, S. POMMIER, F. BUMBIELER - *Variable Amplitude Fatigue Crack Growth, Experimental Results and Modelling*. Int Jal of Fatigue. Vol 29. Num 9-11. Pages 1634-1646. 2007

[29] G. HOCHSTETTER - *Propagation des fissures à haute temperature dans le superalliage N18 pour disques de turbomachine. Interactions entre la nature des sollicitations mécaniques et des effets d'oxydation.* Thesis of ENSMP, Paris, 1994

[30] F. HOURLIER, A. PINEAU(1982) - *Propagation of Fatigue Cracks under Polymodal Fatigue.* Fatigue of Engineering Materials and Structures, Vol5 (4), pp. 287-302.

[31] J. TONG , S. DALBY , J. BYRNE , M.B. HENDERSON , M.C. HARDY - *Creep, Fatigue and Oxidation in Crack Growth in Advanced Nickel Base Superalloys.* International Journal of Fatigue 23, 897–902, 2001

[32] K. KARHUNEN - *Über Lineare Methoden in der Wahrscheinli - Chkeitsrechnung*. Mat.-Phys., 37 (1947), 1–79.

[33] S. KRUCH, J-L. CHABOCHE, S. PRIGENT - *A Fracture Mechanics Based Fatigue-Creep-Environment Crack Growth Model at High Temperatures.* Int. J. Press. Vess. And Pipping, 59:141-148, 1995

[34] J-C. LAUTRIDOU, J-Y. GUEDOU, Y. HONNORAT - *Effects of Inclusions on LCF Life of PM Superalloys for Turboengines Disks,* Conf. high temperature materials for power engineering, eds. Kluwer academics publishers, 1163, 1990

[35] V. LAZARUS, J. B. LEBLOND, ET AL. (2001) - *Crack Front Rotation and Segmentation in Mixed Mode I+III or I+II+III. Part I: Calculation of Stress Intensity Factors.* Journal of the Mechanics and Physics of Solids 49(7): 1399-1420.

[36] J. LEMAITRE, J.L. CHABOCHE(1988). *Mécanique des matériaux solides.*

[37] C. S. LI(1989) - *Vector Ctd Criterion Applied to Mixed-Mode Fatigue Crack-Growth.* Fatigue & Fracture of Engineering Materials & Structures 12(1): 59-65.

[38] P. LOPEZ-CRESPO, S. POMMIER - *Numerical Analysis of Crack Tip Plasticity and History Effects under Mixed Mode Conditions*. Journal of Solid Mechanics and Materials Engineering, Outstanding Researches by Promising Young Researchers in Mechanics and Materials Division III. Vol. 2 (2008), No. 12, pp 1567-1576

[39] A. M. A. MAGEED, R. K. PANDEY (1992) - *Studies on Cyclic Crack Path and the Mixed-Mode Crack Closure Behavior in Al-Alloy.* International Journal of Fatigue 14(1): 21-29

[40] R. C. MCCLUNG (1991) - *Crack Closure and Plastic Zone Sizes in Fatigue.* Fatigue & Fracture of Engineering Materials & Structures 14(4): 455-468.

[41] A.J. McEVILY, R. J. DONAHUE, et al. (1972) - *Crack Opening Displacement and Rate of Fatigue Crack Growth.* International Journal of Fracture Mechanics 8(2): 209-219.

[42] R. MOLINS, G. HOSCHTETTER, J-C. CHASSAIGNE, E. ANDRIEU - *Oxydation Effects on the Fatigue Crack Growth of Alloy 718 at High Temperatures.* Acta. Mater., Vol 45, N°2, pp. 663474, 1996

[43] H. NAYEB-HASHEMI, M. E. TASLIM (1987) - *Effects of the Transient Mode-II on the Steady-State Crack-Growth in Mode-I.* Engineering Fracture Mechanics 26(6): 789-807.

[44] P. NEUMANN (1969) - *Coarse Slip Model of Fatigue.* Acta Metallurgica 17(9):1219-&.

[45] P. NEUMANN (1974) - *The Geometry of Slip Processes at a Propagating Fatigue Crack—II.* Acta Metallurgica 22(9): 1167-1178.

[46] J.C. NEWMAN (1976) - *A Finite-Element Analysis of fatigue crack closure.* American Society for Testing and Materials: ASTM STP 590, pp. 281-301.

[47] J.C. NEWMAN, W. ELBER (1988) - *Mechanics of Fatigue Crack Closure.* ASTM STP 982 PA 19103.

[48] R. M. N. PELLOUX (1969) - *Mechanisms of Formation of Ductile Fatigue Striations.* Asm Transactions Quarterly 62(1): 281-&.

[49] S. PERUSIN - *Conséquences de l'oxydation haute température sur l'injection de défauts et le comportement mécanique des matériaux métalliques.* Thèse de l'Institut Polytechnique de Toulouse, 2004

[50] R. PIPPAN, J. POKLUDA (2005) - *Can Pure Mode III Fatigue Loading Contribute to Crack Propagation in Metallic Materials?* Fatigue & Fracture of Engineering Materials & Structures 28(1-2): 179-185.

[51] R. PLANK, G. KUHN (1999) - *Fatigue Crack Propagation under Non-Proportional Mixed Mode Loading.* Engineering Fracture Mechanics 62(2-3): 203-229.

[52] S. POMMIER - *Cyclic Plasticity of a Cracked Structure Submitted to Mixed Mode Loading.* Key Engineering Materials. Vol 348-349. Pages 105-108. 2007

[53] S. POMMIER, R. HAMAM - *Incremental Model for Fatigue Crack Growth Based on a Displacement Partitioning Hypothesis of Mode I Elastic-Plastic Displacement Fields.* Fatigue & Fracture of Engineering Materials & Structures. Vol 30. Num 7. Pages 582-598. 2007

[54] S. POMMIER, P. LOPEZ-CRESPO, P.Y. DECREUSE (2009) - *A Multi-Scale Approach to Condense the Cyclic Elastic-Plastic Behaviour of the Crack Tip Region into an Extended Constitutive Model.* Fatigue & Fracture of Engineering Materials & Structures 32(11): 899-915.

[55] S. POMMIER, M. RISBET - *Time-Derivative Equations for Fatigue Crack Growth in Metals*. Int Jal of Fracture. Vol 131. Num 1. Pages 79-106. 2005

[56] S. POMMIER, M. RISBET - *Time-Derivative Equations for Mode I Fatigue Crack Growth in Metals.* Int Jal of Fatigue. Vol 27. Num 10. Pages 1297-1306. 2005

[57] J. QIAN, A. FATEMI (1996) - *Mixed Mode Fatigue Crack Growth: A Literature Survey.* Engineering Fracture Mechanics 55(6): 969-990.

[58] J.R. RICE, R. THOMSON (1974) - *Ductile Versus Brittle Behavior of Crystals*. Philosophical Magazine, vol. 29, p.78.

[59] J.A. RUIZ-SABARIEGO, S. POMMIER - *Oxidation Assisted Fatigue Crack Growth under Complex Non-Isothermal Loading Conditions in a Nickel Base Superalloy*. Int. J. Fatigue, vol. 31, pp. 1724–1732, (2009)

[60] J. SCHIJVE - *An evaluation of a Fatigue Crack Growth Prediction Model for Variable Amplitude Loading* (PREFFAS), NLR – 537, (1987).
[61] J. SCHIJVE - *Some Formulas for the Crack Opening Stress Level.* Engineering Fracture Mechanics, 14, pp. 461-465 (1981).
[62] E. THIEULOT-LAURE, S. POMMIER, S. FRECHINET - *A Multiaxial Fatigue Failure Criterion Considering the Effects of the Defects.* Int Jal of Fatigue. Vol 29. Num 9-11. Pages 1996-2004. 2007
[63] E.K. TSCHEGG (1983) - *Mode-III and Mode-I Fatigue Crack-Propagation Behavior under Torsional Loading.* Journal of Materials Science 18(6): 1604-1614.
[64] A.K. VASUDEVAN, K. SADANANDA, R.L. HOLTZ - *Analysis of Vacuum Fatigue Crack Growth Results and its Implications*. International Journal of Fatigue 27 (2005) 1519–1529
[65] R.P. WEI, G.W. SIMMONS - *Recent Progress in Understanding Environment-Assisted Fatigue Crack Growth.* Int. J. Fract., 17(2), 235–247, 1981
[66] H. WESTERGAARD (1939) - *Bearing Pressures and Cracks.* Journal of Applied Mechanics, 6:49–53.
[67] O.E. WHEELER - *Spectrum Loading and Crack Growth.* ASMR 72 MetX also G.D. Report FZM 5602, (1970)
[68] J. WILLENBORG, R.M. ENGLE, H.A. WOOD - *A Crack Growth Retardation Model Using an Effective Stress Concept*. AFFDL-TM-71-1-FBR. (1971).
[69] S.T. WLODEK, M. KELLY, D. ALDEN - *The Structure of N18 Superalloys.* Ed S. D;. Antolovitch et al., T.M.S, 467-476, 1992
[70] G.A. WOODFORD - *Gas Phase Embrittlement and Time Dependent Cracking of Nickel Based Superalloys*. Energy Materials, Vol 1, No 1, pp 59-79, 2006

AUTHOR

Sylvie Pommier graduated from the Ecole Centrale de Lyon (ECL - 1992) and from the Ecole Centrale Paris (French PhD in 1995). She first joined the Ecole Centrale Paris as a faculty member (1995-2003) and then the Ecole Normale Supérieure de Cachan as a Professor in Mechanical Engineering.

From 2009 to 2012 she was the Dean of the doctoral School of the Ecole Normale Supérieure de Cachan (ENS Cachan). From 2012 to 2014 she was vice-president of ENS Cachan in charge of research and doctoral training and was involved in the set-up of the doctoral college of University Paris Saclay. Since 2014, she has been in charge of the doctoral college of University Paris Saclay.

Sylvie Pommier is a specialist in fracture mechanics and works in the field of defect tolerance design methods under non-linear conditions (inelastic material behavior, non-isothermal loading conditions, chemo-mechanical coupling, mixed-mode crack growth under non-linear conditions) for aerospace, nuclear and naval applications.